International Symposium on Lunar and Planetary Science

ISLPS 2016

June 9-10, 2016 / Wuhan, China

NSFC

科學技術發展基金
FDCT

王寬誠教育基金會
K. C. WONG EDUCATION FOUNDATION

中国地质大学
CHINA UNIVERSITY OF GEOSCIENCES

澳門科技大學
MACAU UNIVERSITY OF SCIENCE AND TECHNOLOGY

Schedule and Contents

9-June

8:00-8:45 Opening, Chair **Ouyang Ziyuan**

Session 1 Lunar Rocks

Chairs: Clive Neal and Yangting Lin

8:45-9:10	**Clive Neal** and D. S. Draper *Are Ferroan Anorthosites Direct Products of the Lunar Magma Ocean?*	1
9:10-9:25	**Y. H. Lin**, E. S. Steenstra, W. van Westrenen *Hydrous Early Moon? Constraints from Hydrous Lunar Magma Ocean Solidification Experiments*	3
9:25-9:40	**Y.Miura** and T. Tanosaki *Lunar Minerals and Rocks: Volatiles Separted by Impact and Volcanic Events*	5
9:40-9:55	**X. Y. Zhang**, A. A. Xu, Z. S. Tang, Z. Y. Ouyang, Y. Z. Wu *Mineralogical Variation of the Late Stage Mare Basalts*	6
9:55-10:10	**Xianmin Wang** *Identification of Rock Suits on the Lunar Surface*	8
10:10-10: 25	**Ying Sun** *Quantitative Spectral Analysis with M3 Images Applied to the Theophilus Central Peak*	9
10:25-10:40	Coffee Break	

Session 2 Surface Processes on the Moon

Chairs: R. Bugiolacchi and Zhiyong Xiao

10:40-10:55	**Bo Li**, Jiang Zhang, Zongcheng Ling, Jian Chen *Displacement-Length Relationship and Amount of Strain for Lunar Wrinkle Ridges in Mare Serenitatis and Tranquillitatis*	12
10:55-11:10	**Bo Wu**, Tao Jun Lin, Jinyi Li, and Yiran Wang *Distribution and Population Characteristics of Lunar Craters in Orientale Basin from the Recent High-Resolution Remote Sensing Datasets*	14
11:10-11:25	**Zhiyong Xiao** *Emplacement History of Self-Secondaries*	16
11:25-11:40	**R. Bugiolacchi** *Survey and Analysis of the Craters Population in the Apollo 17 Region: Wider Implications for Crater Geochronology*	18

11:40-11:55	**Jun Du**, Wenzhe Fa, Minggang Xie, And Meng-Hua Zhu *Thickness of Lunar Maria Basalts: New Results Based on Degraded Partially Buried Craters*	20
12:10-14:00	Lunch Break	

Session 3 Lunar Interior

Chairs: Mark A. Wieczorek and R. Yamada

14:00-14:25	**Mark A. Wieczorek** *New Results from NASA's Lunar Gravity Mapping Mission GRAIL*	22
14:25-14:40	**Qian Huang** *Mass Anomalies Beneath the Surface of Lunar Volcanic Complexes from GRAIL Bouguer Gravity Field*	23
14:40-14:55	**X. Y. Wang**, Q. Liang *Linear Structures of Lunar Gravity Anomalies*	25
14:55-15:10	**Yan Jianguo**, Zhang Yi, Li Fei, Ye Mao, Chen Chao, Du Jinsong *High Resolution Lunar Mascon Density Structure Revealed by Grail Gravity*	27
15:10-15:25	**Y. Harada**, S. Goossens, K. Matsumoto, J. Yan, J. Ping, H. Noda, And J. Haruyama *The Deep Lunar Interior with a Low-Viscosity Zone: Revised Constraints from Recent Geodetic Parameters on the Tidal Response of the Moon*	28
15:25-15:40	**Yu Shuoran**, Tosi Nicola, Wong Hon-Cheng *Competition Between Stagnant Lid Thickening and Development of Lunar Magma Ocean Overturn*	29
15:40-15:55	***R. Yamada**, Y. Ishihara, N. Kobayashi, H. Murakami, S. Tanaka, et al.* *Scientific Results Expected from the APPROACH Mission*	31
15:55-16:10	Coffee Break	

Session 4 Atmosphere and Space Physics

Chairs: Jun Cui and Yong Wei

16:10-16:35	**Jun Cui** *How to Interpret the Temperature Variability in Titan's Upper Atmosphere*	33
16:35-:16:50	**Zhenfei Zhang**, Qian Huang *Magnetic Field-Associated Dielectric Anisotropy of the Martian Ionosphere Detected by MARSIS*	34
16:50-17:15	**Y. Wei** and W. Wan *Comparative Aeronomy as a Planetary Perspective on Earth's Environmental Evolution*	36

17:15-17:30	**Lianghai Xie,** Xiaoping Zhang, Yongchun Zheng, Dawei Gu *Solar Wind-Generated Current in the Lunar Dust Experiment*	37
17:30-17:45	**K. C. Chow**, K. L. Chan, and K. V. Tam *Numerical Modeling of the Atmospheric Circulation and Dust Cycle on Mars*	39
17:45-18:45	**Poster Session** (Page 75-124)	

10-June

Session 5 Water on Mars

Chairs: J. W. Head III and Timothy D. Glotch

8:00-8:25	**J. W. Head III** *Late Noachian "Cold and Icy Highlands" Model: Geological Predictions for Equilibrium Environments and Non-Equilibrium Melting Scenarios*	41
8:25-8:40	**D. R. Hood**, S. Karunatillake, D. Susko *Martian Bulk Soil Hydration Revealed by Principal Component Analysis of Regional Chemical Data*	43
8:40-8:55	**S. Hu**, Y. T. Lin, W. Yang, J. C. Zhang, J. L. Hao, W. F. Xing, T. Zhang *Martian Water: Origin and Evolution*	45
8:55-9:20	**T. D. Glotch,** M. M. Osterloo, J. L. Bandfield *Composition, Physical Properties, and Hydration State of Halite-Bearing Deposits on Mars*	47
9:20-9:45	**J. P. Bibring** *Mars History Revisited: Building New Paradigm*	48
9:45-10:00	Coffee Break	

Sesssion 6 Mars Surface Geology

Chairs: Long Xiao and Goro Komatsu

10:00-10:15	**S. Gou**, K. Di, and Z. Yue *Characterization of Hydrous and Mafic Minerals in Tyrrhena Terra, Mars*	49
10:15-10:30	**Zongyu Yue**, S. Gou, H. Xie, K. Di. *An Investigation into the Paradox for the Platy-Ridged-Polygonized Terrain in Elysium Planitia, Mars*	51
10:30-10:55	**Goro Komatsu** *The Utility of Field Conferences in Harnessing the Scientific Potential of Terrestrial Analogs in Asia for Planetary Geology Research*	54
10:55-11:20	**Long Xiao,** J. Wang, Y. N. Dang, Z. Y. Cheng, T. Huang, J N. Zhao, J. Huang, Y. Xu, Z. Y. Xiao *Qaidam Basin, NE Tibetan Plateau: A New Unique Mars Analogue Site for Its Wet Past and Dry*	55

Sesssion 7 Mineralogy and Geochemistry

Chairs: Liping Qin and Aicheng Zhang

Sesssion 8 Small Bodies

Chairs: Jianyang Li and Noriyuki Namiki

17:00-17:25	T. Mizuno, H. Senshu, H. Noda, **N. Namiki**, S. Oshigami, T. Kase, T. Shiina, et al. *Development and Initial Operation of Hayabusa2 LIDAR*	71
17:25-17:40	**Zhuo-Xi Huo** and Jiang-Chuan Huang *CROWN: A Constellation of Heterogenous Wide-Field NEO Surveyors*	72
17:40-17:55	**Koji Matsumoto** and H. Ikeda Moments of Inertia of Phobos with Inhomogeneous Internal Structure	73
17:55-18:10	Closing Remarks, Chair **James W. Head III**	

Posters

Print Only

Are Ferroan Anorthosites Direct Products of the Lunar Magma Ocean?

C. R. Neal[1] and D. S. Draper[2], [1]Dept. Civil & Env. Eng. & Earth Sciences, University of Notre Dame, Notre Dame, IN 46556, USA (neal.1@nd.edu), [2]ARES, NASA Johnson Spaace Center, 2101 NASA Parkway, Houston TX 77058, USA (david.draper@nasa.gov).

Introduction: According to Lunar Magma Ocean (LMO) theory, lunar samples that fall into the ferroan anorthosite (FAN) category represent the only samples we have of of the primordial crust of the Moon (e.g., [1]). Modeling indicates that plagioclase crystallizes after >70% LMO crystallization and formed a flotation crust (e.g., [2-6]), depending upon starting composition. The FAN group of highlands materials has been subdivided into mafic-magnesian, mafic-ferroan, anorthositic-sodic, and anorthositic-ferroan, although it is not clear how these subgroups are related [7]. Recent radiogenic isotope work has suggested the range in FAN ages and isotopic systematics are inconsistent with formation of all FANs from the LMO [8-12]. While an insulating lid could have theoretically extend the life of the LMO to explain the range of the published ages [3], are the FAN compositions consistent with crystallization from the LMO? As part of a funded Emerging Worlds proposal (NNX15AH76G), we examine this question through analysis of FAN samples. We compare the results with various LMO crystallization models, including those that incorporate the influence of garnet [13,14].

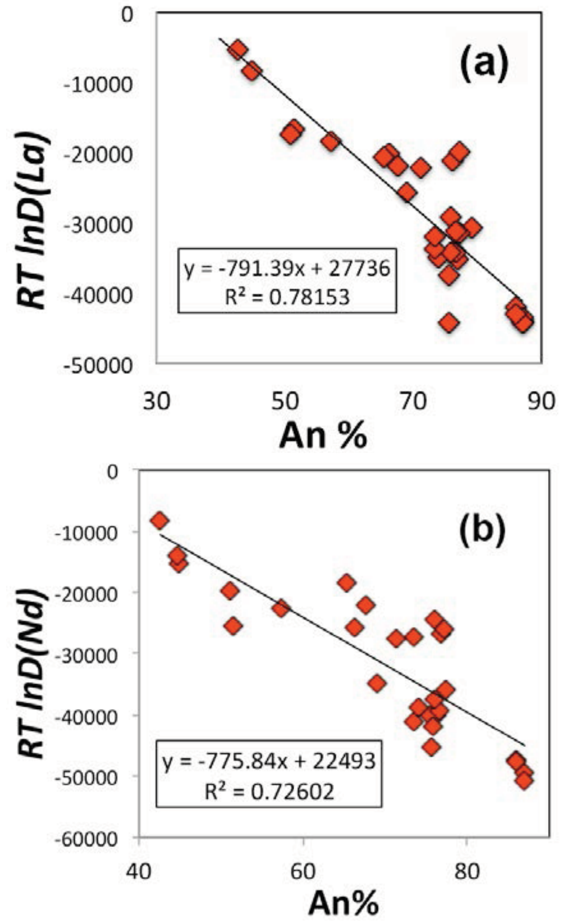

Fig. 1: Correlation of experimental plagioclase trace element partitioning data that allows calculation of partition coefficients based upon An content [19].

Samples and Methods. As an initial step in this project, we use published data to examine the hypothesis that FANs are a direct product of the LMO. Plagioclase major and trace element data from FAN samples are used [15,16]. Partition coefficients are calculated using the method of [17,18] that was modified by [19]. This method uses the Anorthite (An) content of the plagioclase to calculate partition coefficients using an array of experimental data to define a correlation between *An%* and *RT lnD* (**Fig. 1**). This approach allows realistic estimates of the liquid compositions from which the plagioclase in each FAN sample crystallized. The equilibrium data are then compared with the models of LMO crystallization [2-7].

LMO Crystallization. Crystallization of the LMO has been modeled in several studies, both theoretical (e.g., [2,3]) and experimental [4-6]. The trace element composition of the LMO can be modeled assuming a starting composition (3 × chondrites after [2]). As shown by [14], the different mineral proportions in the models of [2-6] can approximate KREEP REE patterns, but these are better generated by incorporation of 3-5% garnet once the LMO has become saturated in Al_2O_3 (see [2-6] for details). Following the methods of [20], the REE evolution of each LMO model has been calculated. These evolution paths have been compared with the equilibrium liquid compositions of the FAN plagioclases. Results are shown in **Figs. 2 & 3**.

Discussion. The LMO models terminate at ≥99% crystallization, which is considerd to be the amount of crystallization required to generate urKREEP. The high-K KREEP composition of [20] is plotted in **Figs. 2 & 3** for comparison. In the LMO modeling, various amounts of garnet are included at the expense of plagioclase when plagioclase is a liquidus phase. If the FANs crystallized from the LMO, the equilibrium liquids should plot along the LMO evolution lines where plagioclase is a liquidus phase.

The slope of the light REE is examined by plotting La vs. Nd (**Fig. 2**), and the slope of the overall REE profile is examined by plotting La vs. Er (**Fig. 3**). The FAN plagioclase equilibrium liquids do plot along the LMO evolution paths in regions where plagioclase is a liquidus phase. The equilibrium liquids can be generated by either the “No Garnet” or “3-5% Garnet” evolution lines (**Figs. 2ab, 3ab**). These model results permit up to 10% garnet fractionation from the LMO. Our subsequent work will evaluate this possibility in more detail.

Conclusions. The data presented here are consistent with the FANs crystallizing from the LMO. The range of equilibrium compositions also demonstrates that plagioclases contained in FANs crystallized throughout the final stages of LMO solidification, including when urKREEP was formed. The range of FAN ages reported in [12] appears inconsistent with a direct origin from the LMO. However, a combination of an insulating “lid” coupled with tidal friction could extend the crystallization of the crystallizing LMO to account for the FAN age range [3]. Elkins-Tanton et al. [3] concluded “*The resulting crust will be heterogeneous and nonmonotonic in age and composition as a function of depth, and it would be expected to contain rocks with ages ranging over ~200 Ma*.” The fact that FAN subgroups are difficult to relate to each other is consistent with this. The range of equilibrium liquids calculated in this study are consistent with an extended lunar crust formation. This initial study of FAN petrogenesis posits that those FANs with plagioclase that crystallized from a liquid with relatively low REE abundances are older than those that crystallized from liquids containing high REE abundances. This hypothesis remains to be tested.

References: [1] Dowty E. et al. (1974) EPSL 24, 15-25. [2] Snyder G.A. et al. (1992) GCA 56, 3809-3823. [3] Elkins-Tanton L.T. et al. (2011) EPSL 304, 326-336. [4] Rapp J. & Draper D. (2012) LPSC 43, abstract #2048. [5] Rapp J. & Draper D. (2013) LPSC 44, abstract #2732. [6] Rapp J. & Draper D. (2014) LPSC 45, abstract #1527. [7] James O.B. et al. (1989) Proc. LPSC 19, 219-243. [8] Boyet M. & Carlson R. (2007) EPSL 262, 505-516. [9] Boyet M. et al. (2015) GCA 148, 203-218. [10] Borg L.E. et al. (1999) GCA 63, 2679-2691. [11] Norman et al. (2003) MaPS 38, 645-661. [12] Borg L.E. et al. (2011) Nature 477, 70-72. [13] Neal C.R. (2001) JGR 106, 27865-27885. [14] Neal C.R. & Davenport J.D. (2014) LPSC 45, abstract #1181. [15] Papike J.J. et al. (1997) GCA 61, 2343-2350. [16] Floss C. et al. (1998) GCA 62, 1255-1283. [17] Blundy J. & Wood B.J. (1991) GCA 55, 193-209. [18] Bindeman I.N. et al. (1998) GCA 62, 1175-1193. [19] Hui H. et al. (2011) GCA 75, 6439-6460. [20] Warren P.H. (1989) LPI Tech. Rpt. 89-03, 149-15.

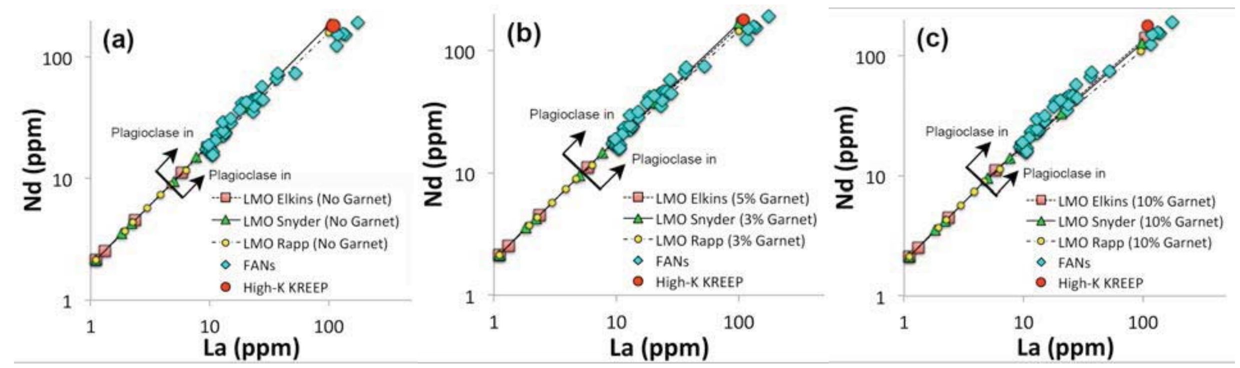

Fig. 2. La vs. Nd for LMO evolution with no garnet (a), 3-5% garnet (b), and 10% garnet (c). The LMO models are from [2] (LMO Snyder), [3] (LMO Elkins), and [4-6] (LMO Rapp). High-K KREEP is from [20] FAN data are from [15,16].

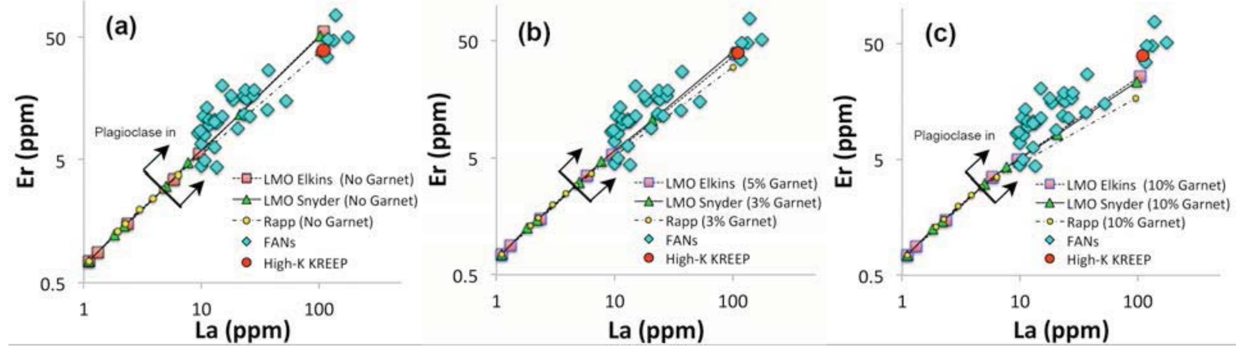

Fig. 3. La vs. Er for LMO evolution with no garnet (a), 3-5% garnet (b), and 10% garnet (c). The LMO models are from [2] (LMO Snyder), [3] (LMO Elkins), and [4-6] (LMO Rapp). High-K KREEP is from [20] FAN data are from [15,16].

HYDROUS EARLY MOON? CONSTRAINTS FROM HYDROUS LUNAR MAGMA OCEAN SOLIDIFICATION EXPERIMENTS.

Y. H. Lin*, E. S. Steenstra and W. van Westrenen, Faculty of Earth and Life Sciences, VU University Amsterdam, The Netherlands (y.lin@vu.nl)

Introduction: Since ~2008, the traditional view of a dry Moon [1] has been challenged by the identification of water in lunar pyroclastic glasses [2, 3], lunar minerals including apatite [3–12] and melt inclusions in lunar olivine [3, 13, 14]. Water could therefore play an important role in the evolution of the Moon, including perhaps during the cooling and crystallization of an early lunar magma ocean (LMO). Numerical [15] and recent experimental [16, 17] models simulating solidification of the LMO were all performed under anhydrous conditions. Although some models of the effect of water on the evolution of the Moon have been published [e.g. 18], these are based on experimental data of physical and chemical rock properties obtained under anhydrous conditions. Water has been shown to greatly affect the physical and chemical properties of minerals and magmas, even at low concentrations [19]. Therefore, the presence of significant amounts of water in the ancient lunar interior requires a reassessment of lunar evolution models.

This study: Here, we show results of a ~95% crystallization sequence of a wet LMO using experiments at pressure-temperature (*P*-*T*) conditions that are directly relevant to the evolution of the lunar interior. A ‘two-stage’ model of magma ocean solidification is assumed, which features early efficient crystal suspension in magma and corresponding equilibrium crystallization, followed by fractional crystallization of the later residual magma ocean. The crystallization sequence and composition of the resulting concentric cumulate layers with different mineralogical assemblages are of primary importance for further understanding key events in lunar evolution, including the thickness of a plagioclase-rich crust [20]. The aim of this work is to solve two main questions: (1) What is the crystallization sequence of a hydrous LMO and how do the chemical compositions of cumulates and corresponding residual LMO vary with progressive solidification under hydrous conditions. (2) What are the quantitative differences between dry and wet LMO solidification scenarios. Answering the latter question could provide new constraints on the amount of water that can/should/might be present in the Moon during LMO crystallisation.

Experimental: Except for the water content of the experiments, we use a similar experimental approach as in our companion work focusing on the evolution of a dry LMO [17]. Hydrous experiments were performed from the fifth step of our dry LMO solidification model [17], which is the first step in which plagioclase starts crystallizing. In the first set of experiments reported here, we simulate a hydrous LMO by adding quantitative amounts of $Mg(OH)_2$ to produce 2 wt.% OH (1 wt.% H_2O) upon melting from the fourth step of the dry LMO solidification series [17]. This implies a water content of 3150 ppm H_2O in the initial LMO. The water concentrations in subsequent starting materials are calculated and added based on mass-balance and the percent of the residual liquid of the previous crystallization step with removal of the corresponding crystals. Future experiments will start with different initial water concentrations.

Analytical: All experiments were analyzed with a JEOL electron microprobe at Utrecht University (15kV, 25nA for Si, Ti, Al, Fe, Mg and Ca), and checked for contamination and/or iron loss. The mineral and melt proportions were determined both by mass balance calculations and area percentage using an EDAX EDS system in imaging mode.

Results: Unsurprisingly, our results differ markedly from our companion experimental study performed on the same bulk magma ocean composition under anhydrous conditions [17]. There are obvious differences in formation conditions and the amount of crystallized minerals between the anhydrous and wet LMO [15,17] (Fig. 1). Under hydrous conditions, plagioclase first appears between 73 and 77 per cent crystallisation (PCS) (68–76 PCS for [17]). Ca-rich pyroxene starts crystallizing at 70–73 PCS, and olivine does not crystallize at >77 PCS. Plagioclase starts crystallizing at 1200 ℃ in our experiments, 40 ℃ lower than that for a dry system [17]. Subsequently, the crystallizing amounts of plagioclase are smaller than those produced at the same P-T conditions in a dry system (Fig. 1). From 89 to 95 PCS, spinel, ilmenite and quartz appear and coexist with plagioclase and cpx. Corresponding residual LMO compositions also differ markedly from those produced under dry conditions [17].

Discussion and conclusions: The presence of water significantly suppresses the crystallization of plagioclase [19], and results in the formation of spinel. At ~95 PCS, the anorthosite crust has a thickness of 32.2 km, which is about 26 km thinner compared to ~58 km under dry conditions [17]. This suggests that improved estimates of lunar crustal thickness [e.g. 21,22] could be used as a hygrometer for the early lunar interior.

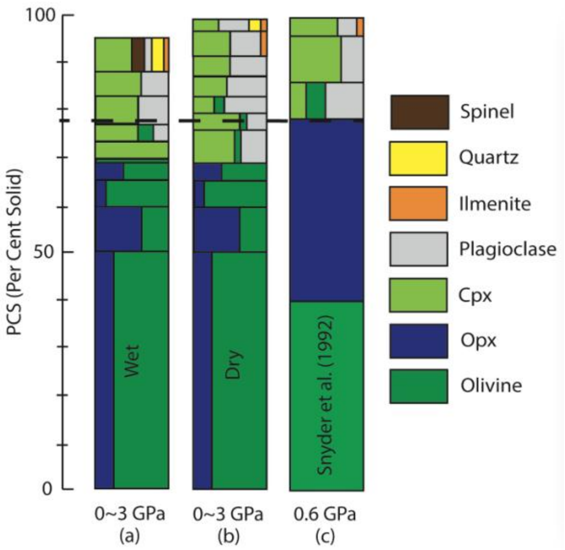

Figure 1: Comparison of experimental LMO solidification models ((a) this study, wet Moon, (b) from [17], dry Moon, (c) from [15], dry Moon)

Outlook: At the meeting we plan to provide further updates on the progress of our LMO crystallisation study. Upcoming experiments will be focused on constraining estimates of the total predicted thickness of the plagioclase crust under different lunar interior water contents.

References:

[1] Taylor S. R. et al. (2006) *Rev. Mineral. Geochem. 60, 657–704.*
[2] Saal A. E. et al. (2008) *Nature, 454, 192–195.*
[3] Saal A. E. et al. (2013) *Science, 340, 1317–1320.*
[4] McCubbin F. M. et al. (2010a) *Proc. Natl. Acad. Sci. U.S.A., 107, 11223–11228.*
[5] McCubbin F. M. et al. (2010b) *Am. Mineral. 95, 1141–1150.*
[6] Boyce J. W. et al. (2010) *Nature, 466, 466–469.*
[7] Greenwood J. P. et al. (2011) *Nat. Geosci. 4, 79–82.*
[8] Hui H. J. et al. (2013) *Nat. Geosci. 6, 177–180.*
[9] Tartèse and Anand (2013) *Earth Planet. Sci. Lett. 361, 480–486.*
[10] Tartèse R. et al. (2013) *Geochim. Cosmochim. Acta 122, 58–74.*
[11] Tartèse R. et al. (2014) *Geology, 42, 363–366.*
[12] Barnes J. J. et al. (2014) *Earth Planet. Sci. Lett. 390, 244–252.*
[13] Hauri E. H. et al. (2011) *Science, 333, 213–215.*
[14] Chen Y. et al. (2015) *Earth Planet. Sci. Lett. 427, 37–46.*
[15] Snyder G. A. et al. (1992) *GCA, 56,* 3809–3823.
[16] Elardo S. M. et al. (2011) *GCA, 75,* 3024–3045.
[17] Lin Y. H. et al. (2016) *LPSC.*
[18] Elkins-Tanton and Grove (2011) *Earth Planet. Sci. Lett. 307, 173–179.*
[19] Sisson T. and Grove T. (1993) *CMP, 113, 143–166.*
[20] Shearer C. K. et al. (2006) *Reviews in Mineralogy and Geochemistry, 60,* 365–518.
[21] Wieczorek M. et al. (2013) *Science, 339,* 671–675.
[22] Martinot M. et al. (2016) *LPSC.*

LUNAR MINERALS AND ROCKS: VOLATILES SEPARTED BY IMPACT AND VOLCANIC EVENTS.

Y.Miura[1] and T. Tanosaki[2], [1]Yamaguchi University (Yamaguchi, Japan; yasmiura50@gmail.com), [2]Kogakuin University (Tokyo, Japan).

Introduction: The lunar materials of rocks and minerals filled on the surface are solidified phases without any global air and water. The main purpose of the present paper is to discuss lunar minerals and rocks with volatiles of light elements which have been separated by meteoritic impacts and volcanic events triggered by gravitational tidal process in waterless body.

Characteristics of extraterrestrial solid rocks: All solid states of rocks and minerals with main refractory elements mixed with light to heavy elements can be found relatively stable at low temperature (and high pressure) condition throughout the extraterrestrial Solar System with different sizes and shapes. All extraterrestrial rocks including water-and air-planet (Earth) are starting materials to be formed as local to global air and water. Therefore, volatile elements formed at high temperature and pressure conditions should be discussed to be formed by 1) mixed and remained solids, 2) evaporated from the solids, or 3) less mixture of solids on evolved Earth-type planets or any impacted satellites including the Moon [1-3].

Volatiles escaped from rocks to form air-water: Primordial solids formed in the cosmic space include remained volatile elements during impact growth processes, because impacted rocks are aggregated grains easily mixed with volatiles. Therefore, the following three types of rocks are formed in the Solar System (except water-and-air planet Earth) [1, 3]:

1) Impacted rocks mixed and remained volatiles, which might be found at Asteroids and dwarf planets,

2) Volcanic rocks evaporated for volatiles, which might be obtained by gravitational tidal force of rotated planets (Mars and Venus etc.) and some satellites without global water system.

3) Multiple mixed rocks with less volatiles escaped during the formation process, which are found on any impacted satellites including the Moon.

4) Terrestrial crystalline-rocks with less isolated volatiles, which are found large crystalline-rocks formed by plate-tectonic melting and slow-cooling process triggered by global ocean and air systems.

Characteristic volatiles on the Moon: Characteristic cations of volatile elements are summarized on the collected Apollo samples as follows [1-3]:

1) Typical cations of hydrogen (H), nitrogen (N), sulfur (S) and carbon (C) which are included in all lunar rocks shows the most enriched in regolith soils formed by impact fragmentation on the volatiles (H, N, He, S, Cl, C), where these elements are recycle process between impacted extra-lunar meteorite and lunar rocks. This is proved by evidences that meteoritic elements (Fe, Ni, Co) are enriched in regolith solid than volcanic basalts on the Moon [1].

2) Carbon and chlorine (Cl) elements are enriched in polymict breccias, where these elements can be remained after impact process through melt-solid process.

Characteristic Fe, Mg-rich lunar plagioclases: Characteristic mixtures of mafic and light elements in lunar plagioclases are summarized as follows:

1) Fe and Mg contents of plagioclase are varied from highland anorthosite (0 to 1.5wt.%), melted breccias (0-0.5wt.%) to basalts (0 to 2.6wt.%) , where lunar plagioclases are relatively local and rapidly cooled (especially in lunar basalts) [1].

2) Lunar plagioclases of melted breccias with less Fe and Mg have enriched carbon contents reveal high Ca contents and An content, where Ca and C contents are indicator of quenched impact process on lunar plagioclases [1-3].

Lunar plagioclase with Ca-C-bearing grains: Recent electron microscopic FE-SEM observations of the lunar samples indicate the following results:

1) Lunar samples contain Ca-C-bearing nano-grains, which are formed by carbon-bearing fluids process [3].

2) On waterless Moon, lunar plagioclase samples contain fluid-related grains with carbon [3].

Summary: Lunar minerals and rocks are summarized as follows: 1) Lunar minerals and rocks with high mafic and less volatile elements are separated by meteoritic impacts and volcanic events on waterless and airless lunar surfaces. 2) Multiple mixed rocks with less volatiles on any impacted Moon show limited composition and crystals. 3) Volatile cations enrich in impact-related fragments are re-circulated between extra-lunar meteorites and lunar surface rocks. 4) Terrestrial crystalline-rocks with less isolated volatiles, which are found large crystalline-rocks formed by plate-tectonic melting and slow-cooling process triggered by global ocean and air systems. 5) Lunar plagioclases with mafic and carbon elements shows Ca-C-bearing micro-grains by impacts.

References: [1] G. Heiken, D. Vaniman and B. French, *Lunar source boo*k (Cambridge Univ. Press) (1991), 30-632. [2] Miura and S. Fukuyama (1999), *J. Materials Proc. Tech.* (Elsevier), 85, 192-193. [3] Y. Miura et al. (2016), *LPSC (LPI) 47,* abstract #1415.Submitted, #2077. Submitted , #6029.

MINERALOGICAL VARIATION OF THE LATE STAGE MARE BASALTS.

X. Y. Zhang[1], A. A. Xu[1], Z. S. Tang[1], Z. Y. Ouyang[2] and Y. Z. Wu[3], [1]Space Science Institute, Macau University of Science and Technology (zhangxunyugeology@gmail.com), China, [2]National Astronomical Observatories, Chinese Academy of Sciences, China, [23]School of Geographic and Oceanographic Sciences, Nanjing University, China.

Introduction: The last major phases of lunar volcanism mainly occurred in Oceanus Procellarum and Mare Imbrium and produced spectrally distinct hight-Ti basalts [1, 2, 3]. The composition and distribution of these late stage mare basalts provide a record of the most recent thermal history of the Moon [4]. To study the spectral and mineral variation of the late stage mare basalts within Oceanus Procellarum and Mare Imbrium, the aim of this paper is to map different units of these regions by using various remote sensing data, as well as to study their inferred mineralogical characteristics by analyzing spectral features of the small fresh craters.

Methods: The Moon Mineralogy Mapper (M^3) data, with wide band coverage and high resolution, provides an accurate way to study the spectral features of small fresh craters [5]. This study focused mainly on the resolvable small fresh craters, smaller than 500 m. For most craters, the spectra were extracted from only one pixel to represent the the corresponding crater. After a careful selection, 420 smaller fresh craters from Optical Periods 1B (OP1B) of M^3 data were selected.

To map accurately the potential stratigraphic boundaries of the late stage mare basalts, a range of reflectance maps and color images were used to trace the most significant albedo and hues boundaries within Oceanus Procellarum and Mare Imbrium, such as, Clementine-derived images, WAC false color images, the Integrated Band Depth (IBD) image [5, 6, 7] and false color images of M^3 data. Further, the individual stratigraphic flow fronts of several late stage basalt flows within the Mare Imbrium can be observed in WAC- low solar altitude image, which was used to map the stratigraphic sequences of these flows.

Absorption band center is a key spectral parameter for mineral identification [8, 9]. The 1000 nm (Band I) center and 2000 nm (Band II) center provide a qualitative way to access the composition of pyroxenes [10]. The Band Area Ratio (BAR) is defined as the ratio between Band II and Band I absorption features[11, 12]. The relationship of the Band I center and BAR is helpful to estimat the relative abundances of pyroxene and olivine in basalts [12].

Results and Discussions: The most significant albedo and hues boundaries within Oceanus Procellarum and Mare Imbrium were traced by using several reflectance maps and color images. Some individual stratigraphic lava flows of the late stage mare basalts within the Mare Imbrium were noted during the mapping process. In total, 31 distinct areas within the late stage mare basalts were mapped, which represent potentially distinct mare flows. Figure 1 shows the mean non-processed reflectance spectra (vertically offset for clarity) of the fresh craters from each late stage basalt unit. Overall, most spectra of the late stage mare basalts displays strong and asymmetric Band I absorption, as well as relatively weak Band II absorption, which is consistent with the presence of olivine.

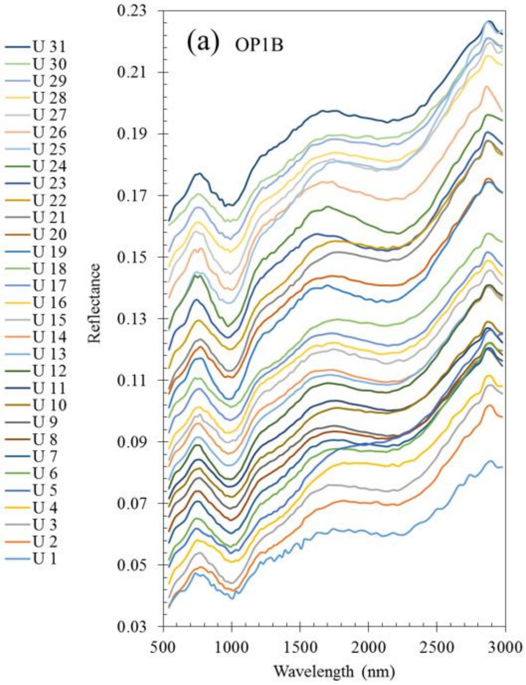

Fig. 1. Mean non-processed reflectance spectra of each unit with vertical offset (OP1B data).

The results from Band I center and BAR are mapped using the Inverse Distance Weighing (IDW) interpolation method (Figures 2 and 3). In general, the values of Band I center and BAR show a good correlation. Most craters within the late stage mare basalts, which have larger Band I center value (the redder hue shown in Figure 2), usually have smaller BAR value (the bluer hue shown in Figure 3), and vice versa. Broadly, the units around Lichtenberg crater (Units 4 and 5) have the largest Band I center values and the smallest BAR values among all the units. In contrast, the units near both Kepler (e.g., Units 13, 14, 15 and 16) and Euler craters (e.g., Units 19, 20 and 23) have smaller Band I center values and larger BAR values than other units. These spectra occur mainly in the small local areas (e.g., Units 19 and 20), or the regions which are generally old. Some units (e.g., Units 2, 3, 6 and 7), which have relatively larger Band I center values and smaller BAR values, occur mainly in the regions around Units 4 and 5 (Figures 2 and 3). On the whole, it shows a trend where, starting from Units 4 and 5 to the units far away from them (e.g., Unit 5 to 13), the Band I center value is decreasing, but the value of BAR keeps increasing.

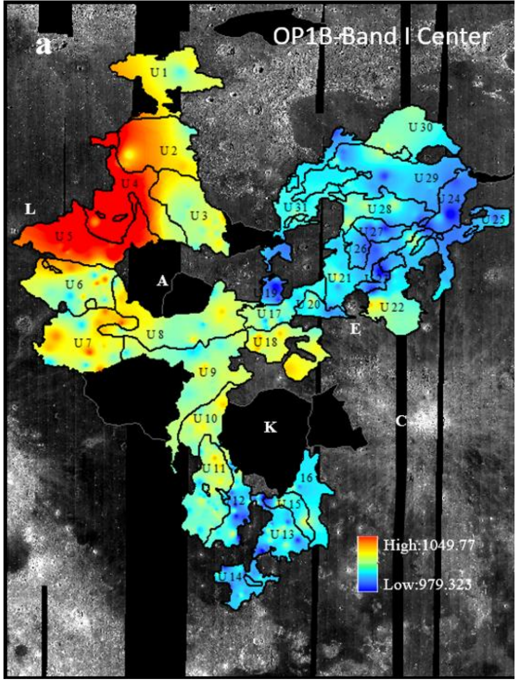

Fig. 2. The distribution of Band I center values (OP1B data). The black areas represents regions not included in this study. The base map is a M^3 mosaic.

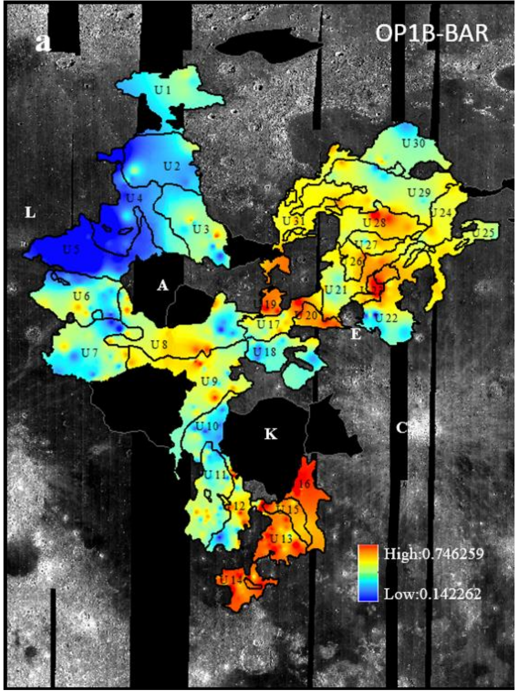

Fig. 3. The distribution of BAR values (OP1B data). The black areas represents regions not included in this study. The base map is a M^3 mosaic.

However, for the units within and around Mare Imbrium, the variations of Band I center values and BAR values are more complicated to interpret. The units that have relatively larger Band I center value and smaller BAR value, occur mainly in the northwestern part of Mare Imbrium (e.g., Units 29 and 30) and the regions around Euler crater (e.g., Units 18, 21 and 22) (Figures 2 and 3). The units in central Mare Imbrium (e.g., Units 26 and 27) mostly have relatively smaller Band I center value and larger BAR value.

Conclusion: In Oceanus Procellarum, the mafic olivine/pyroxene ratio decreases with distance from Units 4 and 5. In Mare Imbrium, the northern and southern units have higher olivine/pyroxene ratios than the central units. In general, the inferred abundance of olivine appears to vary stratigraphically, with the younger flows being more olivine rich. However, the younger basalts in Mare Imbrium, which are mainly around L Euler (e.g., Units 21 and 22), were found to have lower olivine/pyroxene ratios than some older basalts in Oceanus Procellarum (e.g. Unit 6). One interpretation is that the stratigraphically younger basalts in Oceanus Procellarum might originate from a more evolved source than those in Mare Imbrium.

References: [1] Pieters, C. M. (1978) LPS 9th, 2825-2849. [2] Hiesinger, H. et al. (2003) JGR, 108(E7), 5065. [3] Wu, Y. Z. el. al. (2016) LPSC, 47th, #1406. [4] Taylor, S. R. (1989) Tectonophysics, 161, 147–156. [5] Mustard, J. F. et al. (2011) JGR, 116(E6). [6] Besse, S., et al. (2011) JGR, 116(E6). [7] Wu, Y. Z. el. al. (2015) LPSC, 46th, #2187. [8] Pieters, C. M. et al. (1980) JGR, 85, 3913-3938. [9] Wu, Y. Z. et al. (2010) Sci China Phys Mech Astron, 53(12). [10] Klima, R. L. et al. (2007) Meteoritics & Planetary Science, 42(2), 235-253. [11] Cloutis, E. A. et al. (1986) JGR, 91(B11). [12] Gaffey, M. J. et al. (1993) Icarus, 106(2), 573-602.

Acknowledgments: This study was supported by the Macau Science and Technology Development Fund (048/2012/A2, 039/2013/A2, 091/2013/A3).

IDENTIFICATION OF ROCK SUITS ON THE LUNAR SURFACE.

X. Wang[1]. [1] (Institute of Geophysics and Geomatics, China University of Geosciences, Wuhan, 430074, China, xianminwang@163.com).

Introduction: There are mainly five types of rock suits (Ferroan Anorthosite Suite, Magnesian Intrusive Suite, Alkali Intrusive Suite, KREEP Basalt and Mare Basalt) on the lunar surface [1]. These five rock suits were transported to the lunar surface by magmatism, impacting and volcanism [1,2]; thus, the distribution of the five rock suits on the lunar surface provides an interesting clue for lunar evolution [3]. However their accurate distribution features have still kept as a mystery. Here a general distribution of the five rock suits is present. Six oxides and elements (TiO_2, Al_2O_3, FeO, MgO, CaO, Th) are employed as the lithology signature. Based on the abundances of the above six oxides and elements observed by Lunar Prospector (LP) Gamma Ray and Neutron Spectrometers [4,5], decision tree algorithm C5.0 and boosting technique are adopted to obtain the distribution of the five rock suits on the lunar surface [3].

Results: The ferroan anorthosite (FAN) suite and magnesian suit are mixed with each other and mainly distributed outside of the Procellarum KREEP Terrane (PKT). There is also very limited magnesian rocks spreading within the PKT. Alkali suite is primarily located around the peripheral area of the PKT and in the central region of the South Pole-Aitken Terrane (SPAT). KREEP basalts lie in the highland area around the Imbrium Basin. Mare basalts actually lacks on the surface of many basins [3].

Compared with the previous studies, as for the ferroan anorthosite suite, Yamamoto et al. [6] presented purest anorthosite (PAN) mainly concentrated outside of the PKT. With regard to the magnesian suite, Cahill et al. [7] suggested this rock suits also distributed outside of the PKT. Prissel et al. [8] proposed the magnesian magmatism may have globally intruded into the felspathic crust. Pieters et al. [9] indicated that the new member PSA (pink-spinel anorthosite) of the Mg-rich suite is globally distributed. This research on the FAN and Mg-rich suits also shows these two types of rocks appear a global distribution outside of the PKT [3]. With repect to the alkali suite, Lucey et al. [10] suggested that the rock type near the region of Compton and Belkovich is mainly alkali anorthosite. Difrancesco [11] proposed that alkali anorthosite appears isolatedly and widely distributed over the lunar surface. In this result, there are alkali rocks spread in Compton and Belkovich, and alkali suite appears isolated points widely distributed outside of theire concentrated region: the outskirt of the PKT and the center of the SPAT [3]. As for KREEP basalts, Jolliff et al. [12] indicated that this type of rocks is confined to the PKT. Li et al. [13] and Du et al. [14] indicated that KREEP basalts are primarily concentrated encircling the Mare Imbrium. The result of this research [3] on KREEP basalts shows that this rock type is unique to the surrounding highland of the Imbrium basin, but its area is much smaller than the ones in Li et al. [13] and Du et al. [14]. With regard to mare basalts, Pieters et al. [8] indicated that the Moscoviense basin appears higly feldspathic without the filled mare basalts, and the PSA is localized as isolated areas along the inner ring. In this research, this basin is dominated by the FAN suit with some magnesian suite along its periphery [3].

The limit of this research lies in two points: (1) the number and positions of the lunar rock samples, (2) the resolution of the oxide and element concentrations observed by LP Gamma Ray Spectrometer (GRS). All the lunar rock samples [1] employed in this research are located on the lunar nearside not far from the PKT. The resolution of LP GRS measurement is 60 km × 60 km [4,5], which results in many local important features of lithology distribution can not be well refleted.

This research has already been published in Wang et al. [3]; the specific results, conclusions and discussions refer to Wang et al. [3].

References: [1] Wieczorek M. A. et al. (2006) *Rev. Mineral. Geochem.* 60**,** 221–364. [2] Shearer C. K. et al. (2006) *Rev. Mineral. Geochem.* 60**,** 365–518. [3] Wang X. and Pedrycz W. (2015) *Sci. Rep*. 5, 17075. [4] Prettyman T. H. et al. (2006) *JGR*. 111, E12007. [5] Prettyman, T. H. (2012) *NASA Planetary Data System*. Available at: http://pdsgeosciences.wustl.edu/missions/lunarp/grs_elem_abundance.html.(Accessed: 24th October 2012). [6] Yamamoto et al. (2012) *GRL*. 39, l13201. [7] Cahill et al. (2009) *JGR*. 114, E09001. [8] Prissel et al. (2014) *EPSL*. 403, 144-156. [9] Pieters et al. (2014) *AM. Mineral*. 99, 1893-1910. [10] Lucey P. et al. (2006) *Rev. Mineral. Geochem.* 60**,** 83-219. [11] Difrancesco et al. (2015) *AM. Mineral*. 100, 983-990. [12] Jollif et al. (2000) *JGR*. 105, 4197-4216. [13] Li Y. et al. (2007), Acta Petrol. Sin. 23, 1169-1174. [14] Du J. et al. (2010), Chinese J. Geophys. 53, 2059-2067.

QUANTITATIVE SPECTRAL ANALYSIS WITH M3 IMAGES APPLIED TO THE THEOPHILUS CENTRAL PEAK.

Y. Sun[1], [1] College of Geoexploration Science and Technology, Jilin University, Changchun 130062, China, sunying7@jlu.edu.cn

Introduction: Integrated analyses of lunar samples returned by Apollo and Luna missions, lunar meteorites and remote sensing data lead to the recognition that the lunar crust is laterally and vertically heterogeneous [e.g. 1, 2]. The compositional investigations with the first global, hyperspectral images of the Moon (Moon Mineralogy Mapper [M^3]) should result in a new perspective to the crustal structure, and in turn may lead to profound impacts on the traditional perception of crustal magmatism. Qualitative spectral analysis with M^3 images for the lunar crater central peaks was conducted to investigate the mineral composition of the lunar crust suggested new compositional trends across the entire lunar crust [3]. However, results of qualitative spectral analysis only can provide approximately compositional variations because of inaccurate spectral unmixing. For instance, it is nearly impossible to identify the presence of crystalline plagioclase in the mixture with even only 10% of pyroxene on the basis of qualitative spectral analysis. Therefore, a hybrid quantitative spectral analysis method is developed in this study to address the compositional diversity of the lunar crust.

Dataset and preprocessing: M^3 L2 images of 166 craters were geometrically corrected and smoothed for noise reduction [3]. For the geometric correction, the images were warped based on latitude and longitude values of each pixel. For the noise reduction, a moving average was used. Our previous working experience confirms that after spectral smoothing, 72 bands from 540 nm to 2537 nm sensitive to mineral diagnostic absorptions are retained for further quantitative analysis.

Quantitative spectral analysis: spectral mixture analysis (SMA) and radiative transfer model (RTM) are the effective quantitative compositional analyses which do not require the ground truth data.

SMA assumes that the spectrum of each mixed pixel is a linear combination of spectra of distinct endmembers (EMs) and the weights of EMs represent the abundances of EMs in the mixed pixel. The maximum number of EMs that SMA can map is limited by the number of bands in the image data. Multiple endmember spectral mixture analysis (MESMA) was proposed to overcome the limitations of traditional SMA [4]. MESMA decomposes each pixel using different combinations of possible endmembers, allowing a large number of end-members to be utilized across a scene. This process starts with a two-endmember model and constructing a three-endmember model if two-endmember models don’t meet the criteria of endmember selection. Large endmember models can be tested when needed. This method was successfully used to decompose Clementine UVVIS images with 13 EMs of rock types [5]. However, interpretation of mineral composition directly by MESMA from M^3 images is a challenge, because it is very difficult to extract the appropriate EMs of pure minerals.

RTM is an effective method for computation of the reflectance spectra of mineral, and mixtures of minerals. A number of studies have used Hapke’s RTM to solve for chemical and mineral abundance in mineral/rock mixtures [e.g. 6-10]. For example, Cahill et al. [6] used RTM to interpret mineral abundance of 55 crater central peaks with Clementine data in order to reflect the vertical compositional variations of the lunar crust. However, RTM is very time consuming when applied to the Clementine data at 100 m/pixel, and this weakness will be exacerbated when hyperspectral data such as the M^3 images are used.

To overcome the weakness of MESMA and RTM, a hybrid method is used in this study (Fig. 1). MESMA is linear unmixing model, however, the mixing of reflectance spectra is not linear. So the M^3 reflectance has to be converted to single scattering albedo (SSA) first using equation from [11]. For each crater central peak, 2-endmember and 3-endmember MESMA are applied to M^3 images for the quantitative analyses of lithology bearing unique mineral or mineral assemblages (EMs). The EMs are selected for each crater central peak separately in order to avoid the difference among multi-temporal images.

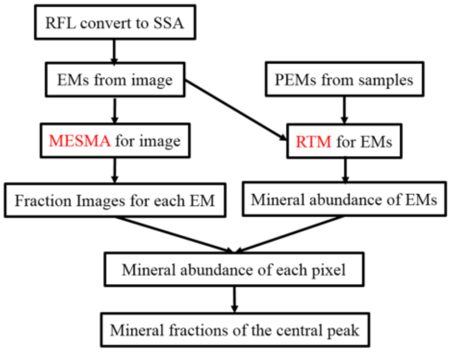

Fig. 1 The flow chart for quantitative spectral analysis

The EMs used in MESMA are be decomposed with pure mineral EMs (PEMs) with RTM. The pure mineral EMs are selected from Lunar Soil Characterization Consortium (LSCC) and USGS (Fig. 2). We have implemented RTM model by using of Newton's method

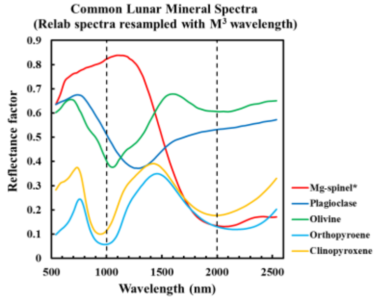

Fig.2 Laboratory spectral reflectance of common lunar minerals used in RTM as PEMs.

and least square minimization [12] for both forward and inverse modeling to achieve a better computational efficiency for estimating the abundance of minerals. This improved RTM is simplified and used in this study. All factors except abundance of minerals are fixed to simplify the calculation. A similar method has been used in [6], however, we add a new endmember, Mg-spinel, to this model. The PEM of Mg-spinel is selected from terrestrial samples due to a lack of occurrence in lunar samples. The mineral abundance of EMs is obtained from RTM. Integrated the results of the fraction images from MESMA and the mineral abundance of EMs, the mineral abundance of each pixel can be computed. Finally, the weighted average of minerals can be calculated to represent the mineral fractions of the central peak. Integrated the result from this hybrid method with the excavation depth of central peaks, mineral abundance variation of the lunar crust with depth is obtained.

Preliminary results: The results of one example crater central peak is shown here. Theophilus has a diameter of ~98 km and is located in the northwest of the Nectaris basin, which overlaps the north rim of the crater Cyrillus. The petrological diversity of the central peak of Theophilus was observed with remote sensing techniques. Tompkins and Pieters [2] suggested the central peaks of Theophilus are mostly composed of anorthosite with a small amount of troctolite. 25.3% of olivine in the central peaks of Theophilus was determined based on the result of radiative transfer modeling with Clementine images [6]. Recently the central peak of Theophilus attracted much attention because of the discovery of Mg-spinel using M^3 images [e.g. 13-15].

The result of qualitative spectral analysis is shown in Fig. 3. The fraction images from MESMA are displayed in Fig. 4. Compared with the qualitative results, we found some pixels are missed due to lack of representative endmembers. The magnitude of the spectrum should be considered when we select the EMs. In order to verify the MESMA program we compiled, the modeled spectra are calculated to compare with original SSA (Fig. 5). The good fitting curve demonstrate the feasibility of MESMA. Next step the EMs are decomposed by RTM with the PEMs (Fig. 2). Fig. 6 shows the curve fitting of EMs and all of them has low RMSE. And the mineral abundance images are displayed in Fig. 7. Finally, we estimate the weighted average mineral abundance of Theophilus crater central peak: Mg-spinel 4.36%, Olivine 15.98%, Orthopyroxene 5.71%, Clinopyroxene 3.63% and Plagioclase 70.33%. This result is agreement with previous studies and demonstrate the hybrid method is feasible.

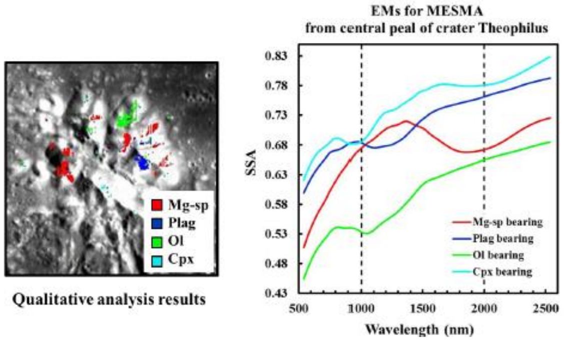

Fig.3 left: qualitative results for Theophilus central peak; right: EMs selected for MESMA

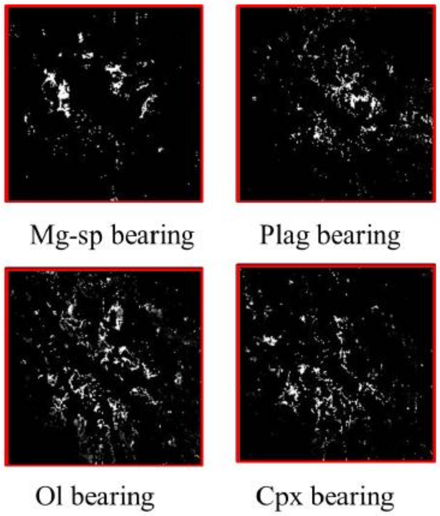
Mg-sp bearing Plag bearing

Ol bearing Cpx bearing

Fig. 4 fraction images of MESMA for Theophilus central peak

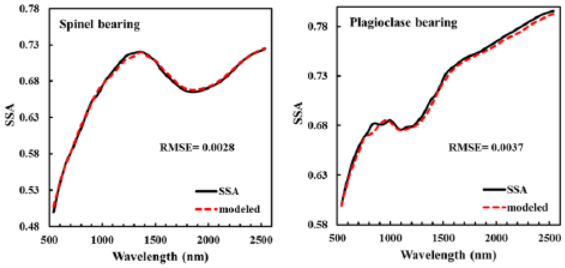

Fig. 5 comparison between modeled spectra with original SSA spectra for verification of MESMA process

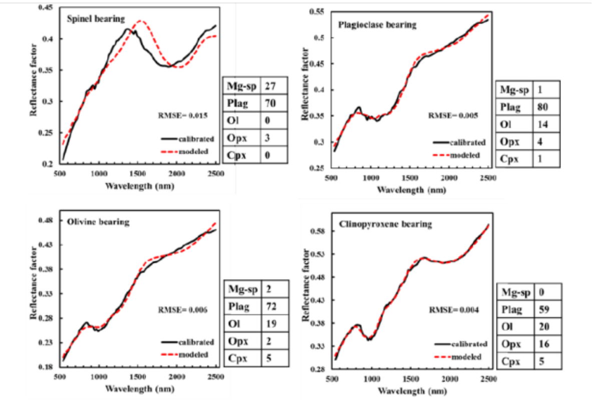

Fig. 6. Curve fitting for RTM results, the table beside of spectral plot show the mineral abundance of spectra

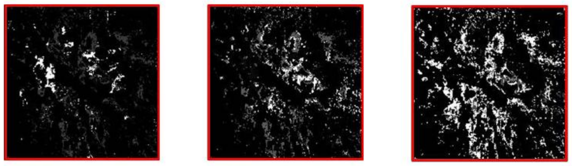

Mg-sp (0-27%) Plag (59-80%) Ol (0-20%)

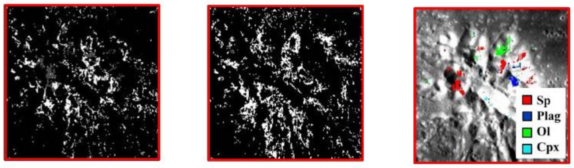

Opx (2-16%) Cpx (0-5%)

Fig. 7 mineral abundance from RTM results

References: [1]Jolliff et al. (2000) *JGR*, 105(E2), 4197-4216; [2]Tompkins and Pieters (1999) *Meteoritics & Planet. Sci.*, 34(1), 25-41; [3] Sun and Li (2015) *LPSC XXXXVI*, Abstract #2941; [4]Roberts et al. (1998) *RSE*, 65(3), 267-279; [5]Li and Mustard (2003) *JGR*, 108(E6), 5053; [6]Cahill et al. (2009) *JGR*, 114, E09001; [7]Lawrence and Lucey (2007) *JGR*, 112(E7); [8]Lucey (2006) *JGR* 111(E8); [9]Lucey and Noble (2008) *Icarus*, 197(1), 348-353; [10]Wilcox et al. (2006) *JGR*, 111(E9); [11] Yan et al. (2010) *Icarus*, 208(1), 11-19; [12]Li and Li (2011) *JG*R, 116, E09001; [13]Dhingra et al. (2011) *LPSC XXXXII*, Abstract #2431; [14]Sun et al. (2013) *LPSC XXXXIV*, Abstract #1393; [15]Pieters et al., (2014) *American Mineralogist*, 99(10), 1893-1910.

DISPLACEMENT-LENGTH RELATIONSHIP AND AMOUNT OF STRAIN FOR LUNAR WRINKLE RIDGES IN MARE SERENITATIS AND TRANQUILLITATIS.

Bo Li[1*], Jiang Zhang[1], Zongcheng Ling[1], Jian Chen[1]. 1 Shandong Provincial Key Laboratory of Optical Astronomy and Solar-Terrestrial Environment; Institute of Space Sciences, Shandong University, Weihai 264209, China, (libralibo@sdu.edu.cn)

Introduction: Field observations indicate that there is a correlation between the maximum amount of displacement (*D*) on a fault and the length (*L*) of the fault trace. Data relevant to the scaling of *D* with *L* have been collected for the various fault types (normal, thrust or strike-slip), in a wide variety of tectonic environments, and for a range of length scales.

There are two reasons why establishing the form of the fault scaling relationship is useful. First, the relationship between displacement on a fault and its length implies a description of fault growth over geologic time. Furthermore, Scholz & Cowie showed that if a relationship between *D* and *L* can be established for a population of faults in a deformed region or the whole planet, the total brittle strain (ε) can be calculated[1]. Thus, determining the strain and the relationship is important for us to discriminate between global or local contractional models and resultant styles of tectonism and to place constraints on the timing and amount of secular cooling[2].

Wrinkle ridges are complex landforms that mostly occur in lunar mare basalts. Their origin is attributed to basin localized compressional stresses that induce folding and/or thrust faulting[3]. Wrinkle ridges was formed as result of basin-localized tectonics rather than as a consequence of global thermal contraction, and we think the formation and distribution of ridges may be reflect the long-time basin-localized contraction. In this paper, we used the high resolution lunar images (LRO WAC) and topographic data (LOLA DEM) to: (1) identify the wrinkle ridges in Mare Serenitatis and Mare Tranquillitatis and extract their topographic parameters, (2) confirm the relationships between the displacement and length of these identified wrinkle ridges and compute the parameter γ from a linear fit to the *D*-*L* data, (3) study the contractional strain result in formation of wrinkle ridges in Mare Serenitatis and Mare Tranquillitatis and find the differences between them.

Measurements of wrinkle ridges: According to the morphological characteristics, we identified wrinkle ridges as expression of surface rupture and displacement occurring along lineaments of variable length based on the WAC global mosaic image with resolution of 100m. The height (*h*) of a ridge can be defined as the elevation difference between the highest and lowest points inside the whole ridge. Using the LOLA data, the calculation of the height includes the following steps: First, for each wrinkle ridge, we make several section lines across the wrinkle ridge. The longer the ridge is, the more number of section lines we make. Then, the elevation profile of each section line is generated in ArcGIS software which represents the shape and elevation changes of the ridge. In the last, the one peak point and the lowest points on the left and right of the profile are identified, and their highest elevation difference among all the profiles is calculated as the height of the ridge.

Based on the WAC mosaic image, we identified and digitized the 21 ridges in Mare Serenitatis with a total length of 3272.8 km, and 44 ridges in Mare Tranquillitatis with a total length of 3110.6 km. In Mare Serenitatis, the length of ridge ranges from 41.7 km to 460.3 km and the height of ridge ranges from 60m to 584 m. While In Mare Serenitatis, the length of ridge ranges from 21.3 km to 237.8 km and the height of ridge ranges from 51m to 776 m. The mean height and length of ridges in Mare Serenitatis are 203.4 m and 154.3 km, while in Mare Tranquillitatis are 225.6 m and 70.7 km respectively.

Displacement-length relationship of wrinkle ridges: Studies of terrestrial faults show that the maximum *D* on a fault scales with the *L* of the fault and the relationship holds for planetary faults[4-5]. It has been proposed that *D* is related to *L* by:

$$D = cL^n, \qquad (1)$$

where *c* is a constant related to material properties and *n* is estimated to be >1. Supported by studies of faults in populations formed in uniform rock types, there is a linear relationship between displacement and length of a ridge:

$$D = \gamma L, \qquad (2)$$

where γ is a constant determined by rock type and tectonic setting (where $n = 1$, $\gamma = c$). Parameter γ is the ratio of displacement to fault length for the fault populations ranges between 100 and 10^{-3} [4].

The estimated *h* values of 21 wrinkle ridges in Mare Serenitatis range from 60 m to 584 m with an average of 203.4 m. Assuming fault plane dips of 30°, according to the Eq. (2), we computed the *D* values of these ridges. A linear fit to the *D*-*L* data for the wrinkle ridges yields a value of $\gamma \sim = 2.25 \times 10^{-3}$ for $\theta = 30°$. The estimated *h* values of 44 wrinkle ridges in Mare Tranquillitatis range from 51 m to 776 m with an average of 225.6 m. A linear fit to the *D*-*L* data for these ridges yields a value of $\gamma \sim = 5.72 \times 10^{-3}$ for $\theta = 30°$. The γ values of ridges in Mare Tranquillitatis is 2.5 times bigger than the γ value of ridges in Mare Serenitatis. We can conclude that the *D*-*L* relationship of ridges in the two basins represent the different compressional process. The non-uniform ratio of D to L means that the ridges formed in Mare Serenitatis Mare Tranquillitatis cannot due to an isotropic global cooling and contraction of the lunar interior but may be result from local stresses associated with mare basaltic units loading.

Amount of strain and contraction in Mare Serenitatis and Tranquillitatis: According to the previous studies, if the D-L relationship of a fault population is known, the strain can be calculated using fault lengths alone. The strain (ε) for faults where the fault length L >= the maximum depth of faulting is given by:

$$\varepsilon = \frac{\cos(\theta)}{A}\sum_{k=1}^{n} D_k L_k \qquad (3)$$

where θ is the fault plane dip, A is the survey area, n is the total number of faults[6].

Wrinkle ridges was formed as result of basin-localized tectonics rather than as a consequence of global thermal contraction. We think the formation and distribution of ridges may be reflect the basin-localized contractional strain. Thus, the contractional strain which formed the ridges can be estimated using the D-L relationship of these ridges. Using the ArcGIS software, we extracted the boundaries of Mare Serenitatis and Tranquillitatis as two polygon features, and calculated the areas of the two polygons which are 307883 km^2 and 370293 km^2 separately. Then, using the γ value (2.25×10^{-3} for Serenitatis and 5.72×10^{-3} for Tranquillitatis) and the total length (3316.4 km for Serenitatis and 3196.4 km for Tranquillitatis) of the ridges measured in this paper, the contractional strains in Mare Serenitatis and Tranquillitatis are estimated to be 0.49% and 0.43% (for $\theta = 30°$).

References: [1] Scholz, C. H. and Cowie, P. A. (1990), *Nature*, 346, 837-839. [2] Melosh, H. J. (1977). *Icarus*, 31, 221-243. [3] Wilhelms, D. E. (1987). Washington, DC. [4] Cowie, P. A. and Scholz, C. H. (1992).*J. Struct. Geol.*, 14, 1149-1156. [5] Watters, T. R. and Robinson, M. S. (1999). *J. Geophys. Res.*, 104, 18981-18990. [6] Cowie, P. A., Scholz, C. H., Edwards, M., and Malinverno, A. (1993). *J. Geophys. Res.*, 98, 17 91117 920.

Acknowledgements: This work was supported by the National Natural Science Foundation of China (41373068, U1231103), the national science and technology infrastructure work projects (2015FY210500), the Natural Science Foundation of Shandong Province (ZR2015DQ001, JQ201511), Young Scholars Program of Shandong University, Weihai (2015WHWLJH14) and the Fundamental Research Funds for the Central Universities (2015ZQXM014).

DISTRIBUTION AND POPULATION CHARACTERISTICS OF LUNAR CRATERS IN ORIENTALE BASIN FROM THE RECENT HIGH-RESOLUTION REMOTE SENSING DATASETS.

Bo Wu, Tao Jun Lin, Jinyi Li, and Yiran Wang, Department of Land Surveying & Geo-Informatics, The Hong Kong Polytechnic University, Hung Hom, Kowloon, Hong Kong. (bo.wu@polyu.edu.hk).

Introduction: Based on the high-resolution remote sensing datasets (images and laser altimetric measurements) collected by the recent lunar missions, we measured the impact craters ⩾1 km in diameter in the region of the orientale basin on the Moon and analyzed their distribution and population characteristics. The crater densities inside the orientale basin and the nearby region were analyzed. Impact crater size-freqency distribution (SFD) analyses were carried out to estimate the surface age of the region. The spatial distribution and morphological characteristics of craters in this region were also investigated.

The orientale basin serves as a transition between two major populations of impactors in early solar system history (Head et al., 2010). A detailed investigation of the distribution and population characteristics of impact craters inside and surrounding this region is of significance for lunar surface geology.

Crater Density: An image and DEM integrated approach(Wu et al., 2014) was used for crater detection based on the SLDEM2015 (Barker et al., 2015) with a resolution of 512 pixels-per-degree and the SELENE TC imagery (Haruyama et al., 2012) with a resolution of 10m/pixel, to automatically extract craters with diameters ⩾ 1 km. Then, a manual checking process was carried out with the assistance of a 1-km reference grid overlaid on the SELENE TC imagery. Finally, there were 47505 craters with diameters ⩾ 1 km extracted in the study area, and the list of craters are recorded as our crater catalogue (Fig. 1).

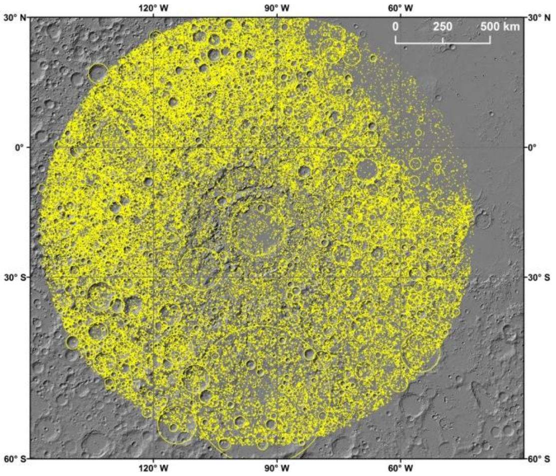

Figure 1. Craters mapped in the study area overlaid onto a hillshade rendering of SLDEM2015.

SFD Analysis for Surface Age: SFD analyses (Neukum et al, 2001) were carried out to estimate the surface age of the region based on the 47505 detected craters. The lunar crater catalogue LU78287GT by Salamunićcar et al. (2013) is currently the most updated and complete catalogue of lunar impact craters. 8908 crater records from the LU78287GT were identified in the study area, and they were used to estimate the surface age as well. Fig. 2 shows the results. The red curve in Fig. 2 is the result from the 47505 craters detected by us, in comparison with the black curve, which is the result from the LU78287GT. The estimated surface age of the study area is 3.87 Ga from our results, which compares well with the reference age of 3.83 Ga obtained based on the LU78287GT catalogue, and most recent age estimation 3.85 Ga for Nectarian-Lower Imbrian transition (Hiesinger et al. 2010).

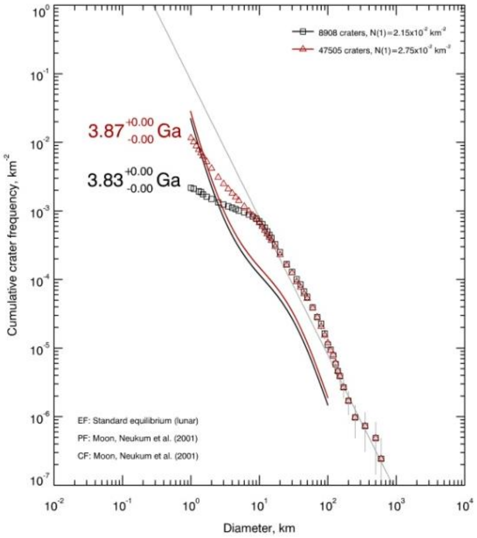

Figure 2. The cumulative curves of craters in Orientale basin.

Spatial Distribution and Morphological Characteristics: The spatial distribution and morphological characteristics of the craters were analyzed. The radial distribution of craters from our catalogue shows the removal of pre-existing craters by Orientale impact also occurs in the range of 600-700 km from the basin rim crest, in comparison with the conclusion of about 500 km obtained by Head et al. (2010). The majority of the craters in our catalogue have the depth-to-diameter ratios around 0.1. As for the wall slope of craters, there are considerable amount (~20%) of craters with wall slope ⩾ 16°.

Conclusion: The results show that our crater catalogue in the region of the orientale basin can produce reliable estimation of the surface age of the region. Our work also provides thorough updates on population distribution, spatial distribution, and morphological characteristics of craters in this region.

References: [1] Head, J. W., III, et al. (2010) Global Distribution of Large Lunar Craters: Implications for Resurfacing and Impactor Populations. *Science*, **329**, 1504-1507. [2] Wu, B., et al. (2014) Topographic Modeling and Analysis of the Landing Site of Chang'E-3 on The Moon. *Earth and Planetary Science Letters*, **405,** 257-273. [3] Barker, M. K., et al. (2015) A new lunar digital elevation model from the Lunar Orbiter Laser Altimeter and SELENE Terrain Camera. *Icarus*. [4] Haruyama, J., et al. (2012) Lunar Global Digital Terrain Model Dataset Produced from SELENE (Kaguya) Terrain Camera Stereo Observations. Proc. of the LPSC2012. [5] Neukum, G., et al. (2001) Cratering Records in the Inner Solar System in Relation to the Lunar Reference System. *Space Science Reviews*, **96**, 55-86. [6] Salamunićcar, G., et al. (2013) Hybrid Method for Crater Detection based on Topography Reconstruction from Optical Images and the New LU78287GT Catalogue of Lunar Impact Craters, *Advances in Space Research*. [7] Hiesinger, H., J. et al. (2010), Ages and Stratigraphy of Lunar Mare Basalts in Mare Frigoris and Other Nearside Maria based on Crater Size-Frequency Distribution Measurements. *Journal of Geophysical Research*, **115**.

EMPLACEMENT HISTORY OF SELF-SECONDARIES. Zhiyong Xiao[1,2,3]. [1]Planetary Science Institute, China University of Geosciences (Wuhan);[2] Centre for Earth Evolution and Dynamics, University of Oslo; [3]Space Science Institute, Macau University of Science and Technology (zyxiao@cug.edu.cn).

Introduction: Self-secondaries are secondary craters formed by ejecta that have both large launch angles regarding to the target plane (i.e., close to vertical) and high ejection velocity so that their emplacement postdate that of continuous ejecta deposits. Such secondaries are located on top of ballistic ejecta deposits adjacent to the rim of the parent crater, and/or within the rim of the parent crater. Compared with normal secondaries on Moon which usually occur in chains and clusters, self-secondaries are spatially more scattered and they exhibit more circular morphology. The possible existence of self-secondaries was firstly raised in 1969 [1], but debate exists about whether or not self-secondaries affect crater populations in a statistical sense [e.g., 2, 3].

A major controversy in the debate was whether self-secondaries [2] or target properties [3] were the main cause for crater density variations observed on different parts of ejecta deposits around a given crater [e.g., 4]. Recent numerical modelling [e.g., 5], high-resolution crater statistics [e.g., 4, 6], regional context analyses [7], and morphological studies [8] all suggest that self-secondaries could be numerously formed during impact cratering, and their non-uniform distribution and special trajectory compared with normal impact ejecta could be attributed to the above observations. Therefore, crater frequencies measured on the continuous ejecta deposits of a crater do not necessarily represent its formation age, and challenge the prevalent age determination methods and production functions descriptions [8].

On the other hand, presently known impact cratering mechanics does not predict high (e.g., >80 ° from the target plane) launch angle ejecta. Understanding the launch mechanism for ejecta that form self-secondaries will promote our understanding about impact cratering processes. A missing bridge between present observations about self-secondaries and their origin is the time sequence of their emplacement in the frame of impact cratering in general.

Emplacement sequence between self-secondaries and ‘normal’ ballistic ejecta. Ejecta forming self-secondaries also follow ballistic trajectories. Here ‘normal’ ballistic ejecta refer to ejecta deposits that form more distant secondaries and continuous ejecta deposits. Many recent crater counts have demonstrated that observable self-secondaries postdate the emplacement of continuous ejecta deposits [e.g., 2, 4, 6, 7]. Soon (i.e., on the order of ages comparable with those of Giordano Bruno and Tycho craters on the Moon) after the formation of a crater, self-secondaries dominate the small crater population accumulated on top of the continuous ejecta [e.g., 4, 7].

Emplacement sequence between self-secondaries and impact melt flows on top of ‘normal’ ejecta. A layer of melt deposits are frequently observed on the top of continuous ejecta deposits on various planetary bodies [e.g., 9]. The flow paths of such melt deposits are clear around fresh impact craters, and some embayment relationships between the melt flows/deposits and self-secondaries suggests that many self-secondaries have been accumulated on the ‘normal’ ejecta while the melt was still flowing [e.g., 4, 5]. Besides the embayment relationship, the crater densities on the ‘normal’ ejecta, melt veneers over restricted areas of normal ejecta, and small melt pools at local topographic lows also support this emplacement sequence (Fig. 1) [7].

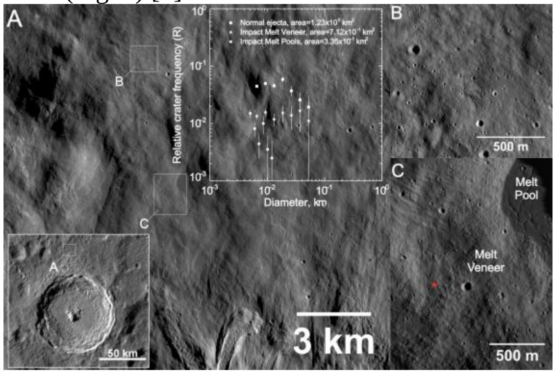

Fig. 1. Tycho crater on the Moon and the emplacement history of continous ballistic ejecta deposits, impact melt, and self-secondaries [7].

Did self-secondaries still being deposited when or after the melt deposits were emplaced? Recent observation [8] find that around very young parent craters, self-secondaries on ‘normal ballistic ejecta deposits’ have circular shapes, but craters on both the melt veneer and melt pools exhibit irregular shapes with large spalled boulders around the crater rims, hinting that the craters on the melt deposits are also self-secondaries, and their irregular morphology was caused by the combined effect of low re-impact velocity and half-molten melt deposits. However, the effect of target property and impact velocity on crater morphology is not well understood.

Hokusai is the youngest complex crater on the northern middle–high latitudes of Mercury [10]. Impact melt deposits are more abundant both within and around Hokusai compared with similar-sized

Mercurian craters, covering many secondaries (Fig. 2). The highly-elliptical orbit of the MErcury Surface, Space ENvironment, GEochemistry, and Ranging (MESSENGER) spacecraft about Mercury has captured unprecedented high resolution images for the northern hemisphere, permitting us to study the detailed distribution of secondaries around Hokusai [10]. The 'normal' ejecta of Hokusai have been all/mostly covered by subsequent outward melt flows, if self-secondaries have once accumulated on the buried 'normal' ejecta, they are not clearly visible on the surface.

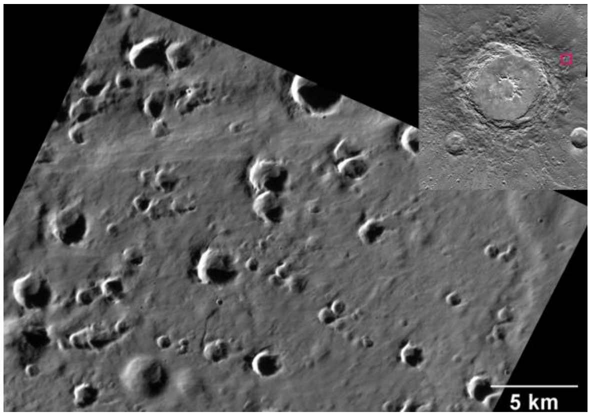

Fig. 2. Hokusai crater on Mercury and the emplacement sequence of self-secondaries, 'normal' ballistic ejecta, and melt flows close to the crater rim [10].

Small craters clearly postdating the melt flows are visible. The crater density (N(D>=100 m)/10^6 km^2) on top of the melt flows shows variations at different azimuths regarding to the impact direction, and the density is substantially higher at the uprange (Fig. 3). Only few complex craters at the northern hemisphere of Mercury are younger than Hokusai, suggesting that the small crater population on the melt flows may be dominated by the self-secondaries of Hokusai instead of being distant secondaries from other craters.

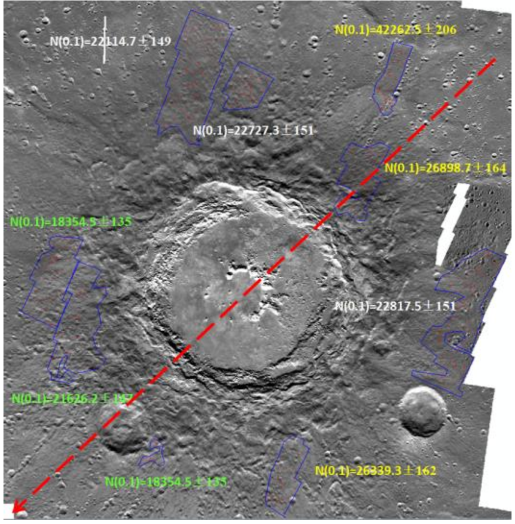

Fig. 3. The small crater population on top of the melt flows around Hokusai has larger density at the uprange [10].

Emplacement sequence between self-secondaries and melt ponds: Few small craters are visible on the floor of Hokusai, suggesting either that most self-secondaries have been formed when the impact melt within the crater floor was settled, or that self-secondaries have also accumulated on the melt pools on the crater floor, but the hot melt could not support the topography of the self-secondaries.

Numerous melt pools are also deposited on the crater rim of Tycho. Crater densities on 6 different melt pools do not show variations [6], although the morphology of these craters is dramatically different from that of self-secondaries on normal ejecta [8], suggesting that self-secondaries might have ceased forming when the melt pools were emplaced. However, this preliminary comparison should be extended to more cases.

Emplacement history and possible formation mechanism for self-secondaries. Ejecta that formed elf-secondaries should have both large ejection angles and velocities so that they land after the 'normal' continuous ejecta deposits were emplaced, and they are still dropping when the impact melt was flowing over the normal ejecta. The flight time depends on the launch velocity and angle, but it must be at least on the order of minutes. Possible reasons causing such high-angle ejecta include: (1) spalled fragments at the rear of the projectile; (2) chaotic interaction of shock wave and heterogeneities in the target.

References: [1] Shoemaker E. M. et al. (1969) *JGR*, *74*(*25*), 6081–6119. [2] Plescia J. B. et al. (2010) *LPS XXXXI*, 2038. [3] van der Bogert C. H. (2010) *LPS XXXXI*, 2165. [4] Zanetti M. et al. (2015), *Workshop on Issues in Crater Studies and the Dating of Planetary Surfaces*, #9041. [5] Prieur N. C. et al. (2015), *Bridging the Gap III: Impact cratering in nature, experiment, and modeling*, #1096. [6] Xiao Z. and Strom R. G. (2012) *Icarus*, *220*, 254–267. [7] Xiao Z. and Werner S. C. (2015); *JGR*, *120*, doi:10.1002/2015JE004860. [8] Plescia J. B. and Robinson M. S. (2015), *46th LPSC*, # 2535. [9] Osinski G. R. et al. (2011), *EPSL*, *310*(*3*), 167–181. [10] Xiao Z. and Werner S. C. (2015), *Bridging the Gap III: Impact cratering in nature, experiment, and modeling*, #1064.

Acknowledgement: This work was initiated by the support of the Research Council of Norway (235058/F20 CRATER CLOCK).), and through the Centres of Excellence funding scheme, project number 223272 (CEED). It is currently supported by National Natural Science Foundation of China (No. 41403053) and fund CUG130106 of China University of Geosciences (Wuhan).

SURVEY AND ANALYSIS OF THE CRATERS POPULATION IN THE APOLLO 17 REGION: WIDER IMPLICATIONS FOR CRATER GEOCHRONOLOGY.

R. Bugiolacchi, Macau University of Science and Technology (MUST), Avenida Wai Long, Taipa, Macau. rbugiolacchi@must.edu.mo

Introduction: The scientific value of small craters surveys (<1 km diameter) on the Moon and other planetary bodies divides the planetary research community. Some interpret the sub-km population mostly as the product of secondary impacts, thus not suitable for cratering chronology based on size frequency distribution [1]; others claim it to be mostly primary, although with caveats [2]. An exhaustive and cross-tested survey of the crater population in the Apollo 17 landing region (extended to include parts of the neighbouring uplands areas) was carried and offers a unique opportunity for comparing their distribution across an uncommon wide typologies of sampled lunar morphologies, ranging from ancient mare and highlands to gently-to-steeply sloped terrains. Even more interesting is the opportunity of assessing the small craters distribution across areas of known and relatively recent resurfacing time (~100 Ma, [3]) and compare it with unaffected neighbouring areas.

Method and Data: Two Narrow Angle Camera (NAC) image pairs [4] were used, with similar average pixel size (1.43 m) but different incident illumination angles, ~57° (M104311715LRE, basemap, Fig. 1A), and ~81° (M101949648LRE), to detect morphological features of interest. Using both pairs of images allowed for a more confident differentiation of morphological units within much of the Taurus-Littrow valley, based on surface texture and albedo, crater populations, and morphology (Fig. 1B). However, it is worth stressing that the proposed morphologically distinct units (each within the maria and uplands domains) are chemically heterogeneous, except for the uppermost layer belonging to the Light Mantle (a mixture of highland and mare mineralogies).

42,090 craters larger than 5 meters were noted (Fig. 1B) over a total surveyed surface area of 400 km^2, 53% of which are mare units. 79% of all craters were found on the valley floor (density, 160 craters km^{-2}) against a lower observed density of 47 craters km^{-2} on slopes and upland surfaces ('UP').

Conclusions: This work found:

a) the smallest craters populations in the region follow a three-mode representation pattern (Fig. 2), with the 10/15 m crater bins diameter ratio >>1 for the central valley area ('CC, LM, LM2'), >1 for the older mare ('MO'), and <<1 for the uplands ('UP'). This could be related to differences in decay with time dictated by the physical properties of target materials, where the smallest craters (<10 m) erode faster on older and more saturated surfaces ('UP' and 'MO'). This suggests the smallest fractions over the central valley are still relatively young, although if we take 100 Ma since the time of the Tycho's surge resurfacing event, most of the associated small secondaries should have eroded to become undetectable by now.

b) Small craters distribution in the region is patchy and display localised associations (Fig. 3). We concluded that this could be explained by either: 1] a different survival times according to targets' properties (and preferentially around the central area of the valley; or 2] a later, and relatively recent arrival of secondaries from a nearby impact, or maybe even from one of the central craters, such as Steno; or 3] adjusting the projected age of the Tycho event to the lower end of estimates, around the 30 Ma mark.

c) A survey of the d/D ratios of most of the largest craters in the valley points to complex and potentially multiple-stage scenarios of formation. Crucially, their distribution pattern does not preclude any of the hypotheses formulated in this work, including a bi-modal influx.

d) Cratering chronology based on our data proved inconclusive for age estimates, given unlikely resurfacing times. We conclude that, providing we address the issue of primary vs. secondaries representation in the smaller crater fractions, more effort should be dedicated on gathering global statistics on these sizes and refine present cumulative chronology functions.

Summuray: this paper proposes that d/D profiles and localised size-frequency distribution of small craters, backed by evidence from average exposure ages across the region does not exclude two main and distinct secondary influx events, linked to the arrival of secondary products from major distal impacts some 80 Ma year apart. Tycho's ejecta have long been linked to many of the prominent surficial expressions across the region, including the Light Mantle area, with an age estimate of around 100 Ma (e.g., [4]). However, new estimates based on model ages derived from crater counts at Tycho, has widened the time window of formation to 30-95 Ma. Indeed, a new age estimate for this key geological event closer to the 30 Ma would agree with most of the findings of this work in terms of small crater populations, larger craters morphologies, boulders distribution, and known exposure ages.

Alternatively, within the currently favoured single region-wide resurfacing event hypothesis, we may interpret the present overrepresentation of small crater population in the central valley region to signify a record of primary and secondary impacts since its occurrence, and its patchy distribution a consequence of differential decay regimes governed by the targets' mechanical properties. Their crater size frequency distribution would thus help constrain the production function for smaller sizes in the last 100 Ma.

This work concludes that the study of small craters represents a useful tool in lunar research, in agreement with other recent findings (i.e., [2]).

References:

[1] Xiao Z. and Strom R. G. (2012) *Icarus*, *220*, 254–267. [2] Williams J. P. et al. (2014) *Icarus.*, *235*, 23-36. [3] Arvidson R. (1976) *PLSC VII*, 2717–2832. [4] Stöffler D. and Ryder G. (2001) *Space Sci. Rev.* 96, 9–54.

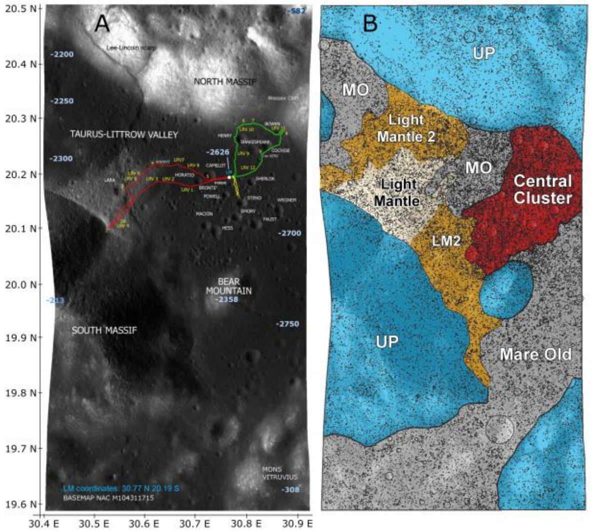

Figure 1. **A** - Area under investigation. Apollo 17 exploration path and stations; **B** - Morphological boundaries derived from observation of variations in surface texture, cratering distribution, and albedo. Circles represent >40,000 craters >7 m in diameter.

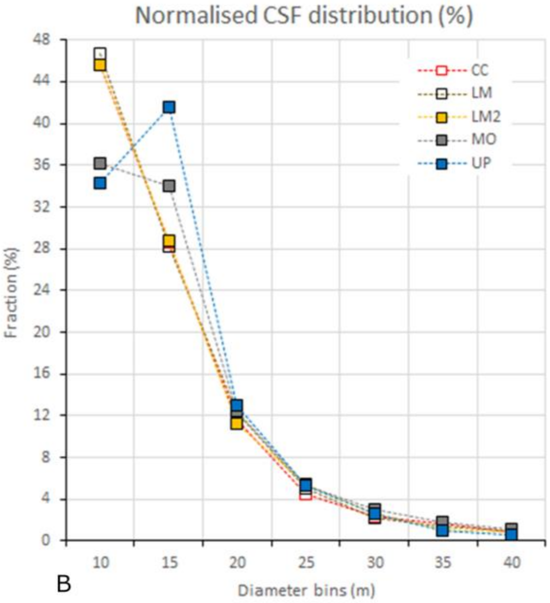

Figure 2. Normalised Crater Size Frequency (CSF) to bin representation (5 m) and expressed as fractions of 100 (%); for instance, UP (massifs and Bear Mountain) has ~34% craters in the 10 m bin size, ~42% 15 m, ~13% 20 m. and ~5% at 25 m (a total of ~95%).

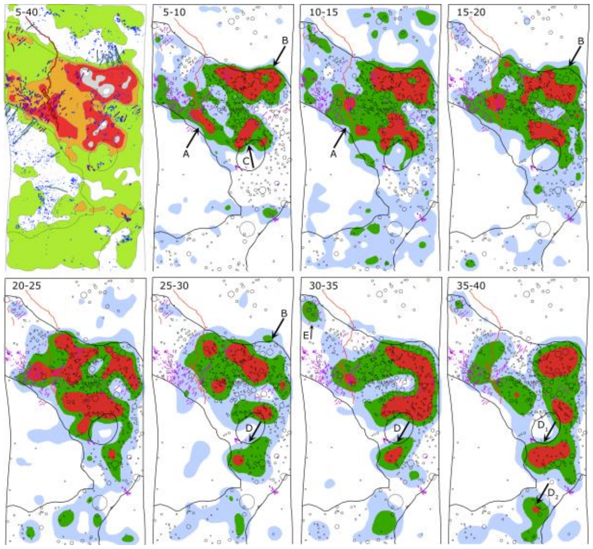

Figure 3. Top-left frame shows overall kernel density distribution of crater size 5-40 m with discretional boundaries ranging from lowest values to the highest (in the order, white-green-orange-red-grey). Blue dots represent boulders and larger tracks for comparison. Purple lines are surficial striations; red are fault lines. Following panes display kernel density distribution of craters within 5 m bin sizes, from low to high (white-blue-green-red). Background grey circles show all craters >40 m. Arrows highlight regions of interest (see text for discussion).

THICKNESS OF LUNAR MARIA BASALTS: NEW RESULTS BASED ON DEGRADED PARTIALLY BURIED CRATERS. Jun Du[1], Wenzhe Fa[1,2], Minggang Xie[2], and Meng-Hua Zhu[2], [1]Institute of Remote Sensing and Geographical Information System, Peking University, Beijing 100871, China (jundu@pku.edu.cn, wzfa@pku.edu.cn), [2]Lunar and Planetary Science Laboratory, Macau University of Science and Technology, Taipa, Macau.

Introduction: Lunar maria basalts are magmatic materials that generated from partially melted mantle and then extruded out to the lunar surface [1]. The volume of maria is of great scientific significance, since it can be used to derive the eruption rate of volcanism that can further constrain the thermal evolution of the Moon [1]. The volume of maria basalts can be estimated as the product of its surface area and thickness. The surface area of basaltic lava flows can be determined based on spectral properties, which is about 6.2×10^6 km^2 (17% of the lunar surface) [2]. Thickness of maria basalts was estimated by multi-source remote sensing techniques in previous studies [3–9]. However, results from these methods are highly model-dependent and vary significantly from several meters to several kilometers, making it difficult to quantify the basalts volume and hence the eruption rate. Therefore, a clear and precise thickness estimation of lunar maria basalts is needed.

Traditionally, basalts thickness estimation methods can be divided into three classes: impact craters [3–6], radar detection [3, 7], and geophysical techniques [8, 9]. As for methods based on impact craters, the thickness of maria basalts can be determined based on outcrops in crater inner walls [3], ejecta composition [4], crater size-frequency distribution (CSFD) [5], and crater morphology [6]. In a few ideal cases, layering structures of lava flows can be observed in the crater walls (e.g., Bessel crater), which provides the most direct technique for the basalts thickness estimation [3]. In most cases, the layering features are masked out by the post-impact mass wasting events, and the basalts thickness can be estimated based on ejecta composition [4]. In this case, the basalts thickness is correlated to the extent of crater ejecta with different compositions based on the crater excavation model [4]. For a large population of lunar craters, the flooding basaltic lava flows will affect their CSFD, and basalts thickness can be inferred from the “knee” in the resulting CSFD [5]. For an individual partially buried crater (PBC), the basalts thickness can be determined from crater rim heights (relative to pre-flooding background level) with and without considering the emplacement of surrounding lava flows [6]. Thanks to the penetration capability of radar waves, the layering features can be directly observed by spaceborne radar sounder [3] or ground penetrating radar [7]. In these cases, the basalts thickness can be retrieved from the time delay between surface and subsurface echoes. It should be noted that, however, as for radar detection a reliable result depends on the knowledge of vertical dielectric constant profile, which is another highly model-dependent parameter. In addition, the basalts thickness was also estimated by gravity measurements [8] and seismic experiments [9], since the emplaced lava flows have a different density compared with the underlying materials thus may result in differences on the gravity field and the velocity of seismic wave. These methods, however, are highly dependent on the geophysical parameters (e.g., porosity and density) of maria basalts at depth, which are still poorly constrained at present. The estimated basalts thickness from the above methods for the same area varies significantly from several meters to several kilometers, which indicates that the estimation of basalts thickness is greatly model-dependent.

Considering the precision and feasibility of the above models, in this study we report an estimation method for basalts thickness based on the rim height of degraded PBCs, and discuss possible improvements to this method with considering the crater degradation process.

Methods: In the case of a PBC, the basalts thickness is the difference of rim heights with and without considering the surrounding lava flows. In previous method to determine the basalts thickness around a PBC [6], the rim height (relative to pre-flooding background level) without considering the basalts emplacement can be estimated based on the empirical relation between rim height and crater diameter of a fresh lunar crater [10], and the rim height with considering the basalts emplacement can be directly measured by the elevation difference between rim crest and surrounding lava flows. It should be noted that, however, present lunar craters have been eroded by meteorites bombardments after their formations. As a result, crater diameter increases and rim height decreases [11]. A recent study based on topographic diffusion theories shows that the degradation process of lunar craters is of great significance. For example, after 4 Ga the rim height of a 5 km-diameter crater is expected to decrease significantly from 184 to 118 m [12]. In this case, if the rim height of a fresh crater is applied to the basalts thickness estimation, the thickness value will be overestimated [2]. Therefore, the crater degradation process should be considered when estimating the basalts thickness from the PBC rim height.

The geologic events related to a PBC can be described as follows. A fresh crater formed on the pre-impact background region, and it began to be eroded by meteorites bombardments afterwards. The basaltic lava flows then flooded and embayed the crater with only the rim crest protruding above mare plains. Then, this PBC continued to be hit by subsequent meteorites, and finally degraded to present status. By modeling the above processes, our method yields the basalts thickness estimation by matching the simulated crater profile with the observation. In our model, the modeled crater profile (H_{model}) of a present PBC is a function of initial crater diameter (D_{ini}), elevations of basalts surface in crater interior (h_i) and exterior (h_e), and ages of PBC (t_{PBC}) and emplaced maria basalts ($t_{basalts}$). In order to compare the modeled and observed crater profiles at the same horizontal level, a vertical offset (z_0) is introduced to shift the observed crater profile (H_{obs}) to match the modeled one. As a result, the inversion problem can be described as eq. (1), which yields the best-fit interior (T_i^0) and exterior (T_e^0) basalts thicknesses around the given PBC:

$$\left[T_e^0, T_i^0\right] = \underset{h_i\in[h_{floor}, h_{rim}], h_e\in[0, h_{rim}]}{\operatorname{argmin}} \left\{\left[H_{model}\left(D_{ini}, h_i, h_e, t_{PBC}, t_{basalts}, z_0\right) - H_{obs}\right]^2\right\} \quad (1)$$

where h_{floor} and h_{rim} are elevations of crater floor and rim crest, and interior (exterior) basalts thickness is the difference between elevations of crater interior (exterior) and basalts surface. In our estimation, the profile of fresh craters was taken from optical rayed craters [13].

Results and Discussions: An unnamed crater (29.39°S, 39.09°W; 3.8 km) located at the H2 unit (3.69 Ga [14]) in the southern Mare Humorum was selected as a case study. This crater was flooded by subsequent lava flows and the crater rim is highly flattened, indicating that it is a PBC (red arrows in Figs. 1a and b). If the crater degradation is not considered, the basalts thickness is estimated to be ~130 m [6].

In our study, the Kaguya DTM was selected as the elevation data since it has a high spatial resolution (7 m) [15]. The assignments (range; increment) to the above six parameters are given as follows: initial crater diameter (2.2 to 3.8 km; 0.1 km), elevation of basalts surface in crater interior (crater floor elevation to rim height; 10 m) and elevation of basalts surface in crater exterior (0 m to rim height; 10 m), PBC age (1 to 4.2 Ga; 0.1 Ga), basalts unit age (1 Ga to PBC age; 0.1 Ga), vertical offset (crater floor elevation to rim height; 10 m). In total, 3,571,963 combinations of the above six parameters were realized. The best-fit result (with RMSE=5 m) shows that, this crater formed 4.2 Ga ago (red) with a diameter of 2.9 km, then degraded (green) and was embayed (blue) by lava flows 4.1 Ga ago, and was finally eroded to present status (pink), which is generally consistent with the observed profile (black) (Fig. 1c). The inverted thickness of maria basalts exterior to the PBC is 50 m, significantly smaller than the value of 130 m if crater degradation is not considered [6].

The basaltic thickness derived from the PBC rim height was further compared with that inferred from the crater excavation model [4]. It can be seen that a crater with a diameter of 800 m (black arrow) penetrated layers with high (red) and medium (yellow to green) TiO_2, and excavated subsutrate layer with low (blue) TiO_2 (Fig. 1d) [16]. This indicates that the basaltic fillings in this region can be divided into three units with high, medium, and low TiO_2 contents from mare surface to basin floor (Fig. 1d), and it can be found that the selected PBC is embayed by the lava flow with medium TiO_2 content. Therefore, the stratigraphic relation and TiO_2 content around the PBC imply that the basalts thickness given by our model actually refers to that of medium TiO_2 basaltic unit. The excavation depth and ejecta radius of this 800 m crater are estimated to be 80 m (1/10 crater diameter) and 800 m (twice crater radius) [11], and the medium TiO_2 ejecta occupies about half of the ejecta in extent. Therefore, according to the crater excavation model, the thickness of medium TiO_2 lava flow is ~40 m [4], which generally agrees with our result.

Conclusions: In this study, a basalts thickness estimation method was proposed based on the degraded PBC rim height. As compared with previous studies, the erosion of crater rim during the post-impact modification process was considered in our method. A case study of a PBC over Mare Humorum shows that basalts thickness may be significantly smaller than the results given by previous models. If our estimation is correct and this method can be applied globally, then the volume and eruption rate of melted mantle materials would be much smaller than previous estimations. In our future works, a global isopach map of lunar maria basalts is expected to be produced, and geologic interpretations from basalts thickness distribution will be studied.

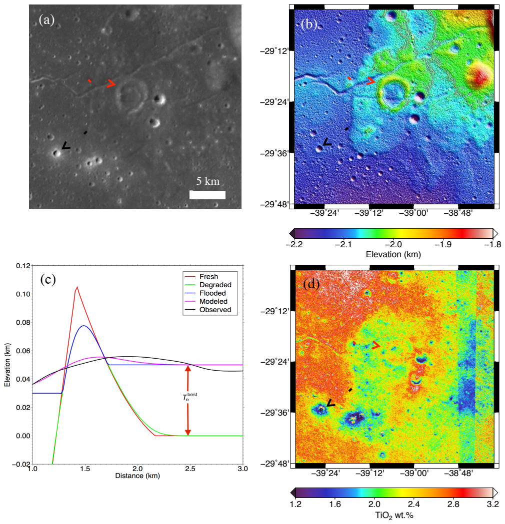

Fig. 1. Case study of a PBC in Mare Humorum: (a) LROC/WAC image, (b) Topography from Kaguya DTM, (c) Inversion result on basalts thickness, and (d) TiO_2 content map from Clementine UVVIS.

References: [1] Head J. W. (1981) *Moon Planets, 26,* 61–88. [2] Hörz F. (1978) *LPS IX,* 3311–3331. [3] Oshigami S. et al. (2012) *Icarus, 218*, 506–512. [4] Thomson B. J. et al. (2009) *GRL, 36,* 1–5. [5] Hiesinger H. et al. (2002) *GRL, 29*, 1–4. [6] De Hon R. A. (1974) *LPS IV,* 53–59. [7] Xiao L. et al. (2015) *Science, 347,* 1,226–1,229. [8] Talwani M. et al. (1973) *NASA Spec. Pub. 330*, 13-1–13-13. [9] Cooper M. R. et al. (1974) *Rev. Geophys., 12*, 291–308. [10] Pike R. J. (1977) *Pargamon Press, New York,* 489–509. [11] Melosh H. J. (1989) *Oxford Univ. Press, New York,* 78–190. [12] Xie M. and Zhu M. (2016) *EPSL, 440*, 71–80. [13] Fassett C. I. and Thomson B. J. (2014) *JGR, 119*. [14] Hiesinger H. et al. (2000) *JGR, 105,* 29,239–29,275. [15] Haruyama J. (2012) *LPS XLIII,* 1200. [16] Lucey P. G. and Blewett D. T. (2000) *JGR, 105,* 20,297–20,305.

New results from NASA's lunar gravity mapping mission GRAIL.

M. A. Wieczorek, Insitut de Physique du Globe de Paris, 75013, Paris, France (wieczor@ipgp.fr).

Summary. The Gravity Recovery and Interior Laboratory (GRAIL) mission, NASA's 11th Discovery mission, has successfully mapped the Moon's gravity field to unprecedented accuracy. The scientific objectives of the GRAIL mission were to determine the structure of lunar highland crust and maria, addressing impact, magmatic, tectonic and volatile processes that have shaped the near surface and crust.

GRAIL is the lunar analog of the successful GRACE twin-spacecraft terrestrial gravity recovery mission that has been mapping Earth's gravity field since its launch in 2007. During the three month primary mission, and from a mean altitude of about 50 km, a global gravity field to spherical harmonic degree 660 was obtained. During the subsequent three month extended mission, the average altitude was lowered to about 25 km, allowing for the construction of gravity models that exceed spherical harmonic degree 900. Current models in that are in development exceed spherical harmonic degree 1500. In addition to the static gravity field, GRAIL has also determined the degree-2 and 3 Love numbers, and is searching for time variable signals related to inner core precession.

In this presentation, a review of the most recent results from the GRAIL mission will be given, including the structure of large impact basins, subsurface magmatism, the density and porosity of the lunar crust, and constraints on interior structure.

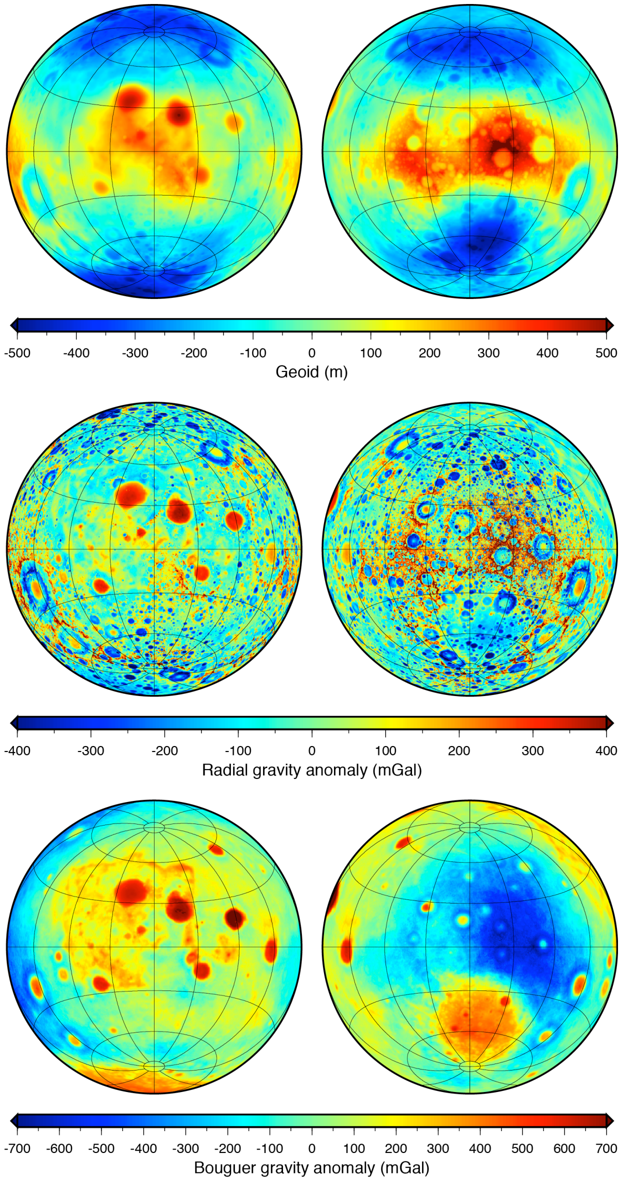

Figure 1. The geoid (top), radial free-air gravity (middle), and Bouguer gravity (bottom) of the Moon as determined by data collected from the GRAIL mission. These images were constructed using the model JGGRAIL_900C11A that is developed to spherical harmonic degree and order 900. Each row shows two images, which are centered on the nearside (left) and farside (right) hemispheres. Each image covers 75% of the Moon's surface and is projected in a Lambert azimuthal equal-area projection.

Mass anomalies beneath the surface of Lunar Volcanic Complexes from GRAIL Bouguer gravity field. Q. Huang[1], [1]Planetary Science Institute, China Univeristy of Geosciences (#388 Lumo Road, Hongshan District, Wuhan, Hubei, China, 430074. qianhuang@cug.edu.cn)

Introduction: Large volcanic complexes, such as the Rumker Hills, Aristarchus Platea, Marius Hills are likely sites of intense and substained magmatic activity occurred during the main phase of mare volcanism on the lunar nearside [1-2]. The subsurface structures of these volcanic regions are important on deciphering their formation mechanisms, and further help us to understand the thermal history of the lunar nearside crust and mantle.

The Bouguer gravity anomaly, which is the gravity field corrected for surface topography, contains directly the mass anomalies beneath the lunar surface. The Gravity Recovery and Interior Laboratory (GRAIL) and its extended mission has mapped the lunar gravity filed with dramatically high resolution [3-5], making it possible to analyze the interior structures of these relatively small volcanic complex regions.

In our previous study, we carried out localized spectral analyses for these regions by combing GRAIL gravity and topography data from Lunar Reconnaissance Orbiter (LRO) laser altimeter [6], and obtained their crustal bulk densities [7]. Constrained bulk densities of Rumker Hills, Marius Hills, Gardner and Kepler are generally higher than 2850 kg m^{-3}, which suggests that the shallow crusts of these regions are mainly compolsed of dense intrusive or extrusive magmatic units. Whereas the Aristarchus Plateau and Hortensius have relatively lower crustal and load density, with mean value around 2550 kg m^{-3}, which are well consistent with the average bulk density of the lunar highland crust.

Localized spectral analyses provide a useful way to constrain the densities of the volcanic complexes, but this technique is hard to resolve how the materials vary with depth. We have tried to use the band-limited Bouguer gravity (BBG, [8]) and the Bowin [9] limiting relation between spherical harmonic degree and its accumulating depth to identify how the mass vary beneath these regions [10], but it was difficult to specify spherical harmonic degree (l) to isolate contributions from different depths without good constraints from lunar seismology.

Method: Zuber [11] tried to construct the relationship between degree ranges and depths zones within lunar crust by using a forward modeling method. Here, we make use of this method to the volcanic complex regions and tried to use two other methods to verify the results.

We directly use the recent Bouguer gravity model that was downloaded from the Planetary Data System (http://pds-geosciences.wustl.edu/grail/grail-l-lgrs-5-rdr-v1/grail_1001/shadr/; gggrx_0900c_bouguer_sha.lbl). It's a 900 degrees and orders spherical harmonic models derived from the GRGM900C gravity model [5] and the LRO topography data. A uniform crustal density of 2500 kg m^{-3} and a finite-amplitude correction of the 9th order has be used. Though we noticed that there is a newly updated gravity model with 1500 degrees and orders [4], we find no obvious difference on calculating the Bouguer gravity anomalies between these two gravity models by truncating to a reliable degree to 570 [5] or 550 [4].

Results: Figure 1 shows how the mass concentrations varying with different depth, indicating potential different subsurface structures for these volcanic complexes. For the first 271 to 540 degree ranges (representing depth between 10 and 20 km in the crust), there is no obvious mass anomalies within this layer for eight volcanic complexes. Gardner starts to exhibit positive mass concentration at the second layer (181 to 270 degree, 20-30 km), where Rumker Hill, Prinz and Marius Hills show a positive signal at the third layer from depth 30 to 45 km ($120 < l < 180$). These kind of mass concentration disappears quickly for Rumker Hills, but seems increased beneath Gardner, Prinz and Marius Hills. There results suggest that sources of magma units that feed the surface volcanic activity of the Gardner had different head depths from others.

The strongest positive anomalies beneath Rumker Hills and Prinz at a layer of 120 to 180 degree, suggesting that dense material, possible solidified intrusive igneous rocks, are mainly concentrated at a depth of 30-45 km (the bottom of the lunar crust, Wieczorek et al., 2013). Gardner and Marius Hills seem to have positive mass anomalies accumulating with depth, and Marius Hills has a mantle source (>45 km) region deeper than Gardner.

The Bouguer gravity anomalies for the Kepler, Aristarchu, Hortensius and Cauchy show no obvious residual anomalies at the first three layers, indicating that no substrantical dense material has been accumulated beneath these volcanic complexes. Alternatively, it is possible that small volumes of intrusive igneours units, such as dikes and sills, may exist within the curst at such depths, but their contribution to the gravity signal might be too small to be distinguished from recent GRAIL data.

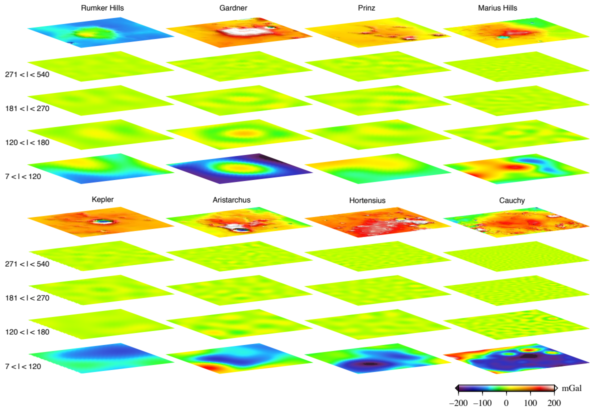

Figure 1. Bouguer gravity anomalies of the eight volcani complexes at different spherical harmonic degree ranges. The crust has been breaked into degree ranges of $271 < l < 540$ (10-20 km depth), $181 < l < 270$ (20-30 km depth), and $120 < l < 180$ (30-45 km depth). The lower degress ($7 < l < 120$) correspond approsimatedly to mantle depths. The top layer is the LOLA topography map. The figures are in cylindrical equidistant projections, and looked at the surface from SE at 12-degree elevation.

Discussion: Band-limited Bouguer gravity (Featherstone, et al., 2013) provides a comparative way to indentify the mass concentration variations beneath these volcanic complexes. We artifically choose the trancated degrees from 300, 150, 100, 50 and 7 to 550, and calculate the accumulating bouguer gravity anomalies for eight volcani complexes. As shown in Figure 2, there is no mass anomalies from degree 300 to 550 for all the regions. Positive mass concentration start to appear from degree 150 to 550 for Rumker Hills, Gardner and Prinz, but from degree 100 to 550 for Marius Hills. Results from Band-limited Bouguer gravity are consistent with those from Figure 1.

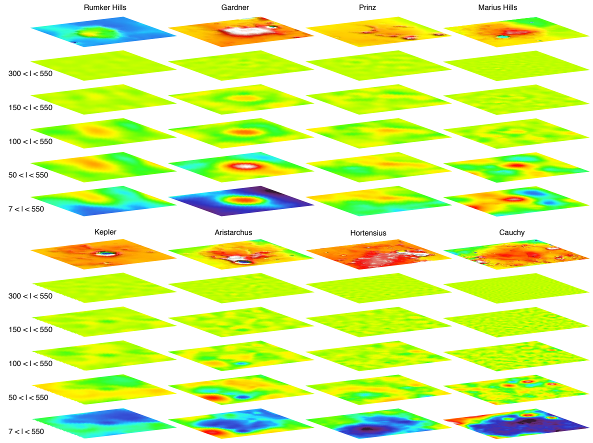

Figure 2. Band-limited Bouguer Gravity (BBG) anomalies of eight volcanic complexes at different accumulating degree ranges. The figure is with same projection and color bar of Figure 1.

According to the theory of potencial field, the signals caused by shallow mass sources will attenuated faster than deeper ones. We tried to calculated the Bouguer gravity anmoalies with different reference height. As shown in Figure 3, Rumker Hills, Gardner, Prinz and Marius Hills are all have mass concentration at the calculating height of 10 km, but these signals almost disappear at a height of 50 km except Marius hills. Figure 3 shows that Marius Hills has a mass anomaly source deeper than other three regions, which are consistent with the previous two methods.

Summary: The Bouguer gravity anomaly is an efficient database to study the mass concentration beneath the lunar volcanic complexes. Results show that dense materials with different source depth that might be solidified intrusions exist beneath Rumker Hills, Gardner, Prinz and Marius hills, but no substantial dense materials have been detected beneath Aristarchus, Hortensius, Kepler or Cauchy.

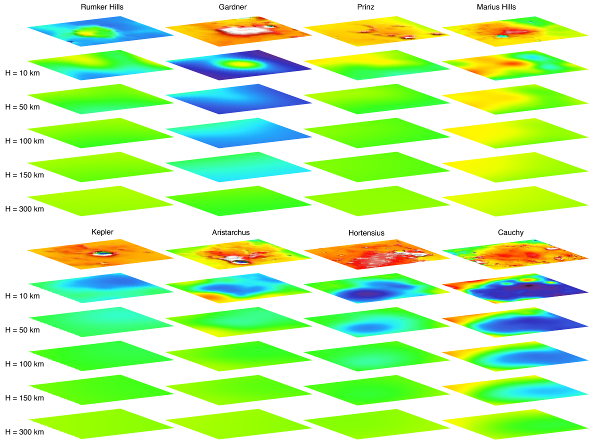

Figure 3. Bouguer gravity anomalies of eight volcanic complexes calculated from different reference heights (10, 50, 100, 150 and 300 km). The figure is with same projection and color bar of Figure 1.

References: [1] Head J. W. et al. (1976) Rev. Geophys., 14, 265-300. [2] Whitford-Stark J. L. and Head J. W. (1980) JGR, 85, 6579-6609. [3] Zuber M. A. et al. (2013) Science, 339, 668-671. [4] Konopliv A. S. et al. (2014) GRL, 41, 1452-1458. [5] Lemoine F. G. et al. (2014) GRL, 41, 3382-3389. [6] Smith D. E. et al. (2010), GRL, 37, L18204. [7] Huang Q. et al. (2014), Icarus, 243, 48-57. [8] Featherstone W. E. et al. (2013) JGR-Planets, 118, 1-17. [9] Bowin C. (1983), Mar. Geod., 7, 61-100. [10] Huang Q. et al. (2014), LPSC 45th, Abstract #1790.pdf. [11] Zuber M. T. (2016), LPSC 47th, Abstract #2105.pdf.

Acknowlegement: We thank the GRAIL and LOLA teams making their gravity and topography data publicly available. The localized spherical harmonic analyses were performed using SHTOOLS, which is available at http://shtools.ipgp.fr. This work was supported by the National Natural Scientific Foundation of China (11403020, 41373066).

LINEAR STRUCTURES OF LUNAR GRAVITY ANOMALIES.

X. Y. Wang[1], Q. Liang[1], C. Chen[1], J. S. Du[1]
[1]Hubei Subsurface Multi-scale Imaging Key Laboratory, Institute of Geophysics and Geomatics, China University of Geosciences, Wuhan 430074, China, geo_xywang@126.com, qliang@cug.edu.cn.

Introduction: The precise and high resolution lunar gravity data obtained by the Gravity Recovery and Interior Laboratory (GRAIL) mission [1] provide more chances for the detection of lunar subsurface structures. Using Bouguer gravity gradient, some significant charateristics subsurface linear features have been detected, including the ancient vertical tabular intrusions or dikes [2] and the new PKT border structures [3]. Here we attempt other edge detection methods used in the interpretation of potential field to study the subsurface structures of the moon.

Methods: Bouguer gravity can reflect the subsurface density changes. We used GRAIL gravity model GRGM900C_BOUGUER [4] filtered to include degrees 2 to 600. The normalized standard deviation [5] and normalized total horizontal derivatives [6] were applied to the Bouguer gravity to detect linear edge structures.

We also investigated the ring structures in some mare basins. Ring structures associated with the basins may result from not only tectonic offsets of subsurface density interfaces but also surface mare basalts ponding [2]. We think the former is the major part. Since we had used Canny operator [7] on the Bouguer gravity anomalies calculated at different altitudes to detect the edge in Sinus Iridum-Mare Imbrium northwest area and analyze the density variation tendency below [8], the same method was also applied to mare Crisium and Serenitatis. Gravity anomalies calculated at higher altitudes, as like upward continuation of potential field, can highlight deeper density anomaly. We assumed that the higher the calculated altitude of gravity anomaly is, the deeper source characters will be reflected. Certainly, the efficient altitude value is limited. When edge detection results of different calculated altitudes for gravity anomaly overlaid together, the subsurface density anomaly source's tendency feature can be showed qualitatively [8].

Results: Both the normalized standard deviation map and normalized total horizontal derivatives map show linear and ring structures, including the PKT boundary (Figuer 1). Some ring structures are associated to the identified quasi-circular mass anomalies[9]. Moreover, it is obvious that the ring structures in mare Moscow manifest two semi-circles, which may be associated with the proposition that two basins exist here [10].

For Canny operator methods, with the increase of the calculated height of gravity anomaly, the ring structures in mare Crisium firstly have a tendency to contract and then extend, meaning a depression in the lower depth for the deep density interface and then extend around when deeper. We find this tendency agreeing with the crust-mantle interface from Wieczorek et al. (2013) in Mare Crisium area. In mare Serenitatis, however, the ring edges are not so regular and present a pear-shaped form (Figuer 2).

References: [1] Zuber M. T. et al. (2013) *Science, 339*, 668-671. [2] Andrews-Hanna J. C. et al. (2013) *Science, 339*, 675-678. [3] Andrews-Hanna J. C. (2014) *Nature, 514*, 68-71. [4] Lemoine F. G. et al. (2014) *GRL, 41*, 3382-3389. [5] Cooper G. R. J. and Cowan D. R. (2008) *Geophysics, 73*, H1-H4. [6] Cordell L. (1979) *New Mexico Geol. Soc. Guidebook, Field Conf.*, 59-64. [7] Canny J. (1986) *IEEE Transactions on Pattern Analysis and Machine Intelligence, 6*, 679-698. [8] Wang X. Y. et al. (2015) *Earth Science-Journal of China University of Geosciences, 40*, 1566-1575. [9] Evans A. J. et al. (2016) *GRL, 43*, 2445-2455. [10] Ishihara, Y. et al. (2011) *GRL, 38*, L03201. [11] Wieczorek M. A. et al. (2013) *Science, 339*, 671-675.

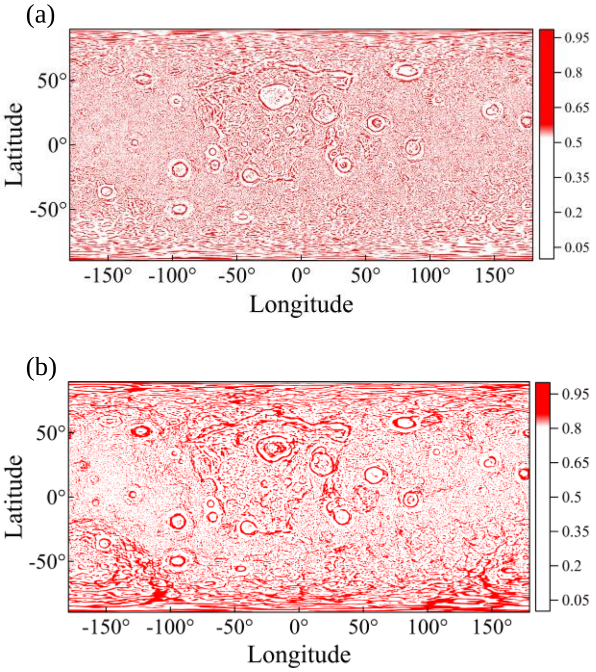

Figuer 1. (a) Normalized standard deviation of bouguer gravity anomaly map. (b) Normalized total horizontal derivatives of bouguer gravity anomaly map.

(a)

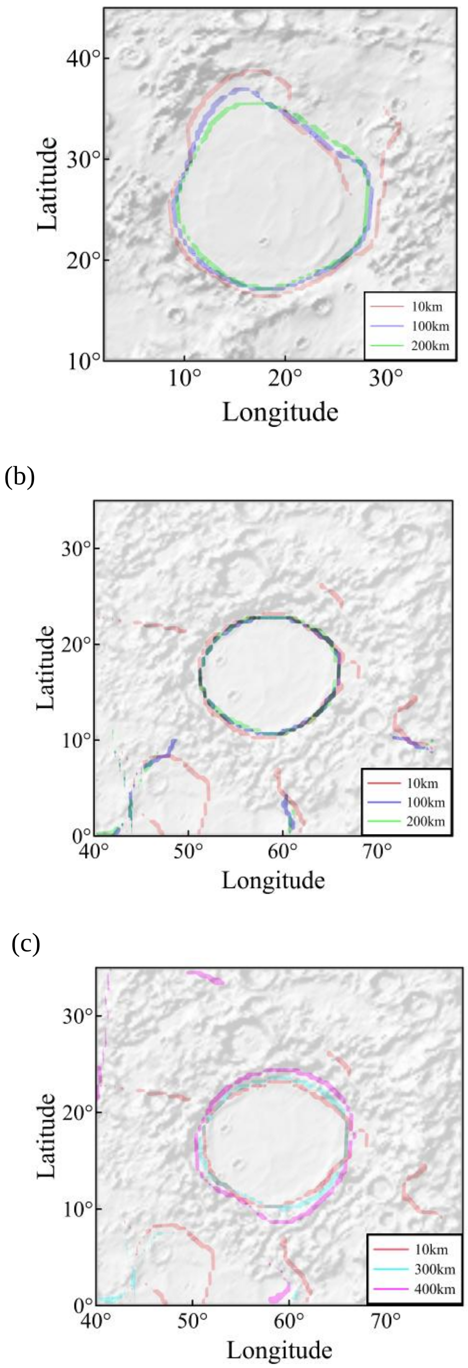

Figuer 2. Canny operator results for mare Serenitatis(a) and mare Crisium (b) (c) extracted from bouguer gravity anomalies at different height levers relative to the reference sphere of 1738 km.

HIGH RESOLUTION LUNAR MASCON DENSITY STRUCTURE REVEALED BY GRAIL GRAVITY. Yan Jianguo[1], Zhang Yi, Li Fei, Ye Mao, Chen Chao, Du Jinsong. [1]State Key Laboratory of Information Engineering in Surveying, Mapping and Remote Sensing, Wuhan University. Wuhan 430079, China. (jgyan@whu.edu.cn)

Abstract: In the history of the moon exploration, the most amazing achievement is that some mass concentrated areas were found on the near side of the moon. These mass concentrated areas, which are referred to mascons, are usually covered with a positive gravity anomaly peak, and surrounded by negative gravity anomalies with low geographical elevation. Here we proposed a gravity inverse method including geological constraint to obtain density structure of the lunar mascons. The method was implemented in spherical coordinates and validated with simulation test. Using this method we obtained high resolution density anomaly structure of lunar nearside maria mascons basins and farside highland mascons. The high resolution depth information and density anomalies structure of the lunar mascons are presented for the first time. By comparing the nearside maria mascons with farside mascons, we found all the mascons have an annulus density structures in their shallow stratums; the mascon depth information also indicates that the mascon depth on lunar far side is much deeper than that on the near side. These results indicate various origination mechanism between nearside and farside mascons.

THE DEEP LUNAR INTERIOR WITH A LOW-VISCOSITY ZONE: REVISED CONSTRAINTS FROM RECENT GEODETIC PARAMETERS ON THE TIDAL RESPONSE OF THE MOON.

Y. Harada[12], S. Goossens[3], K. Matsumoto[4], J. Yan[5], J. Ping[6], H. Noda[4], and J. Haruyama[7], [1]Space Science Institute, Macau University of Science and Technology (Avenida Wailong, Taipa, Macau, China, yharada@must.edu.mo), [2]Earthquake Research Institute, the University of Tokyo (1-1-1 Yayoi, Bunkyo, Tokyo 113-0032, Japan, harada@eri.u-tokyo.ac.jp), [3]Center for Research and Exploration in Space Science and Technology, University of Maryland, Baltimore County (1000 Hilltop Circle, Baltimore, Maryland 21250, USA, sander.j.goossens@nasa.gov), [4]National Astronomical Observatory of Japan, National Institutes of Natural Sciences (2-12 Hoshigaoka, Mizusawa, Oshu, Iwate 023-0861, Japan, koji.matsumoto@nao.ac.jp, hirotomo.noda@nao.ac.jp), [5]State Key Laboratory of Information Engineering in Surveying, Mapping and Remote Sensing, Wuhan University (129 Luoyu Road, Hongshan, Wuhan, Hubei 430079, China, jgyan@whu.edu.cn), [6]National Astronomical Observatories, Chinese Academy of Sciences (20A Datun Road, Chaoyang, Beijing 100012, China, jsping@bao.ac.cn), [7]Institute of Space and Aeronautical Science, Japan Aerospace Exploration Agency (3-1-1 Yoshinodai, Chuo, Sagamihara, Kanagawa 252-5210, Japan, haruyama.junichi@jaxa.jp).

Abstract: We revisit the constraints on the deep lunar interior with a possible low-viscosity layer at the core-mantle boundary obtained from our previous forward modeling [1] by describing the lunar tidal response. In here we consider several tidal parameters that have been improved or are newly determined from recent geodetic observations and analyses. First, providing the internal structure of the Moon, especially its viscosity profile, we compute its tidal quality factors (Q) and Love numbers (k2, k3, and h2) for the monthly, annual, triennial, and sexennial tidal periods. Second, we compare the numerical model with the latest observational data, especially from GRAIL (i.e., gravity, e.g., [2, 3, 4]), LRO (i.e., shape, e.g., [5]), and LLR (i.e., rotation, e.g., [6]). As a result of this comparison, we can find a viscosity profile with the low-viscosity zone which is in principle consistent with the frequency dependence of the quality factors [6] although its viscosity range is slightly larger than that constrained previously [1]. In addition, we can completely or nearly explain each Love number [2, 3, 4, 5, 6] by considering the above constraint on the viscosity range revised here, at least limited to the monthly tide. Finally, we conclude that our results lead to a low-viscosity layer which is much thicker than that in our earlier investigation [1] and reaches just below or inside the place where many seismic nests of deep moonquakes are located [7, 8, 9].

Keywords: The lunar interior; A low-viscosity zone; The tidal response; The Love number; The quality factor

Acknowledgements: This work was supported by Research Funding (No. 039/2013/A2) at the Science and Technology Development Fund of the Macau Special Administrative Region, and also Research Grant (No. 0434) at Macau University of Science and Technology. In addition, a part of this work was achieved using Grant of Visiting Fellow Program with Seminar supported by the Research Coordination Committee at National Astronomical Observatory of Japan.

References: [1] Harada Y. et al. (2014) *Nat. Geosci.*, *7*, 569-572. [2] Konopliv A. S. et al. (2013) *J. Geophys. Res. - Planet.*, *118*, 1415-1434. [3] Lemoine F. G. (2013) *J. Geophys. Res. - Planet.*, *118*, 1676-1698. [4] Lemoine F. G. (2014) *Geophys. Res. Lett.*, *41*, 3382-3389. [5] Mazarico E. et al. (2014) *Geophys. Res. Lett.*, *41*, 2282-2288. [6] Williams J. G. and Boggs D. H. (2015) *J. Geophys. Res. - Planet.*, *120*, 689-724. [7] Nakamura Y. (2005) *J. Geophys. Res. - Planet.*, *110*, -. [8] Weber R. C. et al. (2011) *Science*, *331*, 309-312. [9] Zhao D. et al. (2012) *Global Planet. Change*, *90-91*, 29-36.

Competition between Stagnant Lid Thickening and Development of Lunar Magma Ocean Overturn.

Shuoran Yu[1,2], Nicola Tosi[3,4], Hon-Cheng Wong[2]. [1] Space Science Institute, Macau University of Science and Technology, Macau SAR, China, shuoran.yu@icloud.com. [2] Faculty of Information Technology, Macau University of Science and Technology, Macau SAR, China, hcwong@must.edu.mo. [3] Institute for Planetary Research, German Aerospace Centre (DLR), Berlin, Germany, nicola.tosi@dlr.de. [4] Department of Astronomy and Astrophysics, Berlin Institute of Technology, Berlin, Germany.

Introduction: The crystallisation and differentiation of the lunar magma ocean determines the initial internal structure of the Moon but could lead to a gravitationally unstable stratification that overturns via solid-state convection into a stable configuration. As the major carrier of titanium among lunar minerals, ilmenite crystallises when about 87-95 vol. % magma ocean has solidified [1, 2]. With a density of 4800 kg m^{-3}, the ilmenite-bearing cumulate (IBC) is much denser than the underlying mafic cumulates (with a density of 3000-3300 kg m^{-3}) and is expected to sink into the deep mantle. This so-called "lunar magma ocean overturn" hypothesis has been invoked as a potential explanation for the origin of high-Ti basalts [3] and other geophysical anomalies in the deep lunar interior, such as the correlation between the distributions of mare basalts and the location of deep moonquake [4], the low-viscosity zone above the core-mantle boundary [5] and the magnetic field anomaly between 3.9 and 3.6 Ga [6].

Even though the overturn hypothesis provides a suitable explanation for many aspects of the early lunar evolution, it still encounters some difficulties related to the dynamics of the overturn process. Elkins-Tanton et al. [7] suggested that the stagnant lid forming on top of lunar mantle may entrap the IBC layer preventing it from sinking into the mantle. This problem is critical to the understanding of the early history of the Moon and this study aims at quantitatively analysing the competition between stagnant lid thickening and onset of the lunar magma ocean overturn.

Dynamic Model: We use the mantle convection code GAIA [8] to solve the dimensionless conservation equations of mass (1), momentum (2), thermal energy (3), transport of composition (4), and of heat sources (5) assuming incompressible Stokes flow of a Newtonian fluid under the Boussinesq approximation:

$$\nabla \cdot \mathbf{u} = 0 \tag{1}$$

$$-\nabla p + \nabla[\mu(\nabla \mathbf{u} + (\nabla \mathbf{u})^T)] = (Ra_T\, T - Ra_C\, C)\mathbf{e_r} \tag{2}$$

$$\partial T/\partial t + \mathbf{u} \cdot \nabla T = \nabla^2 T + Q \tag{3}$$

$$\partial C/\partial t + \mathbf{u} \cdot \nabla C = 0 \tag{4}$$

$$\partial Q/\partial t + \mathbf{u} \cdot \nabla Q = 0 \tag{5}$$

where $\boldsymbol{u}$ is the velocity, p the dynamic pressure, μ the viscosity, Ra_T the thermal Rayleigh number, Ra_C the compositional Rayleigh number, $\mathbf{e_r}$ is the unit vector in the radial direction, T the temperature, Q the rate of internal heat generation given by

$$Q = Q' \exp(-\ln 2\ t/\tau_{1/2}) / Q_0 \tag{6}$$

where Q' is the dimensional heat generation rate, $\tau_{1/2}$ is the period of half decaying, Q_0 is the heat generation rate in the primitive lunar mantle. The field C tracks the distribution of compositional density and is calculated as following

$$C = (\rho - \rho_0)/(\rho_{ibc} - \rho_0), \tag{7}$$

where ρ_{ibc} is the density of IBC layer, ρ_0 is the reference density. In the diffusion creep regime, the dimensionless viscosity can be calculated from the Arrhenius law

$$\mu = \exp(E/RT - E/RT_r), \tag{8}$$

where E is the activation energy, R the gas constant, and T_r the reference temperature (1573 K) at which we defined the reference viscosity μ_r. The thermal Rayleigh number and compositional Rayleigh number are defined as following

$$Ra_T = \alpha\rho_0 g \delta T D^3/(\mu_r \kappa_0) \tag{9}$$

$$Ra_C = (\rho_{ibc}-\rho_0) g D^3/(\mu_r \kappa_0) \tag{10}$$

where α is thermal expansivity (2×10^{-5} K^{-1}), ρ_0 is reference density, ρ_{ibc} is the density of IBC layer, g is gravitational acceleration rate (1.6 m s^{-2}), δT is the temperature difference, D is the thickness of lunar magma ocean, κ_0 is thermal diffusivity (10^{-6} m^2 s^{-1}).

Initial Conditions: The thickness of lunar magma ocean and lunar crust are set to 1000 km and 40 km respectively. Adopting the stratification of magma ocean cumulus suggested in [2], the thickness and mean density of the IBC layer can be determined as about 60 km and 3700 kg m^{-3}. The background composition of the primitive lunar mantle is approximated by

KLB-1 peridotite and accordingly, the reference density ρ_0 is set to 3300 kg m^{-3}.

The initial distribution of *Q* depends on the distribution of heat sources Th, U and K in the primitive lunar mantle. Here we adopt a three-layer stratification where heat sources are mainly enriched in the lunar crust and IBC layer while the underlying mafic cumulate layer is depleted in heat sources. Adopting a U abundance of 30 ppb for primitive lunar mantle [9] and Th/U and U/K 3.8 and 2500 [10], Q_0 can be determined as 6×10^{-12} W kg^{-1}.

To determine the rates of heat generation in lunar crust and IBC layer, the bulk U abundance 46 ppb estimated from Apollo heat flux experiments [11] is adopted here. Because anorthosite and ilmenite crystallises almost at the same time, we assume that the U abundances in lunar crust and IBC layer are identical. In this case, the U abundance within lunar crust and IBC layer can be determined as about 6 times of that in the part depleted in heat sources.

We start our simulations at the time when the entire lunar magma ocean has just solidified. Thus the initial temperature profile is assumed to coincide the solidus temperature of the lunar mantle. Here we adopt the experimental solidus of KLB-1 peridotite to approximate the solidus [12].

Results: The occurrence of lunar magma ocean overturn requires that the entire IBC layer starts sinking before being entrapped in the growing stagnant lid. Our simulations indicate that the reference viscosity and activation energy of lunar mantle are the two key parameters that control this process. A lower activation energy leads to a slower rate of stagnant lid thickening, while the time needed for the onset of convective overturn is proportional to the reference viscosity (i.e. the viscosity at reference temperature). Therefore a relatively low activation energy and a low reference viscosity are beneficial to the occurrence of overturn.

We inferred the necessary activation energy for the occurrence of overturn in two typical cases. At a reference viscosity of 10^{21} Pa s, characteristic of a relatively dry mantle, for the overturn to be possible, an activation energy lower than 100 kJ mol^{-1} is needed. For an activation energy between 100 and 200 kJ mol^{-1}, only the lower part of the IBC layer can sink downwards while the upper part is entrapped in the stagnant lid. For an activation energy greater than 200 kJ mol^{-1}, the overturn of the IBC layer cannot take place.

For a reference viscosity of 10^{19} Pa s [13], characteristic of a wet mantle, an activation energy of about 100-200 kJ mol^{-1} is still required. For an activation energy between 200 and 300 kJ mol^{-1}, only the lower part of IBC layer precipitates. For activation energy larger than 300 kJ mol^{-1}, again the overturn cannot occur.

Discussions and Conclusions: The values of activation energy required by the overturn in the last two cases are far lower than the typical activation energy of peridotite (300-400 kJ mol^{-1}) obtained from laboratory experiments [14]. A potential explanation is that the effects of dislocation creep are not considered in our simulations. Christensen et al. [14] suggested that the effective activation energy in the regime of dislocation creep can be obtained multiplying by a factor of 0.3-0.6 the activation energy of diffusion creep, depending on whether viscous dissipation is considered or not in the dynamic model. Given the typical activation energy of peridotite in the regime of dislocation creep (about 400-500 kJ mol^{-1}), the effective diffusion creep activation energy can be determined as about 120-300 kJ mol^{-1}. Therefore the lower activation energy required by overturn could actually be indicative of the need to account for a non-Newtonian rheology. In future investigations, we will include the effects of dislocation creep into our dynamic model in order to assess the influences of non-Newtonian rheology on the lunar magma ocean overturn.

Acknowledgements: This research is sponsored by the Science and Technology Development Fund of Macau SAR (080/2012/A3) and by the Helmholtz Association (VH-NG-1017).

References: [1] Snyder et al. (1992) GCA, 56(10), 3809-3823, 1992. [2] Elkins-Tanton et al. (2011) EPSL, 304, 326-336, 2011. [3] Ringwood and Kesson (1976) LSC 7th, 2, 1697-1772. [4] Qin et al. (2011) Icarus, 220, 100-105. [5] Harada et al. (2014) Nature Geoscience, 7, 569-572. [6] Stegman et al. (2003) Nature, 421, 143-146, 2003. [7] Elkins-Tanton et al. (2002), EPSL, 196(3), 239-249. [8] Hüttig et al. (2013) PEPI, 220, 11-18. [9] Waenke et al. (1977) LPSC Proc., 8, 2191-2213. [10] Taylor (1982) Planetary Science: A Lunar Perspective, LPI. [11] Langseth et al. (1976) LPSC Proc., 7, 3143-3171. [12] Hirschmann (2000) G3, 1, 1042-26. [13] Zhang et al. (2013) JGR, 118, 1789-1840. [14] Christensen (1984) Geophys. J. Intern., 77(2), 343-384.

Scientific results expected from the APPROACH mission.

R. Yamada[1], Y. Ishihara[2], N. Kobayashi[2], H. Murakami[3], S. Tanaka[2], N. Takeuchi[4], H. Shiraishi[2], M. Hayakawa[2], K. Goto[2], K. Shirai[2], F. Kikuchi[1] and K. Nishida[4], [1]National Astronomical Observatory of Japan, RISE project (2-12 Hoshigaoka, Mizusawa, Iwate, 023-0861, Japan, E-mail: r.yamada@nao.ac.jp), [2]Institute of Space and Astronautical Science, Japan Aerospace Exploration Agency, [3]Kochi University, [4]University of Tokyo.

Introduction: The internal structure and thermal state of a planetary body are necessary information to study origin and thermal history of the body, and the seismic and heat flow data can give important constraint on the interior. A penetrator is a hard-landing probe to deploy on-board sensors such as a seismometer and a thermometer on planetary surface by free-fall from an orbiter. The penetrator is typically smaller and lighter than a soft-lander because it does not require the complicated landing system and the thermal control system, and it is an advanced system to deploy a geophysical network on the planetary bodies.

The penetrator for lunar exploration has been developed through Japanese lunar explorer 'LUNAR-A' mission (Fig. 1). The Japanese penetrator has two components of short-period seismometers and seven thermometers in the body. We have already confirmed that the seismometers can maintain the performance to detect moonquakes even after a shock over the impact to the lunar surface [1] and the communication instrument can properly operate for data transmission [2]. As the next step, we have to demonstrate operation of the penetrator system and acquisition of the geophysical data on the Moon.

APPROACH mission: To establish utility of the penetrator system, we proposed a mission plan, named APPROACH (Advanced Penetrator PRObe Applied for a Challenge of Hard-landing), so as to load two small-sized penetrators on a small satellite launched by the Epsilon Launch Vehicle. In this proposal, we aim to reduce size of the penetrator to two-thirds sizes keeping the already established high shock durability to load two probes on the small satellite. It is important to achieve the redundancy of observation and obtain more scientific results.

Scientific observations: In the APPROACH mission, we have plans of seismic and heat-flow observations using two penetrators. From analysis of the Apollo seismic data, the crustal thickness has been determined by some researches (e.g., [3],[4]), but it still remain large errors of about 30 % [5]. The better determination of location and origin time of the meteoroid impacts by the ground observations of impact flashes and use of high sensitive seismometer will enable determination of crustal thickness under the seismic station with better accuracy. Using the crustal thickness of the reference point, we can construct better model of the lunar entire crustal thickness distribution through utilization of recent lunar gravity data [6,7]. Finally, we aim to derive the lunar crustal volume and aluminum bulk abundance from the new lunar crustal model. In this study, we have predicted the number of impact events located by the ground observations to be detected by our seismometer during the mission period and modelled the accuracy of the crustal thickness derived from these events. We will show the results quantitatively in this presentation.

The penetrators should be deployed on the high longitude areas of the lunar near-side for the seismic observations because the impact flashes can be detected only around the area. For the heat flow observation, we have considered to deploy the penetrators on both areas where the radioactive elements are concentrated (Procellarum Kreep Terrain) and poor (highland crust). The two observations are important to estimate bulk abundance of uranium and thorium. In this presentation, we will show the possible candidates as the landing sites, then we also discuss how we can progress the study about lunar origin and evolution through the geophysical observations in the APPROACH mission.

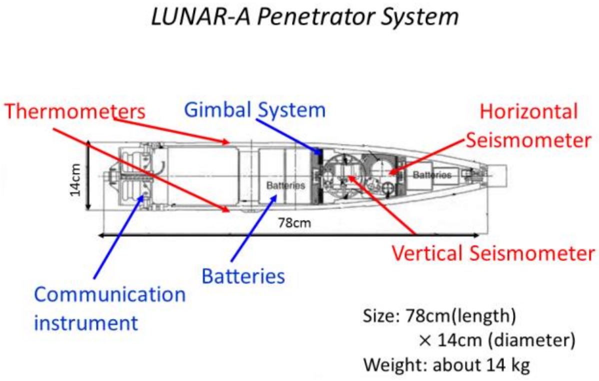

Size: 78cm(length)
× 14cm (diameter)
Weight: about 14 kg

Fig.1 Cross section diagram of the penetrator for the lunar exploration

References: [1] Yamada R. et al. (2009) *PSS, 57*, 751–763. [2] Tanaka S. et al. (2011) *JPSJ*, *20*, 3, 208-210. [3] Toksöz M. et al. (1974) *The Moon*, 9, 31–42. [4] Chenet. H. (2006) *EPSL*, 243, 1-14. [5] Yamada R. et al. (2014) *PEPI*, 231, 56-64. [6] Konopliv A. S. et al. (2013) *GRL*, 41, 1452-1458. [7] Lemoine, F. G. et al. (2014) *GRL*, 41, 3382-3389.

How to interpret the temperature variability in Titan’s upper atmosphere?

J. Cui[1,2]
[1]National Astronomical Observatories, Chinese Academy of Sciences (cuij@nao.cas.cn)
[1]Lunar and Planetary Science Laboratory, Macau University of Science and Technology (jcui@must.edu.mo)

Abstract: Typically, the temperature in the upper atmosphere of a Solar System planet is controlled by the balance between solar EUV/X-ray heating, infrared cooling via molecular ro-vibrational line emission, as well as thermal conduction. Other heating mechanisms may also function such as heating via magnetospheric particle precipitation and wave dissipation.

On Titan, Cassini observations have indicated an extremely large temperature variability of ~ 60 K near the exobase (Snowden et al. 2013). It is well known that solar heating is far insufficient to account for such a large variability. Cross-instrument comparisons revealed an apparent correlation between the mean temperature in Titan’s upper atmosphere and the local plasma environment in terms of the charged particle precipitation pattern, indicating that the thermal structure near Titan’s exobase is plasma driven instead of solar driven (Westlake et al. 2011). However, the recent calculations made by Snowden & Yelle (2014) indicat that the variability in the ambient plasma environment only contributes to a temperature variability of ~ 7 K. Meanwhile, we note that the typical thermal timescale on Titan is much longer than the timescale over which plasma environment varies, implying that the plasma driven scenario lacks

In this study, we investigate alternative possibilities that may cause the observed temperature variability in Titan’s upper atmosphere, including the wave-driven scenario (Cui et al. 2013, 2014) and the scenario with variable HCN rotational cooling rates (Yelle 1991).

MAGNETIC FIELD-ASSOCIATED DIELECTRIC ANISOTROPY OF THE MARTIAN IONOSPHERE DETECTED BY MARSIS.

Zhenfei Zhang[1], Qian Huang[2]. [1]Institute of Mathematical Geology and Remote Sensing, China University of Geosciences, 388 Lumo Rd., Hongshan, 430074, Wuhan, China. E-mail: zfzhang@cug.edu.cn; [2]Institute of Planetory Science, China University of Geosciences, 388 Lumo Rd., Hongshan, 430074, Wuhan, China. E-mail: qianhuang@cug.edu.cn.

Introduction: The main body of the dayside Martian ionosphere (M2) is basically a Chapman layer, with electron density peaked at ~130 km altitude and decreasing upward with a scale height of a few tens of kelometers [1, 2, 3, 4, 5, 6]. However, this morphology is modified, especially on the southern hemisphere of Mars, where many patched crustal magnetic anomalies develop [7,8]. The field lines constraint the ionospheric plasma motion to form local plasma bulges, cylinders, and quasi-statbe flux ropes, which were detected at altitudes up to 400 km [1, 9, 10, 11, 12, 13]. Where these modifications occur, the ionospheric plasma are magnetized to some extent. Therefore, it is expected that during radio sounding of the ionosphere, an anisotropy of the dielectric properties of the ionosphere may be observed. The anisotropy may produce different modes of waves associated with the magnetization. In this study we report the finding of a special type of MARSIS (Mars Advanced Radar for Subsurface and Ionosphere Sounding, which is on board the ESA mission Mars Express (MEX) [1]) signals, which may be best interpreted as signatures of the R-mode waves (the right-handed circularly polarized waves propagating along the magnetic field lines).

Phenomena: Figure 1 shows 2 successive ionograms (frames 160 and 161) on the MEX orbit No. 2359, wherein a special feature, a “fixed” combination of several oblique echo traces, can be clearly seen. We call this feature an “epsilon-shaped signature” or “ε-signature”, following Dyson and Benson [14, 15] who described similar features found in the terrestrial F-region ionosphere by the International Satellites for Ionospheric Studies (ISIS). In Fig. 1 the individual traces are specifically labeled. The upper, middle, and lower branch of the ε-signature is labeled “R2”, “R1+R2”, and “2R1+R2”, respectively. Below the ε-signature is a diffuse echo trace which is labeled “R”. Above the ε-signature, close to (or overlapping) the vertical echo trace, is an oblique echo labeled “R1”.

We examined all the released MARSIS AIS (Active Ionosphere Sounding) data (~120,000 sweep-frequency observations) and found about 70 occurrences of the ε-signature. They are mostly “incomplete”, that is, only one of two of its three trace braches are discernable. Statistically, the ε-signatures have the following characteristics: (1) They usually present on multiple (2 – 10) successive MARSIS frames on a MEX orbit; (2) They are unamimously accompanied by electron cyclotron echo traces in ionograms (In Fig. 1 the electron cyclotron echoes are indicated); (3) Spatially thay are distributed near the crustal magnetic field intensity peaks; (4) They are mostly (80%) observed at relatively low altitudes (<400 km); (5) They are mostly observed when the solar zenith angle (SZA) is relatively low (<60°); (6) The “cutoff” frequency (denoted f_R, the common lowest frequency of the 3 trace branches) can be constant, or changeable (between 0.7 – 2.0 MHz) regularly with the spacecraft motion, over a number of successive frames; (7) When the in situ plasma frequency (f_p) and the in situ electron cyclotron frequency (f_{ce}) can be determined, f_R is found to satisfy

$$f_R > f_{\text{cutoff,R}} = \frac{1}{2}\sqrt{f_{ce}^2 + 4f_p^2} + \frac{1}{2}\left|f_{ce}\right| > f_p\,, \qquad (1)$$

where f_{cutoff} is the theoretical cutoff frequency of the R-mode wave. Note that the in situ values of f_p and f_{ce} can sometimes be estimated from the ionograms using the methods described in [16] and [4], respectively.

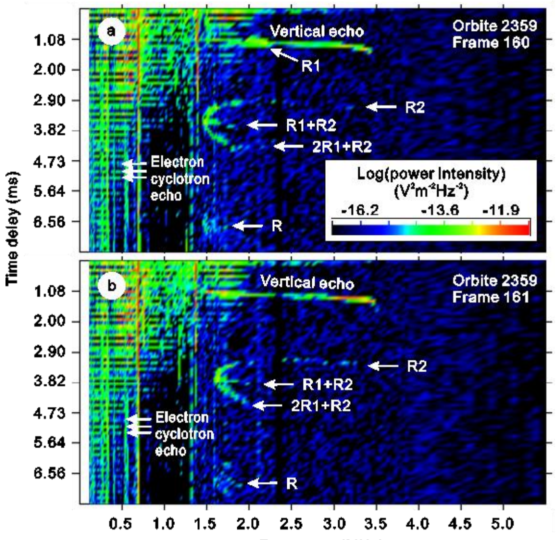

Fig. 1. Two successive MARSIS ionograms wherein an ε-signature can be seen.

Interpretation: The origin of the ε-signatures observed in the terrestrial F-region by the ISIS radar was explained as follows [14, 15]. By the ponderomotive force, the sounder pulse would create an elongated region of plasma depletion (plasma bubble, where density was reduced by a few percent) along the Earth’s dipolar magnetic field between the two Hemispheres. The bubble could serve as a waveguide, along which the wave propagated in two opposite directions. The two waves experienced multiple reflections from the two ends of the bubble to the sensor, producing the ε-signature. The lowest wave frequency of the ε-signature (which corresponds to f_R) was interpreted as the cutoff frequency [14].

We propose that a similar explanation may be applied to the ε-signatures found in the MARSIS ionograms, with different conditions taken into account. For example, on Mars there are only patched crustal magnetic fields instead of a global dipole field as on Earth.

Figure 2 illustrates a possible explanation of the origin of the ε-signatures in Fig. 1. Two plasma bulges associated with two magnetic dipoles situated on the planet surface, a few hundred kilometers apart, are considered. The two bulges are linked by closed field lines. MARSIS is assumed to be somewhere between the two bulges (the point labeled O). MARSIS transmits EM pulses in every direction (except the directions parallel to its dipole antenna). The pulse may create a field-aligned density depleted region which may serve as a waveguide. Along the waveguide the pulse travel in two opposite directions and is reflected at positions (e.g., the points A, B) where the plasma frequency equals the wave frequency. Multiple reflections of the two waves can result in the ε-signature. Specifically, the wave along the path O→A→O produces the R1 branch; the wave along O→B→O results in the R2 branch; the two waves go through the round-trip path between A and B (O→ B→ O→A→O and O→A→O→ B→O) during the same time interval, producing the R1+R2 branch. The waves continue to travel producing the 2R1+R2 and R1+ 2R2 branches. Repeating the above process can produce the R trace which is obscure because of more absorption.

Discussions: The ε-signature is obviously a result of multiple reflections. The multiple reflections can occur when the wave is propagating along a closed field line (which can also associated with only one isolated dipole instead of two as shown in Fig. 2). Therefore, we suggest that the waves represented by the ε-signature are most likely the high frequency R-mode waves. With this suggestion most of the observed phenomena can be explained. Other modes are unlikely. For example, the X-mode (which propagates perpendicular to the field) and the O-mode (which propagates ignoring the field) waves would require very rigorous, unrealistic gemetry of the propagation path and reflecters in order to experience multiple reflections.

We suggest that the ε-signatures observed by MARSIS confirmed that the upper part of the M2 layer of is at least partially magnetized (if only the electrons ions are magnetized whereas the ions are not) by the crustal magnetic anomalies. Radio waves propagating in the ionosphere can be affected not only by the varing plasma density but also affected considerably by the crustal magnetic fields if they present. Taking into account the plasma dielectric anisotropy due to the magnetic fields could be helpful for precise analyses of, e.g., the MARSIS signals.

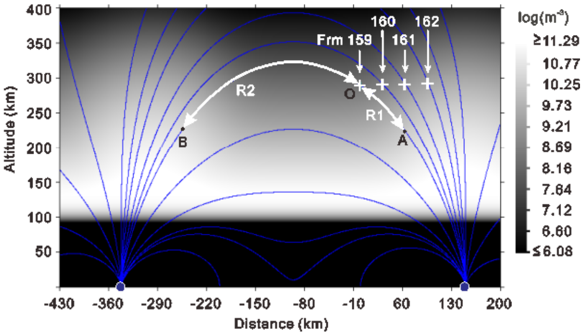

Fig. 3. Sketch illustrating an interpretation of the ε-signatures as shown in Fig. 1. The crosses indicate spacecraft positions; the two dark blue dots on the bottom indicate two vertical magnetic dipoles of different directions; the blue lines are magnetic field lines; the plasma density (m^{-3}) is gray-grade coded; the double-headed arrows represent wave propagation paths along field lines; the paths are labeled by R1 and R2, which correspond to the same labels in Fig. 1; A and B are two points on the same field line and identical cutoff frequencies; O labels one of the spacecraft positions.

References:

[1] Gurnett, D.A. et al. (2005), Science 310, 1929 – 1933. [2] Fox, J.L. and Yeager, K.E. (2006), JGR 111, A10309. [3] Nielsen, E. et al. (2006), Space Sci. Rev. 126, 373 – 388. [4] Gurnett, D. A. et al. (2008), Adv. Space Res. 41, 1335 – 1346. [5] Morgan, D. D. et al. (2008), JGR 113, A09303. [6] Němec, F. et al. (2011), JGR 116, E07003. [7] Acuña, M. H., et al. (2001). JGR 106 (El0), 23,403-23,417. [8] Lillis, R. J. et al. (2008), Icarus 194, 575–596. [9] Ness, N.F. et al. (2000), JGR 105, 15991 – 16004. [10] Mitchell, D. L. et al. (2001), JGR 106 (El0), 23,419-23,427. [11] Krymskii, A. M. et al. (2002), JGR 107(A9), 1245. [12] Duru, F., et al. (2006), JGR 111, A12204. [13] Morgan, D. D. et al. (2011), JGR 116, A02319. [14] Dyson, P. L. and Benson, R. F. (1978), GRL, 5, 795-798. [15] Benson, R. F. (1997), J. Atmos. Solar-Terres. Phys. 59 (18), 2281-2293. [16] Duru, F. et al. (2008), JGR 113, A07302.

Comparative aeronomy as a planetary perspective on Earth's environmental evolution. Y. Wei[1] and W. Wan[1], [1]Insititute of Geology and Geophysics, Chinese Academy of Sciences, Beijing, China (weiy@mail.iggcas.ac.cn)

The planet Earth we can see today is a consequence of long-term evolution for billions of years. To understand such an evolution, the researchers have taken advantage of the memory retained in Earth's chemistry, the isotopes, the geophysical observations, and even the presence of the Moon. However, more processes and events may have no memory left, especially those occurred in space. We propose that the in-situ observations on Mars and Venus could provide critical information for understanding some physical processes in Earth's space during the past, and further comparative aeronomy may help to interpret Earth's environmental evolution. As an example, we will discuss how the knowledge of Martian atmospheric loss helps to build a linkage between geomagnetic reversals and mass extinctions during Phanerozoic time.

SOLAR WIND-GENERATED CURRENT IN THE LUNAR DUST EXPERIMENT. Lianghai Xie[1], Xiaoping Zhang[1], Yongchun Zheng[1, 2], Dawei Gu[1], [1] Lunar and Planetary Science Laboratory, Macau University of Science and Technology, Macau, China, [2] National Astronomical Observatories, Chinese Academy of Sciences, Beijing, China.

Introduction: Lunar horizon glows (LHG) are attributed to forward scattering of sunlight by lofted dust grains. The dust density calculated from the Apollo data is on the order of 10^4 m^{-3} [1], but observations from Clementine and Lunar Reconnaissance Orbiter (LRO) show the density is only about 1 m^{-3} [2], [3]. Recently, in-situ measurements of lunar exospheric dust have been done by the Lunar Atmosphere and Dust Environment Explorer (LADEE) spacecraft, with the upper limit of dust density less than 10^2 m^{-3} [4]. Nevetheless, the density lacks an altitude dependence, implying the lofted particles may come from other sources.

In fact, Lunar Dust Experiment (LDEX) on board LADEE is an impact ionization dust detector and ions with energy less than 30 eV can also contribute to the measured current. Here we present some positive evidences for the current caused by the backscattered solar wind (SW) protons, focusing on the dependences on SW parameters and solar zenith angles (SZA). It is proved that the so-called current associated with lofted lunar dust is actually dominated by the backscattered SW protons.

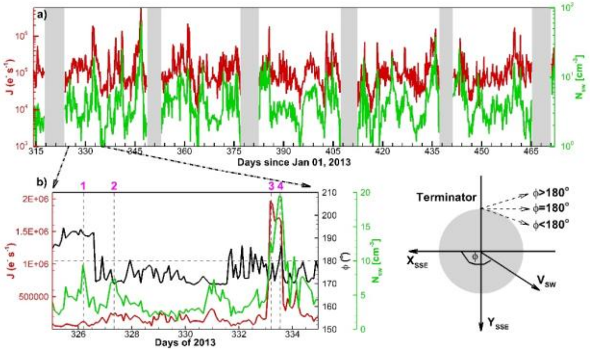

Figure 1. (a) The correlation between the measured current J (red line) and SW number density N_{sw} (green line). The gray bars indicate the times when LADEE is in Earth's magnetotail, where the data have been excluded. (b) The observations from Day 325 to Day 334 of 2013. The black line represents the SW direction, where ϕ is the SSE longitude as shown in the right bottom panel.

SW dependence: Here we use the average current measured from 5:30 LT to 6:30 LT to represent the current near the terminator. As shown in Figure 1a, a good correlation between the current and the SW density can be obtained, with the correlation coefficient of 0.75, suggesting the current should be mainly casued by the backscattered SW. In addition, a smaller ϕ can result in a larger J, as it corresponds to a smaller incident angle of SW, which then cause a larger incident flux at the surface and finally bring a larger proton-scattering flux into LDEX. As shown in Figure 1b, though with a smaller N_{sw}, Day 327 (marked by number 2) still has a larger J than Day 326 (marked by number 1). The reason should be the smaller ϕ of Day 327. Similar features can be also found between the measurements marked by number 3 and number 4.

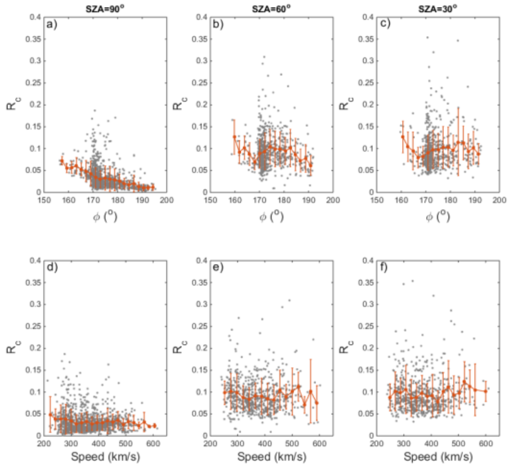

Figure 2. The ϕ and SW speed dependences of R_C for SZA=90° (a) and (d), SZA=60° (b) and (e) and SZA=30° (c) and (f). The gray dots indicate all the LDEX's measurements at each SZA and the red dots show the average ϕ and speed in the increments of 2° and 20 km/s, respectively.

SZA dependence: To discuss the affecting factors besides N_{sw}, we define a new variable, R_C, by normalizing the current with SW density: $R_C = J/(N_{sw} \times 10^6)$. As shown in Figure 2a, R_C basically decreases with ϕ as expected. Besides, the current favors a smaller SW speed as shown in Figure 2d, since smaller-speed protons can turn into low-energy ions more easily. However, the situation can be different at lower SZAs resulting from the picked-up ions from lunar ionosphere[5] and the SZA dependence of scattering function [6].

picked-up ions can bring large current when the convection electric field is pointing to LDEX, but fail to affect the current when the electric field is back to

LDEX. With all the measurements taken at SZA=30° and SZA=60°, we find the current actually shows a better correlation with N_{sw} than the convection electric field. It can be concluded that the backscattered SW protons dominate the measured current at least when SZA ≥ 30°.

We use the measurements when the convection electric field is back to LDEX to discuss the ϕ and SW speed V dependences on the dayside. As shown in Figure 2, differing from monotonic decreases with both ϕ and V for SZA=90°, there are a peak with ϕ and a raised tail with V at lower SZAs. The peak should be caused by the asymmetry in scattering angular distribution. SW ions are mainly reflected in the anti-SW direction for a moderate SZA. We call this direction as prevailing direction and the angle between the prevailing direction and the surface normal as exit angle. When ϕ increasing, the total scattered SW should decrease. But on the other hand, the LDEX boresight is closer to the prevailing direction and the relative influx of proton get larger. Then a peak R_C appears as shown in Figure 2b and 2c, where the R_C first decreases with ϕ, then increases up to a peak and finally decreases again. However, the ϕ where R_C peaks for SZA=30° is about 10° larger than the value for SZA=60°, as a larger ϕ is required for SZA=30° to make the LDEX boresight closer to the prevailing direction.

Besides, Chandrayaan-1 observations taken near the subsolar point show proton-backscattering efficiency can increase with SW speed [7], which results in the smoothed heads and raised tails in Figure 2e and 2f. Nevertheless, the V dependence of proton-backscattering efficiency gets weaker as SZA increases and the incident angle should be important for proton-surface scattering.

Discussion: Since the current is mainly caused by backscattered SW, the dust density should be further smaller than the value of 10^2 m^{-3} estimated by Szalay et al. and closer to the recent measurements from Clementine and LRO. This result provides a positive evidence for impact-generated dust exosphere.

It seems the backscattered protons have a similar scattering function to ENA at low altitude, and the protons are mainly reflected in the anti-SW direction especially when SZA=50°. In addition, the proton-backscattering efficiency depends on both the SW speed and SZA. These results should be very useful for proton-surface scattering study. In the future, we will use the observations from KAGUYA to verify the results. Also, some experiments and numerical simulations should be done for further analysis.

References:

[1] McCoy J. E. (1976) Proceedings of the 7th Lunar Science Conference, 1087-1112. [2] Feldman P. D. et al. (2014) *Icarus, 233:106–113*. [3] Glenar D. A. (2014) *Space Sci., 59(1):1695–1707*. [4] Szalay J. R. and Horányi M. (2015) *Geophys. Res. Lett., 42:5141–5146*. [5] Poppe A. R. et al. (2014) the 45th Lunar and Planetary Science Conference, p. 1393. [6] Schaufelberger A. et al. (2011) Geophys. Res. Lett., 38:L22202. [7] Lue C. et al. (2014) *J. Geophys. Res., 119: 968–975.*

Numerical Modeling of the Atmospheric Circulation and Dust Cycle on Mars

K. C. Chow[1], K. L. Chan[1], and K. V. Tam[1]. [1]Space Science Institute / Lunar and Planetary Science Laboratory, Macau University of Science and Technology, Room A505, Administration Building, Block A, Avenida Wai Long, Taipa, Macau. E-mail: kcchow@must.edu.mo.

Introduction: Dust storms are prevailing weather events in the Martian atmosphere. Dust particles suspending in the atmosphere can have a heating effect in the atmosphere which may significantly affect the atmospheric circulation, and thus plays a role in the climate of the Martian atmosphere. Understanding the dust cycle is important to understanding the climate system of Mars. At present, researches on Martian dust storms are mainly based on numerical modeling with general circulation models (GCM). These global models usually have relatively coarse horizontal grid resolution (200 km or above). However, some recent studies suggest that the climatological dust cycle on Mars may be related to mesoscale circulations that cannot be resolved in GCMs. In this study, we adopt the multi-scale global model MARSWRF to simulate the Martian climate system, which is basically the Mars version of the PlanetWRF model [1] developed on the basis of the National Center for Atmospheric Research (NCAR) Weather Research and Forecasting (WRF) model for Earth. One advantage of using MARSWRF is its two-way nesting approach, which provides a higher resolution simulation of the mesoscale circulation over a region of interest.

Model Configuration: The MASWRF model is configured with two domains. The coarse global domain has 36 x 72 grid points (horizontal resolution ~ 5 degree or 300 km), while the nested domain has 33 x 42 grid points (resolution ~ 1.7 degree or 100 km) located at the Hellas Basin. There are 46 vertical sigma levels, and the model top is set at 0.0 Pa. The model has a specific radiation scheme (Martian wide-band model [1]) for short wave and long wave, which has considered the heating/cooling effects of dusts and CO_2. The PBL scheme and physical parameterization are the usual schemes in WRF for Earth (MRF and Monin-Obukhov scheme). However, the land surface model is specific for Mars (Martian 12-layer subsurface diffusion scheme).

The model also includes some physical process parameterizations which are specific to Mars such as the carbon dioxide cycle (described in [2]) and dust cycle. The parameterization of the water cycle is still not yet available in the model.

The parameterization of the dust process in the model includes an interactive scheme and a dust devil scheme [3]. The interactive scheme is similar to those models on Earth. The emission of dust is depending on the surface wind stress, while the suspended dusts may change the atmospheric radiation and so the circulation. The process of dust devils is parameterized to provide the background dust field, with amount mainly depending on the surface temperature.

The model was run for two years starting from 0° solar longitude (0°Ls). The first year is considered as the spin-up time. The nested domain was initiated about 30 days before the beginning of the second year. Results presented here are from the model run in the second year.

Results from the Simulation: It has been illustrated in [1] that the MARSWRF is capable of simulating the large-scale general circulation and temperature field on Mars. In this abstract, we only focus on the simulation of the model on the dust cycle and diurnal circulation in the region of the Hellas basin, which is a huge and deep crater (about 8 km deep) on Mars. Some studies (e.g. [4]) reported that the strong global dust storm in 2001 was initiated in the Hellas basin region.

Simulation of the dust cycle. Fig. 1 shows the time evolution of zonal-mean dust optical depth normalized at the surface level for one Martian year. In general, the MARSWRF could capture the basic pattern of variation in optical depth (Fig. 1 upper) when comparing with the observational results averaged for six Martian years (Fig. 1 lower, from [5]). In particular, the significant increase in dusts over the southern hemisphere between 200°and 300°Ls can be simulated. However, the second episode in dusts starting from about 320°Ls

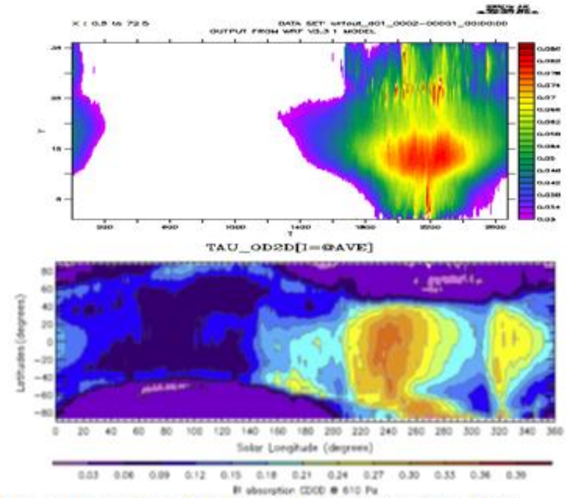

Fig. 1 Time series of dust optical depth at surface from model (upper) and observation (lower)

cannot be captured by the model. This second episode is likely related to the surface wind associated with the re-condensation of CO_2 ice in the southern hemisphere.

Diurnal variation in the Hellas Basin. The simulated 5-day mean diurnal variation of the surface wind and dusts over the Hellas Basin region is shown in Figs. 2 and 3. The time is around 180 °Ls (autumn equinox). This is the period when the CO_2 ice in the south is about to melt, and an occurrence of global dust storm were recorded [4]. The diurnal variation of surface wind is clearly related to the variation in solar radiation over the planet (right of Figs. 2 and 3). As in most valley regions on Earth, diurnal variation of the circulation is strong in the Hellas Basin. During night (local) time (Fig. 2 left), a dominant down-slope wind can be seen. The wind is stronger in the southern edge of the basin which could contribute to the emission of dusts over there.

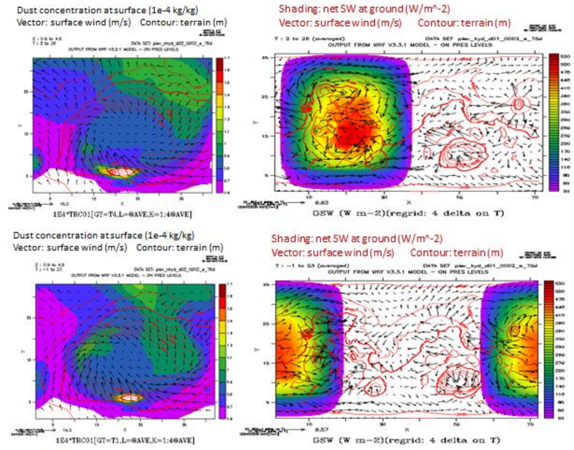

Fig. 2 Diurnal variation of surface wind and dusts at Hour 00 (upper) and Hour 06 (lower)

In contrary to that during night time, up-slope wind is dominant during day time (Fig. 3 left), and the wind is generally stronger in the northern edge. The magnitude of the up-slope wind is strongest in Hour 18 (Fig. 3 lower left). The stronger wind during this period appears to be associated with the emission of dusts in the northern edge region during day time (Fig. 3 left).

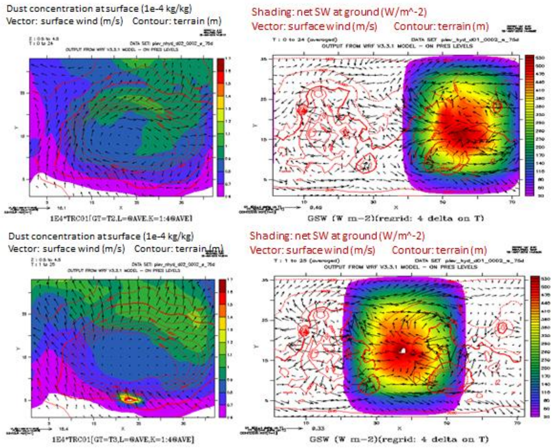

Fig. 3 Diurnal variation of surface wind and dusts at Hour 12 (upper) and Hour 18 (lower)

References: [1] Richardson M. I. et al. (2007) *JGR, 112*, E09001, doi:10.1029/2006JE002825. [2] Guo X. et al. (2009) *JGR*, *114*, E07006. [3] Newman, C.E. et al. (2002) *JGR: Planets*, *107* (E12). [4] Cantor B.A. (2007) *Icarus*, *186*, 60–96. [5] Montabone L. et al. (2015) *Icarus*, *251*, 65-69.

LATE NOACHIAN “COLD AND ICY HIGHLANDS” MODEL: GEOLOGICAL PREDICTIONS FOR EQUILIBRIUM ENVIRONMENTS AND NON-EQUILIBRIUM MELTING SCENARIOS.

J. W. Head, Dept. Earth, Environmental and Planetary Sci., Brown Univ., Providence RI 02912 USA (james_head@brown.edu).

I. Introduction: Forget et al. [1] and Wordsworth et al. [2,3] recently presented improved 3D global simulations of the early martian climate performed assuming a faint young Sun and denser CO_2 atmosphere, including a self-consistent representation of the water cycle [2], with atmosphere–surface interactions, atmospheric transport, and the radiative effects of CO_2 and H_2O gas and clouds taken into account. They found that for atmospheric pressures greater than a fraction of a bar, atmospheric-surface thermal coupling takes place and the adiabatic cooling effect (ACE) causes temperatures in the southern highlands to fall significantly below the global average. Long-term climate evolution simulations indicate that in these circumstances, water ice is transported to the highlands from low-lying regions for a wide range of orbital obliquities and that an extended water ice cap forms on the southern pole (Fig. 1). Conditions are too cold to allow long-term surface liquid water. Punctuated events, such as meteorite impacts and volcanism, could potentially cause intense episodic melting under such conditions. Because ice migration to higher altitudes is a robust mechanism for recharging highland water sources after such events, Wordsworth et al. [2,3] suggested that this globally subzero, Late Noachian ‘icy highlands’ (LNIH) climate scenario may be sufficient to explain much of the fluvial geology without the need to invoke additional long-term warming mechanisms, or an early “warm and wet” Mars. Here we explore the predictions for geologic settings and processes in both equilibrium and non-equilibrium climate states [4-6] as first steps in the comprehensive testing of the “icy highlands” model.

II. Geology of the “icy highlands” equilibrium environment: 1) ***Global permafrost***: With mean annual temperature (MAT) consistently well below 0 °C [2], LNIH Mars is characterized by a global permafrost layer that forms a shallow perched aquifer [7,8] composed of a dry active layer whose thickness is defined by vapor diffusive equilibrium with the atmosphere. Permafrost thickness is determined by local and regional geothermal heat flux and mean surface temperatures, is thinner than today and varies with altitude and latitude, likely averaging several km thick [9,10]. **2)** ***Surface hydrological cycle***: The LNIH climate is dominated by an expanded south polar cap, snow and ice accumulation in the highlands, and a global cryosphere; H_2O at lower elevations will be mobilized and transported to the highland cold traps (Fig. 1). Altitude-dependent distribution of snow and ice is further modulated by both latitude dependence and atmospheric circulation patterns [2,3]. **3)** ***Thickness and continuity of snow and ice***: To a first order, mean thickness will be determined by total water inventory and the percentage of the inventory available at and near the surface, neither value being well constrained for the Late Noachian [11]. We assume the current polar/near-surface water ice inventory (~5 M km^3; ~30 m Global Equivalent Layer (GEL)) and thus that available ice is *supply limited* [12]. Snow and ice will occur in several highlands environments: a) Snow patches and continuous snow cover: These will vary with seasonal and short term climate change, and locally with wind patterns and insolation shadowing as seen in Antarctica [13]. b) Non-Flowing Ice Deposits: Accumulations in excess of a few meters will occur as firn/ice deposits [14] but will not be thick enough to flow [15]. c) Flowing Glacial Ice Deposits: Where ice thickness exceeds hundreds of meters and has an appropriate basal slope [15], it will flow, but still be cold-based unless it is thick enough (unlikely in the supply limited scenario) to raise the local melting geotherm into the base of the ice [16]. **4)** ***LNIH global distribution of snow and ice***: Based on typical conditions simulated by the GCM [1,2] we assume a plausible Equilibrium Line Altitude (ELA) of +1 km; Fig. 2 portrays the LNIH. a) *Poles*: There is no north polar cap under nominal obliquity and the south polar cap is much larger [2,3], approximately the size of the Dorsa Argentea Formation (DAF), interpreted to be an ice-sheet remnant [17]. On the basis of glacial flow modeling [18], the thickness of the DAF may have approached 3 km, and involve limited basal melting. b) *Hellas hemisphere*: Snow and ice are focused on the rim of Hellas, across the southern midlands, and in the Elysium rise; ice deposit margins are very closely coincident with the distribution of valley networks (VN), open-basin lakes (OBL) and closed-basin lakes [6]. c) *Tharsis hemisphere*: The LNIH Tharsis rise, a region thought to be characterized by an elevated geothermal gradient, is covered with snow and ice, a phenomenon that may help explain the charging of the Tharsis aquifer to source the outflow channels [19,20]. Classic VN (Warego Valles) are also near the margins of the ice accumulation [21].

III. LNIH melting scenarios: 1) ***Equilibrium top-down heating and melting***: Under some climate equilibria, extreme orbital parameter-induced seasonal top-down melting might occur, producing daily or seasonal temperatures above 0 °C [2]. This could produce transient melting conditions, as observed in the McMurdo Dry Valleys [7]. **2)** ***Punctuated top-down melting***: a) *Impact*: Impacts [22] are predicted to produce a runaway greenhouse atmosphere, rain and short-term flooding. Local ejecta deposits and impact-generated widespread dust could change surface albedo and influence melting [23]. b) *Volcanism*: Gases (SO_2, H_2S, CO_2) released by punctuated volcanism [4,5]; such punctuated phases may be constantly recurring, but warming may only last for decades [5], and may be regional [24]. Local to regional dispersed volcanic ash [23,25] could alter melting patterns. c) *Direct ice melting*: Lava flows emplaced on or against ice deposits can induce melting and flooding [26]. **3)** ***Sustained top-down heating***: Should top-down heating be maintained long enough (10^1-10^2 yrs), water in the upper permafrost would begin to melt at the top of the ice table. Longer sustained heating (10^4-10^6 yrs) could melt through the permafrost, first locally, then regionally. **4)** ***Bottom-up heating and melting***: Accumulation of ice to thicknesses exceeding hundreds of m [15] could raise the global mean melting geotherm to the base of ice but on a regional scale ice thickness may be supply-limited. In enhanced heat flow areas (e.g., Tharsis), basal melting may occur [19]. **5)** ***Combinations of factors***: Any one (or more) of these can combine with orbital parameters already favoring melting. **6)** ***Timescales to penetrate cryosphere***: Starting with a nominal LNIH climate scenario [2,3] and heat flux [18], we calculate that it would take of order 10^4 to 10^6 yrs for the nominal global cryosphere to be breached and for the hydrological cycle to change from horizontally stratified (with a perched aquifer) to influent and vertically integrated with the groundwater system. The difficulty in sustaining MAT above 0 ℃ for sustained periods [2] makes this scenario unlikely globally; local regions of elevated heat flux (e.g., Tharsis, Elysium) will be exceptions [19]. **7) *The role of impacts in cryosphere penetration*:** Impacts of sufficient size (in excess of ~25 km) can penetrate the cryosphere and potentially form a short term connection to a groundwater reservoir [27]; effects depend on global groundwater budget and regional hydrostatic pressure.

IV. Nominal Late Noachian Icy Highlands (LNIH) climate model and geological process predictions: For most of the Late Noachian, an icy highlands caused by atmospheric-surface coupling and the adiabatic cooling effect appears to be the nominal equilibrium state (Fig. 1). Orbital parameter variations cause regional redistribution of ice, with limited melting only under extreme circumstances; any local meltwater rapidly freezes and returns to the highlands. Non-equilibrium conditions that could raise MAT above 0 ℃ can be reached through punctuated events such as impact crater formation and high rates of volcanic outgassing, but the duration of the warming effects of individual events is very short geologically. This leads to some predictions for processes that can be used to test the LNIH model:

1) <u>Global cryosphere</u>: For most top-down melting scenarios, the global cryosphere remains intact.

2) <u>Altitude dependence of melting</u>: Melting should preferentially occur around the lower margins of ice deposits, where closest to melting point.

3) <u>Water reycling</u>: During and following any melting events, water returns to the uplands, constantly recharging the source region.

4) <u>Relative constancy of source region locations</u>: Because of the general constancy of LN topography, meltwater returns to the same place, providing automatic recharge of source areas.

5) <u>Character of ice source regions</u>: Variations in topography, altitude, slope and insolation geometry will govern ice accumulation and melting particularly near ice margins.

6) Melting rates and recharge: Raising MAT to >0 ℃ will provide significant volumes of meltwater from top-down melting to form VN and create OBL.

7) Likelihood of multiple events: Top-down melting scenarios favor multiple events; transition to equilibrium returns water to icy source regions.

8) LNIH hydrological cycle model: Long-term equilibrium icy highlands climate alternating with multiple episodic, but widely spaced short pulses of top-down melting; cycle favors immediate recharge of ice in same source regions.

9) Valley network formation: Caused by multiple episodic melting events (number, duration and intensity currently unknown) of snow/ice in icy highlands; presence of shallow ice table during melting events influences infiltration and channel shape and enhances erosion rates [8]. Stream/network geometry controlled by cold-based ice patterns [8].

10) Tharsis and Elysium: Areas with elevated geotherms are favored for basal melting and aquifer recharge [19]. These predictions provide a basis for further analysis and testing of the LNIH model [2,8,14-17].

References: 1. F. Forget *et al*., *Icarus*, 222, 81 (2013); 2. R. Wordsworth *et al*., *Icarus*, 222, 1 (2013); 3. R. Wordsworth *et al*., *5th Mars Atmos.* (2014); 4. J. Head, L. Wilson, LPSC 42, #1214 (2011); 5. I. Halevy, J. Head, *3rd Conf. Early Mars*, #7043 (2012); *5th Mars Atmos.* (2014); 6. J. Head, *LPSC 44*, #1523 (2013); *5th Mars Atmospheres Workshop* (2014); 7. J. Head and D. Marchant, *Antarctic Science*, in review (2013); 8. J. Head et al., *LPSC 45* (2014); 9. S. Clifford, *JGR* 98, 10973 (1993); 10. M. Mellon et al., *JGR* 102, 19357 (1997); 11. M. Carr, J. Head, *LPSC 45* (2014); 12. J. Fastook, J. Head, *PSS*, in press (2013); 13. D. Marchant, J. Head, *Icarus* 192, 187 (2007); 14. J. Cassanelli, J. Head, *LPSC 45* (2014); 15. J. Fastook, J. Head, *LPSC 45* (2014); 16. M. Carr, J. Head, *GRL* 30, 2245 (2003); 17. J. Head, S. Pratt, *JGR* 106, 12275 (2001); 18. J. Fastook *et al*., *Icarus* 219, 25 (2012); 19. P. Russell, J. Head *PSS* 55, 315 (2007); 20. J. Cassanelli, J. Head, LPSC 45 (2014); 21. K. Scanlon *et al*., *GRL* 40, 4182 (2013); 22. T. Segura *et al., Icarus* 220, 144 (2012); 23. L. Wilson, J. Head, *JVGR* 185, 290 (2009); 24. L. Kerber *et al., 5th Mars Atmos.* (2014); 25. L. Kerber *et al*., *Icarus* 219, 358 (2012); 26. J. Head, L. Wilson, Ann. Glaciol., 45, 1 (2007); 27. P. Russell, J. Head, *GRL* 29, 1827 (2002). 28. J. Head et al. LPSC 45, #1412 (2014).

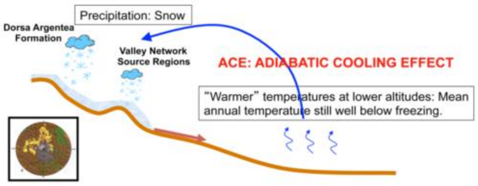

Fig. 1. *Noachian icy highlands climate regime*; snow at high elevations, a MAT well below 0 ℃, and a horizontally stratified hydrologic system.

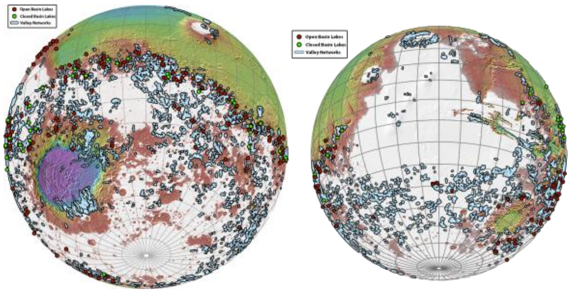

Fig. 2. Global view of the *Noachian icy highlands* (white areas above the surface ice stability line). Top) Hellas hemisphere: km-thick Dorsa Argentea Formation ice cap near bottom; 10-100s m thick ice cover (white) extends to the vicinity of the dichotomy boundary. Bottom) Tharsis hemisphere. Valley networks (blue), closed-basin lakes (green dots), and open-basin lakes (red dots) are well-correlated with margins of ice sheets.

Martian Bulk Soil Hydration Revealed by Principal Component Analysis of Regional Chemical Data.

D. R. Hood[1], S. Karunatillake[2], and D. Susko[3], [1]Geology and Geophysics, LSU, Baton Rouge, LA 70803 (dhood7@lsu.edu) [2,3]Geology and Geophysics, LSU, Baton Rouge, LA 70803.

Introduction: Water has been detected on or near the martian surface by a variety of instruments [1]–[4], however the nature of that water remains an open question. Solid H2O in the form of ice has been observed in northern and southern high latitudes by several instruments [5], [6] and by the phoenix lander in 2008 [7]. It has also been suggested to occur in lower latitudes in the form of regolith mantled subsurface ice [8], [9]. H2O has also been observed to be a chemical constituent of minerals in both high latitudes [10] and equatorial regions [11]. There is even potential for transient liquid water in equatorial regions in the form of observed slope lineae [12], [13] and predicted perchlorate deliquescent brines [14]. Given that H2O is seen in such a variety of forms and settings, one must carefully assess the nature of H observed via remote sensing, where observations cannot always be placed in a specific geologic context. Observations from the GRS instrument provide a global picture of elemental abundances in the shallow subsurface of Mars. The variations seen at these depths (10s of centimeters) and spatial resolution (5^{O}X5^{O}) are subtle, requiring extensive work to draw out only a few areas of interest [15]–[17]. While there are many multivariate methods that have been used in analyzing remote sensing data [17], previous work [16], [18], [19] has shown that Principal Component Analysis (PCA) is well suited for sensing subtle variations present in remote sensing and *in situ* data and localizing chemical anomalies. Here, PCA is used to assess the correlation between H_2O and other elements in the shallow subsurface of Mars. This is motivated in part by previous work [20], suggesting a meaningful correlation between H_2O and S in martian regolith. This new analysis will further the previous work, investigating whether this correlation presents itself naturally in the data.

Methods: Currently, there are 9 chemical maps that have been generated from GRS data: Al, Ca, Fe, Cl, S, H (i.e., as stoichiometrically equivalent H_2O), K, Th, and Si. These nine elemental datasets are combined with Ruff and Christensen's Dust Cover Index (DCI)[21] to form a 10-dimensinal dataset that covers all of Mars, excluding the polar regions. To analyze our data, multivariate analysis techniques are applied to reduce the dimensionality of the data. Two of the most prominent methods available are Independent Component Analysis (ICA) [22] and Prinicipal Component Analysis (PCA) [16], [19], however we found that PCA was better suited to drawing out potential mineral components. While ideal for drawing out non-gaussian components [17], ICA will disfavor Gaussian components, whereas PCA will generate components that are generally Gaussian, consistent with the expected distribution of hydrated minerals on Mars. PCA was implemented in the *Python* [23] language using *matplotlib* [24]. The primary result of PCA is 10 orthonormal axes, called Principal Components (PCs) that describe the data more succinctly than the original axes. In analyzing the GRS+DCI combined data, the first 2 PCs typically describe over 50% of the variance in the dataset. Therefore, our primary analyses is based on these two PCs in order to focus on bulk soil properties that are prevalent across regional scales. It is worth noting that it is difficult to gain extensive insight from individual principal components. In general, it is unlikely that any one PC will represent a certain mineral or even mineral assemblage. As such, covariance between two elements in one PC, or even in many PCs in one analysis is insufficient to interpret a mineralogical correlation. For this reason, our analysis examines correlation between elements within PCs in both global analysis and sub-regional analyses.

Error Incorporation. To incorporate error, we chose to use the modified test parameter, t [15].

$$t_i = \frac{x_i - \bar{x}}{\sqrt{\sigma_i^2 + s^2}}$$

Where x_i is the mass fraction of a particular element in the *ith* bin, $\bar{x}$ is the average value of that element, σ_i is the error of the *ith* bin, and s is the standard deviation of the element distribution globally where data are available. Processing the data before the PCA process allows the incorporation of error without modifying the standard PCA procedure.

Enriched and Depleted Zones. In our analysis PCA is applied to several subsets of the data. To separate these regions, a mask is applied to the "global" data, selecting regions that are above +1 or below -1 in terms of t-values, roughly representing 1 standard deviation above or below the mean. These enriched and depleted regions are used to identify chemically "atypical" regions of Mars. Examinations of these smaller regions will inform us of covariations at a local scale. These covariations are not necessarily representative of regional properties, but occur in a more restricted geologic context. With the overall trends observed in global analyses, and the local variations observed in the enriched and depleted zones, we will be able to create an accurate picture of elemental covariance in soil at both scales

Similarity Analysis using the Dot Product. The PCA process projects the original data into a new, orthonormal space. In this space, Euclidian geometry and distance have similar meaning to that in typical 3-D space. Therefore, the angle between the vectors of a given element in PC-space can be used as a descriptor of the similarity of those two elements in PC-space. Elements with a small relative angle and a similar length in PC-space can be considered covarying. Similar comparisons were made by Gasnault et al. [16], albeit in a qualitative fashion.

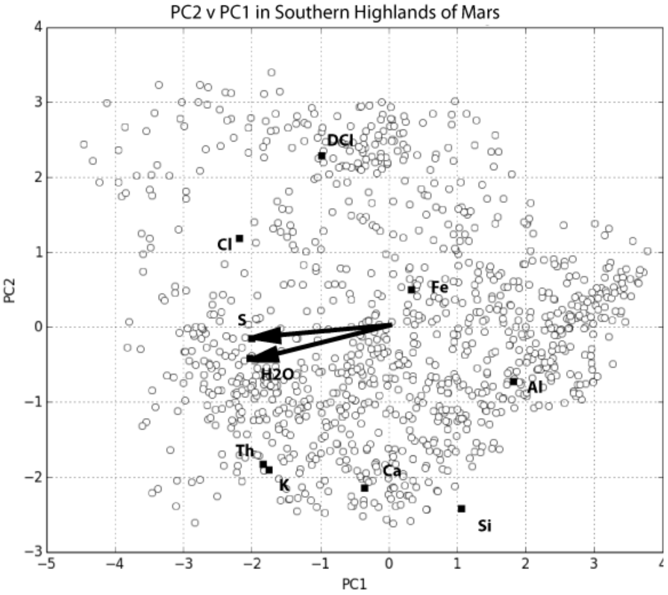

Figure 1. A biplot of PCA results from analysis on the Southern Highlands of Mars. White circles represent the elemental data projected into PC1 and PC2, black squares represent elemental axes projected into PC1 and PC2. Note the similarity in size and direction of the H_2O and S Vectors.

Discussion: In several settings on Mars strong correlations are observed between H and S. These correlations persist independent of the size, elemental composition, and geologic context of the analyzed regions. This suggests that, across the surface of Mars, the concentration in H and S covary and are a significant control on variation in martian soil. We interpret this to show that a group of hydrated sulfate minerals have a strong effect on variation in soil composition across the surface of Mars and are the dominant reservoir of chemically-bound H_2O in martian soil. Across every analyzed region, S is never more than 45 degrees away from H_2O, and only greater than 30 degrees in two regions. This suggests that apart from being consistently hydrated in the martian subsurface, sulfate minerals are the best candidate to be the primary hydrator. Previous work [20] has suggested, using molar ratios, that the correlation between H and S is well described using a variety of Fe-sulfates with H_2O:S ratios (i.e., hydration state) near 3:1. However Fe lacks strong correlations with H_2O, while Ca has a weak but observable correlation. This may suggest that Ca-sulfates, rather than Fe-sulfates, may play a significant role in hydrating bulk soil. Mg-sulfates also provide appropriate H_2O:S ratios, and may be necessary to balance out the relatively low hydration states of previously observed Ca-sulfates. Mg, however, remains undetectable by GRS, and cannot be incorporated into this analysis. Nevertheless, our results support the possibly increased significance of Mg and Ca-sulfates.

References: [1] W. C. Feldman, et al, J. Geophys. Res. E Planets, vol. 109, no. 9, pp. 1–13, 2004. [2] J. Audouard, et al, J. Geophys. Res. Planets, vol. 119, no. 8, pp. 1969–1989, 2014. [3] S. E. Ackiss et al, Icarus, vol. 243, pp. 311–324, Nov. 2014. [4] W. V. Boynton, et al, J. Geophys. Res., vol. 112, p. E12S99, Dec. 2007. [5] M. T. Mellon, et al, Icarus, vol. 169, no. 2, pp. 324–340, 2004. [6] M. Vincendon, et al, J. Geophys. Res. E Planets, vol. 115, no. 10, pp. 1–13, 2010. [7] S. Cull, et al, Geophys. Res. Lett., vol. 37, no. 24, p. n/a–n/a, Dec. 2010. [8] N. B. Karlsson, et al, Geophys. Res. Lett., p. n/a–n/a, 2015. [9] A. M. Bramson, et al, Geophys. Res. Lett., vol. 42, pp. 1–9, 2015. [10] M. H. Hecht, et al, Science (80-.)., no. July, 2009. [11] M. Nachon, et al, J. Geophys. Res. Planets, vol. 119, pp. 1991–2016, 2014.. [12] A. S. McEwen, et al, Nat. Geosci., vol. 7, no. 1, pp. 53–58, Dec. 2013. [13] L. Ojha, et al Geophys. Res. Lett., vol. 40, no. 1–6, p. GL057893, 2013. [14] F. J. Martín-Torres, et al, Nat. Geosci., no. April, pp. 1–5, 2015. [15] S. Karunatillake, et al, J. Geophys. Res., vol. 114, no. E12, p. E12001, Dec. 2009. [16] O. Gasnault, et al, Icarus, vol. 207, no. 1, pp. 226–247, May 2010. [17] A. D. Rogers et al, J. Geophys. Res. Planets, vol. 120, no. 1, pp. 62–91, 2014. [18] D. R. Klassen, Icarus, vol. 204, no. 1, pp. 32–47, 2009. [19] E. Jones, J. Geophys. Res. Planets, pp. 1023–1043, 2015. [20] S. Karunatillake, et al Geophys. Res. Lett., vol. 41, no. 22, pp. 7987–7996, 2014. [21] S. W. Ruff et al, J. Geophys. Res., vol. 107, no. E12, p. 5127, 2002. [22] A. Hyvärinen et al, Neural Networks, vol. 13, no. 4–5, pp. 411–430, 2000. [23] G. van Rossum, “Python Tutorial, Technical Report CS-R9526,” Amsterdam, 1995. [24] J. D. Hunter, Comput. Sci. Eng., vol. 9, no. 3, pp. 90–95, 2007.

Martian Water: Origin and Evolution. S. Hu, Y. T. Lin, W. Yang, J. C. Zhang, J. L. Hao, W. F. Xing and T. Zhang, Affiliation (Key Laboratory of Earth and Planetary Physics, Institute of Geology and Geophysics, Chinese Academy of Sciences, Beijing 100029, China, husen@mail.iggcas.ac.cn).

Introduction: It is generally accepted that there was liquid water on Mars based on topographic features [1-3], identification of alteration products [4-7], and analyses of hydrous minerals from Martian meteorites [8-10]. However, cold and arid conditions may have prevailed on Mars's surface for over 4 billion years [6, 11, 12]. The water content and hydrogen isotope of Martian mantle vary greatly revealed by different worker [13-16]. The origin and evolution of martian water is still poorly constrained.

Experiments: Four Martian meteorite (Y 984028, NWA 6162, Tissint and NWA 7034) with ages varying from 4.4 Ga to ~170 Ma [17, 18] were studied in this work. Petrography was carried out using FE-SEM and mineral chemistry was acquired using EPMA at the Insititute of Geology and Geophysics, Chinese Academy of Sciences (IGGCAS). Water contents and hydrogen isotopes of apatite and magmatic inclusions were acquired using NanoSIMS 50L at the IGGCAS [19].

Petrography: Magmatic inclusions (MIs) were enclosed by olivine in all samples except black beauty (NWA 7034), with diameter varying from 10-100 μm. They usually show round shape with a thin Ca-rich pyroxene outer rim, and mainly consist of feldspathic glasses with minor opaque minerals. Apatite was found in Y 984028 and NWA 7034. The apatite of Y 984028 is occurred in the interstial area. The apatite of NWA 7034 is occurred as mineral fragments in matrix and intergrowths with pyroxene and plagioclase in igneous clasts.

Water Contents and Hydrogen Isotopes of Apatite: The water contents and hydrogen isotopes of apatite of NWA 7034 vary from 197 ppm to 3540 ppm and -20 ‰ to +2000‰, respectively, with negatively correlation between them. The water content of the zoning apatite is 936 ppm at the rims and gradually decreasing to 197 ppm towards the cores. However, the hydrogen isotope of the zoning apatite shows "M" type zoning with δD higher than +1000‰. The water contents and hydrogen isotopes of apatite of Y 984028 vary from 1180 ppm to 4320 ppm and +1161 ‰ to +3304 ‰, respectively. They are negatively correlated, similar with the trend reported by Leshin [8].

Water Contents and Hydrogen Isotopes of MIs: The water contents and δD values of MIs are 14-5782 ppm and -145-+7073 ‰ for Y 984028, 60-3190 ppm and -83-+5599 ‰ for Tissint, and 10-2444 ppm and -313-+5057 ‰ for NWA 6162. Tissint and NWA 6162 show positive correlation between the water contents and the hydrogen isotopes, similar with the trend of GRV 020090 [13]. Whereas, Y 984028 show complex correlation between the water contents and the hydrogen isotopes.

Discussions: For ancient NWA 7034, the apatite would be originated from varied sources according to their textures. However, the water contents and the hydrogen isotopes of apatite share a similar negative trend. The zoning apatite seems crystallized from a closed system. The water content of the parent magma is estimated around 74 ppm, if the cores of the apatite is equilibrated with the residual parent magma according to the method of Vander Kaaden [20]. Compared with water contents of martian magma estimated from GRV 020090, Mars seems poor in water in the early times. The water contents of apatite of Y 984028 was not discussed here because of the high contamination by epoxy.

The maximum δD values of all samples studied in this work show power law correlation with the crystallization ages, gradually increasing from +3303 ‰ around 4.4 Ga up to +7073 ‰ around 170 Ma, which would represent the evolution history of Martian water. The minimum δD values and water cotents of all samples studied in this work varied from -313 ‰ to -83 ‰ and 10 ppm to 60 ppm, respectively, suggesting water is heterogeneously distributed in Martian mantle.

This work was finically supported by National Natural Science Foundation of China (Grants: 41430105, 41573057 and 41521062).

References: [1] Baker V. R. (2001) *Nature*, 412, 228-236. [2] Malin M. C. and Edgett K. S. (2000) *Science*, 288(5475), 2330-2335. [3] McEwen A. S. et al. (2007) *Science*, 317, 1706-1709. [4] Arvidson R. E. et al. (2005) *Science*, 307, 1591-1594. [5] Bibring J. -P. et al. (2005) Science, 307, 1576-1581. [6] Ehlmann B. L. et al. (2011) *Nature*, 479, 53-60. [7] Ehlmann B. L. et al. (2008) *Science*, 322(5909), 1828-1832. [8] Leshin L. A. (2000) *GRL*, 27(14), 2017-2020. [9] Leshin L. A. et al. (1996) *GCA*, 60, 2635-2650. [10] Watson L. L. et al. (1994) *Science*, 265(5168), 86-90. [11] Jakosky B. M. and Phillips R. J. (2001) *Nature*, 412(6843), 237-244. [12] Shuster D. L. and Weiss B. P. (2005) *Science*, 309, 594-597. [13] Hu S. et al. (2014) *GCA*, 140, 321-333. [14] McSween H. Y. et al. (2001) *Nature*, 409(6819), 487-490. [15] Sugiura N.

and Hoshino H. (2000) *MAPS*, 35(2), 373-380. [16] Wanke H. and Dreibus G. (1994), *PTRSA*, 349(1690), 285-293. [17] Shih C. Y. et al. (2011) *Polar Science*, 4(4), 515-529. [18] Yin Q. -Z. et al. (2014) *LPSC*, abstract#1320. [19] Hu S. et al. (2015) *JAAS*, 30(4), 967-978. [20] Vander Kaaden K. et al. (2012) *LPSC*, Abstract#1247.

COMPOSITION, PHYSICAL PROPERTIES, AND HYDRATION STATE OF HALITE-BEARING DEPOSITS ON MARS.

T. D. Glotch[1], M. M. Osterloo[2], and J. L. Bandfield[3], [1]Department of Geosciences, Stony Brook University, Stony Brook, NY, USA (timothy.glotch@stonybrook.edu), [2]University of Colorado Boulder, [3]Space Science Institute

Introduction: Chloride-salt bearing deposits have been observed on Mars using both mid-infared (MIR; THEMIS and TES) and visible/near-infrared (VNIR; OMEGA and CRISM) data sets [1-6]. They occur primarily in ancient Noachian terrains in the southern highlands in a variety of geologic settings, including as discontinuous plains units, crater fill, and channel deposits [2]. In TES and THEMIS emissivity data, these deposits exhibit blue slopes over the ~8-50 μm range [1-3,6]. In CRISM and OMEGA ratio reflectance data, the deposits exhibit featureless red slopes over the 1-2.5 μm region and an inverted 3 μm feature, indicating that these deposits are desiccated compared to the surrounding regolith. [3-6]. Although halite (NaCl) does not contain strong spectral features over the VNIR-MIR wavelength range, a combination of laboratory and theoretical studies and geological arguments have strongly suggested that it is the most likely candidate for the chloride salt phase present on Mars [6-7]. Halite abundance is constrained to 5-20 wt.% for most deposits, and while phyllosilicates have been found in close contact with some deposits [4-5], there appear to be no hydrated or evaporite phases intermixed with them. A better understanding of the associated evaporite phases (if any) and the hydration state of these deposits is the focus of our current work.

Atmospheric Correction: To search for additional phases associated with the halite-bearing deposits, we atmospherically correct CRISM images using the DISORT radiative transfer-based method of [8-9]. This method results in an atmospherically corrected surface image in units of single scattering albedo (SSA). This has three primary advantages: (1) VNIR spectra add linearly in SSA space, allowing us to perform quantitative mineralogical anlaysis of the site; (2) SSA in the 3 μm region is related to the effective single particle absorption thickness (ESPAT), which has been shown to be quantitatively related to water content [10]; (3) it allows us to utilize factor and target transformation (FATT) techniques to search for minerals with low abundances in the scene that might not otherwise be apparent.

FATT: The factor analysis technique can be applied to any dataset in which the components of the data set vary independently and the measurements within the data set can be approximated as a linear sum of the components. The technique results in a series of orthogonal eigenvectors that can be linearly fit to laboratory mineral spectra. If the fit results in a match, the mineral is likely a component of the scene. If it does not, then it is unlikely to be a component. Figure 1 shows preliminary results from CRISM image FRT0000A253, which includes both halite- and phyllosilicate-bearing surfaces. Halite, vermiculite, olivine, and augite are all fit well, while other phyllosilicate phases, carbonates, perchlorate, and nitrate are not.

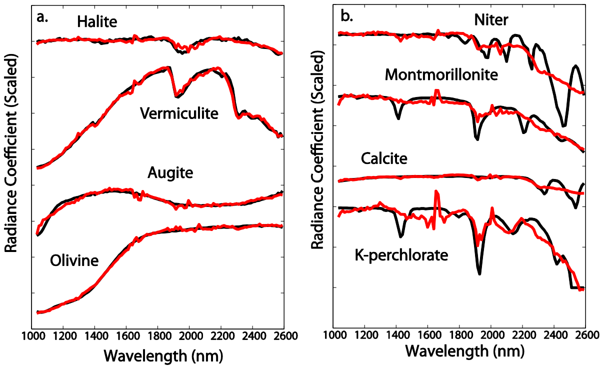

Figure 1. FATT results for CRISM image FRTA253. a) Laboratory spectra of halite, vermiculite, augite, and olivine, are well fit by the eigenvectors, indicating their likely presence in the scene. b) Niter, montmorillonite, calcite, and K-perchlorate are not adequately fit, indicating their likely absence from the scene.

Future Work: We are in the preliminary stages of a comprehensive study of CRISM images that cover halite-bearing deposits on Mars. Thus far we have performed the DISORT-based atmospheric correction on >20 CRISM images. We will use the techniques described here and report on the the identification of associated alteration phases as well as attempts to constrain the absolute water content of the deposits.

References: [1] Osterloo M. M. et al. (2008), Science, 319, 1651-1654. [2] Osterloo M. M. et al. (2010) *J. Geophys. Res.*,115, E10012 [3] Murchie, S. M. et al. (2009) *J. Geophys. Res.*, 114, E00D06. [4] Glotch, T. D. et al. (2010), *Geophys. Res. Lett.*, 37, L16202. [5] Ruesch, O. et al. (2012), *J. Geophys. Res.*, 117, E00J13. [6] Glotch, T. D. et al. (2016), *J. Geophys. Res.*, 121, doi:10.1002/2015JE004921. [7] Jensen, H. B. and T. D. Glotch (2011), *J. Geophys. Res.*, 116, E00J03. [8] Liu Y. et al. (2012), *J. Geophys. Res.*, 117, E00J11. [9] Liu Y et al. (2016), *J. Geophys. Res.*, in review. [10] Milliken R. E. et al. (2007), *J. Geophys. Res.*, 112, E08S07.

MARS HISTORY REVISITED: BUILDING NEW PARADIGM. J. P. Bibring (jean-pierre.bibring@ias.u-psud.fr)

Over the past decade, the coupling between remote (orbital) observations and in situ (rover) measurements has led to an in-depth revisiting of Mars history. In particular, the access to the composition of the minerals, both igneous and aqueously altered, at a sub-kilometer scale, put into their geomorphological context, has demonstrated its huge potential to trace the evolution of Mars environment, which prevailed over its climatic and geological history. As a key outcome, an early era during which liquid water was likely stable at the surface is exhibited; it strongly advocates for a potential habitable era at Mars, in its ancient past.

Mars has thus preserved, uniquely in the solar system, sites recording most steps that paved its History, including those which took place soon after the planet formed. Most of them have been unambiguously identified and located: they constitute favored sites for future in situ missions with astrobiological relevance.

We shall present and discuss the major results acquired at Mars over the past decade from which a renewed Mars History has been drawn, triggering a fundamental change of paradigm, in particular in the address of the time and space scale of Earth and life unicity.

CHARACTERIZATION OF HYDROUS AND MAFIC MINERALS IN TYRRHENA TERRA, MARS. S. Gou, K. Di, Z. Yue, State Key Laboratory of Remote Sensing Science, Institute of Remote Sensing and Digital Earth, Chinese Academy of Sciences (P.O. Box 9718, Datun Road, Chaoyang District, Beijing 100101, China. gousheng@radi.ac.cn, dikc@radi.ac.cn, yuezy@radi.ac.cn).

Introduction: Tyrrhena Terra (centered at 11.9° S， 88.84° E), straddles the Amenthes and Mare Tyrrhenum quadrangles, locates in highly cratered and partially dissected Noachian highlands of Martian southern hemisphere, with Isidis Planitia and Hellas basin in its south and north respectively. A large number of hydrated silicates outcrops have been detected by OMEGA spectrometer onboard Mars Express firstly [1], then confirmed and refined with higher spatial resolution CRISM spectrometer onboard Mars Reconnaissance Orbiter (e.g., [2]). This highland terrain is characterized by fluvial valleys and various hydrous minerals, indicating a past aqueous environment. Though a basic distribution mapping of pyroxene and olivine from spectral index have been done by [3], the composition of these mafic minerals still needs to be studied to better understand its formation and subsequent evolution history. Here we analyze 208 targeted CRISM hyperspectral cubes in this region to search for the presence of hydrated minerals, such as carbonate, Al-phyllosilicates by their diagnostic absorption features and discern the compostion of mafic minerals.

Datasets and Pre-processing: The standard CRISM processing pipeline is applied on each targeted image cube to obtain surface reflectance by using CRISM Analysis Toolkit (CAT), including converting PDS to CAT storage format, correcting for photometric effects by dividing the cosine of the incidence angle, correcting for atmospheric effects by dividing scaled transmission spectrum.

Methodology: Spectral indices [4-5], devised on diagnostic absorption features, are used for preliminary and quick investigation on hydrous and mafic minerals over Tyrrhena Terra. The indices include BD1900, BD2100, BD2210, BD2290, BD2300, BDCARB, etc..

Modified Gaussian Model (MGM) [6-7], which deconvolves overlapping electronic transition induced absorptions of mafic mineral spectra into fundamental absorption components (band center, band width, and band strength), can be used to retrieve modal and chemical compositions from laboratory mineral power mixture spectra [8], rock slab spectra [9-10], and planetary relfectence spectra, e.g., [11-13]. Following [13-14], a automatic MGM modelling procedure has been implemented with all possible 7 mafic minerals mixture configurations in order to detect and characterize all possible mafic assemblages on unknown spectra after selection through spectroscopic criteria.

Mineral Characerization Results: Average spectrum derived from region of interest (ROI) on spectral indices maps are further investigated. The extracted average spectrum is ratioed to the average spectrum in the same column near the spectrum of interest in order to remove systematic artifacts and highlight spectral features.

Identifaicaiton of hydrous minerals. Hydrous minerals are discerned by multiple absorption features on spectral indices map, and extracted spectra are compared with laboraty spectra. For example, carbonates-bearing rocks are found on crater uplifts from frt00009e58 and hrl000082e8, phyllosilicate-bearing outcrops are found in frt0000a14f (Fig. 1) and frt00012b8a.

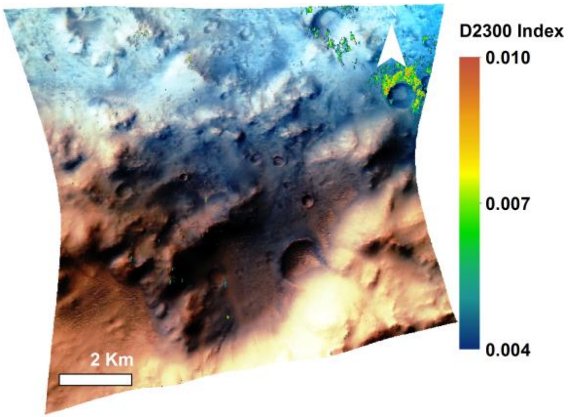

Fig. 1. Detection and distribution of phyllosilicates on crater rims in CRISM frt0000a14f through spectral indices.

Discrimination of mafic minerals. MGM fitting and filtering results show clinopyroxene and olivine are widespread in Tyrrhena Terra, while orthopyroxene only outcrops in a few limited locations. The modelled clinopyroxene absorptions mainly center at 2140 nm and 1050 nm (Fig. 2), suggesting the compositions are relatively close to diopside-hedenbergite join, and modelled orthopyroxene absorption mainly center at 1880 nm and 950 nm, suggesting the compositions are chiefly enstatite. And MGM predictes Fo value of olivine ranges from 39 to 96 in the whole Tyrrhena Terra.

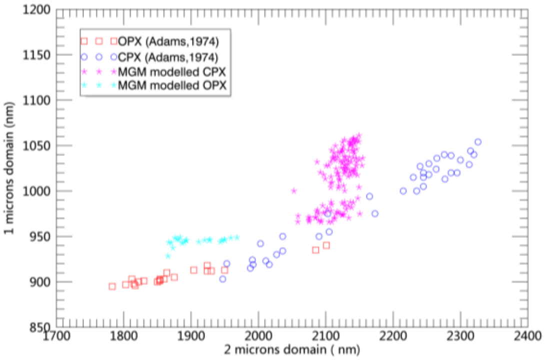

Fig. 2. Comparison between MGM modelled clinopyroxene and orthopyroxene absorption centers (respectively purple and cyan stars) in the whole Tyrrhena Terra and Adams reference trend with blue circles for clinopyroxene and red rectangles for orthopyroxene

Conclusions and perspectives: Hydrous and mafic mierals can be detected from orbital spectra. There are various hydrous minerals distribute on different landforms in Tyrrhena Terra, for example, crater central peaks, inner walls and rims, and compositions of mafic minerals can be discriminated through MGM modelled band centers. In the future, we will perform a further synergetic analysis by integration of various types of datasets with different resolutions covering Tyrrhena Terra to better understand the geologic settings and evolution history of this region.

Acknowledgment: This study was supported by National Natural Science Foundation of China under Grant 41472303.

References: [1] Bibring J.-P. et al. (2006) *Science*, 312, 400-404. [2] Carter J. et al. (2013) *JGR*, 118, 1-28. [3] Ody A. et al. (2012) *JGR*, 117, E00J14. [4] Pelkey S. et al. (2007)JGR, 112, E08S14. [5] Viviano-Beck C. E. (2014) *JGR*, 119(6), 2014JE004627. [6] Sunshine J.M. et al. (1990), *JGR*, 95, 6955-6966. [7] Sunshine, J.M. and Pieters, C.M. (1993) *JGR*, 98(E5), 9075-9087. [8] Sunshine, J.M. and Pieters, C.M. (1998) *JGR*, 103, 13675-13688. [9] Carli C. et al. (2014) *Am. Mineral.*, 99, pp. 1834-1848. [10] Gou S. et al. (2015) *European Lunar Symp*. 3rd, 77-78. [11] Noble S.K. et al. (2006) *JGR*, 111, E11009. [12] Whitten J. and Head, J.W. (2015) *PSS*, 106, 67-81. [13] Clénet H. et al. (2013) *JGR*, 118, 1632-1655. [14] Clénet H. et al. (2011) *Icarus*, 213, 404-422.

AN INVESTIGATION INTO THE PARADOX FOR THE PLATY-RIDGED-POLYGONIZED TERRAIN IN ELYSIUM PLANITIA, MARS.

Z. Yue[1], S. Gou[1], H. Xie[2], and K. Di[1], [1]State Key Laboratory of Remote Sensing Science, Institute of Remote Sensing and Digital Earth, Chinese Academy of Sciences, Beijing 100101, China. [2]Department of Geological Sciences, University of Texas at San Antonio, San Antonio, TX 78249, USA.

Introduction: Platy-Ridged-Polygonized (PRP) terrain typically comprises rubbly plates, sinuous or linear ridges, and polygonally patterned smooth ground [1] (Fig. 1). The plates (PL) are usually of low albedo, commonly contain meter-sized clasts [2], and are typically in irregular polygonal shapes. The polygonal (PO) terrains are usually of high albedo and are relatively smooth (Fig. 1). Many studies have shown that the crater densities in PO terrains are much lower than those in PL regions [3]. The ridges can develop in the smooth polygonal ground as shown in Fig.1 or can appear as the boundaries of the platy regions.

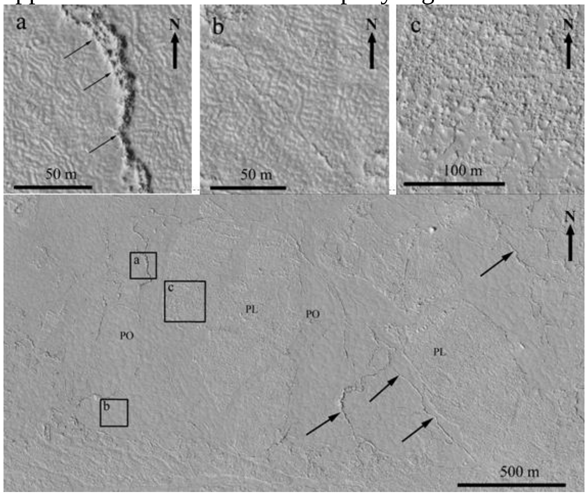

Fig. 1. Platy-ridged-polygonized terrain (Part of HiRISE image PSP_003571_1880_RED.jp2). The ridges are highlighted by arrows and in inset (a) in detail, the smoother material are the polygonized terrain (labeled by PO and shown in inset (b) in detail), and the rougher material is the platy terrain (labeled by PL and highlighted in inset (c)).

A number of models have been proposed to explain the origin of the PRP terrains, and these can be generally classified into two categories based on the agents of water or lava. Currently, the origin of the PRP terrain is still in hot debate. In this work, we give some suggestions on this problem through two different methods. First, we use high-resolution images from the High Resolution Imaging Science Experiment (HiRISE) to explore the detailed geomorphic characteristics and spatial distribution of the PRP terrain with a specific focus on the spatial relation between PRP and other landforms that are clearly related to water. Second, we use the hyperspectral images from the Compact Reconnaissance Imaging Spectrometer for Mars (CRISM) to explore the compositional changes, especially across the boundaries of the PRP terrain to find possible water signatures. We hope this research can give some clues for the recent Martian environment.

Data Sets: In this research, we have collected 866 HiRISE images from the study area of Elysium Planitia from the mission phases of transition, primary science, and extended science prior to April 3, 2015. The footprints of these data are shown in Fig. 2B. In addition, we selected 13 CRISM images in which the PRP terrains are identified from the HiRISE images. The footprints of these data are also shown in Fig. 2B. The CRISM data are mainly used to extract possible water signatures where they are located.

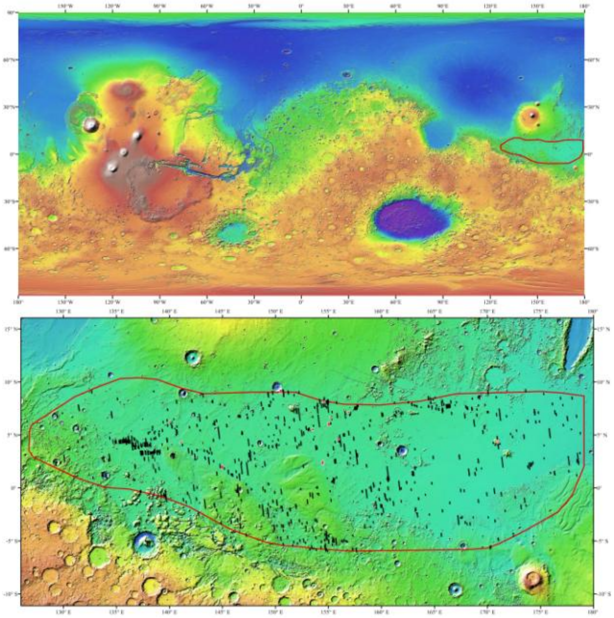

Fig. 2. Locations of the study area and the footprints of the datasets used in the research. (A) Top panel, the location of the study area is represented by the red polygon. (B) Bottom panel, the footprints of the HiRISE images (black) and CRISM data (red color with the white outline) used in the research. Mars Orbiter Laser Altimeter (MOLA) data is the background image.

Methodology: We evaluate the possible origin of the PRP terrain through examining its morphology, spatially associated landforms that could be aqueous in origin, and its possible water signatures. Based on these considerations, the HiRISE images are first used to identify the PRP terrains and aqueous landforms, as well as their spatial distributions. We then use the CRISM data to search for possible water signatures in some of the important locations where the boundaries of the PRP terrains or indications of the fluids are located.

Observations: The footprints of the HiRISE images where the PRP terrains exist are shown in Fig. 3. Among the 866 HiRISE images inside the Elysium Planitia, 328 of them have obvious features of the PRP terrain. In general, the PRP terrains are located in the regional depressions surrounded by the heavily impact-cratered terrains.

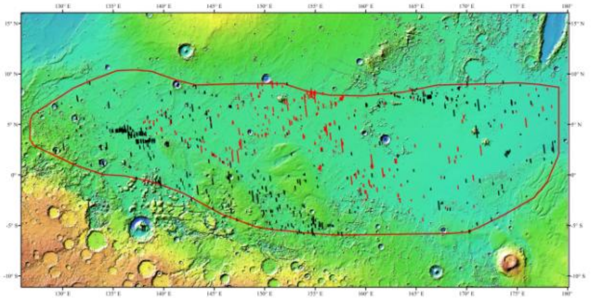

Fig. 3. Distribution of PRP terrains in Elysium Planitia. The footprints of the HiRISE images wherein the PRP terrains exist are shown in red while others are shown in black.

Among the 328 HiRISE images where the PRP terrains exist, 101 of them have pingos (Fig.4), and a large fraction of the secondary smooth polygons (Fig. 4A) can appear around many pingos. According to the stratigraphic relationships, these secondary polygons, and then the pingos, should be formed after the PRP terrain. In this investigation, we also find that 65 images have channels accompanying the PRP terrains; and among them, 37 images have streamlined islands as exemplified in Fig.4B. The channels usually have no obvious vent, and most of them emanate from a wide region with many scarps. It is significant to notice that most of the streamlined islands are not well developed with a very large length/width ratio. Similar to the pingos, the channels and the streamlined islands are also formed after the PRP terrains, because they have cut through the PRP terrain.

In this research, thirteen CRISM hyperspectral images were targeted to search for water signatures in the key areas (footprints are shown in Fig. 2). However, after applying a suitable detection threshold, none of these images showed the signatures for hydrated minerals.

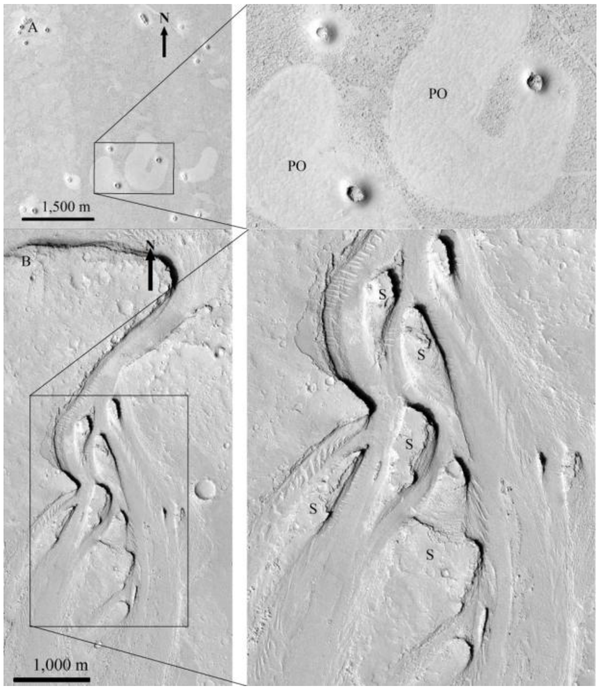

Fig. 4. Examples of the periglacial (pingos) and fluvial (channels and streamlined islands) landforms identified in this study. (A) One pingo field and an enlargement for the details of the pingos (subset of HiRISE image ESP_037222_1820_RED.jp2); (B) One channel and the streamlined islands developed inside (subset of HiRISE image ESP_029864_1880_RED.jp2).

Discussion: Based on the observations from HiRISE images and CRISM data, we propose that the PRP terrains were formed through the following stages.

(1) The water ice was transported and reserved at the shallow surface in Elysium Planitia. Currently, the mechanism for the origin of the ground ice at its various locations is not well understood [4]. It is probably from the frost [5] or ice in the Martian atmosphere [6], and the existence of water ice in the shallow depths of the Martian surface in many locations as has been recently verified [7, 8].

(2) Melting of the water ice occured when the condition was suitable, and the shallow surface layer became muddy and slidable, because of the existence of ice below the liquid-sediment contact. In most cases, the mud flow could only move a short distance and stopped against the high terrain, where the terrain would appear as irregular or ripple-like depending on the mobility.

The necessary climate change can be caused by a variation of the oblique of Mars [9], which was indeed the case a few hundred thousand years ago [10]. In addition, Conway et al. [11] conducted laboratory experiments in which a stream of water flowed over test beds at low temperature and low pressure, which proved that both basal freezing and low pressure can increase the flow propagation speed.

(3) The water in the muddy flow was frozen and finally the textures and morphologies of the PRP terrain were formed. In this period, the polygonized terrain may be formed where the water content is high enough; however, much water could also have evaporated or been infiltrated into the depths, which would result in the indistinct morphologies. Wilson and Mouginis-Mark [12] obtained similar conclusions through a detailed dynamic analysis for the flow deposit in Cerberus Fossae, which also has the textures of the PRP terrains in the study. In addition, the pingos could be formed if the conditions were suitable [13].

Conclusion: In this research, we have conducted a comprehensive investigation into the PRP terrains in Elysium Planitia, Mars. Our investigation supports that the PRP terrains are from some kind of muddy fluid. The fluidity exhibited during the formation process is reflected by the fact that the PRP terrains lap against obstacles and form an elevated frontier. A further analysis with detailed morphology and related aqueous landforms led us to propose that the PRP terrains could be the relic of muddy flow.

Acknowledgment: This study was supported by National Natural Science Foundation of China under Grant 41472303.

References: [1] Balme M. R., Gallagher C. (2012) *Geophysical Research Abstracts*, *14*, EGU2012-10062. [2] Balme M. R., et al. (2011) *Mars. Geol. Soc. Lond. Spec. Publ. 356*, 203–227. [3] Page D. P., et al. (2009) *Icarus*, *203*, 376–389. [4] Sizemore, H. J., et al. (2015) *Icarus*, *251*, 191-210. [5] Bapst J., et al. (2015) *Icarus*, *260*, 396-408. [6] Mateshvili N., et al. (2009) *Planetary and Space Science*, *57*, 1022–1031. [7] Arvidson R. E., et al. (2009) *J. Geophys. Res.*, *114*, 357-369. [8] Dundas C. M., Byrne S. (2010) *Icarus*, 206, 716-728. [9] Costard F., et al. (2002) *Science*, *295*, 110–113. [10] Touma J., Wisdom J. (1993) *Science*, *259*, 1294–1297. [11] Conway S. J., et al. (2011) *Icarus*, *211*, 443-457. [12] Wilson L., Mouginis-Mark P. J. (2014) *Icarus*, 233, 268-280. [13] Burr D. M., et al. (2009) *Planetary and Space Science*, *57*, 541–555.

THE UTILITY OF FIELD CONFERENCES IN HARNESSING THE SCIENTIFIC POTENTIAL OF TERRESTRIAL ANALOGS IN ASIA FOR PLANETARY GEOLOGY RESEARCH.

G. Komatsu, International Research School of Planetary Sciences, Università d'Annunzio, Viale Pindaro 42, 65127 Pescara, Italy (goro@irsps.unich.it).

Introduction: Planetary exploration of a planetary body begins with imaging from a distance, obtaining large-scale topography, then, information improves in scale to regional and eventually to local. Lately in some planetary exploration programs, such as those of the Moon and Mars, the level of information gained through the exploration is reaching even to the outcrop scale. Observation of outcrops is what terrestrial geologists are most accustomed to. In fact, planetary geologists conducting fieldwork and collaborations with terrestrial geologists are increasing.

Asia is emerging as a major center of studies in planetary geology. Japan's Hayabusa and SELENE, China's Chang'E series, India's Chandrayaan and Mangalyaan are some examples of the region's determination to push forward into the new era of planetary exploration.

Terrestrial analogs in Asia: Asia is rich and diverse in geological environments and has much to offer in terms of terrestrial analogs for planetary geologic features. However, in spite of the extremely diverse geological settings that exist in Asia, relatively little attention has previously been paid to this region in terms of terrestrial analog studies for planetary application.

Island arcs in the Western Pacific are characterized by active plate margins, and many volcanoes and hydrothermal systems of diverse types are widely distributed. Marine processes including those of tsunami are recorded along the coastal zones. The Asian Continent is extremely diverse ranging from ancient cratons to younger orogenic belts with large basins and plateaus. Glacial and periglacial processes including permafrost are observable in high elevations and in high latitude zones. Furthermore, excellent examples of ice-magma interactions and catastrophic flooding have been documented. Extensive evidence for paleolakes are noted and modern-day dry lakes occupy in many basins, which are the testimony for drastic and fluctuating climate change. Aeolian processes are active in the continent's dry interior. Although relatively rare, impact craters with good preservation state exist at some localities. All of such geological characteristics are useful in planetary geology research.

Field conferences: Field conferences, in the form of a symposium and accompanying pre and/or post symposium fieldtrip(s), have been utilized by the planetary geology community for learning about terrestrial analog sites, and exchanging ideas and fostering collaborations between planetary and terrestrial geologists. Engineers engaged in building spacecraft and onboard instruments often participate in such field conferences in order to be exposed to real geological environments outside laboratories. At terrestrial analog sites, simulation for human planetary exploration is also conducted, giving insights on what to expect in the fields where humans will have to operate.

An example of field conferences is the 2011PERC (The Planetary Exploration Research Center of the Chiba Institute of Technology) Planetary Geology Field Symposium (see http://www.perc.it-chiba.ac.jp/meetings/pgfs2011/) held with the theme "Planetary Geology and Terrestrial Analogs." The symposium was hosted on 5–6 November 2011 in Kitakyushu City, Kyushu Island, Japan and was followed by a fieldtrip to hotsprings and volcanic features in the Beppu-Shimabara graben [1]. This field symposium was the first of its kind held in Asia [2]. The symposium also produced a special issue of articles in Planetary and Space Science [3].

It is expected that field conferences on the theme of planetary geology and terrestrial analogs will increase in Asia, contributing to the progress in the science of planetary bodies in the Solar System.

References: [1] Komatsu G., Goto K., Shibuya H. (eds) (2011) Volcanic and geothermal activities along the Beppu-Shimabara graben as terrestrial analogs for comparative planetary geology. *Guidebook for Field Trip*. 2011 PERC Planetary Geology Field Symposium, Kitakyushu, 62 p. [2] Komatsu G. and Namiki N. (2012) Planetary Geology and Terrestrial Analogs in Asia. *EOS, 93*, 164, 10.1029/2012EO160004. [3] Komatsu G., Goto K., Tanaka K. L. (2014) Preface. Planetary Geology Field Symposium, Kitakyushu, Japan, 2011: Planetary Geology and Terrestrial Analogs. *Planetary and Space Science, 95*, 1-4, http://dx.doi.org/10.1016/j.pss.2014.04.002.

QAIDAM BASIN, NE TIBETAN PLATEAU: A NEW UNIQUE MARS ANALOGUE SITE FOR ITS WET PAST AND DRY ENVIRONEMNT TODAY

L. Xiao[1, 2]. J. Wang[1], Y.N. Dang[2], Z.Y.Cheng[1], T. Huang[1], J.N. Zhao[1], J. Huang[1], Y. Xu[2], Z.Y. Xiao[1]. 1. Planetary Science Institute, China University of Geosciences, Wuhan, 430074, P. R. China; 2. Space Science Institute, Macau University of Science and Technology, Macau, China. (longxiao@cug.edu.cn)

1. Introduction

Qaidam Basin is the highest, and one of the driest and largest deserts on Earth. It features with extremely low precipitation, high evaporation; various aeolian geomorphologies. In addition, high UV radiation, variety of saline lakes and evaporates in the region make it a candidate base for astrobiology study. Several studies focusing on evaporate sediments and mineralogy have suggested that the Qaidam basin is potentially a promising Mars analog site [1-6]. This study reports major geomorphological features, distinctive evaporate sediments, evolutionary saline lakes, playas, microbial features in Qaidam Basin, and its advantages for Mars exploration simulation test, which are distinct with other analog sites on Earth and should be listed as a new Mars analog site.

2. Methodology

Field survey and interpretation of satellite images were applied to investigate the various landforms in Qaidam Basin. Sampling and microbia isolation from brine water and evaporate sediments were conducted. CTX, HRSC and HiRISE imagery data were applied to study aeolian- and fluid-related geomorphologic features on Mars.

3. Results

Varity of Mars-like geomorphologies well preserved within the Qaidam Basin. The typical ones are aeolian and evaporation desert landforms and vast areas of salt lakes.

In the Qaidam Basin, dunes are morphologically classified as barchans dunes, barchans dune chains, linear dunes and star dunes, similar in shape and size with its counterparts on Mars (Fig. 1). The yardangs within the basin cover an area of ~20,000 km^2, make it the largest yardang region in China. These yardangs are mostly located in the northwest part of the Qaidam Basin, and wind is the dominate force for their formation. These yardangs show different sizes and shapes, such as mesa, zigzag-like, remnant cone-like, ark-shape, capsized boat-shape, and whale back-like yardangs (Fig. 1).

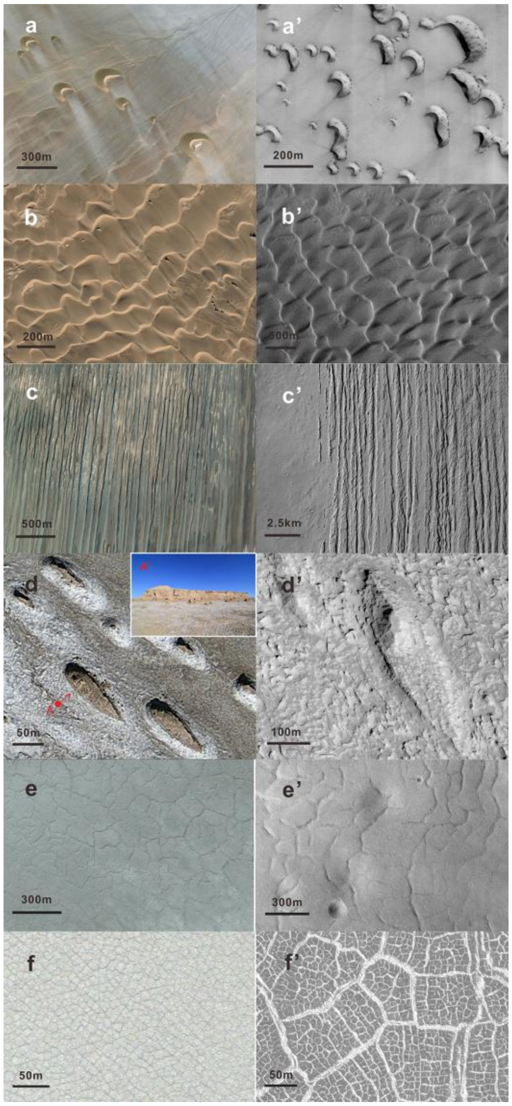

Fig. 1. Dunes (a, b), yardangs (c, d) and polygons (e, f) in Qaidam Basin; a', b', c', d' and e' are their analogues on Mars.

Polygonal surface structures (PSSs) are wide spread surface phenomenon in the Qaidam basin. They are mainly distributed inside the six playas within the basin, namely the Dalangtan, Qahansilatu, Kunteyi, Mahai, Yiliping and Qarhan playas. Generally, these PSSs can be divided into three distinct types according to their size. The small -sized PSSs are commonly less than 10 m in diameter and mainly display as triangle, quadrangle, and hexagon in planar morphology. Middle-sized PSSs (10-100 m diameter) in the Qaidam basin exhibit various appearances, and many of which are with quasi-polygonal pattern. The largest-sized PSSs (100-300m) are distributed in the Dalangtan playa, and the edges of polygons are ridges that are ~ 4 to 6 m wide. Smaller PSSs occur within the largest PSS.

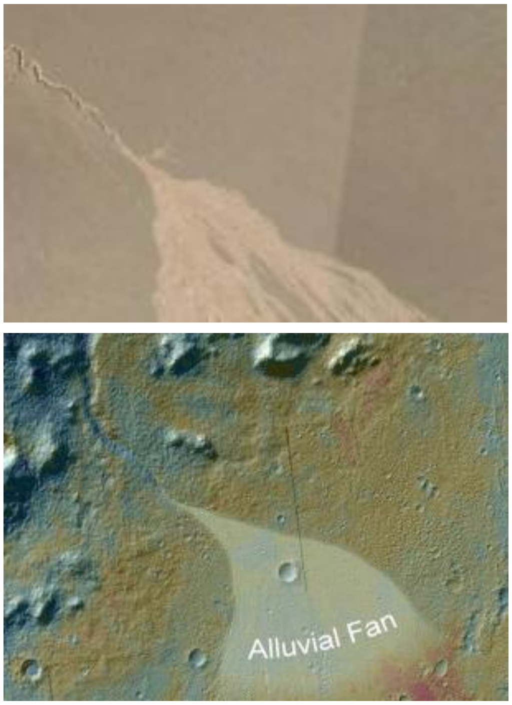

Fig. 2. Alluvial fans in Qaidam Basin (upper) and in Gale crater on Mars (lower).

There are 30 lakes in the modern Qaidam Basin, including 1 fresh lake, 6 brackish lakes, 1 salt lake and 22 brine lakes. Quaternary evaporate deposits are well developed in the six playas. However, they were formed in different time and had distinct physic-chemical evolution history.

Valleys of different scales are widely distributed in the Qaidam Basin, especially in the marginal area of the basin. Most of them originated from the surrounding mountains and formed by glacial meltwater and occasional rainfall (Fig. 2). Gullies in the Qaidam Basin can be tens to hundreds of meters long and usually form on hillsides during or after heavy rains. However, light rain or small water flow can also develop gully when it run through loose sands.

Lipid molecules have been found in saline lakes, and salinity is the main factors influencing the microbial community. Our study suggests that archaeal lipids dominate in units with high salinity, whereas bacterial lipids dominant in detrital units with low-salinity. Twenty three species of bacteria and eight species of fungi were identified from the deposits.

4. Discussion and concluding remarks

Qaidam basin is the highest and one of the largest and driest desert on Earth. It is located at a dry, cold, high UV environment, similar as the surface of Mars.

Variety of aeolian landforms are widely spread in the desert regions of the Qaidam Baisn. Most of dunes and yardangs types have their counterparts on Mars. Detailed study about the origin and evolution of the dunes and yardangs could provide clues on understanding how wind has operated and/or is operating on Mars. Precipitation in Qaidam Basin is very low, the valleys gullies and fluvial fans are distributed along the surrounding hillsides. The 30 salt lakes and playas represent different stages of lake evolution. It provides unique examples to study how fresh water lakes became hypersaline lakes, and finally to playas. This could provide clues on understanding past martian environmental changes. As different evaporate mineral assemblages have been identified in the playas within Qaidam Basin, the origin of their counterparts on Mars could be inferred. Microbial systems are developed in the salt lakes and playas with various species, although no visible life signatures have been recognized in most of the playas and hypersaline lakes.

The variety of epigenetic and endogenetic geomorphic type, sedimentary rocks, salt lakes, evaporite mineral assemblages and Mars-like extreme environment collectively make the Qaidam Basin as a new and unique Mars analogue site on Earth, for both of scientific research and mission test.

References: [1] Mayer et al. (2009). LPSC, XL abstract #1877 [2] Wang and Zheng, (2009). LPSC XL, abstract #1402. [3] Zheng et al. (2009). LPSC XL Abstract #1454. [4] Zheng et al., 2013. Acta Geologica Sinica, 87(3):885-897. [5]Kong et al. (2013). 44th LPSC, #1719. [6] Kong et al., 2014. American Mineralogist, 99, 283-290.

MORPHOLOGY AND COMPOSITION OF POLYGON SURFACE STRUCTURES IN THE QAIDAM BASIN AND IMPLICATIONS FOR MARS.

Y.N. Dang[1], L. Xiao[1, 2], Y. Xu[1], B. Wang[3], 1. Space Science Institute, Lunar and Planetary Science Laboratory, Macau University of Science and Technology, Taipa, Macau; 2. Planetary Science Institute, China University of Geosciences, Wuhan, 430074, P. R. China; 3.School of Li Siguang, China University of Geosciences, Wuhan, 430074, P. R. China. (waisedyn@gmail.com).

Introduction: Polygon surface structures (PSSs) are a very common landforms on Earth and Mars, which have been observed and studied for many years. Small-scale PSSs that occur at middle to high latitudes on Mars are usually regarded as the cause of thermal contraction processes [1], and the PSSs that happened in impact craters floors and depressions with chlorides are attributed to desiccation processes [2,3]. It has been proposed that the morphologies and sizes of the desiccation polygonal cracks can be used as paleoenvironmental, as well as lithological, indicators that could be helpful in planning future missions [3].

Qaidam Basin, located in Tibet Plateau of NW China, has the analogical PSSs on Mars, they are the products of salt lakes dried up in the early days. With its dry, cold, high UV environment, which is similar to the surface of Mars, Qaidam Basin has been suggested as a potential analogue site [4-8]. This work we analyze the morphological characteristics and mineral composition of PSSs in the Qaidam Basin and its possibly forming processes as an analog to Mars, to enhance our understanding of PSSs on Mars.

Data and methods: For the Qaidam Basin, Google Earth image have been used to identify various PSSs and followed by photography, topography measurements, and sample collection. X-ray diffraction (XRD) analysis were used to derive the chemical composition and mineralogy. For Mars, we use the HiRISE dataset [9], which are obtained from Reconnaissance Orbiter (MRO) and have a very high spatial resolution of 30 cm pixel^{-1}, to search for and characterize the Martian PSSs.

Results:

Polygons Morphology. The results indicate that the PSSs cover large floor areas of the Qaidam Basin playas, but occasionally, they occupy isolated patches or regions, especially inside six playas named Dalangtan, Qahansilatu, Kunteyi, Mahai, Yiliping and Qarhan as shown in Figure 1. In this work we focus on the polygonal patterns in Dalangtan playa. Field investigation showed that all PSSs in the Dalangtan playa have a range in size from centimeters to hundreds of meters in diameter (Figure 2), and most of them have raised rims. The troughs extend along the outer margin of each polygon and display width that ranges from ~ 0.5 m up to 10 m, which is approximately consistent with crater floor polygons on Mars [2].

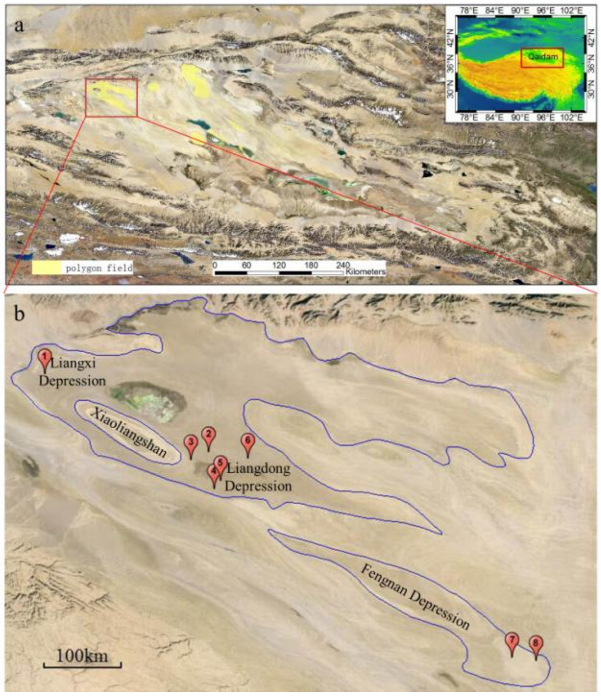

Figure 1. (a) The distribution map of PSSs in the Qaidam Basin, NW Tibet Plateau. The upright map is generated from 90 m SRTM data, showing the location of Qaidam Basin. (b) Red landmarks show the approximate location of sampling sites. Blue lines show the area of Dalangtan playa. Base Image Credit: Google Earth. North is up in all figures.

The small sized PSSs are commonly less than 10 m in diameter and mainly take the form of triangle, quadrangle, and hexagon (Figure 2c). Some of them are spatially arranged by aligning a line or assembled closely forming a honeycomb. This type of PSSs can be found in all sampling sites. However, irregular middle sized PSSs (10-100 m) appear in sampling 6 site (Figure 1b). They display discontinuous borders of approximate 8.5 m in width and 0.6 m in height. The large sized PSSs (100-300 m) occur around sampling 4 site (Figure 1b; Figure 2a). They have borders varying in size from 4 to 6 m wide and most of them have raised rims. Small sized polygons often form in the interiors of these large PSSs. Figure 2b shows the similar landform on Mars.

Mineralogy of Samples. We selected 8 surface samples in Dalangtan playa, the occurrence locations are marked in Figure 1b, and the XRD analysis results are presented in Table1. The results indicate that the halite hold a minimus of 50%, followed by feldspar and quartz. Illite, a kind of clay minerals, was found in nearly all collections except the sample 3. In addition, chlorite appeared in four of all samples. The small-sized PSSs in Figure 2c is located near the sampling site 5, and in circum-hellas region on Mars (Figure 2d), the content chlorite has been detected among these PSSs [10].

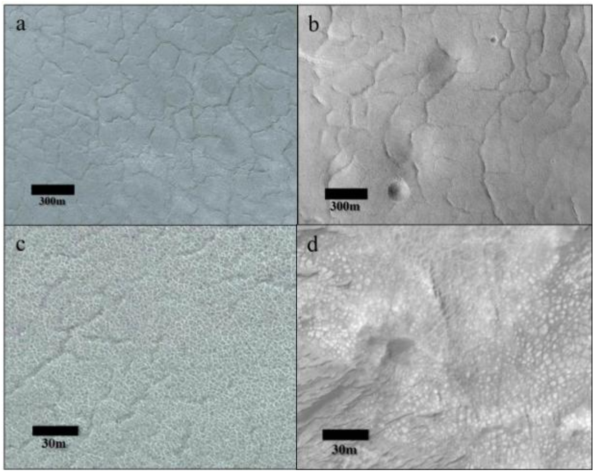

Figure 2. (a) Large sized polygons in Dalangtan palya. (b) Crater Floor Polygons on Mars (HiRISE image subset: PSP_001942_2310_RED). (c) Small sized polygons in Dalangtan playa. (d) Small sized polygons in Circum-Hellas region on Mars (HiRISE image subset: ESP_016259_1535_RED). Image credit for a and c: Google Earth. North is up in all figures.

Discussion: The size and morphology of PSSs in the Qaidam Basin are similar to those PSSs in impact crater floors and depressions with chlorides on Mars (Figure 2). As observed in the Qaidam Basin, most polygons have raised rims, especially those large-sized polygons have remarkable raised rims. The different types of PSSs in the Qaidam Basin reflect distinct enviromental conditions under which they formed. They are most likely the result of desiccation origin. The large (100s of meters in scale) desiccation fractures are in association with intense evaporation and lowering of the water levels [11], revealing an early change of ground water table, particular in Dalangtan region. The evaporation appears to be a key factor in the formation of small sized PSSs. In addition, the higher salt content would limit the scales of PSS formation. The variety occurrence of polygonal terrain in the Qaidam Basin would have undergone a series of stages evolution including drowning of layered salts, evaporative concentration, desiccation and wind erosion, which reveals a possible paleo-environment and subsequent environmental change on Mars.

Conclusions and Future work: We think that salt-rich playas in the Qaidam Basin are the invaluable terrestrial analogs to the chloride-bearing terrains on Mars. As a unique Mars analogue site, the formation mechanism of PSSs within the Qaidam Basin may share a similar mechanism with some crater floor PSSs on Mars. The study of desiccation fractures can reveal climate and environment changes occurring on the Earth and Mars. In the future, we will carry out more field investigation work to gain detailed morphological and chemical information of these PSSs in the Qaidam basin. In addition, the laboratory analysis is also needed.

References: [1] Levy et al. (2009), JGR 114, E01007, doi:10.1029/2008JE003273. [2] El Maarry et al. (2010), JGR 115, E10006, doi:10.1029/2010JE003609. [3] El Maarry et al. (2013), JGR 118, 2263-2278. [4] Wang and Zheng, (2009), LPSC, Abstract #1402. [5] Zheng et al. (2009),. LPSC, Abstract #1454. [6] Zheng et al., 2013, Acta Geologica Sinica, 87(3):885-897. [7] Kong et al. (2013), LPSC, Abstract #1719. [8] Kong et al. (2014), American Mineralogist, 99, 283-290. [9] McEwen et al. (2007), JGR 118, 1245–1256. [10] El Maarry et al. (2014), Icarus, 241, 248-268. [11] Neal. J.T. et al. (1968), Geol. Soc. Am. Bull., 79, 69–90.

Table 1. Summary of XRD Analysis on Samples collected (the values are given as estimated wt %)

	1	2	3	4	5	6	7	8
chlorite	-	-	-	2.83	2.81	1.85	3.33	-
illite	4.37	3.66	-	5.54	5.59	4.87	3.91	7.23
gypsum	-	0.78	2.44	10.95	3.01	1.3	10.53	17.24
quartz	8.39	6.96	5.61	10.08	10.17	8.37	2.39	5.86
feldspar	22.67	18.52	23.82	23.21	16.95	20.97	21.89	16.1
halite	62.82	67.47	66.13	47.38	60.43	58.92	56.82	48.1
calcite	0.93	0.26	0.75	-	0.62	2.69	-	0.54
dolomite	0.81	2.35	1.24	-	0.41	1.03	1.12	4.93

EARTH'S EARLY BIOSPHERE WITHOUT AN OZONE LAYER

YL Li[1] and Kongpeng Lv[1], [1]Department of Earth Sciences, the University of Hong Kong.
(yiliang@hku.hk)

The rise of atmospheric oxygen is the second most important event after the origin of life. The oxygenation of the atmosphere and the ocean triggered the emergence of aerobic respiration that significantly accelerated the evolution of life toward complexity. In the view of the global ecology, the accumulation of atmospheric oxygen led to the formation of an ozone layer that filtered the short wavelengthed UVR from reaching to the surface of Earth. In more than 1.5 billion years of the earliest time, life should have to dwell in the depth of the water column or subsurface to avoid UVR. Our theoretical calculation of several bacterial photosynthetic pigments reveals that those pigments are able to absorb the whole spectrum of UVR. This result suggests that the early life could live in the upper photic zone of seawater or the very surface of the terrestrial environment in the early Archean before the formation of an ozone layer. With the shielding by the photosynthetic cells and their biomats, the terrestrial microbial communities could be developed very early and they might count for a primary productivity higher than previously expected.

YOUNG FLUID ACTIVITY IN THE EARLY SOLAR SYSTEM RECORDED BY APATITE IN A TYPE 3 CARBONACEOUS CHONDRITE.

A. C. Zhang[1,2], Q. L. Li[3], H. Yurimoto[2,4], N. Sakamoto[4], X. H. Li[3], S. Hu[3], Y. T. Lin[3], and R. C. Wang[2], [1]School of Earth Sciences and Engineering, Nanjing University, China (aczhang@nju.edu.cn); [2]Department of Natural History Sciences, Hokkaido University, Japan; [3]Institute of Geology and Geophysics, Chinese Academy of Sciences, China; [4]Isotope Imaging Laboratory, Creative Research Institution Sousei, Hokkaido University, Sapporo 001-0021, Japan.

Introduction: Chondrites are composed of solid materials that have formed in the earliest stage of the solar system. They are unique samples to constrain the physic-chemical conditions and processes in the solar nebula. However, most chondrites were subjected to later fluid-rock interations (i.e., aqueous alteration, metasomatism, and fluid-assisted metamorphism), which changed the mineralogy, chemistry, and isotope compositions of chondrites to various extents [1-2]. It was suggested that the fluid-chondrites interactions could occur in the solar nebula or in the asteroidal settings and could have been driven by different heating sources (i.e., decay of ^{26}Al, heating during accretion of chondritic components tor form asteroidal parent bodies). Dating fluid activities recorded in chondrites is critical to clarify these questions. Previous investigations have dated carbonated minerals, Fe-rich olivine, and magenetite (products of fluid-mineral interactions) by short-lived radionuclide systematics (e.g., ^{53}Mn-^{53}Cr, ^{129}I-^{129}Xe; [2]). They revealed that most alteration events were present in the very early solar system (<15 Myr), although a few studies found that fluid-mineral interaction events could occur at >25 Myr after CAI formation [3]. So far, however, no absolute ages of fluid activities have been reported in the literature. Here, we report the SIMS Pb-Pb isochron age (4450 ± 50 Ma) for apatite in an ungrouped carbonaceous chondrite Dar al Gani (DaG) 978. This is the first absolute age for apatite in carbonaceous chondrites and indicates a young fluid activity in the solar system.

Results: DaG 978 is an ungrouped type 3.5 carbonaceous chondrite [4]. Olivine grains enclosed in Fe-poor, low-Ca pyroxene and those in amoeboid olivine aggregates (AOAs) are Fe-rich. Most chondrules exhibit well-defined chondrule texture; some of them contain glassy mesostasis. However, grain boundary of olivine grains in some AOAs are not visible. In DaG 978, some lath-shaped olivine grains replace low-Ca pyroxene in chondrules or chondrule fragments. Some of lath-shpaed olivine grains contain nepheline, which also occurs as lamellae in anorthite grains in chondrules. Apatite is common in DaG 978. Some of apatite grains are very large, reaching up to 280 μm in size. Three major occurrences of apatite are observed in DaG 978. (1) A few apatite grains occur at the margins of large FeNi metal grains. Phosphate grains included in FeNi metal are mainly merrillite. (2) Abundant apatite grains in DaG 978 are closely associated with altered Ca-Al-rich inclusions (Fig. 1). Many apatite grains have well developed crystal forms. (3) A few anhedral to euhedral apatite grains are set in fine-grained matrix. Some of them exhibit a moniliform distribution. Some apatite grains are closely associated with high-Ca pyroxene and olivine.

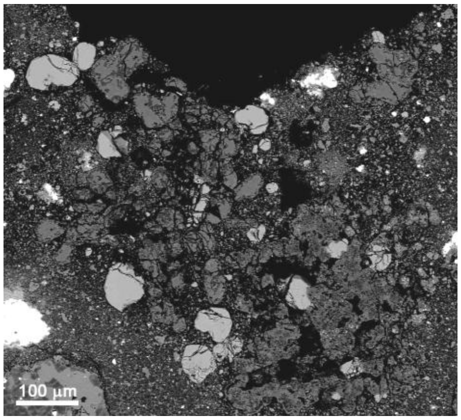

Fig. 1. BSE image of apatite grains (light gray) closely associated with an altered CAI in DaG 978.

Apatite in DaG 978 is highly Cl-rich with a Cl concentration of 4.94-5.61 wt%. The high-Ca pyroxene grains closely associated with apatite contain lower contents of Al_2O_3 and TiO_2 and higher contents of FeO and Na_2O compared with primary high-Ca pyroxene in CAIs in DaG 978. Apatite and its associated diopside show similar oxygen isotope compositions with an average Δ^{17}O value of −1.5 ± 3.2‰ (2σ). Two merrillite grains and nine apatite grains were measured for REE compositions. The two merrillite grains show different REE patterns with one grain having weak and positive Eu anomaly and the other having negative Eu anomaly. However, the apatite grains show similar LREE-enriched REE patterns with consistently positive Eu anomaly although different apatite grains have a variation in the REE concentrations (e.g., La ~26─62 × CI).

The 16 SIMS U-Th-Pb isotope analyses on 13 apatite grains reveal that apatite in DaG 978 contains very low U (<0.178 ppm) and Th (<0.096 ppm). The 16 analyses show a well-defined linear correlation between ^{204}Pb/^{206}Pb and ^{207}Pb/^{206}Pb, giving a ^{207}Pb/^{206}Pb isochron age of 4450 ± 50 Ma (2σ; Fig. 4). Meanwhile, the 3-D least-square fit gives a total Pb/U isochron age of 4448 ± 110 Ma (2σ), well consistent with the $^{207}Pb/^{206}Pb$ isochron age.

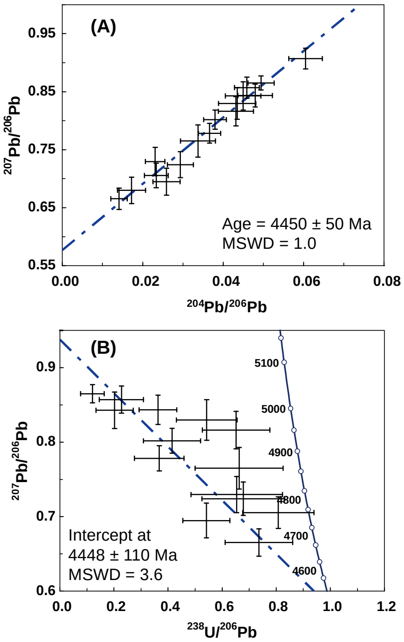

Figure 2. The result of SIMS U-Pb dating of apatite.

Discussion: (1) Formation of apaite through fluid-assisted metamorphism. Apatite is a Cl-rich mineral. Its formation must have been related to fluid activity. However, no phyllosilicate minerals are observed in DaG 978. This indicates that the formation of apatite did not take place at low temperature. Combined with Mg-Fe interdiffusion in olivine and recrystallization of olivine in some AOAs, apatite in DaG 978 should have formed through fluid-assisted metamorphism [5]. The oxygen isotope compositions and REE patterns of apatite generally support this conclusion. The oxygen isotope compositions of apatite and its associated high-Ca pyroxene grains are consistent with those of anorthite and mesostasis in an Al-rich chondrule from DaG 978 [6]; the latter differing from low-Ca pyroxene and olivine in chondrules was interpreted as a result of fluid-assisted metamorphism. The positive Eu anomaly in apatite is similar to that of Ca-phosphate mineral in Allend meteorite and different from those of apatite from highly metamorphosed ordinary chondrites (type 4-6). This might reflect the chemical feature of the fluid from which apatite formed [7-8].

(2) Implications for young fluid activity on carbonaceous chondrite parent bodies. The consistence between the $^{207}Pb/^{206}Pb$ isochron age and the total Pb/U isochron age indicates that the crystallization age of apatite in DaG 978 is 4450 ± 50 Ma. Since apatite in DaG 978 has an origin of fluid-assisted metamorphism, this age has two important implications. First, this age indicates that the fluid activity could have taken place on the parent body rather than in the solar nebula. Second, this age indicates that fluid activity in ESS could have taken place much later than previously thought [2]. Because the crystallization of apatite in DaG 978 post-dates CAI formation by ~120 Ma, it is difficult to explain the formation of fluid by melting of water ice due to decaying heating of short-lived radionuclides. Instead, it is very likely that an impact event at 4450 Ma caused in melting of water ice that could have been buried in the parent body of DaG 978 or a comet impacted and brought fluids into the parent body of DaG 978. Recently, it was noted that many ordinary chondrites and achondrite meteorites recorded shock events at ~4450 Ma [9-12]. The apatite age here implies that the bombardment event at ~4450 Ma in the early solar system might have affected the whole main asteroidal belt.

References: [1] Brearley A. J. (2006) MESS II, 587-624. [2] Krot A. N. et al. (2006) MESS II, 525-553. [3] Tyra M. et al. (2010) *LPSC*, Abstract #2614. [4] Zhang A. C. and Yurimoto H. (2013) *MAPS*, *48*, 1651–1677. [5] Brearley A. J. and Krot A. N. (2013) *MCTR* 659-789. [6] Zhang A. C. et al. (2014) *GCA*, *130*, 78-92. [7] Ebihara M. and Honda M. (1987) *Meteoritics*, 22, 179-190. [8] Jones R. H. et al. (2014) *GCA*, 132, 120-140. [9] Popova O. P. et al. (2013) *Science*, *342*, 1069-1073. [10] Yin Q. Z. et al. (2014) *MAPS*, *49*, 1426-1439. [11] Swindle T. D. et al. (2014) *GSLSP*, 378, 333-347. [12] Bottke W. F. et al. (2015) *Science*, 348, 321-323.

Lifetime of the Solar Nebula Constrained by Meteorite Paleomagnetism and Delayed Onset of a Planetesimal Dynamo

Huapei Wang
Department of Earth, Atmospheric, and Planetary Sciences
Massachusetts Institute of Technology, Cambridge, Massachusetts, USA

Formation of planets largely takes place in the gas-rich solar nebular and protoplanetary disks. Nebular magnetic fields are thought to play a dominant role in global disk evolution by driving angular momentum transport via the magneto-rotational instability and/or magnetized disk winds. Previous paleomagnetic analyses of the Semarkona meteorite found evidence for a ~5-50 μT solar nebular field at ~2-3 My after the formation of calcium-aluminum-rich inclusions (CAIs; ~4568 Ma), which consist of the first solids condensed from the cooling protoplanetary disk. A key remaining question is the lifetime of the solar nebula. To address this, we analyzed the paleomagnetism of angrites, a class of exceptionally well-preserved igneous rocks that retain magnetic records at ~4 My and ~11 My after CAI formation. Our paleomagnetic data of volcanic angrites (D'Orbigny and SAH 99555; 4564.4 Ma) show that the background magnetic field at the angrite parent body region was < 0.3 μT at ~4 My after CAI formation. Because a strong nebular magnetic field was likely present throughout most of the gaseous disk lifetime, our results suggest that the solar nebula had already dispersed by ~4 My after CAI formation. This dispersal time agrees with typical protoplanetary disk lifetimes inferred from infrared excesses for Sun-like protostars. Our results suggest that the formation of the solar system giant planets, as well as the gas phase planetary migration, had largely completed by ~4 My after CAI formation. Furthermore, the formation of chondrules after this period would have not required substantial magnetic fields or nebular gas, thereby favoring planetesimal collision models over nebular shocks and magnetic reconnection. On the other hand, our data of plutonic angrite Angra dos Reis (4557.7 Ma) show that it was formed in the presence of a strong magnetic field of 17 μT probably from a core dynamo at ~11 My after CAI formation. This indicates that the angrite parent body dynamo originated between ~4 and ~11 My after solar system formation. Our paleomagnetic results are consistent with planetesimal evolution models calling for dynamos delayed by at least several million years after core formation. In particular, thermal blanketing effects from ^{26}Al decay in the mantle could initially suppress core convection and dynamo process after planetesimal differentiation.

Opx Enriched Lodranite, Y 983119: Cummulate Rock from Acapulcoite-Lodranite Parent Planetesimal?

M. Yasutake[1, 2] and A. Yamaguchi[1, 2], [1]SOKENDAI (Graduate University for Advanced Studies), Shonan Village, Hayama, Kanagawa 240-0193 Japan, [2]National Institute of Polar Science, 10-3, Midori-cho, Tachikawa-shi, Tokyo 190-8518, Japan, e-mail; yasutake.masahiro@nipr.ac.jp

Introduction: Primitive achondrites show achondritic textures, but have relatively chondritic bulk chemical features. It is thought that primitive achondrites are residual rock formed in planetesimals. Acapulcoites-lodranites clan are the largest group of primitive achondrites. They suffered few% to <20% partial melting. Continuous chemical compositions and O-isotopic compositions indicate that they formed in the same parent body which experienced various degree of heating and partial melting [1]. Therefore they are suitable sample to better understand evolutionary history of a planetesimal.

Yamato (Y) 983119 is an Antarctic meteorite classified into a lodranite [2]. Although its molar mg ratio of pyroxene and olivine, and O-isotopic compositions are within the range of acapulcoites and lodranites, it is unusually enriched in orthopyroxene (Opx) and depleted in olivine. We examined petrology and mineralogy of this meteorite in detail, and we will discuss the origin of this meteorite.

Samples and Methods: We prepared the samples from 2 sampling places which are opposite positions of main mass, and we analyzed one polished thin section of Y 983119, (51-2) and two polished thick sections (51 and 35). These samples are observed by an optical microscope and FE-SEM (JEOL JSM-7100F) at National Institute of Polar Research. Elemental maps were obtained by an EDS-system (Oxford AZtec Energy) equipped with FE-SEM. Modal abundances of each sample were obtained from elemental maps by using of a free software ImageJ (National Institute of Health). Chemical compositions of constituent minerals were obtained by EPMA (JEOL JXA-8200).

Result: Y 983119 has a coarse-grained texture (~0.5-2.0 mm) and composed of mainly Opx and plagioclase, and minor kamacite, taenite, olivine, troilite and augite, and traces of phosphate, chromite and schreibersite. In the 51-2 and 51, Opx is unusually enriched up to about 70% and olivine is depleted (Fig. 1). On the other hand, olivine is relatively abundant in the 35. Opx has a rounded or tabular shape and some grains have zigzagged rim. Most of them contain numerous augite inclusions (few tens of μm in size) and thin lamellae. There are rare augite inclusions partly surrounded by K, Al, Si-rich glass in Opx. Olivine and augite show an amoeboid shape. Most of olivine have rim which seems that it is consumed after crystallization. Moreover, few olivine grains are penetrated by plagioclase and troilite. Plagioclase is distributed interstitially. Some of them enclose olivine and Opx grains. These observations show that plagioclase melt and plagioclase crystallized followed by olivine and pyroxene.

Compositions of mafic silicates are within the ranges of acapulcoites and lodranites: Opx (Wo2 En94 Fs4), augite (Wo45 En53 Fs2) and olivine (Fa3). However, the Mg/Mn ratios of Opx are significantly higher (molar Mg/Mn = 189) than the other acapulcoites and lodranites (molar Mg/Mn = ~100-120). These results indicate that olivine and Opx are more residual than others [3]. Plagioclase has relatively anorthitic composition (Or1.7 Ab69.6 An28.7) than those of the others (An~10-20). Based on Ni content of taenite, Y 983119 had cooled by 100-1000 ℃ / Ma.

Conclusion: Y 983119 has remarkable features. Modal composition and texture are similar to cumulate rock. On the other hand, compositions of constituent minerals show properties of residual rock. It is certain that the formation process of Y 983119 is not only common process which makes residual rocks. More detailed study is needed to determine origin of this meteorite.

References: [1] C. Floss (2000) Meteorit and Planet. Sci., 35, 1073-1085 [2] Yamaguchi et al., (2012) Meteorite Newsletter, vol. 21 [3] Goodrich and Delaney (2000), Geochim. et Cosmochim. Acta, 64, 149-160

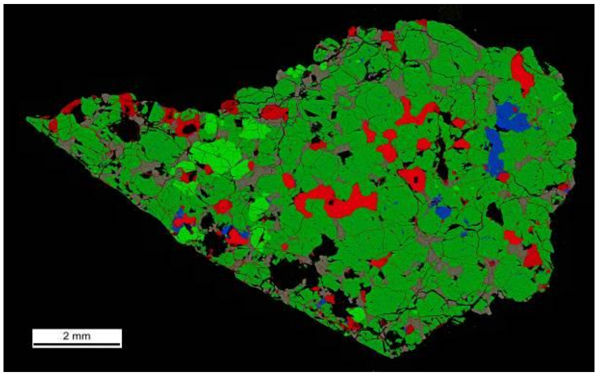

Figure 1. False colored elemental distribution image of Y 983119, 51-2. In this image Opx is showed in dark green. Red: Fe, Green; Mg, Blue; Ca, Yellow; Al.

THE USE OF METAL ISOTOPES TO TRACE PLANETARY PROCESSES.

L. Qin[1], J. Xia[1,2,3], R. W. Carlson[2] and Q. Zhang[1]. [1]CAS Key Laboratory of Crust-Mantle Materials and Environment, University of Science and Technology of China, 96 Jinzhai RD., Hefei, Anhui 230026, China; [2] Department of Terrestrial Magnetism and [3]Geophysical Laboratory, Carnegie Institution of Washington, Washington, DC 20015, USA. (E-mail: lpqin@ustc.edu.cn)

Introduction: With recent advancements in mass spectrometry, unprecedented precisions have been achieved on metal stable isotopic mesurements. The metal stable isotopes have become increasingly useful tools for tracing planetary and terrestrial processes. Chondrites are often used as reference materials for studying the chemical and isotopic composition of the Earth. Differences in the stable isotope composition of metal elements between meteorites and the bulk-silicate Earth (BSE) have been interpreted to reflect isotopic fractionation during the course of planetary formation and differentiation [1-6]. For example, the difference in stable isotopic composition of some refractory elements such as Si and Mo were interpreted to reflect core-mantle differentiaton [5,7]. The difference in stable isotopic composition of elements with varying degrees of volatility were attributed to isotopic fractionation due to volatility [e.g. 8]. In addition, the study of stable isotopic composition of metal elements also adds another dimention to the study of mass-independent isotopic effect, as large mass fractionation of some meteoritic materials relative to terrestrial laboratory standards could potentially affect the accuracy of the measured non-mass dependent effects [9]. Recently, there are debates on the Cr stable isotopic composition of chondrites [10, 11].

Analytical Methods: The addition of double-spike to the sample to monitor and correct mass fractionation generated during chemical purification procedure and during mass spectrometry measurements has so far yield the most promising outcomes on determinations of stable isotopic composition of metal elements with ≥4 isotopes. For MC-ICP-MS measurements, molecular isobaric interferences associated with Ar (e.g. ArN^+, ArO^+, and ArC^+) on Cr isotopes were usually unavoidable. However these molecular isobaric interferences are not concerns for TIMS measurements. In addition, TIMS are superior to MC-ICP-MS in terms of measurement stability. In this work, we seek to minimize potential analytical artifacts on Cr stable isotope measurements of meteorites by combining the ^{50}Cr-^{54}Cr double-spike technique and thermal ionization mass spectrometry (TIMS). The details of our method can be found in [12]. The long-term reproducibility of NIST SRM 979 standard over a period of one year is 0.035‰.

Both the unspiked Cr isotope ratios and the spiked ratios were used to calculate the absolute Cr isotope abundances, from which radiogenic effects on ^{53}Cr/^{52}Cr were subsequently subtracted to calculate mass-dependent isotope effects on ^{53}Cr/^{52}Cr. Becauuse the radiogenic effects are often very limited for most meteorites except for HEDs, the correction to ^{53}Cr/^{52}Cr are usually not significant. The reported Cr isotope data (δ^{53}Cr, relative deviation of ^{53}Cr/^{52}Cr in the sample from the standard times 1000) thus soley reflect the mass-dependent isotope effects.

Results and discussions: All measured chondrites have δ^{53}Cr values within the range (~ -0.2 to 0 ‰, [13]) observed previously for mantle-derived rocks from various mantle reservoirs. Martian and lunar meteorites/samples also show similar Cr isotopic composition with the terrestrial rocks. Our new bulk meteorite Cr isotope data suggest that there is no significant difference between major planetary reservoirs. Thus the new data do not require fractionation of Cr stable isotope composition during Core formation. These results provide evidence for a homogenous inner solar nebula. However, enstatite chondrites show slightly higher δ^{53}Cr values than carbonaceous and ordinary chondrites. The reason needs to be further investigated. Eucrites/diogenites have more negative δ^{53}Cr values than chondrites and mantle-derived rocks. The δ^{53}Cr values of eucrites/diogenites roughly correlate with the MgO contents, and thus might reflect crystallization of pyroxene, as Cr is incompatible in olivine. More work will be conducted to further understand the Cr isotopic variations in meteorites. So far, the silicate Earth and chondrites have similar stable isotope compositions in Mg, Fe and Cr, but different Si, Ni, Cu and Zn isotopic compositions. Any Solar System accretional model needs to accommodate these isotopic results.

References:

[1] Poitrasson F. et al. (2004) *EPSL, 223*, 253-266.
[2] Poitrasson F. et al. (2005) *EPSL, 234*, 151-164.
[3] Regelous M. et al. (2008) *EPSL, 272*, 330-338.
[4] Shahar A. et al. (2009) *GCA, 75*, 7688-7697.
[5] Fitoussi C. et al. (2009) *EPSL, 287*, 77-85.
[6] Chakrabarti R. et al. (2010) *GCA, 74*, 6921-6933.
[7] Burkhardt. C. (2014) *EPSL, 391*, 201-211.
[8] Paniello R. C. (2012) Nature, 490, 376-379.
[9] Qin L. et al. (2010) GCA, *74*, 1122-1145.
[10] Moynier F. et al. (2011) *Science, 331*, 1417-1420.
[11] Schiller M. et al. (2014) *JAAS, 29*, 1406-1416. [12] Shen J. et al. (2015) *G^3, 16*, 3840-3854.
[13] Schoenberg R. et al. *CG, 249*, 294-306.

NanoSIMS analytical methods for extraterrestrial samples.

W. Yang[1], S. Hu[1], J. C. Zhang[1], J. L. Hao[1], and Y. T. Lin[1], [1]Key Laboratory of Earth and Planetary Physics, Institute of Geology and Geophysics, Chinese Academy of Sciences, Beijing 100029, China; yangw@mail.iggcas.ac.cn

Introduction: Several analytical methods for extraterrestrial samples have been established with the NanoSIMS at Institute of Geology and Geophysics, Chinese Academy of Sciences. These methods include trace element distribution images in mineral zoning, high spatial resolution (2-5 µm) Pb-Pb and U-Pb dating, water content and H isotopic analysis for silicate glass and apatite, C isotopic analysis for diamond and graphite, O isotopic analysis for carbonate, S isotopic analysis for sulfides.

Trace element analysis of mineral zonings: A 100 pA O^- primary ion beam with a diameter of approximately 0.7 µm was utilized. A 20 × 20 μm^2 area was scanned and secondary ion images were acquired. Then based on the images, spot analyses were carried out by deflecting the primary beam onto a selected area (3 × 3 μm^2). This method can observe the trace elemental distributions of mineral zonings at micron or sub-micron scales, which has at least three advantages: (1) high spatial resolution, the size of the O- ion beam is as small as 0.7 µm; (2) low detection limit, trace element of g/g level can be quantitatively measured; (3) precise positioning, based on the secondary ion images acquired before spot analysis, interference of fractures and micro mineral inclusions can be avoided.

High Spatial resolution zircon U-Pb/Pb-Pb dating: A 500 pA O^- primary ion beam with a diameter of 1.7 µm was utilized. Magnetic peak-switching mode was applied for Pb-Pb dating, while combined analysis mode was used for U-Pb dating [1]. This method demonstrated that zircon U-Pb dating at < 5 µm scale and Pb-Pb dating at < 2 µm scale can be achieved with NanoSIMS. However, there is a limitation: the sensitivity of Pb is about 4 cps/ppm/nA, which is significantly lower than that of IMS-1280 (13 to 21 cps/ppm/nA) by using oxygen flooding technique. Due to this limitation, this method can only be applied to old zircons, such as ~2.0 Ga [2].

Water content and H isotope analysis for silicate glass and apatite: A 500 pA Cs^+ primary beam with a diameter of 1µm was used. The scanning area was 10×10 μm^2. The outmost 50 % areas of the spots were blanked to decrease the H re-deposition effect around the analytical margins. The analysis standards include 2 apatites and 5 basaltic glasses (1833-1, 1833-11, ND 70-01, 519-4-1 and MORB glasses). The analytical precisions of H isotopes for Kovdor apatite (H_2O =0.98 wt.%) and MORB glass (H_2O =0.258 wt.%) are 40 ‰ (2SD) and 61 ‰ (2SD) [3], respectively. The maximum uncertainty of the slopes of the water content calibration curves is lower than 6.9 % (2SD).

Carbon isotope analysis for diamond and graphite: Two instrumental configurations were carried out for different requirements (3-10 µm) (1) FC-EM mode: ^{12}C and ^{13}C were measured with the FC and the EM, respectively. A 100 pA Cs^+ primary beam with a diameter of 0.5 µm was used to raster over an area of 3×3 μm^2. The precision of $\delta^{13}C$ on the graphite standard was ~0.4‰.(2) FC-FC mode: Both of ^{12}C and ^{13}C were measured with the FCs. A 800 pA Cs^+ primary beam with a diameter of 1 µm was used to rater over an area of 10×10 μm^2. The precision of $\delta^{13}C$ on the graphite standard was ~0.3‰.

Oxygen isotope analysis for carbonate: A 250 pA primary Cs^+ beam with a diameter of ~0.5 µm was used to scan 5 × 5 μm^2 area. $^{16}O^-$ is counted with a FC, and $^{18}O^-$ with an EM. Two reference materials of calcite NBS 18 ($\delta^{18}O_{VPDB}$ = -23.2 ± 0.1‰) and IAEA-CO-8 ($\delta^{18}O_{VPDB}$ = -22.7 ± 0.2‰) were used as standards. The analytical precision is better than 0.5‰ (1 SD) [4].

Sulfur isotope analysis for sulfides: Three instrumental configurations were carried out [5]. (1) FC-FC-FC-EM mode: High analytical precision was achieved by counting ^{32}S, ^{33}S and ^{34}S with FCs and ^{36}S with EM. A 400 pA Cs^+ primary beam with a diameter of 1 µm was used to scan over areas of 5 ×5 μm^2. The standard deviations of spot-to-spot and grain-to-grain (external reproducibility 1 SD) measurements were better than 0.3, 0.3 and 0.7 ‰ for $\delta^{33}S$, $\delta^{34}S$ and $\delta^{36}S$, respectively. (2) FC-EM-EM-EM mode: ^{32}S was measured with the FC and the other signals were measured with the Ems. A 7 pA Cs^+ primary beam with a diameter of 0.3 µm was used to scan over areas of 2 ×2 μm^2. The external reproducibility (1SD) was better than 0.5‰ for both $\delta^{33}S$ and $\delta^{34}S$ and was 1.5‰ for $\delta^{36}S$. (3) EM-EM-EM mode: ^{32}S, ^{33}S and ^{34}S were measured with Ems. A 0.7 pA Cs^+ primary beam with a diameter of 0.1 µm was used to scan over areas of 1 ×1 μm^2. The external reproducibility (1 SD) was better than 1‰ for both $\delta^{33}S$ and $\delta^{34}S$.

References: [1] Yang et al. (2012) *Journal of Analytical Atomic Spectrometry*, 27(3): 479-487. [2] Wang et al. (2014) *Precambrian Research*, 251(0): 181-196. [3] Hu et al. (2014) *Geochimica et Cosmochimica Acta*, 140(0): 321-333. [4] Lin et al. (2014) *Journal of Analytical Atomic Spectrometry*, 29(9): 1686-1691. [5] Zhang et al. (2014) *Journal of Analytical Atomic Spectrometry*, 29(10): 1934-1943.

The occurrence and mineralogy of iron-rich spherules of Taihu lake suggest they likely were airburst fallout rather than groundwater colloidal deposition.

Shuhao Zuo[1] and Zhidong Xie[1], [1]State Key laboratory for Mineral Deposits Research, School of Earth Sciences and Engineering, Nanjing University, Nanjing, China, zuoshuhao@smail.nju.edu.cn, zhidongx@nju.edu.cn

Introduction: Iron-rich concretions including spherules occur in the vicinity of Taihu lake, Southeast of China. Their formation is the key to answer the origin of Taihu lake basin. Many hypotheses of the basin origin were proposed, such as lagoon， tectonics，impact [1-4]. Abundant iron-rich spherules were reported in the bottom of Taihu lake as Fe-Mn concretions [5]. Wang and others suggested that Fe-rich concretions including Iron-rich spherules were ejecta [4]. Huang and Liu stated these concretions were the limonite concretions from groundwater [6]. This paper is to discuss the origin of the Iron-rich spherolitic concretions whether it is related to an airburst fallout deposition, or a groundwater colloidal deposition in mud layer [7, 8].

Occurrence: The mud layer containing Iron-rich concretions was sandwiched between bottom hard loess and top modern mud, and can be found almost everywhere in the vicinity of Taihu lake. The C14 age of the specific mud layer with concretions is about 7kyr-8kyr [7, 8]. The hard loess as lower sandwich slice has the age of ~11kyr- 20kyr [5]. The modern mud layer as upper slice has the age of ~3kyr-4kyr [9]. The longitudinal age discontinuousness and lateral scattering continuousness of the mud layers indicate that the formation of the layer bearing iron-rich concretions were more likely related to one event in a short time.

Mineralogy: The microstructure and mineralogy of the iron-rich spherules are not similar to Fe-Mn concretions and limonite concretions. The spherules have typical sizes ranging from half to 3 mm with a 10-20 micron shell. SEM images show the spherules consist of iron-rich cement, angular quartz grains and clay minerals. EDS data indicates the elements of the iron-rich cement contain Fe, O, Si, Al and C. Powder XRD confirmed that minerals in spherules include quartz, siderite, limonite, feldspar, clay, and element carbon. HRTEM results are consistent to SEM and XRD results, and show many aggregates of several tens nanometer minerals and abundant sub-micron element carbons in spherules. Based on observation, iron-rich spherules are more likely formed by accretion of small solid particles within an airburst vapour plume [7, 8], rather than groundwater colloidal deposition.

References: [1] Chen et al. (1959) Acta Geogr. Sin 25(3): 201-220. (in Chinese) [2] Huang et al. (1965) Oceanol Limnol Sin 7(4): 396-426.(in Chinese) [3] Wang, et al. (1993) Chin. Sci. Bull. 39(5): 149-423. [4] Wang et al. (2009) Geol. J. China Univ 15: 437-444. (in Chinese) [5] Sun and Wu (1987) Chin. Sci. Bull 12:1329-1339. [6] Huang et al., 2012. Geol. J. China Univ 18(2): 379-389. (in Chinese) [7] Xie et al. (2015) LPSC 1754.pdf. [8] Xie et al. (2015) MAPS 5183.pdf. [9] Liu et al. (1996) Acta Palaeontol. Sin 129-135.(in Chinese)

Dawn at Ceres. Jian-Yang Li[1], and Dawn Science Team, [1]Planetary Science Institute, 1700 E. Ft. Lowell Rd., Suite 106, Tucson AZ 85719, USA (jyli@psi.edu).

Dawn started its rendezvous with Ceres from April 2015, and expected to stay in orbit until at least the end of June 2016. Since its arrival, Dawn has been providing new insights into the surface composition, near-surface and interior structure of this mysterious dwarf planet, with implications for its formation and evolution. The surface of Ceres is clearly heterogeneous in terms of albedo and colors, and the major color units are correlated with different geomorphologies and may indicate some level of geographical variation in subsurface composition, as well as the aging processes on the surface. The confirmation of prevailing ammoniated phyllosilicates on Ceres suggests its unusual formation and/or evolutionary history. The surface morphology of Ceres shows evidence for limited topographic relaxations except in some local areas. Craters with central pits resemble those on ice objects. Flow features are also identified on Ceres, probably generated by impact melt in ice-rich surface. The distinct geomorphology the Ahuna Mons is possibly related to cryovolcanism. The distribution of hydrogen, which is likely related to water ice, shows an increasing trend with latitude. However, the lack of global relaxation of craters with respect to latitude seems to suggest a surface that is less viscous than a water ice rich surface. All the discoveries suggest that Ceres' interior characteristics are probably between a rocky planet like the Moon and Vesta, and an icy moon in the outer solar system, and it has gone through a much more complex evolution than we had understood.

Local space weathering mapping on Itokawa based on the AMICA close-up images.

E. Tatsumi[1], N. Hirata[2], S. Koga[1], and S. Sugita[1], [1]Dept. of Earth and Planetary Science, Univ. of Tokyo (tatsumi@astrobio.k.u-tokyo.ac.jp), [2]Dept. of Computer Software, Univ. of Aizu.

Introduction: The Japanese spacecraft Hayabusa revealed surface structures on Itokawa with its high-resolution CCD camera with seven band filters (ul: 381 nm, b: 429 nm, v: 553 nm, w: 700 nm, x: 861 nm, p: 960 nm, zs: 1008 nm) called AMICA (Asteroidal Multi-band Imaging CAmera) [1]. Spectralscopy provides on mineralogical and chemical information. Space weathering is one of the most important properties obtained from spectral analyses. Evaluating the degree of space weathering provides the variation of local exposure duration to the space on an asteroid. Global space weathering maps of Itokawa using 4 datasets which were observed during the Gate Position (GP) phase (15 – 20 km away) have been generated [1, 2].

Detailed analyses of inflight data have revealed that the scattered light inside the optics of AMICA may change the spectral intensity by a few tens percent especially for longer wavelengths [1, 3]. The light contamination may influence our estimates for space weathering, which is evaluated by the intensity ratio between the different bands. Thus, the spectral analyses using AMICA data need a proper correction for scattered light. Correction of the scattered light for global images of ~2 m/pix with large blank area around Itokawa has been proposed subtracting the dim halos of the Moon and Itokawa [3]. However, the correction of high-resolution images is more difficult because their perspectives do not include the edge of whole Itokawa and the same method cannot be applied. In this study, we propose the scattered light correction of high-resolution AMICA images up to ~0.5 m/pix taken from Home Position (HP; ~7 km away) using synthesized images from the shape model. After removing the scattered light, we evaluate the space weathering on Itokawa with multi-band images.

Correction of the scattered light: A high-resolution shape model of Itokawa was constructed from AMICA images by applying multi-image photoclinometry [4]. AMICA raw data and the shape model are archived by NASA/Planetary Data System. Any perspective and illumination condition can be simulated with the shape model by applying Hapke's light scattering model on asteroids [5]. We chose images in Table 1 and constructed synthetic images simulating the perspectives and the illumination condition based on the SPICE kernel (Fig. 1). Once the synthetic global image is obtained, we can conduct the same procedure as the global map cases in [3].

Next, we made convolution images from the synthetic image with the attenuation function, the summation of Gaussian functions derived by [3], and simulated the scattered light for each band image (Fig. 2). Finally, we subtracted the scattered light. Figure 3 shows before and after the correction for a p-band (960 nm) image which has large scattered light. In the space area the scattered light attributed up to ~20 % of intensity which could change color map drastically. However, after the correction the intensity residual is at a-few-percent level of Itokawa's body area.

Table 1 The AMICA image sets used in this study.

	Image	Date	Resolution
(A)	ST_2486640220_b ST_2486649845_v ST_2486659453_w ST_2486669110_p	2005/10/24	~0.5 m/pix
(B)	ST_2487331445_b ST_2487335302_v ST_2487339240_w ST_2487343619_p	2005/10/24	~0.5 m/pix

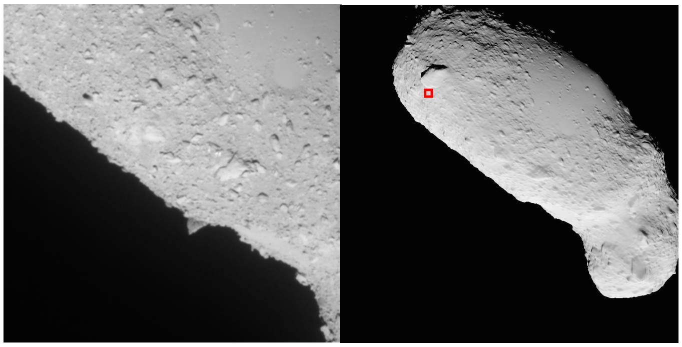

Fig 1. The AMICA image of ST_2486669110 (Left) and the synthetic image of ST_2486669110 (Right).

Local space-weathering maps: The principal component analysis has been conducted for global multi-band imagesets (ul, b, v, w, x, p) and the first principal component (PC1) was supposed to indicate reddening trend corresponding to the characteristic of space weathering [2]. After the scattered light correction and coregistration between multi-band images, the maps of space weathering are acquired by taking an inner product for each point with PC1' vector, which has only four components (b, v, w, p) from PC1 vector because the high-resolution images were taken only with these filters.

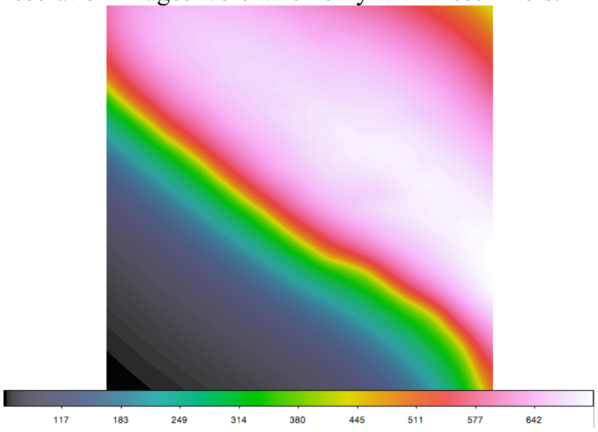

Fig 2. Simulated scattered light by convolving the synthetic image with the attenuation function [3].

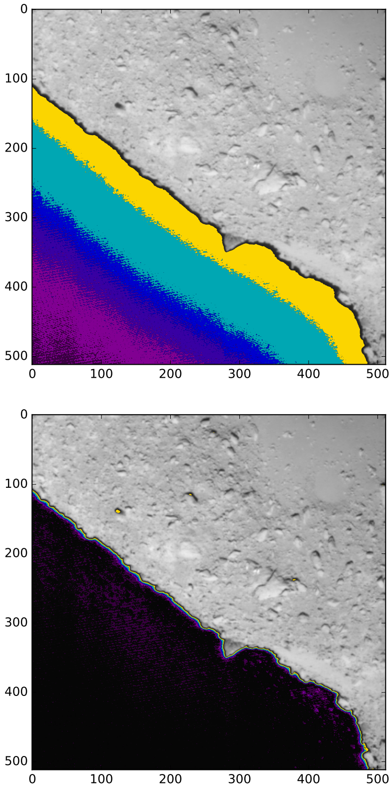

Fig. 3 Contour maps of before (top) and after (bottom) the correction of scattered light for a p-band image (ST_2486669110). Violet area and yellow area indicate 1% and 20% level intensity of Itokawa, respectively. After the correction, the intensity residual is at the 1% level of Itokawa.

Discussions: Figure 4 shows the space weathering maps using the datasets in Table 1. Itokawa shows a non-uniform surface in space weathering from place to place. Several circular morphologies which are fresher areas than the surrounded areas could be impact craters (circles). Interestingly, the center areas of these features are more space weathered. This might suggest the regolith migration [6]. The Muses-C regio (Fig. 4 (b)) shows the gradual change in space weathering degree from high to low which is also possibly caused by regolith migration along a potential gradient towards low potential area (arrows).

Conclusions: The removal of the scattered light in the AMICA high-resolution images (~0.5 m/pix) taken from HP has been conducted by synthesizing the image from the shape model. The scattered light could greatly change the color maps of Itokawa and has to be removed before spectral analyses. Local space-weathering maps are derived from corrected images and the possible regolith migrations are found.

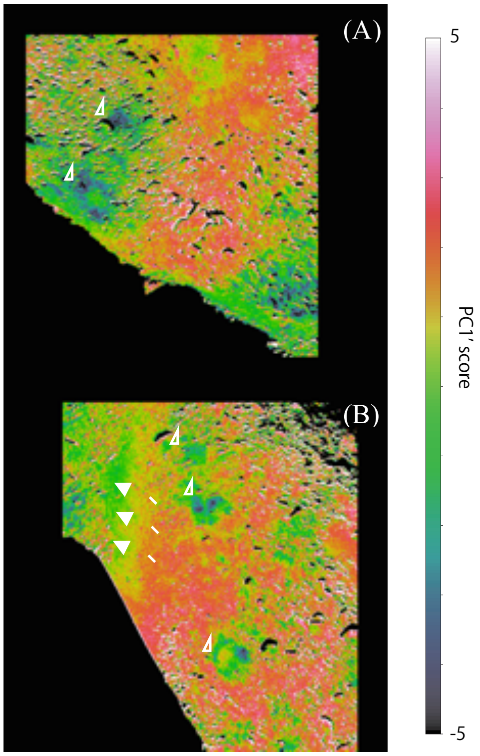

Fig. 4 Local space-weathering maps (PC1' maps) using the datasets (A) and (B) in Table 1. Larger PC1' score indicates more space-weathered.

References: [1] Ishiguro, M. et al., MAPS 42, pp. 1791-1800, (2007). [2] Koga, S. et al., 45th LPSC, #1721, (2014). [3] Ishiguro, M., Publ. Astron. Soc. Japan 66, 55, (2014). [4] Gaskell, R. et al., NASA PDS, (2008). [5] Hapke, B., "Theory of Reflectance and Emittance Spectroscopy", Cambridge University Press, (2012). [6] Miyamoto, H., Science 316, pp. 1011-1014, (2007).

BOULDERS AND CRATERS ON 4179 TOUTATIS AS CLOSELY FLEW BY CHANG'E-2.

Y. Jiang[1], J. H. Ji[1], J. C. Huang[2], S. Marchi[3], Y. Li[4] and W.-H. Ip[4]. [1]Key Laboratory of Planetary Sciences, Purple Mountain Observatory, Chinese Academy of Sciences, Nanjing 210008, China. yjiang@pmo.ac.cn. [2]China Academy of Space Technology, Beijing 100094, China. [3]Southwest Research Institute, Boulder, Colorado 80302, USA. [4]Space Science Institute, Macau University of Science and Technology, Taipa, Macau.

Introduction: On 13 December 2012, Chang'E-2 flew by Asteroid 4179 Toutatis successfully after it accomplished its primary objective (performing lunar exploration) and an extended mission (performing space-environment exploration at the Sun-Earth Lagrangian point). This is the first flyby of an asteroid for China, and is expected to open the door to deep space exploration of asteroids. This flyby at a closest distance of 770 ± 120 m (3σ) allows human for the first time, perhaps the last time, to observe detailed morphology of Toutatis, although only ~ 45% of Toutatis' surface was imaged [1-3]. We identified boulders and craters on the surface of Toutatis according to a series of optical images captured by Chang'E-2, and compared them with those of other asteroids like Eros and Itokawa, in order to dig out important clues for the formation and evolution of Toutatis.

Results: A total of 222 boulders are counted over the imaged area (~ 6.68 km^2), with geometric mean sizes from 10 to 61 m, with an average of 22 m (Fig. 1). Approximate 90% of boulders are less than 30 m in size. As far as the number density of boulders (> 20 m) is concerned, Toutatis (~ 17/km^2) has higher surface density of boulders than Eros (~2/km^2), but lower than Itokawa (~ 30/km^2). The cumulative size-frequency distribution (SFD) per unit area exhibits a slope (power-index) of -4.4 ± 0.1 for boulders > 20 m, since the distribution rolls over at < 20 m due to incompletely counting. In addition, head and body give slopes of cumulative SFD of boulders above 20 m as -3.9 ± 0.2 and -4.5 ± 0.1, respectively.

Discussion: For Toutatis, all boulders with sizes 20-60 m exhibits a cumulative SFD slope of -4.4 ± 0.1. This slope is significantly steeper than that of Eros (-3.2) boulders with sizes 15-80 m and that of Itokawa (-3.3 ± 0.1) boulders with sizes 6-38 m [4, 5]. The steep slope for Toutatis implies that boulders may have experienced high degree of fragmentation.

Boulders on small rocky bodies are generally produced by impact cratering or/and catastrophic disruption of the parent body. During impact cratering, the ejected fragment is associated with the corresponding source crater. For Toutatis, the source crater for the largest boulder (~ 61 m) is ~ 2570 m, which is four times larger than the largest impact crater (~ 530 m) identified on Toutatis. Therefore, we infer that the largest boulder is not produced by the impact cratering. Further, the ratio of the total volume of boulders to the total excavated volume of craters on Toutatis is as high as ~ 10%, which is a bit smaller than Itokawa (25%), but far more than Eros (0.4%). These results imply that most boulders cannot only be produced during impact cratering on Toutatis. Many boulders especially larger than 20 m ones are probably surviving fragments from the parent body of Toutatis, accreted after its breakup.

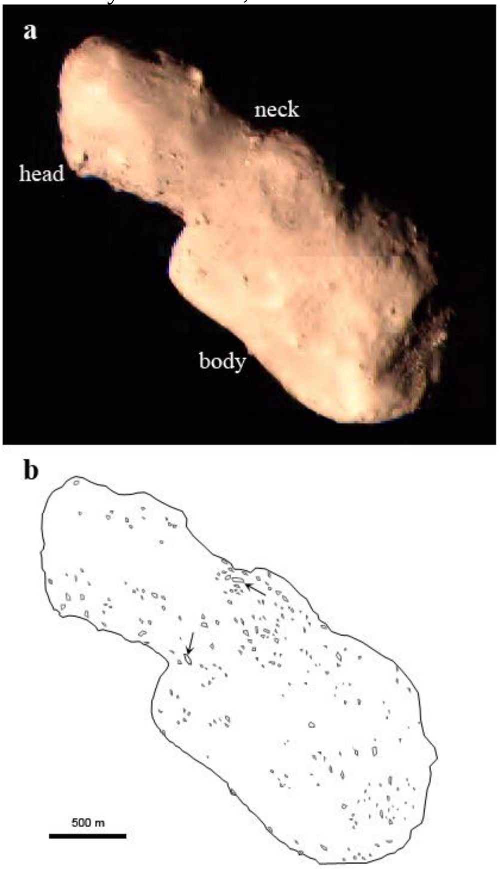

Fig 1. The distribution of boulders on the surface of Toutatis.

References:

[1] Huang, J. C. et al. 2013, Scientific Reports, 3, 3411. [2] Zhao, Y. H. et al. 2015, MNRAS, 450, 3620. [3] Jiang, Y. et al. 2015, Scientific Reports, 5, 16029. [4] Thomas, P. C. et al. 2001, Nature, 413, 394. [5] Mazrouei, S. et al. 2014, Icarus, 229, 181.

DEVELOPMENT AND INITIAL OPERATION OF HAYABUSA2 LIDAR. T. Mizuno[1,2], H. Senshu[3], H. Noda[4], R. Yamada[4], N. Namiki[2,4], S. Oshigami[5], T. Kase[6], T. Shiina[6], M. Mita[1], H. Kunimori[7], M. Kobayashi[3], N. Ogawa[1], N. Hirata[8], F. Yoshida[4], F. Terui[1], Y. Mimasu[1], S. Abe[9], H. Araki[4], Y. Ishihara[1], K. Matsumoto[2,4], H. Takeuchi[1], C. Moore[10], A. Pollard[10], T. Yamaguchi[1], T. Saiki[1], Y. Tsuda[1], [1]Japan Aerospace Exploration Agency, Department of Space and Astronautical Science (3-1-1 Yoshinodai Chuo-ku, Sagamihara, Kanagawa 252-5210, Japan), [2]School of Physical Sciences, SOKENDAI (The Graduate University for Advanced Studies), [3]Planetary Exploration Research Center, Chiba Institute of Technology (2-17-1, Tsudanuma, Narashino, Chiba, JAPAN 2-17-1, Tsudanuma, Narashino, Chiba, 275-0016, Japan), [4]National Astronomical Observatory of Japan, (2-21-1, Osawa, Mitaka, Tokyo, 181-8588, Japan), [5]Kougakuin University (1-24-2 Nishi-Shinjuku, Shinjuku-ku, Tokyo 163-8677, Japan), [6]NEC Corporation (1-10 Nisshin-cho, Fuchu, Tokyo 183-8501, Japan), [7]National Institute of Information and Communications Technology (4-2-1 Nukui-kitamachi, Koganei, Tokyo 184-8795, Japan), [8]University of Aizu, Research Center for Advanced Information Science and Technology (Aizu-wakamatsu, Fukushima 965-8580, Japan), [9]College of Science and Technology, Department of Aerospace Engineering, Nihon University (7-24-1, Narashinodai, Funabashi, Chiba 274-8510, Japan), [10]Space Environment Research Centre (AITC2 Mount Stromlo Observatory, Cotter Road, Weston Creek, ACT 2611, Australia).

Introduction: The Japanese asteroid explorer Hayabusa2 was launched on 3 December 2014 on an H-IIA launch vehicle from the Tanegashima Space Center. Hayabusa2 is supposed to observe the near-Earth C-type asteroid 162173 Ryugu (1999 JU_3) and brings surface material samples back to Earth in 2020. The light detection and ranging (LIDAR) laser altimeter on Hayabusa2 can serve not only as a navigation sensor, but also as observation equipment for estimating the asteroid's topography, gravity and surface reflectivity (albedo) [1]. In January 2015, we conducted the health check of the LIDAR in space and confirmed its functions. Using these data as well as ground test results, we evaluate the performance of the LIDAR in this paper. In addition, we report the most recent achievement of laser link experiment conducted from October to December 2015.

Function: The principal role of the LIDAR is to measure the distance from the spacecraft to the asteroidal surface. The LIDAR has a wide dynamic range, from 25 km to 30 m, as a navigation sensor for rendezvous, approach, and touchdown procedures. Since it was designed for use in planetary explorers, its weight is as low as 3.5 kg [2]. The obtained range data will be used to estimate the asteroid's topography and gravity [1].

Second, the LIDAR can be used to measure the intensities of transmitted and received pulses. These intensity data will be used to estimate the normal albedo of Ryugu at a laser wavelength of 1.064 μm. To perform this estimation, we determined the transfer functions of the laser module and receiver to convert the intensity data into pulse energies, along with the utilization ratio of the returned pulse energy, through verification tests of the LIDAR flight model. The error in the normal albedo due only to the instrument error will be 18.0 % in an observation at a nominal altitude of 20 km [3].

Third, we aim to use the LIDAR to detect dust grains that might be present around Ryugu. The LIDAR on Hayabusa2 will be used to determine whether the energy flux of the return pulse exceeds a certain threshold every 133.33 ns. This simple observation significantly reduces the amount of down link data. The profile of the return pulse is estimated from iterative observations by changing the thresholds. The performance of the dust counter mode is examined using a breadboard model, a flight model, and an engineering model. We also estimate the lower bound of the number density of dust grains that can be detected. It is shown that the LIDAR on board Hayabusa2 is capable of detecting asteroidal dust if grains with the size similar to the Hayabusa sample exist around the Ryugu and their number density exceeds 10^5 m^{-3}[4].

Laser Link: As the first achievement of the LIDAR on Hayabusa2, we report results of a laser link experiment between the LIDAR and ground-based Satellite Laser Ranging stations[5]. This experiment was conducted taking a chance that the spacecraft was near to the Earth for the gravity assist operation. The uplink laser pulses from a ground station were detected successfully at 6.6 x 10^9 m distance, and the field of view direction of the receiving telescope of the LIDAR in the spacecraft frame was determined. Using the range mode, the intensities of the received signals were measured, and the link budget from the ground to the LIDAR was confirmed. And by detecting the two successive pulses, the time period of pulse intervals on the ground-based station were transferred to the LIDAR, and the time transfer from the ground was established.

References: [1] N. Namiki et al. (2014) *Proc. Inter. CJMT-1 Workshop on Asteroidal Science*, 74–96.
[2] Mizuno T. et al. (2016) *SSR*, http://dx.doi.org/10.1007/s11214-015-0231-2.
[3] Yamada R. (2016) *SSR*, http://dx.doi.org/10.1007/s11214-016-0240-9.
[4] Senshu H. et al. (2016) *SSR*, http://dx.doi.org/10.1007/s11214-016-0242-7.
[5] Noda H. et al. (2016), *in preparation*.

CROWN: a constellation of heterogenous wide-field NEO surveyors. Zhuo-Xi Huo[1] and Jiang-Chuan Huang[2], [1]Qian Xuesen Laboratory of Space Technology, No. 104 Youyi Rd., Beijing, 100094, China, [2]China Academy of Space Technology, No. 104 Youyi Rd., Beijing, 100094, China. huozhuoxi@qxslab.cn

Introduction: A constellation of heterogenous wide-field NEO surveyors (CROWN) is proposed in this report. Near-Earth Objects (NEOs) survey is interesting in planetary science and is vital for planet defence. It helps characterize the small objects population of the solar system. It's believed small objects such as asteroids, comets and meteorites are leftovers of the planet formation process. Habitable condition and geological history of the Earth might have been shaped by incoming NEOs during the bombardment era. NEOs survey is necessary to identify potentially hazardous objects (PHOs), which is a prerequisite for NEO alert and response. Space-based NEO surveyor is more efficient and more economic than ground-based large telescopes. With a constellation of heterogenous surveyors distributed in a heliocentric orbit, 90% of NEOs of ~10m or larger could be detected within 3 years. The proposed constellation consists of one satellite (mother surveyor) with a high-resolution telescope on-board and several miniatured satellites (daughter surveyors) with wide-field cameras on-board. This constellation also makes a panoramic observatory which is competitive in astronomical transients monitoring, such as super novae, microlensing, etc.

MOMENTS OF INERTIA OF PHOBOS WITH INHOMOGENEOUS INTERNAL STRUCTURE.

K. Matsumoto[1] and H. Ikeda[2], [1]RISE Project Office, National Astronomical Observatory of Japan (Mizusawa, Oshu, Iwate, 023-0861 Japan, koji.matsumoto@nao.ac.jp), [2]RDD/JAXA (Tsukuba, Ibaraki, 305-8505 Japan).

Introduction: The origin of Phobos is still an open issue. It may be either captured asteroid or formed from a disk of impact ejecta produced by a giant impact. Although it is not straightforward to determine the origin from internal structure alone, it will place important constraints. One of the key parameters related to the internal structure is moments of inertia (MOI). Phobos's MOI can be determined from amplitude of short-period forced libration (θ) and degree 2 gravity coefficients (C_{20}, C_{22}). Currently, the libration amplitude is estimated to be $\theta = 1.09 \pm 0.10°$ from control point network analysis using multiple image data [1]. Although the degree 2 gravity coefficients are estimated from tracking data of Mars Express on its close flyby at Phobos, they are not solved for at sufficient accuracy [2]. Axial difference of MOI can be constrained by the libration amplitude, but currently MOI of Phobos is not known. The observed libration amplitude is consistent with homogenous mass distribution of Phobos, but local mass anomalies cannot be ruled out [1,3].

Here we consider relatively simple two-layer internal structure and assume that ice water or porosity is confined in either layer, and calculate how much MOI deviate from the value for homogeneous body if such an inhomogeneity existed.

MOI from simple two-layer Phobos internal model: Phobos's bulk density of 1.86±0.013 g/cm^3 [4] is lower than most of the samples of carbonaceous material, which requires porosity and/or light elements like water ice. If the low bulk density was explained by water ice, its mass fraction is expected to be 10-35% depending on rocky material grain density [5]. If the mass distribution inside Phobos was inhomogeneous, e.g., water ice was concentrated near the surface or the center, we will observe a deviation of MOI from the value for homogenous interior. Here the MOI differences (ΔMOI) with respect to the homogenous Phobos are calculated for some cases where we assumed that (1) Phobos has a tri-axial ellipsoidal figure (a = 13.03 km, b = 11.40 km, c = 9.14 km), (2) Phobos has a two-layer structure and their boundary also has the similar ellipsoidal figure for which the libration amplitude is 1.15 degrees being consistent with the observed value of [1], and (3) water ice is confined either of the upper or lower layer and rock density is the same for both the layers. The water ice mass fraction is changed between 0 and 30%.

Figure 1 shows the result for the case that upper layer is composed of the rock plus water ice. When the upper layer thickness is 10% of the semi-principal axes (labeled as $R_b = 0.9R$), no more than 14 wt. % of water can be contained in the layer and the maximum OI| is about 9%. When the layer boundary is deeper, more water can be contained, but the maximum OI| is about 16%. Shown in Figure 2 is the result for the case in which the water ice is confined in the lower layer. If the layer boundary is located below 0.6R, no more than 11 wt. % of water can be contained in the layer and the maximum |ΔMOI| is about 8%. When the layer boundary is shallower, more water can be contained, but the maximum |ΔMOI| is about 17%.

We also tested the cases in which the porosity is responsible for the low bulk density. We calculated OI due to inhomogeneous distribution of the porosity using the similar two-layer structure. The results depend on the boundary depth and rock density. In the case that the lower layer is porous, the maximum OI| is about 17% when rock density is 2400 kg/m^3, and about 9% when rock density is 2100 kg/m^3.

MOI from libration amplitude and gravity coefficients: The amplitude of forced libration in longitude for Phobos is expressed as (e.g. [1])

where e is the orbital eccentricity of Phobos and γ is dynamical flattening;

where $A < B < C$ are MOI normalized by MR_0^2 (M: mass, R_0: mean radius) along the principal coordinate axes. Since the libration amplitude is a function of difference in the MOI, it is difficult to determine each of A, B, and C from θ alone. However, by combining with degree 2 gravity coefficients which are also related to the normalized MOI as

each of MOI can be derived as follows (e.g. [6]);

Figure 3 shows error of the least MOI A as a function of errors of the libration amplitude and gravity coefficients, where C_{20} error is assumed to be the same as that of C_{22}. In order to realize a certain accuracy of MOI, it is required to achieve the similar level of accuracy for both the libration amplitude and the gravity coefficients; otherwise the MOI accuracy is dominated by either component with larger error.

Summary and perspectives: We study Δ which is produced by inhomogeneous distribution of water ice or porosity using simple two-layer model for which the boundary has the similar shape as the surface. It is found that, in such a configuration, |ΔMOI| is smaller than 16-17%. 10% accuracy will not be sufficient, and it is required to achieve at least a few percent of MOI accuracy in order to detect it. To this end, the required accuracies for the libration amplitude and the degree 2 gravity coefficients are also a few percent. This level of accuracy will be achieved by future Phobos missions. Our preliminary study on gravity recovery suggests that a precision of a few percent on degree 2 gravity coefficients is feasible when the altitude of spacecraft in a quasi-satellite orbit is as low as about 10 km. More of higher-resolution images of Phobos will also improve the estimate of the forced libration amplitude.

References: [1] Oberst et al. (2014) P*lanet. Space Sci*., *102*, 45-50. [2] Pätzold et al. (2014) *Icarus*, *229*, 92-98. [3] Rambaux et al. (2012) *Astron. Astrophys.*, *548*, A14. [4] Willner et al. (2014) P*lanet. Space Sci*., *102*, 51-59. [5] Rosenblatt (2011) *Astron. Astrophys. Rev.*, *19* (44). [6] Bills and Rubincam (1995) *J. Geophys. Res.*, *100*, 26,305-26,315.

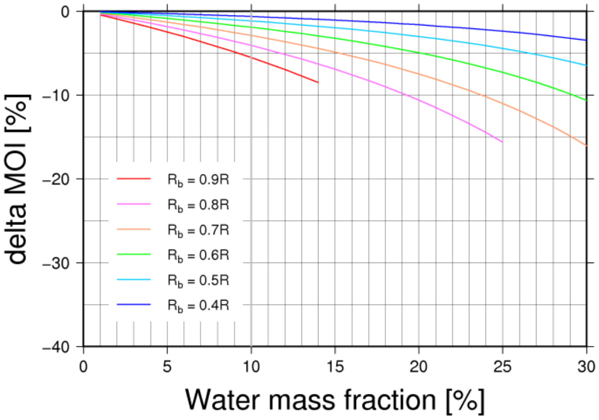

Figure 1. Moments of inertia differences between homogeneous and inhomogeneous Phobos. The inhomogeneity is assumed to be produced by water ice confined in the upper layer. Different color indicates different location of the layer boundary (red: shallow, blue: deep).

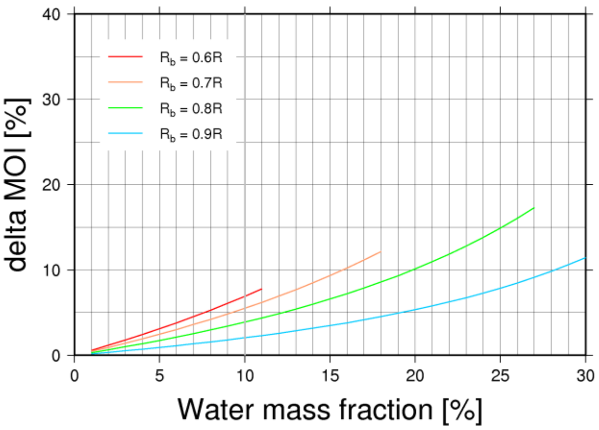

Figure 2. Same as Figure 1, but for the case that water ice is confined in the lower layer. Different color indicates different location of the layer boundary (red: deep, blue: shallow).

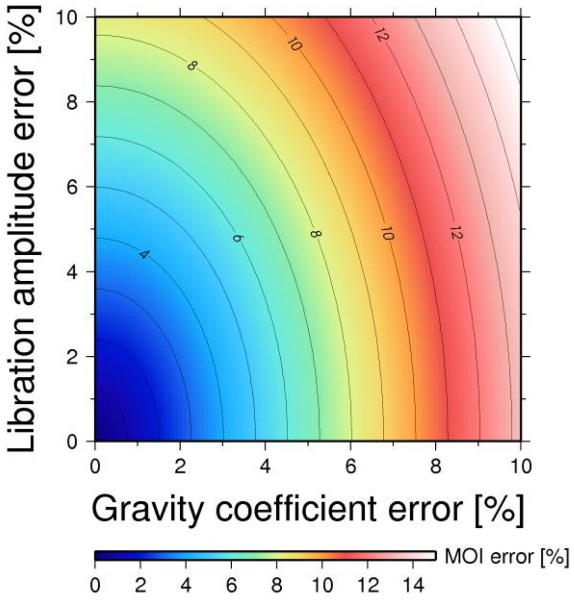

Figure 3. Relation of errors in the forced libration amplitude (θ) and the degree 2 gravity coefficients (C_{20}, C_{22}) to the moments of inertia error.

SPECTRAL PERSPECTIVES OF VARIOUS VOLCANIC DEPOSITS ENCOMPASSING APOLLO BASIN.

J. Chen[1], Z. C. Ling[1], B. Li[1] and J. Z. Liu[2] [1]Institute of Space Sciences, Shandong Provincial Key Laboratory of Optical Astronomy and Solar-Terrestrial Environment, Shandong University, Weihai (180 Wenhua Xilu, Weihai, Shandong, China, zcling@sdu.edu.cn), [2]Institute of Geochemistry, Chinese Academy of Sciences (46 Guanshui Road, Guiyang, Guizhou, China).

Introduction: Lunar volcanic deposits (in the form of mare, cryptomare and pyroclasts, etc.) are mostly located on the nearside, but rare on the farside [1-3]. The presence of these deposits on the surface of the Moon are indicative of its magmatic evolution [4]. Apollo basin (537 km in diameter) centered at 151.8° W, 36.1° S [5], is one of the few farside occurrences of volcanic products (Figure 1a). On the basis of hyperspectral remote sensing datasets from the Chandrayaan-1 Moon Mineralogy Mapper (M^3), we conduct spectral analysis among various volcanic deposits (see details in Table 1) encompassing Apollo basin to examine the mineralogical variations of volcanism occurring in different styles on the farside.

Table 1 Volcanic deposits[1-3, 7] studied in this work

Region	Type	Coordinates
Apollo N	Maria	152.5° W, 36.3° S
Apollo S	Maria	155.4° W, 41.6° S
Apollo W	Maria	159.2° W, 35.8° S
Apollo E	Maria	145.2° W, 39.4° S
Grissom-White	Cryptomaria	154.2° W, 46.8° S
Drygen T	Pyroclast	159.2° W, 33.0° S
Unnamed	Pyroclast	153.0° W, 29.5° S

Method: M^3 RGB color composite map is created to help identify the extent of volcanic deposits (Figure 1b). Integrated band depth (IBD) parameter that integrates the band depth over the entire spectral range of the absorption band relative to the continuum can reveal details of the variations in mineral content such as pyroxene and olivine, etc. [6]. We collect spectra from small fresh craters within mare and cryptomaria as well as flat units within those pyroclasts. All spectra are smoothed with Savitzky–Golay function. As shown in Figure 2a, the reflectance spectra of these deposits show mineral absorption features and continuum related to their maturities. Spectral continuum of 1 and 2μm bands are estimated with individual tangent linear fitting through 0.75 and 2.54μm, and then removed to highlight mineral absorption features obscured by space weathering effects. Figure 2b exhibits various band shapes corresponding to different types of deposits. In order to distinguish mineralogical variation, the absorption band center and relative strength are calculated by Modified Gaussian Model (MGM) for individual spectrum and listed in Table 2 for comparisons.

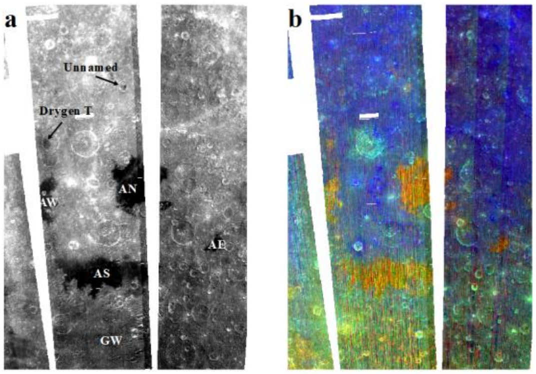

Figure 1 (a) M^3 1μm reflectance. AN=Apollo N, AS=Apollo S, AW=Apollo W, AE=Apollo E, GW=cryptomaria between Grissom and White craters. The black arrows with labels indicate the pyroclasts. (b) RGB color composite image(R: IBD1μm, G: IBD2μm, and B: R1.58μm). Map projection: Lambert azimuthal equal area projection.

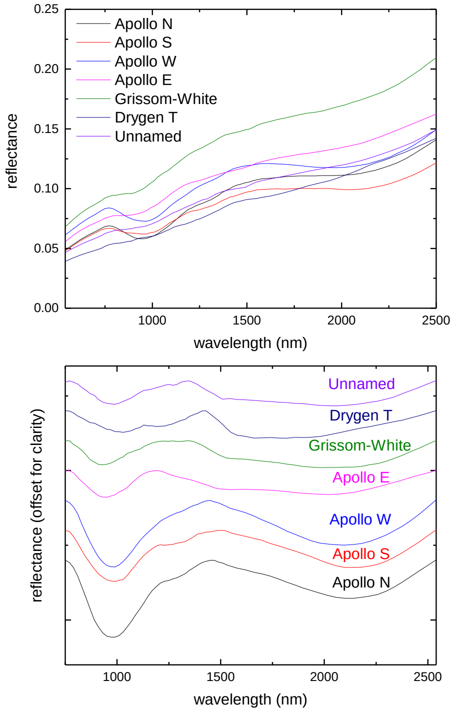

Figure 2 M^3 reflectance spectra of the deposits before (a) and after (b) continuum removal.

Results and Discussions:

Maria & Cryptomaria. MGM deconvolution results (Table 2) of three patches of basalts (Apollo N, Apollo S and Apollo W) indicate the characteristic of olivine-bearing and pyroxene-rich lithology, which contains more high calcium pyroxene (HCP) than low calcium pyroxene (LCP). While the fresh spectra exposed in Maria Apollo E exhibit a strange band shape that 1 and 2μm absorption centers shift to shorter wavelength, resulting from a LCP dominated content as derived by MGM. The cryptomaria between Grissom and White craters was interpreted to represent ancient basaltic deposits superimposed by basin ejecta (e.g., Orientale) [2]. Although its mafic absorptions are indeed shallower than mare basalt, the LCP absorption strength ratios tend to be higher than HCP. The LCP spectral features in Maria Apollo E and Cryptomaria Grissom-White are confusing that they stand for local materials involving with the noritic South Pole Aitken basin (SPA) floor or exotic contaminations.

Pyroclast. Spectral analysis of recently identified pyroclast in Drygen T crater [7] seem to reveal a similar composition with previously identified pyroclastic deposits in a unnamed crater [3]. Other than the mafic absorptions, these pyroclasts display a band centered at ~1200 nm, indicating a mixture of mafic minerals and volcanic glass [6].

Conclusions:

M^3 visible near-infrared spectra of small fresh craters embedded in mare and cryptomaria, as well as smooth pyroclastic deposits are extracted to plumb possible absorption contribution from pyroxene, olivine and volcanic glass with the MGM spectral deconvolution. We have identified olivine, HCP and LCP contents in three mare units except for the smallest Apollo E, whose LCP-rich character is akin to the cryptomaria in SPA. In addition, spectra from two pyroclastic deposits examined by MGM are suggested to contain glass contents.

Various styles of volcanism exposed in Apollo basin reveal diverse nature of lunar mantle and crust, consequently call for further integrated investigations with multisource datasets. Apollo basin has also been regarded as a candidate for future *in situ* detections and sample return missions [8]. Additional samples are expected to catalyze a better understanding of lunar thermal evolution and volcanic history.

Acknowledgement: This work was funded by the National Natural Science Foundation of China (U1231103, 41373068), Natural Science Foundation of Shandong Province (JQ201511 and ZR2015DQ001), and Young Scholars Program of Shandong University, Weihai (2015WHWLJH14).

References:

[1] Nelson D. M. et al. (2014) *LPSC, 45,* Abstract #2861. [2] Whitten J. L. and Head J. W. (2015) *Icarus, 247,* 150–171. [3] Gustafson J. O. et al. (2012) *JGR, 117,* E00H25. [4] Hiesinger H. and Head J. W. (2006) *Reviews in Mineralogy and Geochemistry, 60,* 1-81. [5] Pieters C. M. et al. (2001) *JGR, 106(E11),* 28001–28022. [6] Besse S. J. et al. (2014) *JGR, 119,* 355-372. [7] Jawin E. R. et al. (2015) *JGR, 120,* 1310-1331. [8] Jolliff B. L. et al. (2016) *LPSC, 47,* Abstract #2818.

Table 2 Absorption band parameters for volcanic deposits within Apollo basin

Parameter		Apollo N	Apollo S	Apollo W	Apollo E	Grissom-White	Drygen T	Unnamed
Band 1	Center	858	854	857	927	926	1006	983
	Strength	0.099	0.072	0.087	0.072	0.072	0.066	0.085
Band 2	Center	927	927	927	1011	1032	1206	1178
	Strength	0.204	0.128	0.166	0.038	0.029	0.031	0.020
Band 3	Center	1009	1010	1008	1971	1815	1688	1630
	Strength	0.239	0.155	0.199	0.044	0.085	0.092	0.063
Band 4	Center	1101	1097	1099	2239	2217	2068	2089
	Strength	0.136	0.081	0.099	0.034	0.073	0.081	0.090
Band 5	Center	1237	1248	1212				
	Strength	0.075	0.052	0.066				
Band 6	Center	1944	1934	1912				
	Strength	0.084	0.077	0.120				
Band 7	Center	2229	2226	2227				
	Strength	0.110	0.116	0.126				

THE MONS RÜMKER VOLCANIC COMPLEX OF THE MOON: A CANDIDATE LANDING SITE FOR CHANG'E-5 MISSION.

J. Zhao[1,2], L. Xiao[1], L. Qiao[1]. [1]Planetary Science Institute, China University of Geosciences, Wuhan, 430074, P. R. China (jnzhao@cug.edu.cn), [2]Department of Geosciences, Stony Brook University, Stony Brook, NY 11794

Introduction: Chang'E-5, to be launched in 2017, will be China's first lunar sample return mission. The northern Oceanus Procellarum is a candidate landing region, where Mons Rümker is an outstanding volcanic complex and is a priority landing site for Chang'E-5. This volcanic complex is centered at 301.7°E, 40.7°N and covers an area of ~4000 km^2. Smith (1974) made a geological map of the region based on Lunar Orbiter mosaics [1], but this work is sketchy due to the lack of high-resolution image and spectral data. Other studies have analyzed the morphometry, rheology and mode of the emplacement of Mons Rümker [2], acquired the surface property with Earth-based radar data [3], and studied the pyroclastic mantles with new spectral and photometric data [4]. However, there is no detailed and comprehensive study of this area, which cannot meet the requirement of landing site selection for a sample return mission. In addition, geological evolutionary history of Mons Rümker is still unclear. Therefore, this work uses the latest high-resolution image and spectral data to comprehensively study the geology of Mons Rümker to support the Chang'E-5 mission.

Data and method: High-resolution DTM is obtained from stereopair images (10 m/pixel) of Terrain Camera (TC) onboard SELENE [5]. FeO and TiO_2 abundances are estimated with data acquired by Multispectral Imager (MI) onboard SELENE using the method in [6]. As the spatial resolution of MI data is 20 m/pixel, we can get better results than those derived from Clementine data. Data from Moon Mineral Mapper (M^3) onboard Chandrayaan are processed to analyze the mineral type [7]. Detailed analysis of geomorphologic features is based on images of LRO Narrow Angle Camera and TC.

Results: *Topography.* Mons Rümker is approximately circular in shape and stands up to more than 400 m above the surrounding mare surface (lower than -2400 m). Its central and southern parts are higher with the maximum elevation reached in the summit of a dome, which is about -1250 m. Slope map derived from TC DTM shows that 75% of Mons Rümker are less than 3°. The marginal area of the volcanic complex and some domes can have higher slopes, which can be 5-8°. The steepest part is the inner wall of some craters, which can be more than 15°.

Mineral and rock type. The Mons Rümker region has relatively lower TiO_2 (~2 wt.%) and FeO (~15 wt.%) abundances compared to the surrounding mare region. According to the TiO_2 abundance, rocks in Mons Rümker should be low-Ti basalt [8]. Spectroscopic observation from Moon Mineralogy Mapper (M^3) shows that the southern Mons Rümker has a similar mineral composition with its adjacent mare deposits (Fig. 1), with a high-calcium pyroxene dominated composition. While the northern part shows blue on the M^3 spectral parameter map, indicating a weaker 1 μm mafic absorption band (Fig. 1), probably due to the existence of pyroclastic mantling deposits [4].

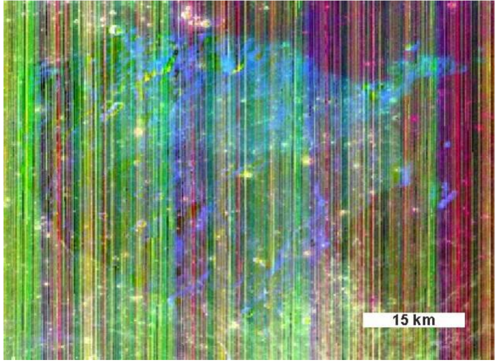

Figure 1 M^3 spectral parameter map of Mons Rümker and surrounding mare regions. R: 1 μm integrated band depth (IBD), G: 2 μm IBD, B: 1578 nm reflectance.

Geomorphology. A variety of landforms can be found in Mons Rümker region. Domes are the most prominent features in Mons Rümker. More than 30 volcanic domes have been identified in this area and they are classified into three types based on their morphology [1]. In this study, we checked these domes with high-resolution imagery and topographic data and found some of the domes have no obvious topographic relief. Meanwhile, some new domes were identified. We finally confirmed 20 domes and proposed a new classification scheme. The domes are divided into two types: steep-sided domes and low domes. Steep-sided domes (eg. "2" in Fig. 2) usually have steeper side slope (>5°). Most domes of this type have a summit crater which may be the volcanic crater. Low domes (eg. "1" in Fig. 2) are usually characterized by gentle side slope and smooth transition between the dome and the surrounding region. Only a small portion of this type have summit craters.

Craters in Mons Rümker are mostly bowl-shaped simple craters. They are usually smaller than 2 km in diameter. There are also many irregular craters and chain craters which should be secondary craters from some young large primary craters nearby (eg. Rümker

E crater to the southeast of Mons Rümker). However, it should be noticed that some craters with irregular shape should be volcanic craters or related to rilles.

Scarps and ridges have been studied in [1] and are considered to be controlled by regional structural direction in Oceanus Procellarum. However, we think original landform and contraction of cooling lava can also result in the formation of scarps and ridges. Besides, in high-resolution images, we found no craters destroyed by the scarps and ridges, which indicates that these features are relatively old in age.

Surface age. Crater size-frequency distribution measurements are performed to acquire model ages of Mons Rümker. We select a large low dome and a steep-sided dome, part of the lineated terrain in the northwest and a non-dome region (Fig. 2) to perform crater counting so that we can compare the formation sequence of each region. Results show that the oldest age occurs in the lineated terrain, which is 3.67 Ga. The low dome has an absolute model age of 3.34 Ga, and its adjacent non-dome area is 3.40 Ga, while the age of the steep-sided dome in the southern Mons Rümker is 3.16 Ga.

Discussion: *Geological evolution of Mons Rümker.* We produced a geological map of Mons Rümker (Fig. 3) and reconstructed the geological evolutionary history. Firstly, lineated terrain (mR1) formed at 3.67 Ga ago. These materials may be ejacta from Iridum crater as the lineations trend east-northeast and are nearly radial to Iridum crater [3]. Then magma intruded and erupted in Mons Rümker and covers most of the surface (mR2) in about 3.4 Ga. In the terminal stage of the volcanism, some domes formed and they may be active last to 3.16 Ga or even longer. However, to better constrain the duration of volcanism in Mons Rümker, more extensive age dating should be carried out. At last, formation of some large Copernican craters nearby results in the secondary craters in Mons Rümker.

Landing site suggestion. We proposed two candidate landing sites for sample collection. One is the steep-sided dome ("A" in Fig. 2). By analyzing the composition of rocks, it can provide us information on the formation mechanism of lunar domes. Meanwhile, age dating of rocks can help us better constrain the duration of volcanism in Mons Rümker and improve the CSFD method. The other landing site is in the northern Mons Rümker and near the boundary of lineated region ("B" in Fig. 2). This area may have complicated compositions and different stratigraphy. Sampling the rocks in the surface and the subsurface can help us analyze the evolutionary history of Mons Rümker and confirm the source of materials in the lineated terrain, which may shed light on the age of some large impact events on the Moon.

Summary: We analyze the topography, compositions, geomorphologic features, and the evolutionary history of Mons Rümker. A geological map of Mons Rümker was produced and two candidate landing sites were proposed for Chang'E-5 sample return mission.

References: [1] Smith E.I. (1974) *The Moon*, 10, 175-181. [2] Wöhler C. et al. (1997) *LPS XXVIII*, Abstract #1091. [3] Campbell B.A. et al. (2009) *JGR*, 114, E01001. [4] Farrand W.H. et al.(2015) *46th LPSC*, Abstract #2440. [5] Haruyama J. et al. (2012) *43rd LPSC*, Abstract #1200. [6] Otake H. et al. (2012) *43rd LPSC*, Abstract #1905. [7] Mustard J. et al. (2011) *JGR*, 116, E00G12. [8] Neal C. R. and Taylor L. A. (1992) *GCA*, 56, 2177-2211.

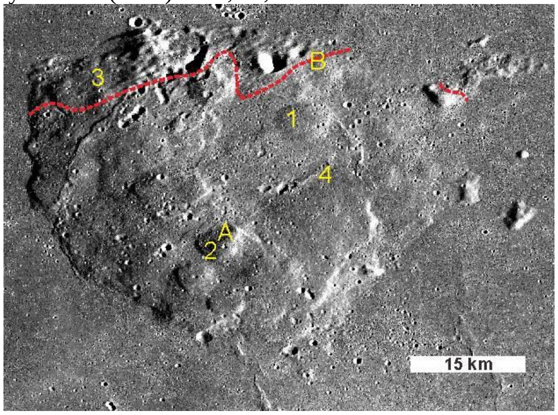

Figure 2 TC image of Mons Rümker. Numbers denote the area we perform crater counting: 1, Low dome; 2, Steep-sided dome; 3, Lineated terrain; 4, Non-dome region. Letters denote the two candidate landing sites. Dashed lines denote the boundary of lineated terrain.

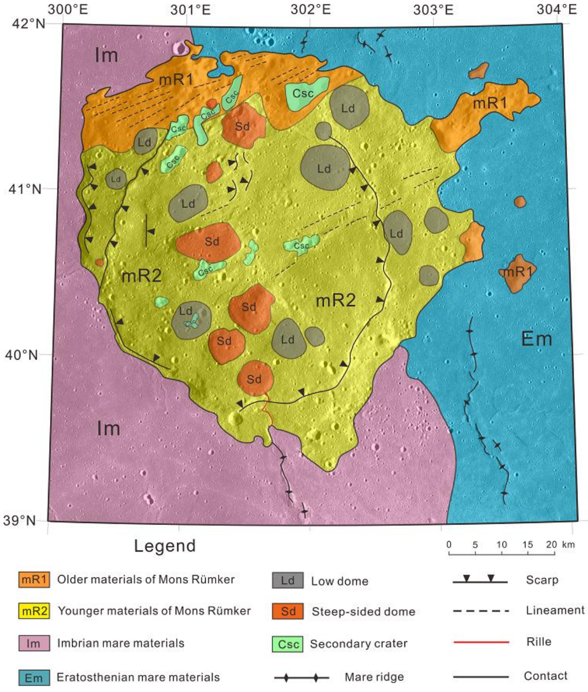

Figure 3 Geologcal map of Mons Rümker.

COMPOUND FLOW FIELDS IN SOUTHWEST MARE IMBRIUM: GEOMORPHOLOGY, SOURCE REGIONS AND IMPLICATIONS FOR LUNAR BASIN FILLING.

L. Qiao[1, 2], J. W. Head[2], L. Wilson[3], M. A. Kreslavsky[4] and L. Xiao[1], [1]Planet. Sci. Inst., China Univ. Geosci, Wuhan 430074, China, [2]Dep. Earth, Env. & Planet. Sci., Brown Univ., Providence, RI, 02906, USA, [3]Lancaster Env. Centre, Lancaster Univ., Lancaster LA1 4YQ, UK, [4]Earth & Planet. Sci., UC Santa Cruz, CA 95064, USA. Contact: le.qiao@cug.edu.cn.

Introduction: Recent advances in the analyses of the generation, ascent, intrusion and eruption of basaltic magma on the Moon [1-6] have provided an important context for the history of lunar mare volcanism and the nature of filling of the major impact basins. Here we review the implications of these treatments [3-5] for the nature and emplacement of effusive eruptions and use this framework to interpret the sequence of filling and styles of volcanism for the southwest quadrant of the Imbrium basin, known to contain some of the longest lava flows on the Moon [7-9].

Background: There are two causes of limits to lava flow length [3-5]: 1) In *supply-limited* or *volume-limited* flows (Fig. 1a), the supply of magma from the source region is exhausted before any cooling limitation can be reached. 2) In *cooling-limited* flows (Fig. 1b), the terminus of the flow cools sufficiently so that forward flow motion ceases; cooling-limited flows can often be recognized by the behavior of the more proximal parts of the flow where cooling has progressed to a lesser degree (Fig. 1b), and the continuing supply of magma to the flow can inflate the flow behind the cooled front and breach the thinner parts of the thermal boundary layer, forming breakout flows. Cooling-limited flow behavior is favored in lower-volume-flux eruptions, which optimize cooling time.

Effusive eruptions are modulated by effusion rate, eruption duration, cooling and supply limitation to flow length, and by pre-existing topography and have been classified [3-5] into four types: 1) Relatively *low effusion rate, cooling-limited flows* lead to small shield volcanoes; 2) *higher effusion rate, cooling-limited flows* lead to compound flow fields (CFF); 3) *even higher effusion rate, long-duration flows* lead to thermal erosion of the vent, effusion rate enhancement, and thermal erosion of the substrate to produce sinuous rilles; 4) *Extremely high effusion rate flows on slopes* lead to volume-limited flows with lengths of many hundreds of kilometers.

The Role of Cooling-Limited Flows and Compound Flow Fields in Mare Basins: Following dike emplacement and cooling of the marginal parts of the dike, effusion dominates over the widest part of the dike and centralizes flow; eruption rates can lie in the range from 10^4 to 10^6 m^3 s^{-1}[3-5] and eruptions that are in the lower part of this range, (~1-2 × 10^4 m^3 s^{-1}) are predicted to produce *cooling-limited* flows (Fig. 1b) commonly less than ~10-20 km wide, ~10 m thick and often up to ~200 km in length. Eruption durations are likely to be 2-3 weeks, and heat loss mechanisms cause cooling to penetrate into the flow interior, slowing its forward motion; when the Gratz number reaches ~300, the flow will stop advancing. At this point, lava is still being extruded from the vent and either causes inflation and breakouts in the flow levees toward the vent in the still-warmest part of the flow (Fig. 1b), or forms a new, often parallel, flow from the same vent. Each new flow emerging from the same eruptive phase will be emplaced in a similar cooling environment, and produce flows with similar aspect ratios. This process will repeat itself until the volume of magma in the eruption is exhausted.

The final result of the process is the production of a *compound flow field* (Figure 2), a series of cooling-limited flows whose general morphology will be related to preexisting topography and the thickness of succeeding flows. We have defined three types of compound flow fields: 1) *Linear-Parallel*: On a sloped surface, a compound flow field will often appear as a set of parallel flows of broadly similar lengths and widths. 2) *Linear-Braided*: On a sloped surface, succeeding parallel flows can be of different thicknesses and overlap with one another, producing a braided pattern. 3) *Knotted*: With decreasing slope and in relatively flat areas, succeeding flows and flow breakouts can meander and significantly overlap, producing a knotted appearance; in these cases, individual flow segments can only be traced for a few to several tens of km, and form complex patterns sometimes broadly radial to the vent area.

How many flows might constitute a compound flow field from a single eruptive phase? From theoretical considerations [3-5], the volume of magma predicted to represent a basaltic eruption on the Moon lies in the range of 100-1000 km^3. If a typical cooling-limited flow is ~15 km wide, ~20 m thick and ~200 km in length (~60 km^3), then these total volumes would imply that the number of cooling-limited flows in a compound flow field would be in the range of ~2-15.

Lunar compound flow fields have not been specifically reported in the literature but theoretical considerations [3-5] predict that they should be common. One reason for their lack of detection is that the extrusion of multiple parallel and overlapping flow lobes will produce a regionally relatively flat mare topographic surface that does not show the prominent lobate flow boundary scarps typical of the discrete and distinctive young Imbrium lava flows [7]. Secondly, following flow field emplacement, regolith formation processes will tend to average out and subdue any topographic variation remaining between adjacent flows. Finally, because compound flow fields by definition derive from the same batch of extruded magma, they are not expected to show any mineralogical or spectral reflectance variation; while they may or may not be different from a succeeding batch of magma, there is no reason to expect significant spectral differences that might reveal the presence of individual flows in a compound flow field.

Analysis of SW Mare Imbrium: New data from the LRO Lunar Orbiter Laser Altimeter (LOLA) instrument has provided insight into the presence and nature of lunar mare compound flow fields [10]. Detrended LOLA data have revealed the presence of compound flow fields in southwest Mare Imbrium (Figs. 3, 4) with typical flows in the range of 10-20 km wide and 100-200 km in length, implying volumes of up to ~50 km^3. Flow field morphology [3-5] illustrates well the role of preexisting topography in their emplacement. The three types of compound flow fields described above are seen (Fig. 3): In the central part of the basin, the oldest flows (Fig. 4) are *Knotted Compound Flow Fields*, likely representing emplacement in the flatter central regions. Along the SW basin margin, intermediate-aged phase B flows form *Linear-Braided Compound Flow Fields*, interpreted to represent formation on the increasing slopes caused by the loading and subsidence of the basin interior. Also along the SW margin, relatively young phase A flows form *Linear-Parallel Compound Flow Fields*, probably due to the increasing slope toward the interior with time. Note that the longest Phase B intermediate flows (up to 600 km long and up to 30-40 km wide in their distal reaches) are so extensive that they are interpreted to represent Type 4 eruptions, "*extremely high effusion rate flows on slopes* that lead to volume-limited flows with lengths of many hundreds of kilometers." Theory [3-5] predicts that for typical lunar eruptions, the number of cooling-limited flows in a compound flow field could be in the range of ~2-15: for the *Linear-Parallel* CFF, we find ~10 flows and for the *Braided-Parallel* CFF, about 13, in agreement with predictions.

The spatial distribution of flow margins seen in the detrended data enables us to trace the source regions of the CFFs back to the southwestern corner of Imbrium basin (Fig 3). The volcanic complex south of Euler crater proposed by Schaber [7] as the shared source region for all the young lava flows, however, is different compositionally, and stratigraphically older than the Imbrium lava flows. We find that Phase B is erupted from the Rima Euler source and the youngest lavas (Phase A) can be traced to linear fissures and cinder cones between crater Euler and Mons Vinogradov.

Conclusions: This SW Mare Imbrium example suggests that compound flow fields may represent a major new insight into the mode of formation and evolution of the lunar maria. Much of the lunar mare lava may have been emplaced in relatively low effusion rate, multiple cooling-limited flows (perhaps 10-20 in any one dike arrival event) producing previously unrecognized compound flow fields.

References: [1] Head & Wilson (1992) *G&CA* 56, 2155. [2] Shearer et al. (2006) *RMG* 60, 365. [3] Wilson & Head (2015) *Icarus*, in press. [4] Head & Wilson (2016) Icarus, in review. [5] Head & Wilson (2016) LPSC 47, #1189. [6] Jozwiak et al. (2015) *Icarus*, 248, 424. [7] Schaber (1973) *LSC IV*, 73. [8] Hiesinger et al. (2000) *JGR 105*, 29239. [9] Bugiolacchi & Guest (2008) *Icarus 197*, 1. [10] Kreslavsky et al. (2016) LPSC 47, #1331.

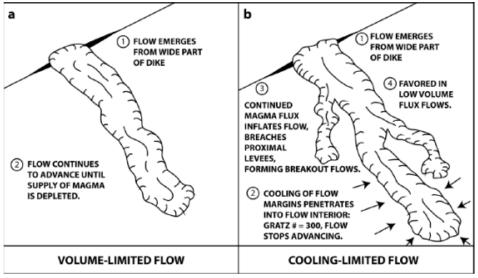

Fig. 1. Limits to lava flow length.

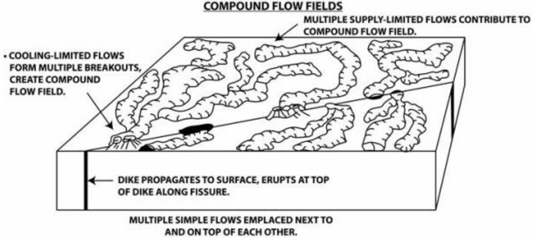

Fig. 2. Compound flow fields.

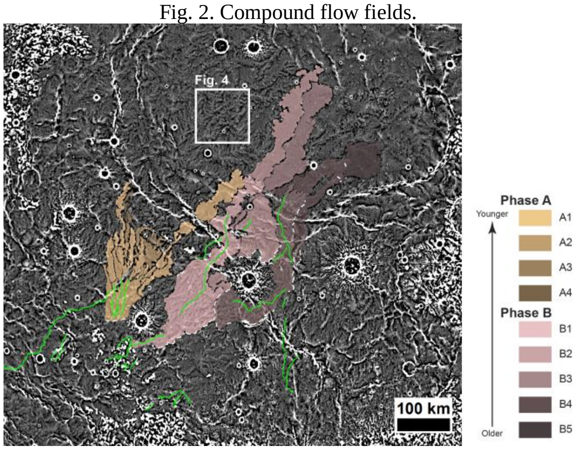

Fig. 3. Detrended LOLA altimetry map of lava flows within southwestern Mare Imbrium [11]. The green lines are lunar rilles, either linear or sinuous.

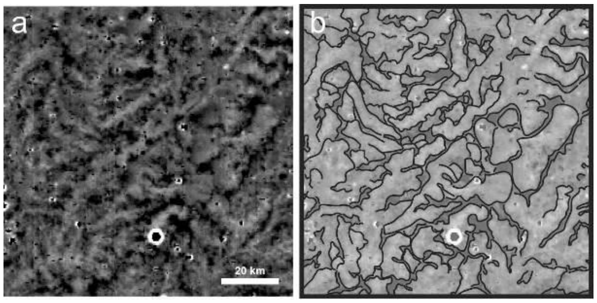

Fig. 4. (a) Detrended topography, (b) sketch map of example of Mare Imbrium compound lava flows. Location shown by box in Fig. 3.

POSSIBLE FORMATION MEAHANISM OF LINEAR FEATURES AT CHANG'E-3 LANDING SITE. X. Q. Liu[1] , L. XIAO[1] ,[1]China University of Geosciences (Wuhan), 388Lumo Road, Wuhan, Hubei, 430074, P. R. China. (897426538@qq.com)

Introduction: Chang'E-3 (CE-3) landed at the northern mare Imbrium of the lunar nearside (44.12 °N, 19.51 °W) on 14 December 2013. During its exploration, some remarkable linear features are visible around the landing site (Fig.1), seen by camera onboard the Yutu Rover. Most of them occur in two preferential directions and are intersected and/or cross-cut with each other. Alternatively, linear features with comparable scales and similar appearances were widely oserved at the Apollo 11, 12, and 15 landing sites.

Different theories exist regarding the cause of formation of these linear features, including retro-rocket jets disturbance, sunlight direction or radial ejecta rays. At Chang'E-3 landing site, although influenced by the retro-rocket jets disturbance, however, this should form linear features at radial direction with the landing site at center which is not consistent with the linear features observed at Chang'E-3's landing site. Wolfe and Bailey studied the linement features at Apollo 15 landing site and suggested these features were not real geological feature but illusion under certain light condition[1]. Xiao et al. proposed that the observed linear features might appear due to small-scale uneven surface under low-angle incident light[2]. We conduct simulation experiment and discuss the possible formation mechanism and influencing factors of these linear features.

Method: Experimental design is shown in Fig. 2. Totally two sets of experiment were conducted. The purpose of the first set of experiment was to estimate the influence the light source incident-light angle, horizontal angle between the incident light and camera view direction, and the camera vertical angle have on the linear features. The purpose of the second set of experiment was to simulate the effect of meteorite impact and retro-rocket jets on the surface, by observing the different results from different lighting condition and camera angle.

The simulation experiments are to answer the following questions: 1) are the linear features real? 2) what is the influence of the incident light angle? 3) what is the influence of the camera vertical angle? 4) what is the influence of the horizontal angle between the incident light and camera view direction? and 5) what is the relationship between these linear features and meteorites impact and retro-rocket jets ejectas?

Discussion and conclusions: In the pictures taken in these experiments, some clear and oriented linear features are observed. As shown in the image, these features are very similar with the linear features observed at the Chang'E-3 landing site. We infer that:

1) The linear features observed on the lunar soil surface are not real geological features exist on the lunar surface.

During the experiment, the simulated lunar soil are evenly spread with no rugged surface. The uppermost layer of simulated lunar soil was sieved and sprayed randomly to make sure they are perfectly even with no linear features. Thus the surface should be isotropic and with no orientation difference. No linear feature actually exist on the lunar surface simulated in our experiment. Therefore we agree with Wolfe and Bailey and Xiao that these features are not really exist, but a illusion caused under certain lighting condition.

2) Decisive influence of incident light angle on the linear features.

The lower the incident light angle is, the more clear the linear features are (Fig.3). The visibility of the linear features reach critical point when the incident light angle (β) reaches 60°: when the angle surpass 60 °, no linear feature is observed (Fig.4). The linear features in the images from Chang'E-3 landing site are all observed under conditions when the incident light angle is roughly 30 °and in accordance with our result.

Camera angle in the vertical direction can also influence the clearance of the linear features but has no decisive influence on whether the linear features appear. The lower the camera angle is, more clearer the linear features are. However, when the incident light angle is small enough, the linear features will only decreased with the increase of the camera angle but won't disappear. We also discovered that the linear features won't change with horizontal angle between the incident light and camera shooting direction.

3) The linear features on the lunar soil surface are not the result of impact ejecta or retro-rocket jets.

We conducted impact and jets experiments to simulate the effect of meteorites impact and retro-rocket jets on the lunar soil surface. The result is shown in Fig. 5. The resulting three simulated impact craters A, B and C are all with similar characteristics with the real lunar surface in crater rim collapse, radial ejecta rays and secondary impact craters and also relatively higher albedo at the retro-rocket jet hit area. When under relatively lower incident light angle, clear linear features are visible on the simulated lunar soil surface while the radial ejecta rays are not obvious and even barely recognizable. Example can be seen in the Fig. 6., we can not figure out the existence of the radial ejecta rays. This is because the accumulated height of ejecta ray material is too thin and has no obvious impact on the uneven micro-terrain of the simulated lunar soil surface and thus can not be observed.

References: [1] Wolfe, E. W., and N. G. Bailey.（1972）Lunar and Planetary Science Conference Proceedings. Vol. 3. [2]Xiao L, Zhu P, Fang G, et al.（2015）Science, 347(6227): 1226-1229

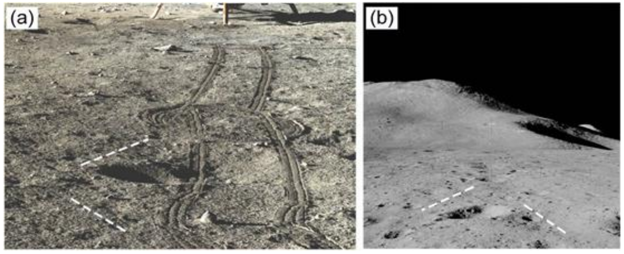

Figure 1. (a) Chang'E-3/Yutu panorama camera image 20131224192152 of the lunar surface near the landing site. The white dashed lines mark the two sets of lineaments. (b) Hasselblad 70 mm image AS15-85-11374HR of the lunar surface at the foot of Mt. Hadley of Apollo 15 landing area. The white dashed lines show the two set of lineaments.

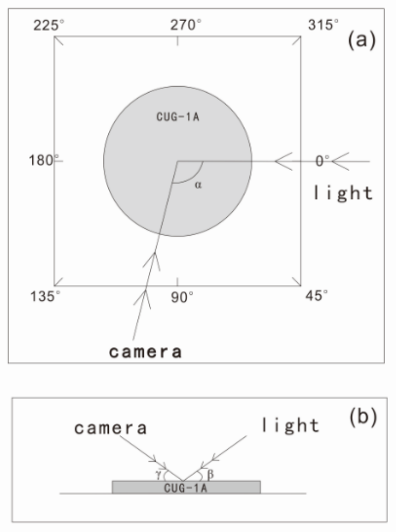

Figure 2. Schematic diagram of the model experiments for lunar lineaments. (a) Overhead view and (b) side view of the experimental setup. α is defined as the horizontal angle between the light source and the camera, α=0 °when the light source and camera are in the same direction , and then increases clockwise to 360 °. β is the incidence angle, defined as the angel between light path and horizontal plane. γ is the camera observing angles, defined as the angle between the scattered light path and the horizontal plane.

Figure 3. Obvious lineaments observed on the lunar regolith simulant (α=315°, β=0°, γ=0°). The white dashed lines mark the two set of lineaments with different directions.

Figure 4. Lineaments at the critical state of observations (α=270°, β=60°, γ=25°).

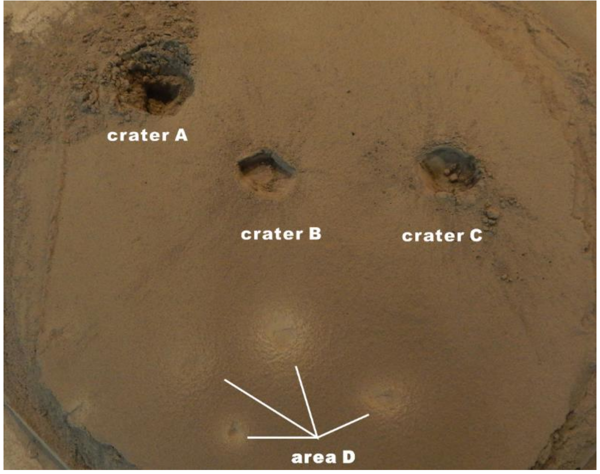

Figure 5. Simulated impact craters A, B, C . Area D is simulated retro-rocket jet hit area with high albedo.

Figure 6. Under relatively lower incident light angle（β=15 °）clear linear features are visible on the simulated lunar soil surface while the radial ejecta rays are not obvious and even barely recognizable.

RESULTS OF THE SOLAR X-RAY MONITOR ON CHANG'E-2.

W. D. Dong[1], X. P. Zhang[2], A.A. Xu[3]
[1]Lunar and Planetary Science Laboratory, Macau University of Science and Technology, Macao, China, dowudong@gmail.com; [2]Lunar and Planetary Science Laboratory, Macau University of Science and Technology, Macao, China, xpzhang@must.edu.mo; [3]Lunar and Planetary Science Laboratory, Macau University of Science and Technology, Macao, China

Introduction: The X-ray spectrometer (CE2XRS), one of the scientific payloads onboard the CE-2 spacecraft, was intended to obtain the distributions of major rock-forming elements (i.e., Mg, Al, Si, Ca, Ti and Fe) on the Moon [1]. The CE2XRS was designed to be a compact detector. It consisted of a lunar X-ray detector, solar X-ray monitor (SXM) and electronics box. The lunar X-ray spectrometer was pointed to the Moon, which made position sensitive observations of the X-rays emitted from the lunar surface [2]. The SXM was pointed to the Sun, which was used to monitor the solar X-ray flux because solar X-rays are the main excitation source of the X-rays emitted from the lunar surface. The primary solar X-ray flux must be known to properly understand the fluorescent spectra emitted from the Moon. The chemical composition of the lunar surface can be determined by carrying a detailed analysis of the X-ray spectroscopy by the two instruments, i.e. lunar X-ray detector and SXM [3]. In addition to being necessary for the Moon science, the data of SXM could also be used for solar science. The SXM provides Moon-based solar X-ray flux and energy spectra for six months in total. The data obtained during this period include several solar flares, as well as quiescent periods, which are crucial to study the variations of the coronal temperature and physical processes during flares.

In this paper, the data process produure of SXM and preliminary results are presented.

Instrument Description: Since the detailed structure and specification of SXM has been presented by Peng et al. (2009) [1] and Cui et al. (2014) [4], we here only give a brief description (Table 1). The SXM was sealed by Si-PIN detector with a 12.5-μm-thin Be window. The nominal detective energy range of the detector was 0.5-10 keV and the energy resolution obtained on the ground was 300eV@5.95keV. The effective area of the detector was limited to 0.28 mm2 with an annular aperture stopper made of copper. The circular field of view of SXM was 60°. The X-ray is collected in 976 energy channels for each 10s integration.

Table 1 Characteristics of the SXM

Detector material	Si
Be Window thickness	12.5 μm
Si-PIN crystal thickness	500 μm
Energy range	0.5-10 keV
Energy resolution	300eV@5.95keV
Number of channels	976
FOV	60°

Data Analysis Procedure: The channel vs. energy relation of SXM was carefully calibrated before launch, which could be found in Cui et al. (2014).

Background Reduction. The background of SXM was determined by summing all measurements in the darkside of the Moon in quiescent Sun period and normalized by the accumulation time. The background was subtracted directly in the spectra obtained in the sunlit side of the Moon.

Efficiency. The X-ray detecting efficiency of the detector was calculated by the data from National Institute of Standards and Technology (NIST) database. The efficiency curves of vertical incidence is shown in Figure 1.

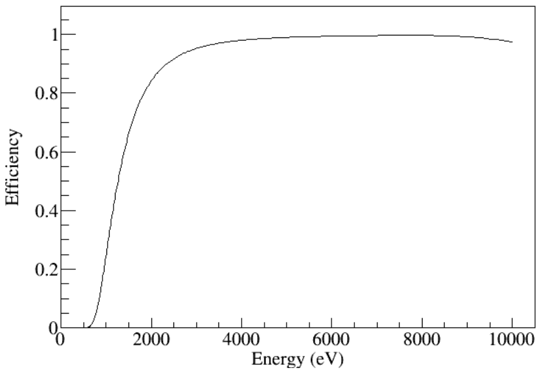

Figure 1. Modeled detector efficiency versus energy for SXM

Collimator Factor. The collimator factor of the instrument is primarily determined by the instrument architecture, which was derived from the SXM observed data. The factor curves with sine values of different solar X-ray incident angles (0-60 degree) is shown in Figure 2.

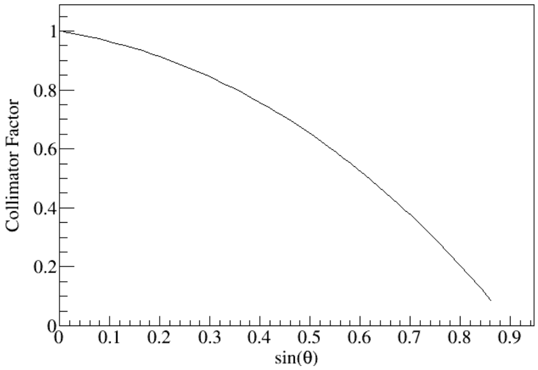

Figure 2. Collimator factor of SXM.

Crosss calibration with GOES. GOES measures the solar flux in two channels (1-8 Å and 0.5-4 Å, corresponding energy is 1.55-12.4 keV and 3.1-24.8 keV) simultaneously in every 3s. The simultaneous one-minute GOES 1-8 Å flux data and SXM flux data was shown in Figure 3. The deadtime of the SXM was about 300 µs, which was measured in the ground [5]. However, when the Sun in active period, e.g. solar flare event occurred, we found that the deadtime was greater than 300 µs. We calibrated the dead time of SXM with the GOES data.

Preliminary Results: The first results show that the calibrated flux obtained from the GOES and SXM were consistent well (see Figure 3).

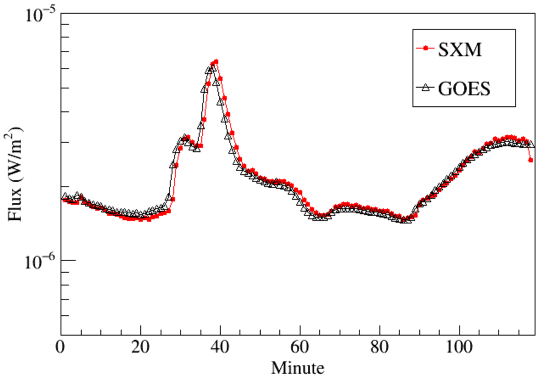

Figure 3. SXM and GOES X-ray one-minute fluxes during the period of orbit 1823 of CE-2 flight. This orbit started at 11:30:54 and ended at 13:28:43 on 6 March 2011 (UTC). The red point represents SXM data and the black triangle represents GOES data.

Acknowledgments: This research is supported by FDCT in Macao (Grant Nos. 048/2012/A2, 039/2013/A2, and 091/2013/A3).

References: [1] Peng W. X. et al. (2009) *Chinese Physics C*, *33*, 819. [2] Dong W. D. et al. (2016) *RAA, 16(1)*. [3] Clark P. E. and Trombka J. I. (1997) *JGR, 102*, 16361. [4] Cui X. Z. et al. (2014) *Solar Phys.*, *289*, 1597-1606. [5] Peng W. X. (2009) *Ph.D. thesis, University of Chinese Academy of Science*.

INVESTIGATION ON THE DEPTH-TO-DIAMETER RATIO OF SUB-KILOMETER CRATERS ON THE MOON. S. Sun, Z. Yue, K. Di, State Key Laboratory of Remote Sensing Science, Institute of Remote Sensing and Digital Earth, Chinese Academy of Sciences (P.O. Box 9718, Datun Road, Chaoyang District, Beijing 100101, China. sunsj@radi.ac.cn, yuezy@radi.ac.cn, dikc@radi.ac.cn).

Introduction: Most of the lunar surfaces are covered by patches of small craters, and the morphological study of small fresh craters is important for our understanding of the impact process and the target properties. Due to the limitation of image resolution, previous studies on crater morphologies mainly focused on craters with diameters larger than 1 km diameter [1-4],. Recent lunar missions such as Lunar Reconnaissance Orbiter (LRO) [5] and Chang'E 2 orbiter [6] had acquired massive high resolution data and made it possible to expand this research into smaller craters.

The ratio of depth (d) to diameter (D) has long been used as a simple descriptor of crater morphology. In earlier studies [1, 7], the d/D ratio is considered as ~0.2 for most simple craters on the Moon. Recently, Mahanti et al. [8] studied the small lunar craters with diameters range from 20 m to 200 m using Lunar Reconnaissance Orbiter Camera (LROC) Narrow Angle Camera (NAC) products and concluded that the d/D ratio is ~0.13. Dauber et al. [9] made similar statistics on craters with diameters range from 17 m to 918 m at two regions on the Moon and get an average d/D ratio of ~0.10. According to Melosh [10], lunar craters with diameter less than 400 m may be dominated by target strength. The d/D ratio of small fresh lunar craters may reflect the properties of target (regolith and bedrock). Therefore, study of small fresh lunar craters is of great significance for future lunar landing missions.

In this research, we use the recently acquired LROC NAC data to perform a comprehensive study on the the depth-to-diameter ratio of the small fresh crater both in lunar mares and in lunar highlands, aiming toprovide reliable measurenents and contribute to the understanding of the related formation mechanism.

Data: In total, 14 experimental regions are selected, including 6 mare regions and 8 highland regions. All these regions are covered by NAC digital elevation models (DEMs) with pixel scale of 2.0 m. The 6 mare regions consist of five Apollo landing sites (except for Apollo 16, which landed in Highland) and one mare region located near Apollo 14 landing site. The 8 highland regions are distributed evenly on the moon. NAC mapping products, including orthophotos and DEMs, are used for identifying small fresh craters and measuring depth and diameter. The data used in this research was downloaded from homepage of LROC (http://lroc.sese.asu.edu/). Most DEMs and corresponding orthophotos at Apollo landing sites have been co-registered except for Apollo 12. There is an offset between the DEM and orthophoto at Apollo 12 landing site, therefore the orthophoto needs to be co-registered to the DEM before identification of craters.

Method: Small fresh craters are identified manually from NAC orthophotos. Craters that are less than 10 pixels are rejected. Rim-to-rim diameter D is measured using ArcMap and CraterTools [11]. The depth of small fresh craters is determined by the difference of the elevation of the lowest point and the average rim elevation.

For the smaller craters with diameter less than 10 m, it is difficult to determine if they are fresh craters only with the orthophotos. We made the hillshade maps from the corresponding DEM products to verify if they are indeed fresh craters. With the help of hillshade maps, a portion of small craters that are not fresh are sifted out.

Results: Table 1 shows the number of small fresh craters that are selected in all the experimental regions. The distribution of small fresh craters is inhomogenous on the lunar surface. In some regions only dozens of small fresh craters are selected, but hundreds of small fresh craters can be found in other regions.

The statistics of our research is illustrated in Table 2. There are totally 1515 small fresh craters selected, with 483 located in mare regions and 1046 in highland regions. The diameter of all these craters ranges from 7.51 m to 352.38 m, while the depth ranges from 0.31 m to 67.34 m. The mean depth-to-diameter ratio of these craters is 0.12, which is in good agreement with that of Mahanti et al. [8] and Dauber et al [9]. The d/D ratios in lunar mares and highlands are generally the same.

Fig. 1 demonstrates the depth-diameter relationship of all the small fresh craters. Consistent with the above statistics, there seems no apparent difference between mare and highland craters. We can also observe from the figure that the d/D ratios of both highland craters and mare craters appear more scattered at smaller diameters. This indicates that the target property may affect the morphologies of smaller craters more than that of larger sub-kilometer craters.

Conclusion: In this research, we conducted an initial investigation on the d/D ratio of sub-kilometer craters on lunar surface using high resolution images and related mapping products. The fresh craters are sampled both from lunar mares and highlands. The results show that the ratios in the sampled craters are about 0.12, which is lower than that of the craters with diameters larger than 1 kilometer. The lower ratio is probably caused by the strength properties of the shallow surface and subsurface. In the future, detailed formation mechanism of small craters should be further studied by means of numerical simulation and/or physical experiment.

Table 1. Number of small fresh craters before and after sifting by hillshade maps.

Region	Coordinates (N, E)	No. of craters before sifting	No. of craters after sifting	Percent of sifted craters (%)
Mare1	(0.65,23.51)	67	62	7.46
Mare2	(-3.04,-23.42)	39	34	12.82
Mare3	(-3.66,-17.48)	120	111	7.50
Mare4	(26.08,3.65)	75	66	12.00
Mare5	(20.17,30.77)	112	106	5.36
Mare6	(-14.66,-8.94)	112	103	8.04
Highland1	(-43.90,153.90)	127	116	8.66
Highland2	(-8.99,15.51)	161	156	3.11
Highland3	(-41.84,95.94)	44	38	13.64
Highland4	(47.07,166.93)	69	62	10.14
Highland5	(5.92,161.42)	206	198	3.88
Highland6	(3.58,-100.13)	89	77	13.48
Highland7	(47.58,-116.11)	54	46	14.81
Highland8	(-47.95,-73.23)	411	354	13.87

Table 2. Statistics of small fresh craters.

Region	Mare	Highland	Total
Number of craters	483	1046	1515
minimum d (m)	0.60	0.31	0.31
maximum d (m)	67.34	31.86	67.34
minimum D (m)	7.54	7.51	7.51
maximum D (m)	352.38	170.22	352.38
mean d/D	0.12	0.12	0.12
standard error (m)	0.04	0.04	0.04

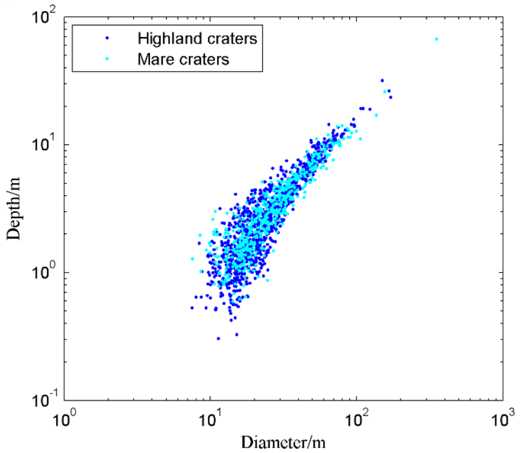

Figure 1. Depth vs. diameter of small fresh craters.

Acknowledgment: This study was supported by National Natural Science Foundation of China under Grant 41590851.

References: [1] Pike R. (1977) *LPS VIII*, 3427-3436. [2] Baldwin R. B. (1965) *The Astron. J.*, 70-545. [3] Pike R. J. (1980) *Moon*, 2159-2189. [4] Cintala M. et al. (1977) *LPSC VIII*, 3409-3425. [5] Robinson M. et al. (2010) *Space Sci. Rev.*, 150(1), 81-124. [6] Zhao B. et al. (2011). *Sci. China Tech. Sci.*, 54, 2237- 2242. [7] Pike R. J. (1974) *Geophys. Res. Lett.*, 1(7), 291-294. [8] Mahanti P. et al. (2014) *LPSC 45*, Abstract #1584. [9] Daubar I. J. et al. (2014) *JGR*, 119(12), 2620-2639. [10] Melosh H. J. (1989) Oxford University Press. [11] Kneissl T. et al. (2011) *Planet. Space Sci.*, 59(11), 1243-1254.

A QUANTITATIVE STUDY OF SUBDIVISION INDEXES OF LUNAR CRATER MATERIAL. J. T. WANG[1,2], J. Z. LIU[1], D. J. GUO[1,2] and J. Z. JI[1,2], [1]Center for Lunar and Planetary Sciences, Institute of Geochemistry, Chinese Academy, Guiyang 550081,China (e-mail for first author: wjtao27@163.com), [2]University of Chinese Academy of Science, Beijing 100049, China.

Introduction: On the moon, crater is one of the main structural styles, and the distribution of impact crater material can reflect the history of the transformation of the lunar crust. In actual lunar geologic mapping, crater material is also one of the most important features. Therefore, the study of crater material is very important and necessary. Among recent researches, crater material was usually divided into five units: central peak, crater floor, crater wall crater rim and radial ray. Crater material subdivision indexes, which are crucial to the scientificity and accuracy of mapping, were always described subjectively and qualitatively in former study. Unfortunately, the differences in material composition and the influence of terrain type were paid little attention.

To compare the effects of crater diameter, age and terrain type on crater material subdivision units, we studied the 1631 craters whose ages are certain and diameters are less than 300Km in the Lunar Crater Database (2015) released by the LPI, by using of the LOLA data and LORC data in Lunar Reconnaissance Orbiter mission, Clementine UVVIS multispectral data and optical maturity data (OMAT), Chandrayaan-1 M3 and Chang'e-1 IIM. Firstly, we classified those craters with the optimal segmentation method based on crater diameter, depth and floor diameter. Then, the variation of slope gradient, texture, maturity and composition characteristics was investigated. Initial investigation shows that crater slope gradient in Highlands is larger than in Maria, which indicates that there is discrepancy in their degree of collapse because of their bedrock. Our study will make it clear that the indication of crater material for the evolution of the Moon, and acquire the quantitative indexes for subdivision crater material. We hope that our study of the crater material will be helpful for the ongoing Chinese geologic mapping program of the moon.

Acknowledgements: This work was supported by the National Natural Science Foundation of China (Grant No. 41490634 and No.41373068) and National Science and Technology Infrastructure Work Projects (Grant No. 2015FY210500).

The equilibrium state of crater populations on the impact deposits of the lunar Orientale basin.

Mengjiao Wang[1] and Zhiyong Xiao[1]. [1]Planetary Science Institute, China University of Geosciences (Wuhan). (zyxiao@cug.edu.cn; wmj717@sina.com).

Introduction: The Orientale basin (*D*=930 km; 20 ° S, 95 ° W) at the western limb of the lunar nearside is the youngest multiring basin on the Moon, which was formed sometime between ~3.85-3.72 billion years ago [1, 2]. The formation of Orientale has long been regarded as the kick point at which the impactor population on both the Moon and the other inner Solar System bodies has changed [e.g., 3, 4]. Before its formation, the inner Solar System has gone trough an intense bombardment history terminated by the hypothesized Late Heavy Bombardment and that crater population was entitled as the Population 1 craters [3]. After its formation, the impact flux in the inner Solar System has dramatically decreased and the impactor size-frequency distribution (SFD) has been more or less stabilized, forming a crater population entitled Population 2 [3].

Recent advances on lunar sample dating [5], crater population analyses [6], and orbital dynamic modeling [7] suggest that the shift from Population 1 to Population 2 may not be as late as the formation of the Orientale basin, and the cratering history predating Orientale may also be much more complicated. One of the observational bases for these arguments is the crater density and SFD for large impact basins older than Orientale [6]. However, the heavily cratered regions on both the Moon and all terrestrial planets have archived the equilibrium state for craters less than certain diameters before the Orientale impact (hereafter we do not use saturation or saturation equilibrium, because they have different meanings literally). Crater equilibrium renders the measurements for crater densities on older terrains unreliable in both absolute and relative senses.

Evaluating the equilibrium state of crater population is critical for age dating using crater statistics. For crater populations accumulated on terrains older than Orientale, empirical equilibrium densities were referred to judge their equilibrium states [e.g., 6, 8], which has recently been proved to be problematic [9]. On the other hand, performing systematically crater counts could recognize the crater production population (hereafter the production population referred to secondaries plus primaries that are not in equilibrium, not only primaries defined in traditional nomenclature) within certain diameter ranges, and identity the equilibrium state, i.e., both the equilibrium onset diameter (D_{eq}) and the SFD for the portion of the crater population that is in equilibrium. The Cayley Plain at the Apollo 16 landing site is interpreted to be ejecta deposits from either the Imbrium or Nectaris basin [cf. 9], which is nevertheless older than the Orientale impact. The D_{eq} over the Cayley Plain is ~850 m, which is substantially smaller than that over the oldest surface on the Moon [9], suggesting that the impact flux has been substantially decreased since the Cayley Plain was emplaced. However, the equilibrium state for the crater population on the ejecta deposits of Orientale is not constrained, which is another critical data point on understanding the change of impactor population and impact flux in the inner Solar System.

Methods: Using the ~7 m/pixel global mosaic obtained from the Terrain Camera onboard the KAGUYA spacecraft [10] and the Clementine color-ratio mosaic (a color image of three channels represented by three UVVIS camera bands: red=750 nm/415 nm, green=750 nm/950 nm; blue=415 nm/750 nm) [11], we selected 4 areas on the relatively smooth surfaces in the southwest quadrant of the Montes Rook Formation (Figure 1), which is thought to be composed of impact melt [13] (Area 1, Area 2, Area 3, Area 4; Figure 1), and collected the crater populations over this area. Surfaces with complicated topography and obvious secondary crater clusters or chains were avoided. The counting areas selected are homogeneous as seen in both the monochrome and multi-band color-ratio mosaic.

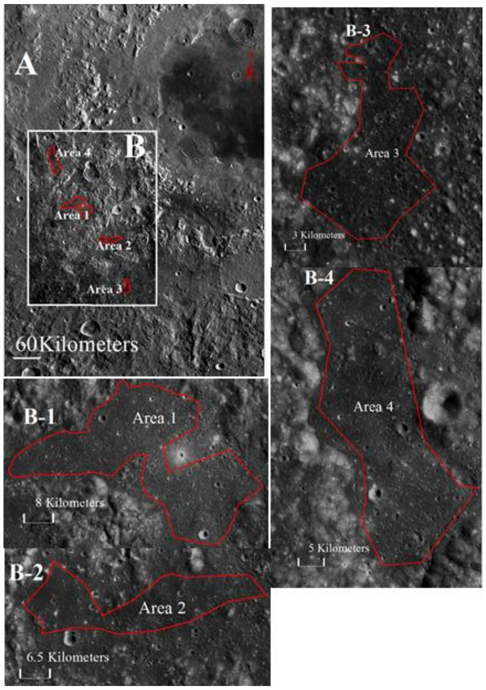

Figure 1. Counting areas of Orientale. LORC WAC image (A; WAC_GLOBAL_E300S2250_100M; 100 m/pixel) shows the locations of counting areas (B) together. Kaguya mosaics (~7 m/pixel) show Area 1 (B-1), Area 2 (B-2), Area 3 (B-3), Area 4 (B-4), respectively.

CraterTools [14] and CraterStats [15] are the main tools employed to collect the craters and perform the data analysis. To ensure the accuracy and completeness of statistics, we have searched craters as small as 30 m to make sure that the datasets are completed to craters ≥100 m in diameter. The datasets have been cross-checked for multi-times by both the authors.

Result and implication: The SFD of crater populations collected at the 4 counting areas are shown at Figure 2. Our results show that: (1) the SFD of Area 1 and Area 4 have cumulative slopes about -1 at *D*<~460 m, and about -3 at *D*>~460 m; (2) the cumulative slopes for Area 2 are about -1 at *D*<~270 m, about -2 at ~270-460 m and about -4 at *D*>~460 m; (3) the cumulative slopes of Area 3 are about -2 at *D*<~460 m and about <-2 at *D*>~460 m. Obviously, the four counting areas all have a change of slope at 460 m; (4) They are almost consistent with each other in density except some variations such as Area 3 has a higher density than others at ~130-230 m.

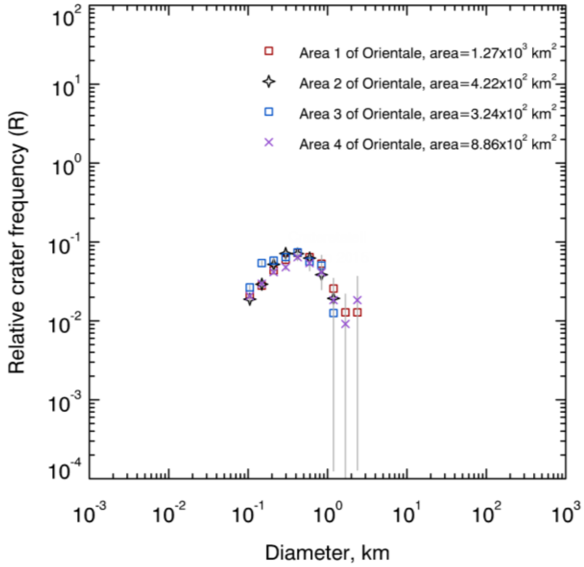

Figure 2. R plot for the four counting areas at the Orientale basin.

Crater populations on different-aged surfaces (the most heavily cratered area on the Moon, Cayley Plain, Sinus Medii, Copernicus and Tycho is from [9]) are compared in Figure 3 in the form of R plot [16]. Our preliminary result further prove the decreased impact flux when the Orientale basin was formed. We will introduce the indication of this study on the conference.

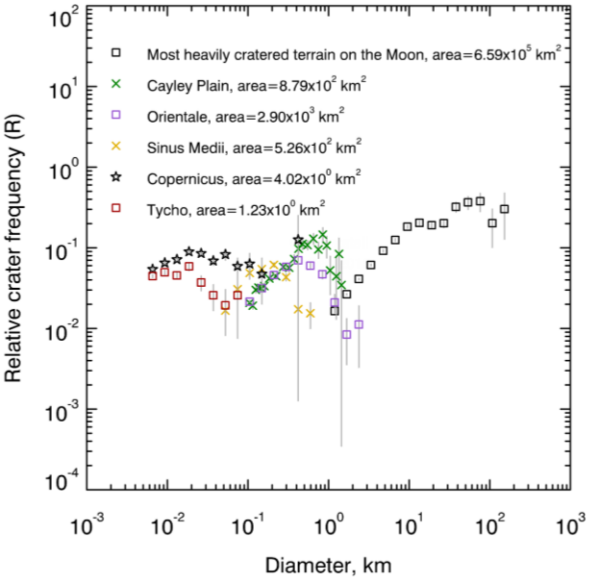

Figure 3. R plot for different-aged surfaces on the Moon, data from this study and [9].

Acknowledgements: This study is supported by National Natural Science Foundation of China (No. 41403053) and fund CUG130106 of China University of Geosciences (Wuhan).

References: [1] Wilhelms D. (1987) USGS Spec. Pub.1348. [2] Bussey D. B. J. and Spudis P. D. (1997) *Geophys. Res. Lett.*, *90*, 1151–1154. [3] Strom R. G. et al. (2005) Science, 309, 1847-1850. [4] Strom, R. G. et al. (2015) *Res Astron Astrophys*, *15*(3), 407-434. [5] Norman M. D. and Nemchin A. A. (2014) *Earth Planet Sc Lett* 388, 387-398. [6] Fassett C. I. et al. (2012) *J. Geophys. Res. Planets 117*(E00H06). [7] Morbidelli A. et al. (2012), *Earth Planet Sc Lett* 355-356, 144-151. [8] Marchi S. et al. (2012) *EARTH PLANET SC LETT*, *325*, 27-38. [9] Xiao Z. and Werner S. C. (2015) *J. Geophys. Res. Planets* 120, 2277-2292. [10] Haruyama J. et al (2008) Earth Planets Space 60, 243-255. [11] Pieters C. M. et al. (1994) *Science*, *266* , 1844-1848. [13] Spudis P. D. et al. (2014) *J. Geophys. Res. Planets* 119, 19-29. [14] Kneissl T. et al. (2011) Planet Space Sci 59, 1243-1254. [15] hrscview.fuberlin.de/craterstats.html. [16] Crater analysis techniques working group (1979) *Icarus*, 37, 467 –474.

Chang'E Microwave Radiometer Data Re-Calibration by Data Mining

K. T. Tsang[1], G. P. Hu[2] , Y. C. Zheng[3], Y. Li[4] and Z. Z. Wang[4]

[1]Statistics Program, Division of Science & Technology, United International College, BNU-HKBU, Zhuhai, China (kentsang@uic.edu.hk); [2]Lunar Planetary Science Laboratory of Macau University of Science and Technology & Partner Laboratory of Key Laboratory of Lunar and Deep Space Exploration of Chinese Academy of Sciences, Macau; [3] Key Laboratory of Lunar and Deep Space Exploration, National Astronomical Observatories, Chinese Academy of Sciences, Beijing, China; [4] Key Laboratory of Microwave Remote Sensing Technology, Chinese Academy of Sciences, Beijing, China

Introduction: Following common practice in microwave remote sensing, raw data from multi-channel microwave radiometers (MRM) onboard the Chinese Chang'E lunar obiters (CE1 & CE2) were acquired as observational antenna voltages, which were then calibrated and converted to brightness temperatures (TB) by a two-point calibration procedure [1]. Subsequently they were distributed to the scientific community as the Level 2C MRM data in PDS format.

While the CE cold calibration antenna is supposed to point to the deep space and taking data for the cold reference point in the two-point calibration scheme [3], in reality, it picked up some undesirable thermal microwave radiation from the lunar surface due to its cone-shaped field of view. Thus the "cold" reference point is not exactly as cold as the 2.7K cosmic background and this affects the quality of the calibration.

As a consequence, minor but puzzling differences between the two sets of Level 2C MRM data released for CE1 & CE2 are quite visible. The discrepancy is much more than can be explained by data accuracy, or seasonal variations. However, it can be easily explained by difference in orbital altitudes between CE1 & CE2, plus the fact that the cold antenna was poluted by thermal radiation from the lunar surface [2,3,4].

Methodology: In this work, quite different from previous efforts [3,4], a data-mining approach is applied to pre-Level 2C (voltage) data directly. Since all the antenna voltage data (Vobs, Vc and Vh) as well as Th in the "Two-point calibration" Equation are directly measurable, statistical learning algorithms can be employed to obtain a single set of statistically-consistent TB by combining raw data from CE1 & CE2. In this process, an optimized set of Tc, which is difficult to calculate from first principle due to the precise direction the cold antenna pointing to and the extent of contamination by thermal radiation from lunar surface are uncertain, can be 'learned/mined' from the combined set of MRM data.

Results: The general methodology stated above can be applied to data from specific locations on lunar surface. The figure below shows the diurnal cycle for TB(37GHz) after re-calibration of CE2 data from Apollo 17 landing site, with a standard error for the residuals at 1.14K and a effective/optimized cold antenna temperature at 47.78 K, which is considerably higher than 2.7K.

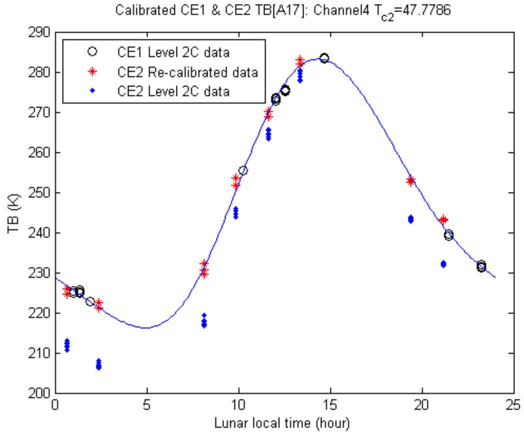

References:

[1] Z.Z. Wang, Li, Y., Zhang, X.H., Jiang, J.S., Xu, C.D., Zhang, D.H., Zhang, W.G., "Calibration and brightness temperature algorithm of CE1 Lunar Microwave Sounder (CELMS)," Sci. China Ser. D Earth Sci., vol. 53, no. 9, pp. 1392-1406, 2010.

[2] K.L.Chan, S.F.Sum, Y.C. Zheng, K.T. Tsang, L.H. Yu,"Alignment of CE1 & CE2 Microwave Data", International Forum on Lunar and Deep Space Exploration, Beijing, September 2013.

[3] K.T. Tsang, S. Fu, J. Gu, M. Zhou, K.L. Chan, and Y.C. Zheng, "A Statistical Learning Approach to Chang'E Microwave Radiometer Data Calibration", the 2014 11th International Conference on Fuzzy Systems and Knowledge Discovery (FSKD 2014) Paper ID : P1321.

[4] K.T. Tsang, S.Y. Liu, Y.R. Ren, K.L. Chan, and Y.C. Zheng "Chang'E Microwave Radiometer Data Calibration by Machine Learning" 2nd Beijing International Forum on Lunar and Deep-space Exploration (LDSE) Sep 7-10, 2015.

Acknowledgement: This work was supported by following research grants: R201626 from United International College, Beijing Normal University-Hong Kong Baptist University, Zhuhai, China, and MLF 2015009 from Key Laboratory of Microwave Remote Sensing Technology, Chinese Academy of Sciences, Beijing, China, and Grant from Lunar and Planetary

Science Laboratory, Macau University of Science and Technology, Macau, China.

A ROCK MODEL FOR CHANG'E MICROWAVE RADIOMETER DATA

G. P. Hu[1,2], Y. C. Zheng[1,2,3], K. L. Chan[1,2] and A. A. Xu[1,2]
[1]Space Science Institute, Macau University of Science and Technology, Macau (gphu@must.edu.mo);[2]Lunar Planetary Science Laboratory of Macau University of Science and Technology & Partner Laboratory of Key Laboratory of Lunar and Deep Space Exploration of Chinese Academy of Sciences, Macau;[3] Key Laboratory of Lunar and Deep Space Exploration, National Astronomical Observatories, Chinese Academy of Sciences, Beijing 100012, China

Introduction: The microwave radiomoters(MRMs) on the Chinese lunar orbiters, Chang'E-1 (CE-1) and Chang'E-2 (CE-2), have measured microwave emission of the lunar surface at four frequency channels: 3, 7.8, 19.35 and 37 GHz [1]. Many anomalous "cold spots" in the 37GHz nighttime map, located at fresh craters (for examples: Tycho, Aristarchus and King) were discovered [2],[3]. The catalogue of lunar thermal anomalies has been compiled to correlate their topographic features and thermal properties of the surface.

Our previous work has established a TB computational model with the topographic effect to explain the TB undulation with respect to the latitude along the profile over old craters [4],[5]. Based on this model, the simuation without rocks over fresh crater can't fit the observation well. Therefore, a rock model has been poposed based on this model to fit the observation measured along the profile of craters in one track. Moreover, the anomalous thermal properties (cold and hot spots) of the microwave emission from the lunar surface in the 37GHz microwave map of the moon can be explained.

Methodology: In this work, the lunar regolith of the fresh crater is divided into 47 layers: the mixed layer, the lunar regolith (45 sublayers) and rock bedrock layer (Fig.1). Here the rocks in our model are limited to the meter-scale rocks on the lunar surface, and the scattering effect of the rocks on the microwave emission at the 37GHz channel is negligible.The mixed layer is made up of rock fragement and lunar dust, and its thermal properties (TP) is modeled as the mixture of rock and dust. The TP of the mixed layer are modeled as: $TP_{rock} \times Ra + (1 - Ra) \times TP_{dust}$, where Ra stands for the rock abundance. The thermal properties of the lunar dust are applied the above model in section 3.1. The Rock modeled a priori using the properties for vesicular basalt described by Horai and Simmons [6]. We used a density of 2940 kg/m^3, thermal conductivity of 1.491 W/(m•K), and a temperature dependent heat capacity of ($-154.9+4.983\,T-0.008207\,T^2 + 0.000005192\,T^3$) J/(kg•K), where T is temperature in K.

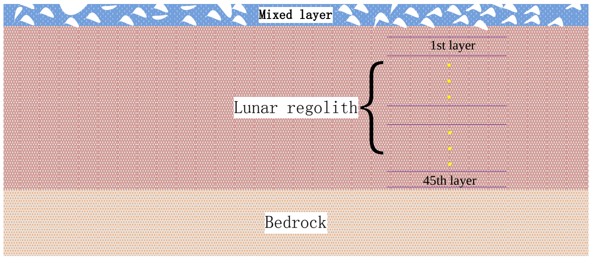

Fig.1 The schematic diagram of the rock model. Rocks and lunar dust constitute the mixed layer.

Results: As an example, Fig.2 shows that the whole variation trend of the simulations with rocks is consistent with that of the observations over crater King. The rock model fits the observation better than the non-rock model. It can be inferred that rocks significantly affect the variaion trend of the TB variation, considering the low iron and abundance over the crater.

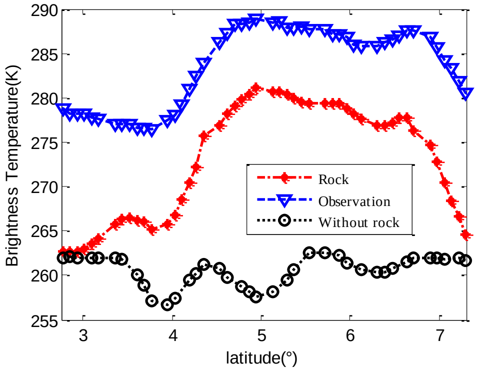

Fig.2 TB variation at 37GHz against the latitude along the profile of crater King based on DEMs (256pp LROC data).

References: [1] Y. Zheng, et al., (2008), PSS, 56, 881-886. [2] Y. C. Zheng, et al., (2012), Icarus, 219,194-210. [3] K. L. Chan, et al., (2010), EPSL, 295(1-2), 287-291. [4] G. P. Hu, et al., (2014) IEEE T GEOSCI REMOTE, 52(8), 4499-4510. [5] G. P. Hu, et al., (2016) IEEE T GEOSCI REMOTE, 54(3), 1598-1609. [6] K. Horai and G. Simmons, (1972), PAA, 28, 243-267.

Acknowledgement: This work is supported by Science and Technology Development Fund in Macao SAR 048/2012/A2 and 039/2013/A2, and the NSFC program (41490633). The CE data was supported by the Key Laboratory of Lunar and Deep Space Exploration (2013DP173157), National Astronomical Observatories, Chinese Academy of Sciences, Beijing 100012, China.

ANCIENT SELENOPHYSICAL STRUCTURE OVER THE GRIMALDI CATER: CONSTRAINTS FROM GRAIL GRAVITY AND LOLA TOPOGRAPHY.

Z. Zhong[1] and J. G. Yan[2]. [1]School of Physics and Electronic Science, Guizhou normal University, 116 Baoshanbei Road, Guiyan 550001, Chian (zzhong@gznu.edu.cn); [2]State Key Laboratory of Information engineering in Surverying, Mapping and Remote Sensing, Wuhan University, 129 Luoyu Road, Wuhan 430079, China (jgyan@whu.edu.cn).

Introduction: The impacting crater Grimaldi is nearly located on the western limb and lies to the southwest of the Oceanus Procellarum. An obvious positive gravity anomaly exists in its low-lying inner wall, implying the subsurface mass concentration beneath the crater. Exploration on this crater could practically address a meaningful and fundamental understanding of a giant impacting process and the structure of mare basins/craters [1]. Confined by the low-resolution of previous gravity field models, it was once impossible to explore the structure beneath Grimaldi. The recent high-resolution gravity data from GRAIL (Gravity Recovery and Interior Laboratory) mission make it possible to break through the dilemma [2].

Combined with the high-resolution topography data from LOLA (Lunar Orbiter Laser Altimeter) [3] and a develped loading model, an admittance analysis is successfully performed between the high-resolution gravity and topography. Within 1σ STD error constraints, we have successfully estimated the best-fitting parameters over the crater Grimaldi.

Results. Our results indicate the predicted admittance spectra highly match with their corresponding observations (see Fig.1), indicating a feasibility of our model employed here. A large load ratio (~2.0) is found over Grimaldi, implying an indispensable subsurface load beneath the crater. Moreover, a more dense crustal density (2820 kg m^{-3}) is found here, which lies between the densities of anorthosite and norite. This result suggests a mixed crust from the anorthositic upper and noritic lower crusts, revealing a possible excavated upper crust in the process of impact cratering.

Finally, All the estimated elastic thicknesses are larger than 50 km, indicating a possible large elastic thickness existed around Grimaldi. Taking into account fewer thermal activities existed on the lunar limb or farside than its nearside, a possible cold lithosphere existed here to developed a thick elastic thickness.

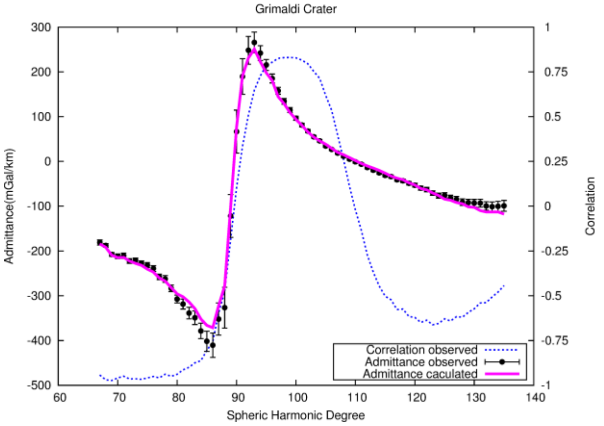

Fig.1 Correlation spectrum observed (dotted line), admittance spectrum observed (error bar) and admittance spectrum modeled (solid line) for crater Grimaldi

References: [1] Jofflif B. L. et al. (2006) Mineralogical Society of America, 721p. [2] Konopliv A. S. et al. (2013) *JGR*, 118, 1415-1434. [3] Smith D. E. et al. (2010) *GRL*, 37, 1-6.

Additional Information: If you have any questions or need additional information regarding the preparation of your abstract, call the PSI (67883001, or send an e-mail message to ispls2016@cugpsi.org).

A Four-way Lunar Lander-Orbiter Relay Tracking Mode for Chang'E-5 and Chang'E-4 mission. M. Ye[1], J. G. Yan[1], F. Li[1,2] ,W. F. Hao[2], W. T. Jin[1] and X. Yang[1], [1]State Key Laboratory of Information Engineering in Surveying, Mapping and Remote Sensing, Wuhan University,Wuhan 430079, China. (e-mail mye@whu.edu.cn); [2]Chinese Antarctic Center of Surveying and Mapping, Wuhan University,Wuhan 430079, China.

Introduction: Chinese Chang'E-5 mission is the third phase of Chinese Lunar Exploration Program(CLEP), its main target is to collect and return lunar samples. After that, the Chang'E-4 spacecraft will be sent to the farside of the Moon on schedule. In this paper, we present a novel tracking mode—Four-way lunar Lander-Orbiter relay tracking mode that possibly can be employed during the Chang'E-5 and Chang'E-4 mission. The mathematical formulas for the Four-way lunar Lander-Orbiter (4W L-O) tracking mode are given and implemented in our newly-designed lunar spacecraft orbit determination and gravity field recovery software, the LUnar Gravity REcovery and Analysis Software/System (LUGREAS)[1]. The simulated observables permit analysis of the potential contribution Four-way lunar Lander-Orbiter tracking could make to precise orbit determination for the Orbiter.

4W L-O RR mathematical model: Fig. 1 gives the 4W L-O tracking mode. The 4W L-O tracking mode adds an extra link between the lander and the orbiter. A transmitter frequency is sent from the earth tracking station T_i at epoch i to the orbiter S_{j} at epoch j. Since the transponder delay at the orbiter and lander can be disregarded for the purposes of simulation in our study, the signal is instantaneously transmitted to the lunar lander L_k at epoch k. From the transponder, the signal is re-transmitted back to the orbiter S_m at epoch m and the tracking station T_n at epoch n will receive the down link signal. Through light time solution process[2], all participants' state vectors and their corresponding time tag could be calculated from $T_n -> S_m -> L_k -> S_j -> T_i$. Assume $X(j)$ as the positon vector of the participant j in BCRS. The four range links are as follows:

$$R_1 = \left| X(S_m) - X(T_n) \right| \tag{1}$$

$$R_2 = \left| X(S_m) - X(L_k) \right| \tag{2}$$

$$R_3 = \left| X(S_j) - X(L_k) \right| \tag{3}$$

$$R_4 = \left| X(S_j) - X(T_i) \right| \tag{4}$$

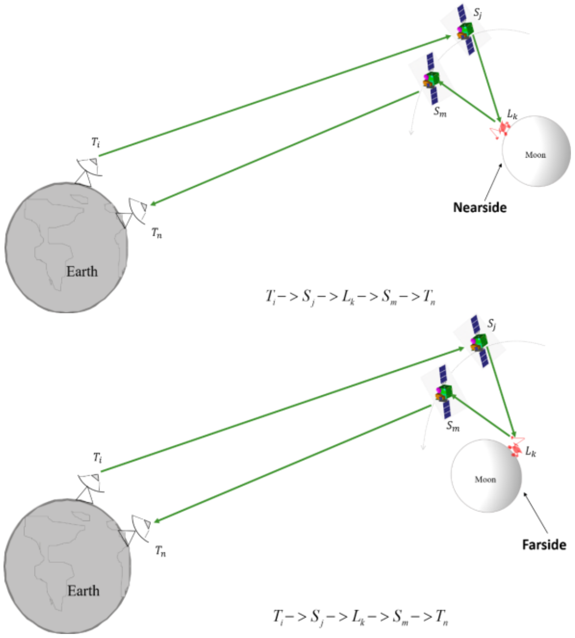

Fig. 1 the Four-way Lander-Orbiter tracking mode

The 4W L-O Range is defined as:

$$\begin{aligned} R &= \left(R_1 + c \cdot RLT_{nm}\right) + R_2 + R_3 + \left(R_4 + c \cdot RLT_{ij}\right) + \\ &\quad c \cdot \left[TDB(i) - UTC(i)\right] - c \cdot \left[TDB(n) - UTC(n)\right] \\ &= c \cdot \left[UTC(n) - UTC(i)\right] \end{aligned} \tag{5}$$

The 4W L-O Range Rate observables are calculated as a difference of ranges between the starting Doppler count time T_s and the end Doppler count time T_e at the receiving tracking station. At each of the two time tags, we extract a 4W L-O R observable, R_s and R_e, from Equation (5). The 4W L-O RR is given as:

$$RR = \frac{\left(R_e - R_s\right)}{T_c} \tag{6}$$

Where the T_c is the Doppler integration interval and equals to $T_e - T_S$.

Simulation study: The 4W L-O tracking measurement type was implemented in LUGREAS. In our simulation study, we set the scenario time to Oct. and Nov. 2017 and designed a circular orbit at a height of 200 km for the Orbiter and chose Oceanus Procellarum (18.4 ° N, 57.4 ° W) as the landing site for the Lander. The tracking station include two stations, Kashi and Qingdao. We used LUGREAS to generate 2W RR and

4W L-O RR observables, added 1 mm/s (1 sigma) noise and 2 mm/s bias to them. With these simulated observables, we investigated the potential contribution 4W L-O RR could make to the Orbiter orbit precision by comparing with the traditional 2W RR observables. In each arc, 50 meters errors are added to the initial orbit position randomly, and the most important systematic errors, including the Lander position error of 50 m deviation and gravity error with a factor of 3 of the gravity field coefficient uncertainty, are also added in our reduction run. Table 1 shows the POD results. It could be seen that after combining 4W RR observables, the accuary of the precision orbit determination for the Orbiter is improved significantly, with the biggest improvement being one order of magnitude, and the Lander position could be constrained to sub-meter level. Fig. 2 illustrate the orbit ephemeris differences between post-fit orbit and the true value in the Radial, Transverse, and Normal directions in J2000. Further investigation shows that the 4W L-O RR observables have better geometric constraint on the orbit, and are more sensitive to the initial orbit elements than the traditional two-way range rate that only tracks data between the earth station and lunar orbiter.

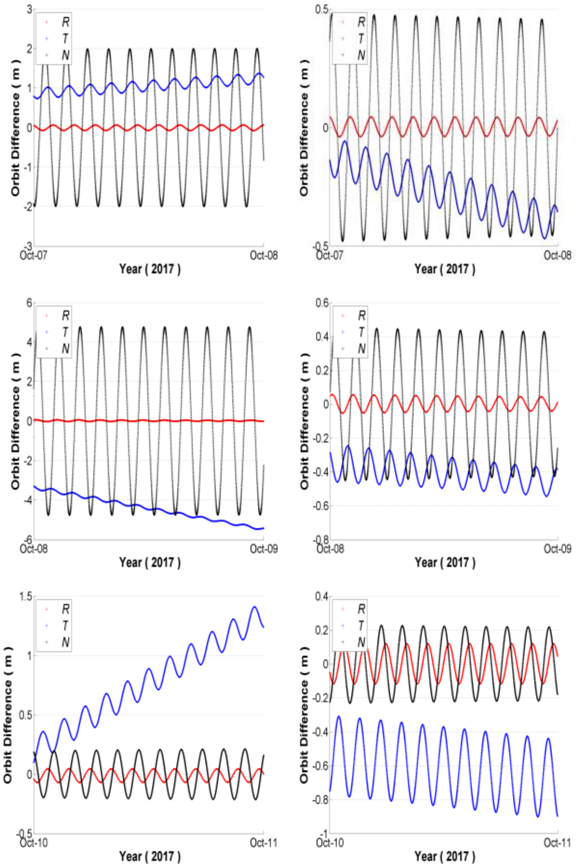

Fig. 2. The orbital differences between the post-fit orbit and true values for the arcs on Oct 7, 8, and 10, 2017. The left column show the 2W RR case, and the right column show the combined case

Conclusion: We proposed a Four-way lunar Lander-Orbiter tracking mode for the upcoming Chang'E-5 mission. The specific mathematical model was given and implemented in our POD software. Using the simulated 4W L-O RR observables, we investigated the contribution our method could make to the precision orbit determination of the Orbiter, finding that after combing the Four-way lunar Lander-Orbiter Range Rate data with the traditional two-way range rate data and considering the Lander position error and lunar gravity field error, the accuary of the precision orbit determination for the Orbiter was improved significantly, with the biggest improvement being one order of magnitude, and the Lander position could be constrained to sub-meter level. This new tracking mode could provide a reference for the Chang'E-5 and Chang'E-4 mission and has enormous potential for the positioning of future lunar farside lander due to its relay characteristic.

References: [1] F. Li, M. Ye, J. G. Yan et al. (2016). Adv. Sp. Res. doi:10.1016/j.asr.2016.03.007. [2] Moyer T. D. (1971), JPL-TR-32-1527.

Table 1 Initial orbit position difference and the Lander positon difference between solution and true one (fixed bias values, with the Landers position error of 50 m deviation and gravity error with a factor of 3 of the gravity field coefficient uncertainty).

Arc No. YYYY-MM-DD	Initial orbit position(m)								Estimated Lander position errors(m)			
	2W RR				2W RR + 4W RR							
	ΔX	ΔY	ΔZ	Errors	ΔX	ΔY	ΔZ	Errors	ΔX	ΔY	ΔZ	Errors
2017-10-07	1.04	-1.78	-0.32	2.08	-0.20	0.32	0.12	0.39	0.13	-0.03	-0.35	0.37
2017-10-08	-1.63	2.31	-2.33	3.66	-0.17	0.13	-0.21	0.30				
2017-10-10	-0.11	0.14	0.12	0.22	0.75	-0.04	-0.22	0.79				
2017-11-04	-0.39	0.18	0.61	0.75	0.15	-0.08	-0.33	0.37				
2017-11-05	-1.11	0.52	0.43	1.30	0.34	-0.12	-0.16	0.39				
2017-11-06	-0.12	0.05	-0.06	0.15	0.53	-0.15	0.24	0.60				

SURFACE ROUGHNESS OF MERCURY AND THE MOON AND RELATIONSHIP TO GEOLOGIC PROCESSES.

Yuzhen Cai[1], Wenzhe Fa[1,2], Zhiyong Xiao[3,2], Wei Tian[4], [1]Institute of Remote Sensing and Geographical Information System, Peking University, Beijing 100871, China (yzcai@pku.edu.cn, wzfa@pku.edu.cn), [2]Lunar and Planetary Science Laboratory, Macau University of Science and Technology, Macau, China, [3]Planetary Science Institute, School of Earth Sciences, China University of Geosciences (Wuhan), China, [4]School of Earth and Space Sciences, Peking University, Beijing, China.

Introduction: Volcanism and impact cratering are two dominant geologic processes on Mercury and the Moon. Volcanism produces various landforms like lava flows, domes, cones and sinuous rilles. Among these, lava flows are the most widely distributed features that have different surface textures (e.g., smooth pahoehoe, rugged a'a) depending on temperature and viscosity of the erupted lava [1]. On the other hand, impact cratering can produce cratered terrains with surface textures depending on the density and shape of the formed craters. Over a long geological history, a surface on Merucry or on the Moon has been shaped and modified by a series of geologic events caused by these two processes, forming the current topography that can be measured by a laser altimeter. As a quantitative measure of topographic relief, surface roughness is directly related to geologic evolution of the two bodies [2].

Previously, surface roughness of Mercury's northern hemisphere (65°N–84°N) [3] and the Moon were studied using laser altimeter data from recent missions [2, 4]. The results show that there is a distinctive contrast in surface roughness at kilometer scale between volcanic plains and cratered terrains, and that roughness constrast at hectometer scale becomes minor. Based on these results, it is suggested that surface roughness at kilometer scale is controlled by geologic events like impact cratering and volcanism, whereas that at small scale is controlled by regolith processes. However, comparsion of topographic roughness between Mercury and the Moon and the quantitative influence of geologic events on surface roughness are not studied. In this study, we compared surface roughness of the major geologic units on Mercury and the Moon, and discussed effect of geologic processes on surface roughness.

Data and Method: In this study, we used Reduced Data Records (RDR) elevation data measured by Mercury Laser Altimeter (MLA) onboard MESSENGER to study surface roughness of Mercury [5]. MLA illuminates surface areas spaced ~300–500 m apart along track, and measures the range from the spacecraft to the surface with an error less than 0.15 m (channel 1). Because the number of measurements at high latitude is much higher than that at low latitude, we chose the latitude >45°N as the studying region. For the Moon, we used RDR elevation data obtained from Lunar Orbiter Laser Altimeter (LOLA) onboard LRO to study topographic roughness of the lunar surface [6]. The spatial resolution is 57 m, and the vertical precision of measurements is 0.1 m [6].

Various methods and parameters can quantify topographic roughness, and median absolute slope and differential slope were chosen in this study as measures of topographic slope. The differential slope can remove larger-scale slope and represent surface slope at the interested scale. The absolute slopes and differential slopes were calculated from the four points of RDR data along the track profile (equation 1 in [7]), and their median absolute values were then obtained from typical geologic units of Mercury and the Moon.

Results: For Mercury, geologic units were divided into smooth plains, intercrater plains, and heavily cratered terrain (Figure 1) [8]. For the Moon, the studying regions include one typical highland region and three regions of the maria (Oceanus Procellarum, Mare Imbrium, and Mare Serenitatis) (Figure 2). The median absolute slope and median differential slope were calculated at baselines ranging from 0.4 to 20 km (Figure 3). In addition, we studied the crater density of mecurian and lunar geologic units and shape of mercurian and lunar craters (Figures S12–S15 in [9]). The results are shown by R values in Figure 4a and ratios of depth to diameter in Figure 4b.

Volcanic plains. The median absolute slopes and median differential slopes of both mercurian smooth plains and lunar maria decrease monotonously with baseline. Mercurian smooth plains are always rougher than lunar maria at the baselines studied.

The lunar maria and most of mercurian smooth plains (~65%) have been identified with volcanic in origin [8], and their surface are filled with lava flows with only a few craters. Because lava flows both on Mercury and the Moon show smooth texture (0.36° and 0.06° at 20 km baseline), we inferred that the roughness difference between mercurian smooth plains and lunar maria is mainly from different densities of impact craters over these two geologic units. Since mercurian smooth plains are generally older (3.7–3.9 Ga) [8] than most of the maria (3.2–3.7 Ga) (for our studying regions) [10] and the cratering rate on Mercury is ~2.6–3.1 times as that over the Moon [11], mercurian smooth plains have a larger crater density compared with lunar maria, as indicated by the larger R values in Figure 4a. The crater density is thus inferred to be a factor that affects topographic roughness of volcanic plains.

Heavily Cratered terrains. The median absolute slopes of cratered terrains decrease monotonously with baseline, whereas the median differential slopes increase firstly, reaching a peak at a certain scale (~2 km for mercurian heavily cratered terrain and ~7 km for lunar highlands), and then decrease at larger baselines. Mercurian heavily cratered terrain is rougher than lunar highlands at <~2 km and becomes smoother than lunar highlands at >~2 km baselines.

The most prominent features of cratered terrains are numerous craters with diameters from tens of meters to hundreds of kilometers, and therefore topographic roughness of cratered terrains on Mercury and the Moon is mainly related to crater density and shape. The crater counting results show that mercurian heavily cratered terrain has higher R values over diameter range <2 km, roughly equal R values at a diameter range of 2–5 km, and lower R values over 5–20 km than lunar highlands. In addition, the ratio of depth to diameter of mercurian craters is generally 32% lower than that of lunar craters, which is mainly from the larger gravity acceleration on Mercury (3.70 m/s^2) than that on the Moon (1.62 m/s^2). These results indicate that at scales <2 km, crater density is the dominant factor that leads to the larger median differential slope of mercurian heavily cratered terrain. At scales >2 km, the combination of these factors induces that mercurian heavily cratered terrain is smoother than the lunar highlands.

Conclusions: We calculated the median absolute slope and median differential slope for typical geologic units on Mercury and the Moon. The results show that smooth plains are always rougher than lunar maria at the scales studied, and mercurian heavily cratered terrain are rougher than lunar highlands at scale <~2 km but smoother at scale >~2 km. We suggest that the differences in surface roughness between Mercury and the Moon are mainly related to the density and shape of impact craters.

References: [1] Head J. M. et al. (2011) *Science, 333*, 1853–1856. [2] Kreslavsky M. A. et al. (2013) *Icarus, 226*, 52–66. [3] Kreslavsky M. A. et al. (2014) *GRL, 41*, 8245–8251. [4] Rosenburg M. A. et al. (2011) *JGR, 116*, E02001. [5] Sun X. and G. Neumann (2015) *IEEE TGRS, 53*, 2860–2874. [6] Smith D. E. et al. (2010) *Space Sci. Rev., 150*, 209–241. [7] Kreslavsky M. A. and J. W. Head (2000) *JGR, 105*(E11), 26695–26711. [8] Denevi B. W. et al. (2013) *JGR, 118*, 891–907. [9] Fa W. et al. (2016) *GRL, 43*, 1–10. [10] Hiesinger H. J. et al. (2010) *JGR, 115*, E03003. [11] Le Feuvre M. and M. A. Wieczorek (2011) *Icarus, 214*, 1–20.

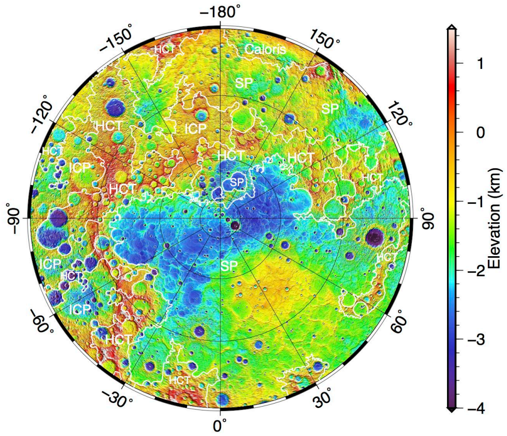

Figure 1. Surface elevation for the northern hemisphere of Mercury (latitude >45°N).

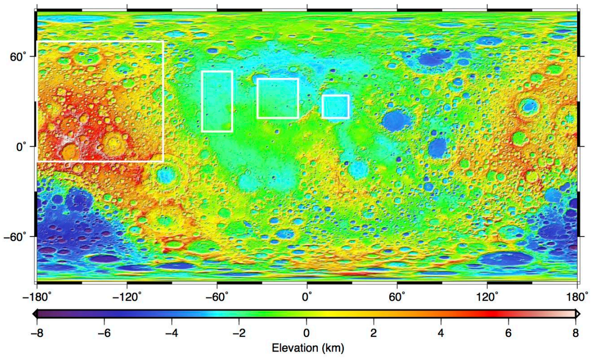

Figure 2. Lunar surface elevation. The white squares show the studying regions of surface roughness of the maria and highlands.

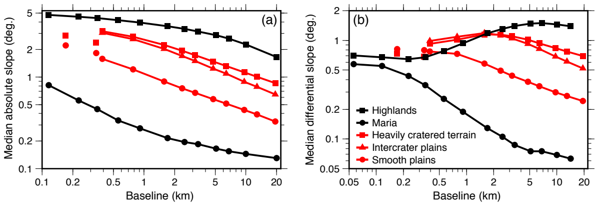

Figure 3. (a) Median absolute slope and (b) median differential slope for typical mercurian and lunar geologic units as a function of baseline.

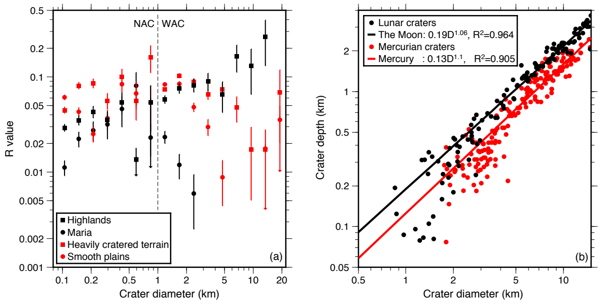

Figure 4. (a) R plots of smooth plains and heavily cratered terrains on Mercury and the maria and highlands on the Moon. (b) Depth/diameter ratios of mercurian and lunar impact craters.

Petrology and chronology of Sayh al Uhaymir 169 regolith breccia.

W. F. Xing[1,2], S. Hu[2], W. Yang[2], J. C. Zhang[2], J. L. Hao[2], L. Xiao[1] and Y. T. Lin[2], [1]Planetary Science Institute, China University of Geosciences, Wuhan 430074, China; [2]Key Laboratory of Earth and Planetary Physics, Institute of Geology and Geophysics, Chinese Academy of Sciences, Beijing 100029, China; xweifan@126.com

Introduction: Sayh al Uhaymir (SaU) 169 is the most KREEP-rich lunar meteorite, which consists of an impact melt breccia and an adherent polymict regolith breccia [1]. Although both lithologies are rich in incompatible elements, they show distinct differences in geochemical compositions, rock types and formation time between them. For example, there is remarkable depletion of K relative to Th in the impact melt breccia, which indicates that it contains only a minor fraction of the regolith at the ejection site [1-2]. Here we report the compositional and petrographic results of different rock clasts in the regolith breccia and in-situ chronological data of zircons to reveal petrogenetic history of SaU169 and geological evolution of its source region.

Experiments: Four polished sections were used in this work. Petrography observation was carried out by FE-SEM. Major and minor composition of minerals were made by EMPA. U-Pb dating of zircon was carried out using NanoSIMS 50L.

Petrography: Two stages of regolith separated by vesicular flow-banded impact-melt glass are different in grain size, matrix content and types of rock clasts. Basalt clasts which comprise ~15vol% of this meteorite (statistics in SaU169A section, same below) vary from Ti-rich to Ti-poor, according to the classification criteria suggested by [3]. In addition to that reported by [1-2], we have recognized some K-rich basaltic clasts (Fig. 1a). Based on their texture characteristics, modal composition and mineral chemistry, we identified a series of highland igneous rock clasts, such as Mg suite norite, gabbronorite, noritic anorthosite (Fig. 1b), alkali suite norite, anorthosite and some highly evolved rock clasts (Fig. 1c). These rock clasts contribute ~25% of this meteorite. Although the mafic silicate minerals in some clasts are similar in composition to ferroan anorthosites and comprising high abundance of plagioclase, the An# of plagioclase are lower than FAN (Fig. 2). This population may represent a compositionally distinct crustal lithology. There're also abundant impact melt breccias and granulitic breccias which comprise ~60% of this meteorite. Some of the granulites are not typical feldspathic with less abundance of plagioclase and high abundance of zircon and phoshapte which leading to high concentrations of incompatible elements (Fig. 1d). All the granulites are ferroan with Mg# less than 67.

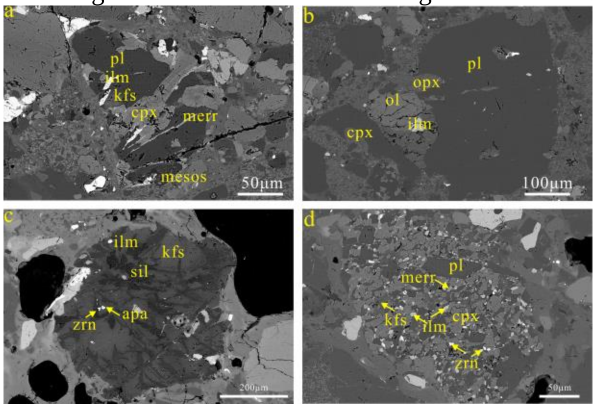

Figure 1: BSE images of rock clasts in the regolith breccias. (a) KREEP basalt (b) noritic anorthosite (c) granite (d) granulite

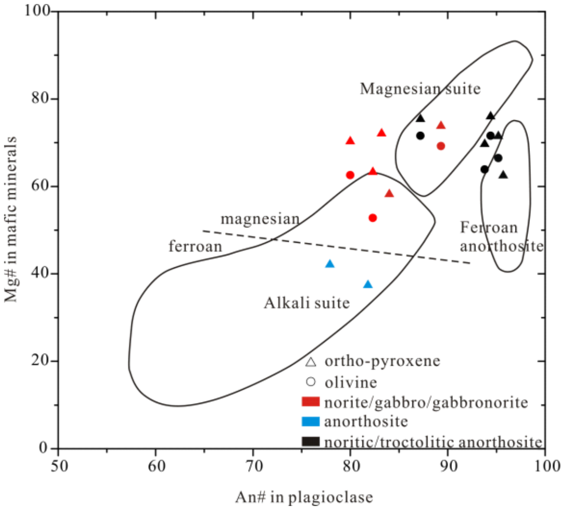

Figure 2: An# in plagioclase vs. Mg# in mafic minerals of highland igneous rock clasts

U-Pb age of zircon: U-Pb isotope system of zircons in the impact melt breccia of SaU169 record the Imbrium impact event at ~3.9Ga [e.g. 1, 4-5]. Zircons in the regolith breccia occur in various rock clasts or as mineral fragments in the matrix. Three peaks of age can be identified based on our preliminary chronology research on zircons in the regolith breccia: ~3.93Ga, ~4.20Ga and ~4.34Ga. (Fig. 3)

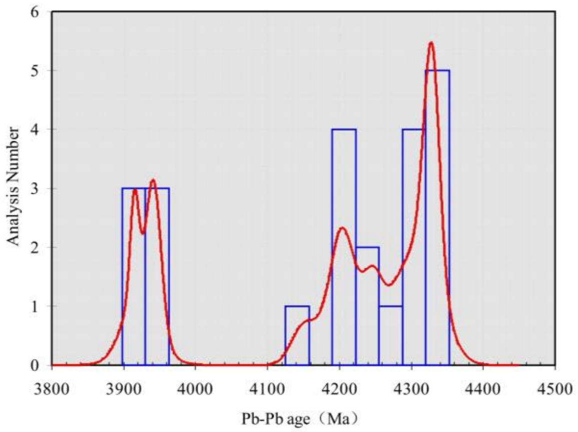

Figure 3: Pb-Pb age of zircons in the regolith breccia

Discussions: SaU169 regolith breccia is significantly rich in KREEP. Comprehensive data set suggest it origins from the Procellarum KREEP terrane [1]. However, SaU169 regolith breccia contains high TiO_2 basalt clasts which were never observed in other KREEP–rich lunar meteorite. It indicates that this meteorite may come from a distinct source region in PKT. The distribution of zircon U-Pb age in SaU169 regolith breccia is similar to that of Apollo 14, indicating a similar material source region. Zircons in alkali suite and highly evolved rock clasts have ages of ~3.93Ga and ~4.34Ga, which record ancient KREEP magmatism around the source region.

References: [1] Gnos E. et al. (2004) *Science, 305,* 657-659. [2] AL-Kathiri A. et al. *Meteoritics & Planetary Science, 42*, 2137-2152. [3] Neal C. R. and Taylor L. A. (1992) *Geochimica Et Cosmochimica Acta, 56,* 2177-2211. [4] Lin Y. T. et al. (2012) *Geochimica Et Cosmochimica Acta, 85*, 19-40. [5] Liu D. Y. et al. (2012) *Earth and Planetary Science Letters, 319-320,* 277-286.

GLOBAL MAPPING AND ANALYSIS OF MARS WRINKLE RIDGE.

Ting Cao[1],Jun Huang[1], [1]Planetary Science Institute,China University of Geosciences,Wuhan ,430074,P.R.China (e-mail:1486251200@qq.com)

Introduction:Wrinkle ridges are linear, asymmetric topographic positive relief that are easily found in lava plains on Mars, and also be interpreted as low-viscosity lava flows. This study was based on previous geologic map of Mars [1] , but redescribed the distribution of wrinkle ridges and proceed some analysis work by using the data acquired by Mars Orbiter Laser Altimeter(MOLA) . MOLA has provided the most reliable topographic data of wrinkle ridges ,which help us use it to test model of their origin better.

Methodology of mapping wrinkle ridges:A global daytime thermal infrared images mosaic acquired by THEMIS and topographic data from Mars Orbiter Laser Altimeter (MOLA) were used in this study. Firstly, the morphology of wrinkle ridges could be approximately identified in the image mosaic .The wrinkle ridges shown by MOLA can usually be recognized by distinct elevation offset across them, and the elevation offset can be easily explained by subsurface thrust faults [2] .And the another characteristic that wrinkle ridges almost occurred in ridge plains can also facilitate our recognition of them [3]. Secondly,wrinkle ridges can be exactly mapped by using the THEMIS daytime infrared images. A rectangle was represented a wrinkle ridge segment that with no distinct change in strike and width .And the rectangles must be most close to the outline of the ridge segment along its orientation (Fig 1a).During mapping the profile, craters must be avoided to eliminate the elevation error.And then drew the lines to represent length and width of each rectangle (Fig 1b).Each rectangle possesses topographic parameters of each corresponding extracted segment, including height (should be calculated) , enclosed area,center latitude and center longitude, while the lines possesses physical parameters of each corresponding rectangle, including length, width, orientation ,which all can be used in further analysis.

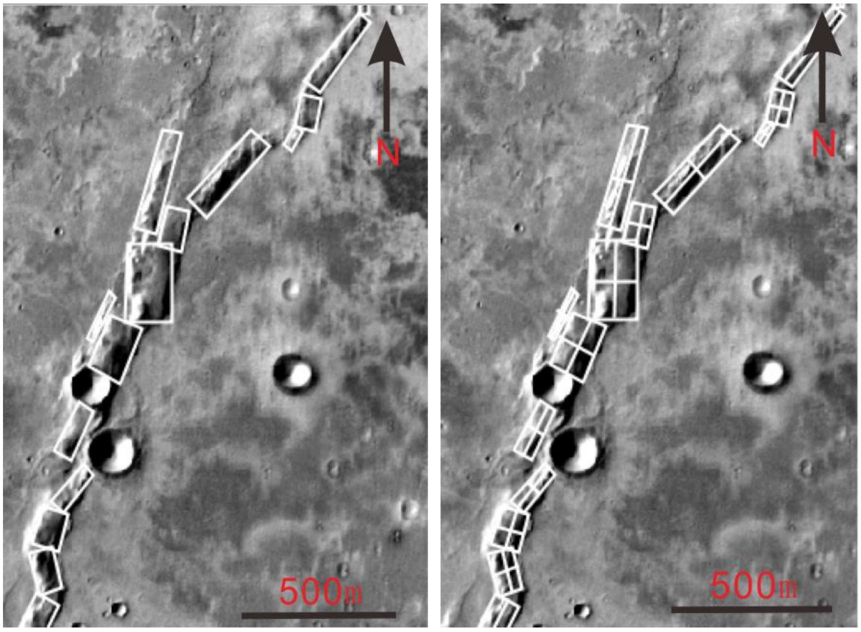

a b

Figure 1.An example of an extracted wrinkle ridge. Fig 1a shows the wrinkle ridge be divided into some segments because of the variation of strike or width , Fig 1b shows the lines in the rectangles which are represented length(orientation) and width.

Result and Conclusion:The study has counted 4886 rectangles with a total length of 54553km,width of 15917km.The mean width, length, height and orientation of all the rectangles are 6.51 km, 22.33 km, 0.12km, and 183.07°E, respectively. The total enclosed area of the martian wrinkle ridges is $7.22\times 10^{7}km^{2}$.The wrinkle ridges mostly concentrated on the region that latitude range between 30°N–35°S, and longitude range between 60°–190°, 270°–310°.And the wrinkle ridge can be grouped into three types: concentric, parallel and isolated.The concentric ridges occur more eastward than the parallel ridges ,the parallel ridges shown in Fig 3 at

270 °–310 °E,and concentric ridges at 60 °–120 °E. The parallel ridges have an obvious preferred northeast orientation , while concentric ridges display a NE or NW orientation in different regions.

The rose diagrams of orientations of all the wrinkle ridges in Mars shows that most ridges display a NE or NW orientation with most at 30 °N–30°S,most ridges' orientation close around 90 °;but the orientation of EW is hardly see in the Fig. 2.

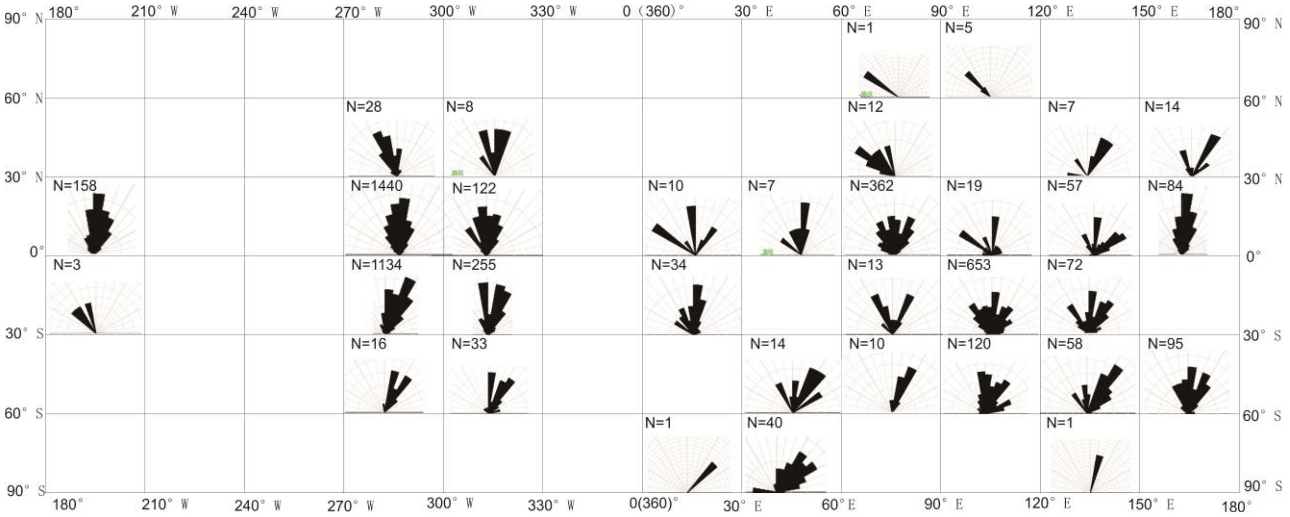

Figure 2. Rose diagrams of all the wrinkle ridges on the Martian surface. The rose diagrams are binned with the size of 5 ° in orientation, and the Martian surface has been segmented into 30 ° × 30 ° boxes in latitudinal and longitudinal dimensions.

Future Work: The study was based on previous geologic map of Mars , but redescribed the distribution of wrinkle ridges and proceed some analysis work. The topographic and physical parameters data statistics by rectangles will be advanced analysis. Analyzing the parallel, concentric and isolated , respectively and summarizing the individual characteristic of each type of wrinkle ridge, such as topographic feature , distribution feature both in microscopic and macroscopic , and the relation with tectonic movement. Then it could be better to explain the formation of wrinkle ridges.

Reference:[1] Kenneth L. Tanaka , James A. Skinner, Jr. , Corey M. Fortezzo, and Trent M. Hare , Geologic Map of Mars,2014.[2] Golombek, M. P., F. S., Anderson, and M. T., Zuber (2001), Martian wrinkle ridge topography: Evidence for subsurface faults from MOLA. *J. Geophys. Res*. 106(E10), 23,811–23,821 , doi: 10.1029/2000JE001308. [3] Michael H. Carr, James W. Head III ,Geologic history of Mars .Earth and Planetary Science Letters 294 (2010) 185–20

MICROORGANISM ISOLATED FROM MARS ANALOGUE SITE: DALANGTAN PLAYA (QAIDAM BASIN, PR CHINA) AND THEIR ASTROBIOLOGICAL IMPLICATIONS

T. Huang[1], L. Xiao[1], H. M. Wang[2], R. C. Wang[2], Z.Y.Cheng[1]. 1. Planetary Science Institute, China University of Geosciences, Wuhan, 430074, P. R. China; 2. State Key Laboratory of Biogeology and Environmental Geology, China University of Geosciences, Wuhan 430074, China. (huanglotte@cug.edu.cn)

1. Introduction

Dalangtan playa is the second largest salt playa (roughly 210 km^2) in Qaidam basin, north-western China. Hyper saline deposition, extremely arid climate and relatively high UV radiation make Dalangtan a promising Mars analogue both for geomorphology [1], saline condition [2] and life preservation [3]. In this study, we reported microbes isolated from the surface and subsurface of Dalangtan Playa. In which, dominated *Bacillus* could be seen as a potential life style living on subsurface or lowland of Mars saline conditions.

2. Methodology

Field investigation and sampling were conducted. Physicochemical parameters as pH, salinity, moisture content and TOC were determined. X-ray diffraction of samples were analyzed. Microbial isolation with MGM media were conducted. Sequencing work and phylogenetic tree were constructed. Scanning electron microscope were used.

3. Results

Seven surface samples (D-S-1 to D-S-7) and samples from two vertical profiles (D-P-4 and D-P-6) were collected (Fig.1). The height of profile D-P-4 is 595 cm containing ten samples and D-P-6 685 cm containing thirteen samples.

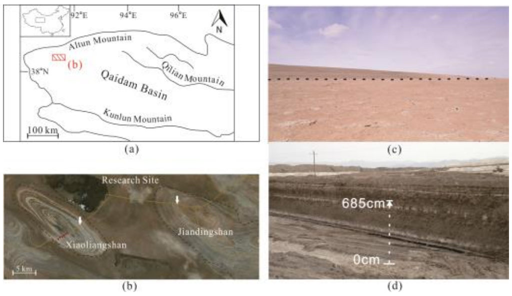

Fig.1 (a) Sketch of the Qaiam basin and (b) the location of sampling sites. (c) Surface sampling sites and (d) profile D-P-6, which were excavated by mining work with a height of 685 cm from bottom the topmost.

Salt mineral composition, pH and TOC values of surface samples were listed in Table 1.

Table 1. Physical and Chemical Characteristics of Surface Samples

Sample	pH	TOC (w/w)	Salt Mineral Composition (w/w)
D-S-1	7.97	0.06%	Halite 99%
D-S-2	8.90	0.03%	Halite 51.3% and Thernardite 45.5%
D-S-3	8.34	0.12%	Halite 71.9% and Gypsum 11.4%
D-S-4	8.30	0.07%	Halite 79% and Gypsum 18.5%
D-S-5	8.50	0.10%	Halite 30.2% and Gypsum 34.0%
D-S-6	8.27	0.09%	Halite 98.1%
D-S-7	7.95	0.11%	Halite 90.4% and Gypsum 6.1%

As to the profiles, samples were tested to be mildly alkaline to alkaline with pH values range from 7.93 to 9.48. A wide range of salinities were tested from 0.4% to 50%. Deposits of Dalangtan playa had a relatively low moisture content range from 0.079% to 12.45%.

Minerals of the subsurface samples were mainly composed by clays, carbonates, sulfates and halite. Fragmentary materials also displayed as associated with salt evaporates.

Twenty-three strains of bacteria were isolated from the surface and subsurface samples (Fig.2). And the bacteria showed over 98% affiliations to *Bacillus, Microbacterium, Nocardiopsis, Oceanobacillus, Halobacillus, Gracilibacllus, Sediminibacillus* and *Thalassobacillus* within three orders

(Bacillales, Micrcoccales and Streptosporangiales) of two phyla (Firmicutes and Actinobacteria). In which, *Bacillus* was major genus accounting for 45%.

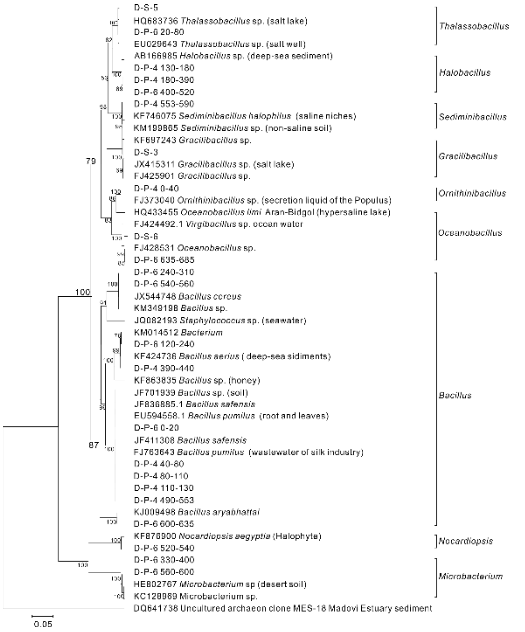

Fig.2 Phylogenetic tree for bacteria from Dalangtan Playa based on 16S rRNA gene sequences. Bootstrap values greater than 50% are shown. The scale bar represents 0.05 fix mutation per nucleotide position.

Four strains of moderately halophilic bacteria isolated from Dalangtan were chose to test growth rates in MGM media with a salinity gradient from 12% to 30% with the interval of 3%. As a result, *Thalassobacillus* sp. and *Ornithinibacillus* sp. preferred to medium with salinity of 12%, while *Oceanobacillus* sp. and *Halobacillus* sp. preferred to medium with salinity of 15% (Fig.3).

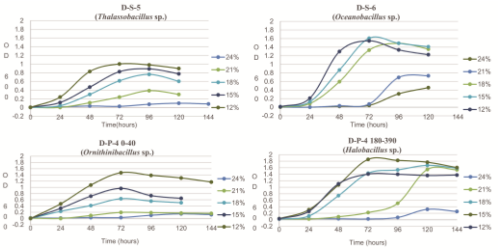

Bacteria were observed under scanning electron microscope and most of them were displayed to be rod shaped with lengths ranged from 1 to 5 μm. Micro particles of salts were observed on the surface of some bacteria.

4. Discussion

Surface of Dalangtan Playa was mainly covered by salt evaporates as halite and gypsum. Mineral composition of subsurface were analyzed as clays, carbonates, sulfates and halite, associated with fragmental materials. The salinity of subsurface deposits was tested to be as high as 50% with moisture content as low as 0.079%. However, twenty-three strains of bacteria were isolated in this extremely arid environment. In which moderately halophilic microbes accounts for ~50%, and 45% were *Bacillus* which can produce spores in tough environment to conquer hard time.

Bacillus have been studied as a target life forms in simulated Mars environment. Spores of *Bacillus subtilis* have been subjected to simulated Martian atmospheric pressure and composition for 19 days and resulted endogenous but not ethical impairment [4]. When exposed to simulated Mars Solar Radiation (254-nm UV light), *Bacillus subtilis* has also retained the possibility to initiate germination-associated metabolic processes and to produce biological signature molecules [5]. Moreover, when exposed to full Martian conditions (UV, low pressure, low temperature and CO_2 atmosphere) for 24 h, positive growth (16.7%) were still exhibited [6]. In addition, spores of Bacillus pumilus, which also isolated from Dalangtan deposits, was exposed to space condition and Mars simulated condition for 18 months, and survivals were detected under dark environments [7].

Bacillus among the other isolates were capable to live in Dalangtan Playa, the very arid and saline extreme environment. And experiments on *Bacillus* under Mars simulated condition showed their resistances to simulated Mars/Space conditions. Thus we suggest *Bacillus* could be seen as a potential life candidate for Mars life detection and astrobiology investigation.

References: [1] Mayer et al. (2009). LPSC, XL abstract #1877 [2] Wang et al. (2013). Icarus, 226: 980-991. [3] Kong et al. (2010) Acta Geologica Sinica, 84: 1661-1667. [4] Nicholson et al. (2005). Astrobiology, 5. [5] Tauscher et al. (2006). Astrobiology, 6: 592-605. [6] Kerney et al. (2011). Astrobiology, 11: 477-485. [7] Vaishampayan et al. (2012). Astrobiology, 12: 487-497.

ARCHAEAL AND BACTERIAL LIPIDS RECOVERED FROM SUBSURFACE EVAPORIYES OF DALANGTAN ON THE TIBETAN PLATEAU AND THEIR ASTROBIOLOGICAL IMPLICATIONS.

Z.Y. Cheng[1], L. Xiao[1, 2], H.M. Wang[3], H. Yang[3], T. Huang[1], Y. Xu[2]. [1] State Key Laboratory of Geological Processes and Mineral Resources, Planetary Science Institute, School of Earth Sciences, China University of Geosciences, Wuhan, China; [2]Macau University of Science and Technology, Macau, China. [3]State Key Laboratory of Biogeology and Environmental Geology, China University of Geosciences, Wuhan, China. (ziye7cheng@126.com)

Introduction: Ancient deposits of chlorides and sulfates were detected in different areas of the Martian surface, some of which may result from chemical precipitation and deposition by evaporate processes [1, 2, 3]. On Earth, terrestrial hypersaline environments of arid regions are the most likely analog of these Martian regions in the search for biosignatures.

To this regard, we focuses on the preservation of biological molecules in hypersaline sediments from the Dalangtan (DLT) located in the northwestern Qaidam basin, on northern margin of the 5000-m-high Tibetan Plateau. Various combinations of high solar and UV radiation, day to night variation in temperature, extremely dry, and the accumulated abundant evaporates make this dry saline lake a suitable location as earth analog to study the preservation of organic compounds in hypersaline sediments [4]. Here, we have examined the concentration and distribution of lipids biomarkers (branched fatty acids, iGDGTs and archaeol) preserved in evaporite deposits from two outcrops in DLT (Fig. 1) as well as their relationships with the associated evaporates, which could increase our understanding of biosignatures preserved in terrestrial evaporate deposits.

Results: The X-ray diffraction (XRD) analyses recovered from the two stratigraphic sections indicate the presence of gypsum, halite, quartz, albite, muscovite, and chlorite (Fig. 2 and Fig. 3). We can identify two different sedimentary units in both the two sections based on the XRD data, salinity, and sediment color information— a high concentration of clay and detrital minerals unit, with lower salinity; a high concentration of gypsum and halite unit, with higher salinity.

Normal, branched, monounsaturated fatty acids were abundant in all the DLT samples, with a carbon number ranging from C_{12} to C_{30}. Archaeol, caldarchaeal and very few bacterial GDGTs were detected in both sections of DLT P_4 and DLT P_6. In addition, the concentrations of branched fatty acids, archaeol and caldarchaeol showed comparable patterns along the profile. In DLT-P_6, the concentrations of archaeol and caldarchaeol increased from the upper detrital unit to the lowest hypersaline unit, while the concentrations of branched fatty acids showed an opposite trend. The same trend was also observed along DLT P_4.

Discussion: The microbial branched fatty acids in DLT evaporites suggest a strong microbial activity has existed in the hypersaline ecosystem. Detected branched fatty acids in our samples are likely to be derived from halophilic and halotolerant bacteria. The halophiles were the most important archaea in the hypersaline sediments, and they are treated as the productor of archaeol, this group may be important contributor to the distribution of archaeol in DLT hypersaline sediments. Moreover, the presence of caldarchaeol suggests a substantial contribution of methanogenic archaea to iGDGTs in DLT.

The systematic change in the relative abundance of archaea and bacteria with salinity was consistent with the fact that most obligate halophiles are archaea. Because of their different requirements for salt, halophilic bacteria and archaea tend to occupy different salinity niches with the former being dominant at low salinity and the latter being dominant at high salinity [5]. Although this generalization has been made previously, our study has definitively demonstrated this.

The detection of abundant hydrated minerals on the Martian surface and sediments suggests a wet past, which would have harbored life sometime. Moreover, Mars is a cold and dry planet today, which is favorable for preservation of molecular. DLT hold a combination of highly water-soluble salts and extreme environmental conditions that make them suitable for collecting reference data for future Martian exploration. Our study of terrestrial analog materials could offer important clues to how Martian life may have adapted and preserved under similar conditions, halophilic life and preservation of their lipids in evaporites are a potentially detectable target during near future missions.

References: [1] El-Maarry et al. (2013) JGR : Planets, 118, 2263-2278. [2] Osterloo, M. et al. (2008) Science, 319,1651-1654. [3] Grotzinger, J. P. et al. (2014) Science, 343, 6169. [4] Wang, A., Zheng, M.(2009) LPI Conference, 1858. [5] Stivaletta, N. et al. (2008) From Fossils to Astrobiology, Springer, 319-333.

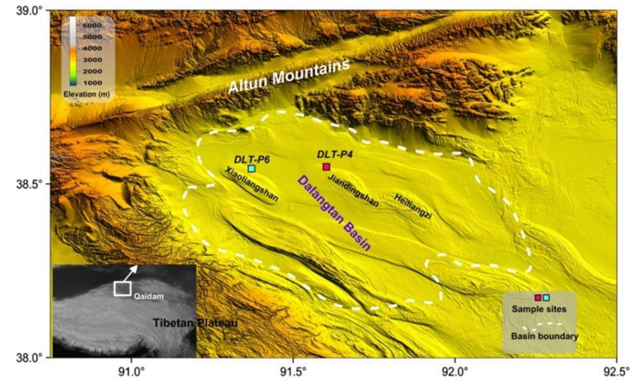

Fig.1. Location of the DLT and sampling sites

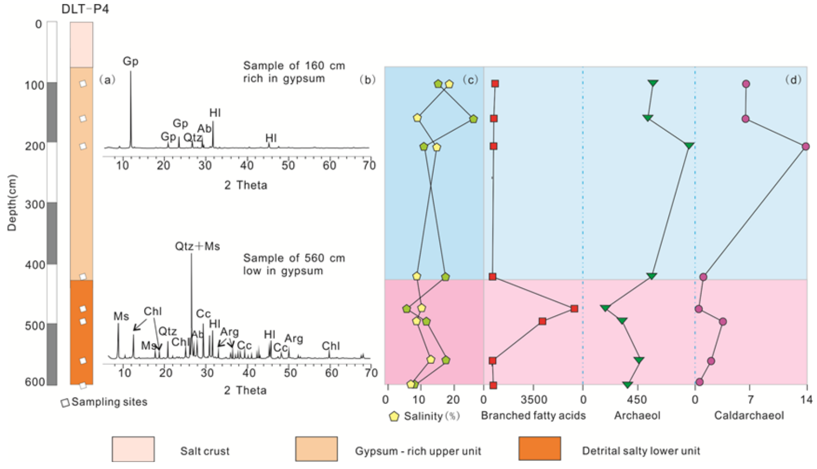

Fig 2. (a) Stratigraphic sections and sampling sites of DLT-P4. (b) Selected XRD analyses of the materials sampled at DLT-P4. Samples come from the depths of 160cm and 560cm. The mineral peaks show: Ab-albite, Arg-aragonite, Cc-calcite, Chl-chlorite, Gp-gypsum, Hl-halite, Mc-microline, Ms-muscovite, and Qtz-quartz. (c)Distribution of salinity and the S/D index that evaluates the intensity of main XRD peaks in salts (gypsum and halite) against detrital minerals (quartz, albite, muscovite, and chlorite) in the evaporites sediments of DLT-P4. (d)Variation in branched fatty acids, archaeol and caldarchaeol abundance with depth of DLT-P4.

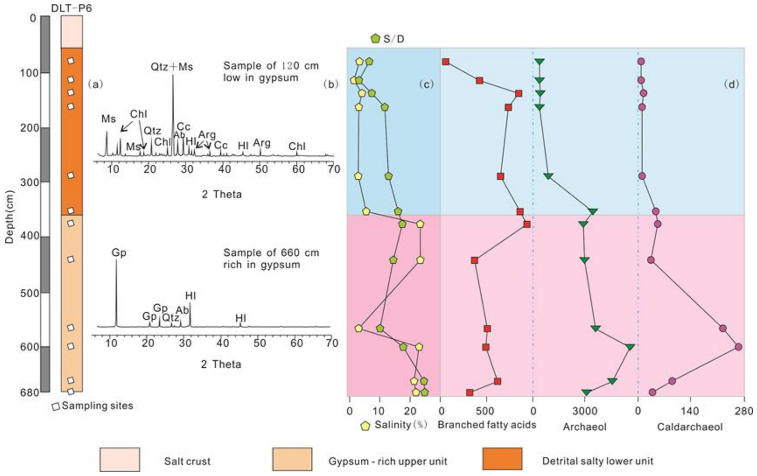

Fig 3. (a) Stratigraphic sections and sampling sites of DLT-P4. (b) Selected XRD analyses of the materials sampled at DLT-P4. (c)Distribution of salinity and the S/D index in the evaporites sediments of DLT-P4. (d)Variation in branched fatty acids, archaeol and caldarchaeol abundance with depth of DLT-P4.

CHLORIDES PREDATED CLAY IN A LACUSTRINE ENVIRONMENT ON MARS AND ITS ASTROBIOLOGY APPLICATION.

Jun Huang[1], M. R. Salvatore[2], P. R. Christensen[2] and Long Xiao[1], [1] Planetary Science Institute, China University of Geosciences, Wuhan, Hubei, P. R. China (junhuang@cug.edu.cn), [2]School of Earth and Space Exploration, Arizona State University, Tempe, AZ, USA

Introduction: Globally distributed chloride-bearing materials have been previously identified on Mars [1] using spectral data from Thermal Emission Imaging System (THEMIS) [2] and Thermal Emission Spectrometer (TES) [3]. These chloride salts (chlorides) are indicators of near-surface water activity in the past, and could have provided habitable environments for haophilic microorganisms and preserved organic matter [4]. However, previous studies have shown many chlorides occurred in local topographic depressions without clear geologic or stratigraphic context [5]. In addition, phyllosilicates have been found to underlie chlorides [6, 7] in many locations, suggesting that these deposits are stratigraphically younger than their surroundings. This proposed young age is not favorable from an astrobiological perspective, given the most likely habitable surface environments on Mars would have occurred very early in martian history [8]. Here we identify the coexistence of chlorides and phyllosilicates in a basin west of Knobel crater (near Gale crater), and show that these chlorides are stratigraphically below iron-magnesium smectite clays. The two distinct depositional events in this Middle-Noachian [9] lacustrine environment can shed light on an environment with interesting astrobiological implications. As such, this site should be considered as a potential site for future martian surface investigations.

Methods: We used imaging data from the THEMIS global mosaic (~100 m/pixel) [2,10] and gridded topographic data from the Mars Orbiter Laser Altimeter (MOLA; 128 ppd) [11] to show the overall regional context. Decorrelation stretch (DCS) [12] images of THEMIS and Compact Reconnaissance Imaging Spectrometer for Mars (CRISM) [13] are used to visualize compositional variations. Spectral information was extracted from CRISM FRT data (~18 m/pixel) and compared to library mineral spectra. THEMIS nighttime infrared (IR) data were used to calculate thermal inertia [14]. We further characterized local and detailed geomorphology using Context Camera (CTX: ~6 m/pix) [15] and High Resolution Imaging Science Experiment (HiRISE: ~30 cm/pix) images [16].

Results: Our investigation focuses on a topographically enclosed basin approximately 3000 km^2 in area centered near 6.078 °S, 132.346 °E (Fig. 1a). Light-toned materials can be seen throughout the study region; the largest occurrence is in the northern part of the fan unit, and tens of smaller occurrences are in isolated “geologic windows” (Fig. 2). These light-toned materials with elevated thermal inertia (Fig. 1b) appear blue (Fig. 1c) in DCS [12] images of THEMIS band 8, 7 and 5 , which is unique to chloride salts [1, 5]. CRISM data were also used to identify and map hydrated materials throughout this basin. In Figure 1d, the red, green and blue channels are assigned to 1.8, 2.38 and 1.15 μm, respectively. This combination causes phyllosilicate-bearing materials to appear red and orange, chloride-bearing materials to appear blue, and low-calcium pyroxene-bearing materials to appear green (Fig. 1d).

The regional stratigraphic relationship of different materials can be determined using CTX and HiRISE imagery. At one location (Fig 2c), chloride-bearing materials occur in the lowest topographic regions in both north and south portion and outcrops of pyllosilicate-bearing materials occur directly above the southern chloride exposure. Possible aeolian deposits compose an upper layer, and erosional windows of chlorides can be observed within it. Therefore, the chronologic sequence, from oldest to youngest, appears to be chlorides, phyllosilicates, and aeolian deposits. Similar chronologic relationship of chlorides and phyllosilicates can be determined at another location (Fig 2d). The chloride-bearing materials filled an old crater and resisted subsequent erosion that destroyed the crater rim. Subsequently, phyllosilicate-bearing materials were deposited on top of the original rim of this eroded crater. A dark toned material with basaltic composition also occurs stratigraphically above the chloride-bearing materials and is present within the inter-crest plains of chloride deposits (Fig 2e). If the basaltic materials are above the phyllosilicates (Fig 2f), their formation may indicate the end of hydrologic activity in the region.

Discussion: The geomorphic and compositional analyses indicate the following sequence of the materials, and we hypothesize their formation environments: 1) Chloride-bearing materials on Noachian base, which were emplaced by high-salinity waters that filled the basin and subsequently evaporated; 2) The observed ridges in chloride-bearing materials were formed by aeolian modification; 3) Phyllosilicate-bearing materials, which was deposited within a very thin layer during transient lacustrine activity that was not capable of dissolving the previously deposited chlorides; 4) An alluvial fan was formed by continued fluvial activity, which superimposes the underlying chloride- and smectite-bearing deposits; and 5) Aeolian deposits, on top of all of the younger geologic units, were formed by subsequent erosion of the fan.

Chlorides and smectite clays have been shown to effectively entrap and preserve microorganisms in terrestrial environments [17, 18]. If ancient Mars was habitable, such a lacustrine setting my have been able to entrap and preserve a record of microbial fossils, should they have existed. The high astrobiological potential of this site makes it an ideal location for future landed mission and possible sample return.

Acknowledgements: J. H. was supported by National Natural Science Foundation of China (No. 41403052).

References: [1] Osterloo, M.M., et al., Science, 2008. **319**(5870): p. 1651-1654. [2] Christensen, P.R., et al.,. SSR, 2004. **110**(1-2): p. 85-130. [3] Christensen, P.R., et al., *JGR*, 2001. **106**(E10): p. 23823-23871. [4] Farmer, J.D. and D.J. Des Marais, *JGR*, 1999. **104**(E11): p. 26977-26995. [5] Osterloo, M.M., et al., *JGR*, 2010. **115**. [6] Murchie, S.L., et al., *JGR*, 2009.**114**. [7] Glotch, T.D., et al., *GRL*, 2010. **37**(16): p. L16202. [8] Carr, M.H. and J.W. Head, *EPSL*, 2010. **294**(3-4): p. 185-203. [9] Tanaka, K.L., et al., Geological Survey Scientific Investigations Map 3292. [10] Edwards, C.S., et al., *JGR*, 2011. **116**. [11] Smith, D.E., et al., *JGR*, 2001. **106**(E10): p. 23689-23722. [12] Gillespie, A.R., A.B. Kahle, and R.E. Walker, RSE, 1986. **20**(3): p. 209-235. [13] Murchie, S., et al., *JGR*, 2007. **112**(E5). [14] Fergason, R.L., P.R. Christensen, and H.H. Kieffer, *JGR*, 2006. **111**(E12). [15] Malin, M.C., et al., *JGR*, 2007. **112**(E5). [16] McEwen, A.S., et al., *JGR*, 2007. **112**(E5). [17] Kennedy, M.J., D.R. Pevear, and R.J. Hill, Science, 2002. **295**(5555): p. 657-660. [18] McGenity, T.J., et al., Environmental Microbiology, 2000. **2**(3): p. 243-250.

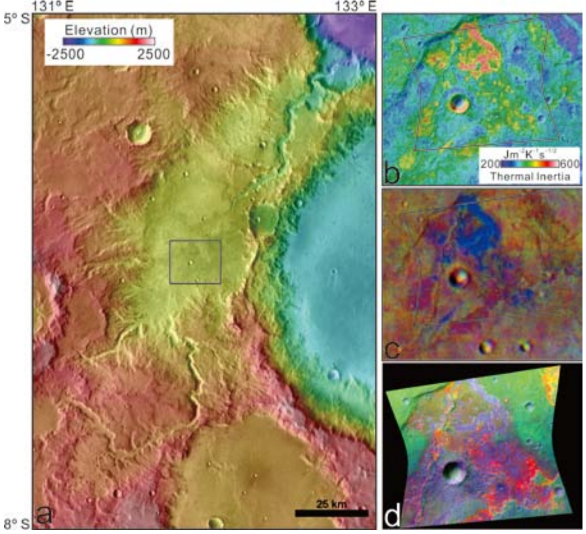

Fig. 1 See text for decription. The black box is Fig. 2a

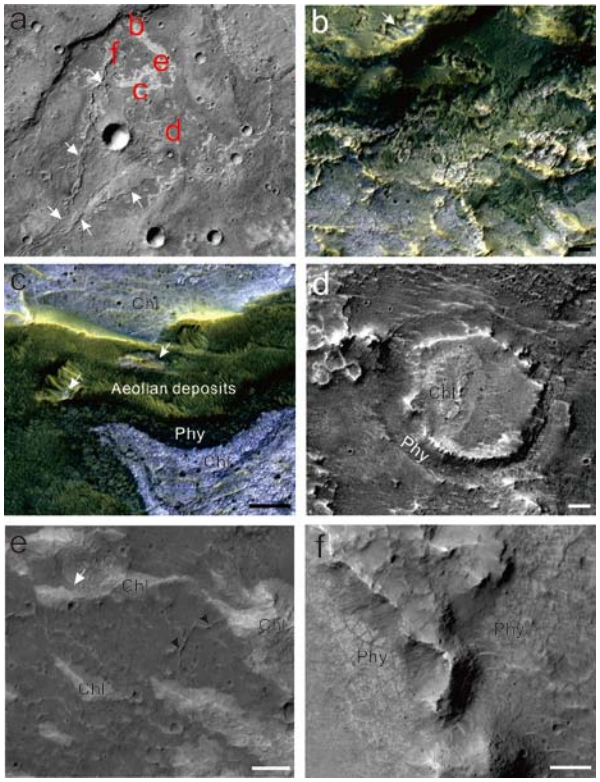

Fig. 2 See text for decription. The scale bars are 50 m

PETROLOGICAL STUDY OF THE OLIVINE PHYRIC SHERGOTTITE NORTHWEST AFRICA 1110.

Q. He[1] and L. Xiao[1]. [1] Planetary Science Institution, China University of Geosciences, Wuhan, 430074, China(qihe_cug@yahoo.com; he_qi@cug.edu.cn).

Introduction: NWA 1110 is one of the few olivine-phyric shergottites that is not light REE depleted and may paied to NWA 1068. Its REE pattern is similar to that of Shergotty, suggesting a possible link between the olivine-phyric and the basaltic shergottites. Here, we report the mineralogy and petrology of this meteorite that, up to date has not got much attention.

Petrology: NWA 1110 has a porphritic texture consisting of olivine phenocrysts (grain size ~ 0.3- 0.5 mm) in a fine-grained groundmass (grain size ~50-100 microns) (Fig. 1). The olivine phenocrysts occur in clusters, of which, some contain chromite and melt inclusions, and some appear corroded/resorbed texture (The olivine grains have been broken apart and intruded by groundmass material, Fig. 2).

The olivine phenocrysts are zoned from Mg-rich cores to more Fe-rich mantles (Fo_{70-57} -Fo_{65-53} from core to rim). However, they are relatively lower Mg compared to most primitive olivine-phyric shergottites such as Y 98 and LAR 06319[1, 2]. Most of the olivine grains are usually euhedral, and corroded olivines are also present. Fig. 3 shows two megacryst olivines. Ol1 has a prominently homogeneous core with a zoned Fe-rich rims, while Ol2's core is inhomogeneous, suggesting a complex petrogenetic history.

The fine-grained groundmass consists mainly of euhedral to subhedral pyroxene crystals and interstitial maskelynite and small unzoned olivine grains (< 0.13mm). Minor phases are chromite, Ti-chromite, ilmenite, sulfides, merrillite, Cl-apatite, fayalite and a K-rich mesostasis glass. Shock-induced melt veins and pockets are observed (Fig. 2).

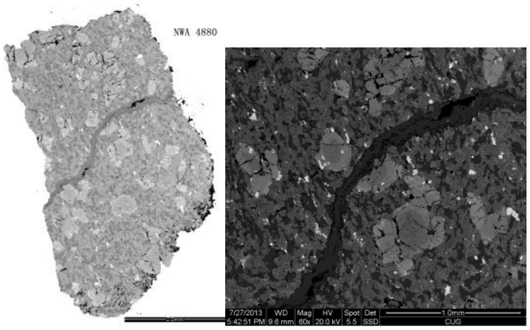

Fig. 1. The back-sattered electron (BSE) image of NWA 1110 thick section used in this study. The enlarged area is shown in the right.

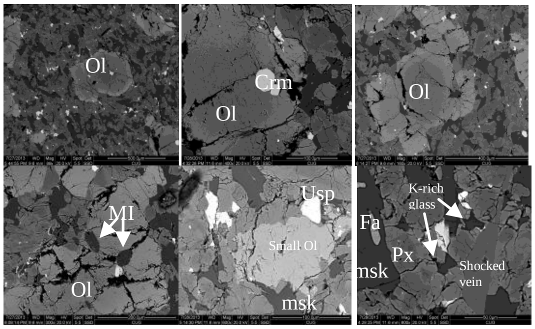

Fig. 2. Petrographic features in NWA 1110. Ol-olivine; Px-pyroxene; msk-maskelynite; Crm-chromite; Usp-ulvöspinel; Fa- fayalite; MI-melt inclusion.

Both pigeonite and augite are present as subhedral to euhedral crystals and they are also zoned (from core to rim $En_{65}Fs_{28}Wo_{7}$ to $En_{46}Fs_{43}Wo_{10}$, and $En_{55}Fs_{25}Wo_{20}$ to $En_{36}Fs_{42}Wo_{22}$). The zoning of pyroxenes in NWA 1110 resembles that observed in NWA 1068[3] as in Shergotty and Zagami (Fig. 4), but is different from that of LAR 06319 (with pigenite core, augite rim and outmost Fe-rich rim [4]).

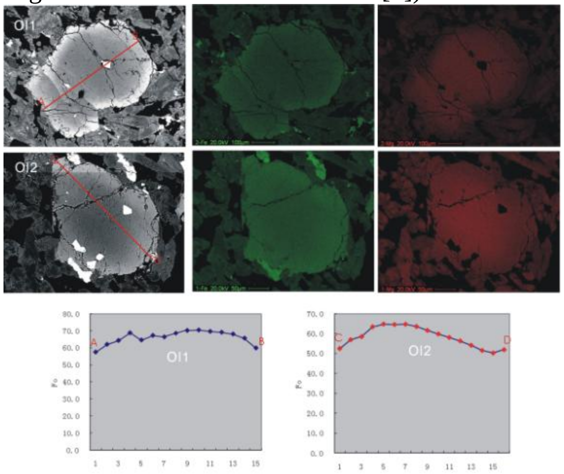

Fig. 3 Back-scattered electron (BSE) images (left) and Fe (middle) and Mg (right) X-ray mappings of two olivine phencrysts. Fe X-ray in green and Mg X-ray in red. The shading shows that olivine megacrysts are zoned from Mg-rich cores (dark) to more Fe-rich mantles (brighter).

Plagioclases have entirely been converted to maskelynite and cluster tightly near a composition of $An_{48-53}Or_{2-5}$. Smaller unzoned olivines in matrix are more Fe-rich ($Fo_{48\pm4}$), and homogeneous in terms of major elements. Small fayalites always occurred in maskelyntes (Fo= 39-41, Fig. 2). Both merrillite and Cl-apatite are present in NWA 4880. The majority is merrillite in composition with 1.4 to 2.8 wt% MgO.

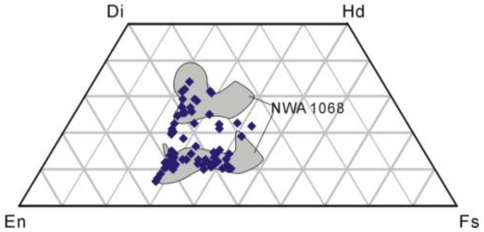

Fig. 4. Pyroxene compositions in NWA 1110 and olivine-bearing enriched shergottite NWA 1068.

Four types of Cr-Fe-Ti oxides are found in NWA 1110(Fig. 5). Chromites, most of which are mainly euhedral or subhedral grains with a composition of $Chm_{76-80}Sp_{12-13}Usp_{1-3}Mt_{5-8}$, are enclosed in the olivine megacrysts. Ti-rich chromites are in contact with maskelynite with a composition ($Chm_{32-46}Sp_{8-12}Usp_{17-26}Mt_{25-35}$) and the edges have less Cr and more Fe. Ulvöspinels are enriched in TiO_2 (19-24wt %), with low Al_2O_3 (2.1-2.5wt %) and Cr_2O_3 (7-9wt %) contents with the composition of $Chm_{11-14}Sp_{5-6}Usp_{55-71}Mt_{11-28}$. Ilmenite always attached to ulvöspinel as the exsolution products (Fig. 5).

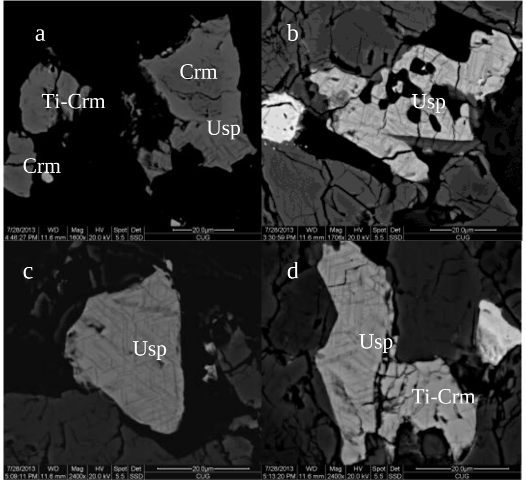

Fig. 5. Backscattered-electron image Cr-Fe-Ti oxides. a, ulvöspinel (clear gray) with a chromite core (gray). b, a skeletal ulvöspinel (clear gray). The crystal contains K-rich mesostasis (black) and is in contact with maskelynite. c and d, ulvöspinel grains have fine exsolution lamellae of ilmenite.

Igneous Petrogenesis and discussion:

The origin of the olivine megacrysts in most olivine-phyric shergottites (e.g. NWA 1068, DaG 476, SaU 005, EETA, LAR 06319) is a matter of debate as they are xenocrysts or cumulate crystals [3-6]. In fact, the occurrence of large corroded crystals and the observation that polycrystalline assemblages are sometimes broken apart and intruded by groundmass material, suggest that the olivine megacrysts are xenocrysts. We suggest that some of the NWA 1110 megacrysts might originate from disrupted cumulates, probably with strong affinities with peridotitic shergottites. The answer could be possibly given by detail analyses of the inclusions, as shown in the DaG, SaU and LAR 06319 shergottites to discuss more precisely the origin of the megacrysts.

Previous studies have shown that martian magmas have a wide range of oxygen fugacities (fO_2) [7]. The Cr-Fe-Ti oxides assemblages are conducive to the application of oxybarometers, and Peslier et al. [4] argued that fO_2 can increase during shergottite magma differentiation process, producing more oxidized magmas. NWA 1110 might also show a variation of the fO_2 with crystallization resemble that of LAR 06319. The crystallization of olivine megacrysts cores to rims, and then small olivine in matrix are concurrently with crystallization from chromites to Ti-rich chromites, and then to ulvöspinel. A Ol- Sp-Px estimate of QFM-3.1 using the most Mg-rich pyroxene, olivine, and the compositions of the most primitive chromites. A Ol-Sp-Px estimate of QFM -0.5 in the matrix using small unzonded Ol, Ulvöspinel and Fe-rich pyroxene. Late stage mineral assemblage Usp-Ilm obtain a fO_2= QFM 0.15.

NWA 1110 shows close affinity in mineral to olivine-phyric shergottite NWA 1068. Both of NWA 1110 and NWA 1068 are distinctly porphyritic, but the matrix in NWA 1110 is much finer grained (0.5-1.0 mm). This may imply that all stages of grain growth apparently occurred more rapid cooling in comparison to other porphyritic shergottites.

References: [1] Usui et al. (2008) Geochim. Cosmochim. Acta 72:1711-1730 [2] Basu Sarbadhikari et al. (2009) Geochim. Cosmochim. Acta 73: 2190–2214 [3] Barrat et al. (2002) Geochim. Cosmochim. Acta 66 , 3505–3518 [4] Peslier et al. (2010) Geochim. Cosmochim. Acta 74, 4543-4576 [5] Geochim. Cosmochim. Acta, 47,1501–1513 [6] Goodrich (2003) Geochim. Cosmochim. Acta 67, 3735–3771 [7] Herd C. (2003) MAPS, 38, 1793-1805; Wadhwa M. (2001) Science, 291, 1527-1530.

Preliminary Results of LUGREAS and its CVT with GEODYN-II.

M. Ye[1], J. G. Yan[1], F. Li[1,2] ,W. F. Hao[2], X. Yang[1] and W. Jin[1], [1]State Key Laboratory of Information Engineering in Surveying, Mapping and Remote Sensing, Wuhan University,Wuhan 430079, China. (e-mail mye@whu.edu.cn); [2]Chinese Antarctic Center of Surveying and Mapping, Wuhan University,Wuhan 430079, China.

Introduction: The interplanetary orbit determination and gravity field science team at LIESMARS are at the mercy of existing POD programs for which we often have little control in the past. From this point of view, a lunar spacecraft precision orbit determination and gravity field recovery software has been developed over the past four years. In this paper, we give a concise decription of LUGREAS (LUnar Gravity REcovery and Analysis System), and show its CVT(Cross Verication Test) results with the mature GEODYN-II.

LUGREAS description: The design of LUGREAS is to solve and analysis lunar gravity field. Its three main functions include: orbit propagation, measurement values simulation and Precision Orbit Determination(BATCH). LUGREAS is written by Fortran 95, with all the similar subroutines contained into a MODULE. The main mathematical reference is [1][2]. Until now, LUGREAS could process interplanetary ranges, range rate, VLBI delay/delay rates observavles. In LUGREAS, we have implemented a four-way relay tracking measurement type which has enormous potential for the positioning of future lunar farside lander.

CVT with GEODYN-II: The LUGREAS has experienced rigorous unit test. After that we then have a Cross Verification Tests(CVT)[3] against GEODYN-II. The CVT results show that: (1) Orbit Propagation: With all the same forces and other set-ups, the predicted orbit difference in R,T,N direction is less than 0.3 mm for one month arc, 5×10^{-3} mm for 2 day arc, compared with GEODYN-II, see Fig. 1; (2) The difference RMS of Computed values of observables for two-way range and two-way range rate are at levels of 0.06 mm and 0.002 mm/s separately, see Fig 2. (3) For BATCH, we reprocessed Chang'E-1 tracking data and validated the results with GEODYN-II arc by arc. The post-fit residuals are almost the same and post-fit orbit difference is in several centimeters level, see Fig. 3 and Fig. 4.

Conclusion and future Work: The paper gave the preliminary results of LUGREAS. In the future, we will have more tests with LUGREAS and extend its Mars and Asteroid function for the upcoming Chinese Mars and Asteroid mission.

References:[1] Moyer T.D., Mathematical Formulation of the Double-Precision Orbit Determination Program (DPODP), Technical Report 32-1527, NASA/JPL,1971. [2] Moyer T.D., Formulation for Observed and Computed Values of Deep Spaces Network Data Tyres for Navigation, Monograph 2, Deep Space Communications and Navigations Series,NASA/JPL, 2000.[3] Budnik F., Morley T., Mackenzie R., ESOC's system for interplanetary orbit determination: implementation and operational experience, 18th international symposium on space flight dynamics, Munich, Germany, 11-15 Oct 2004.[4] F. Li, M. Ye, J. G. Yan et al. (2016). Adv. Sp. Res. doi:10.1016/j.asr.2016.03.007.

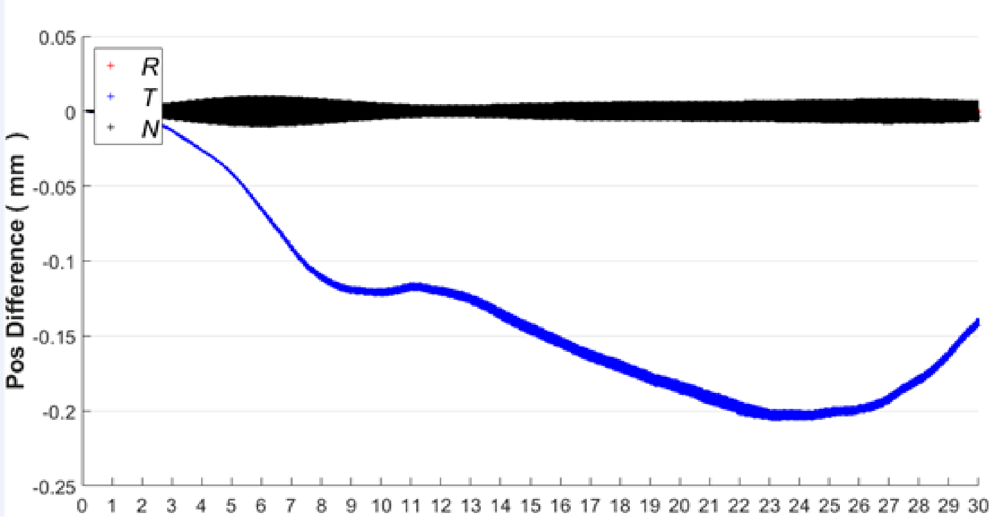

Fig. 1 Orbit propagation difference in R, T, N direction for one month

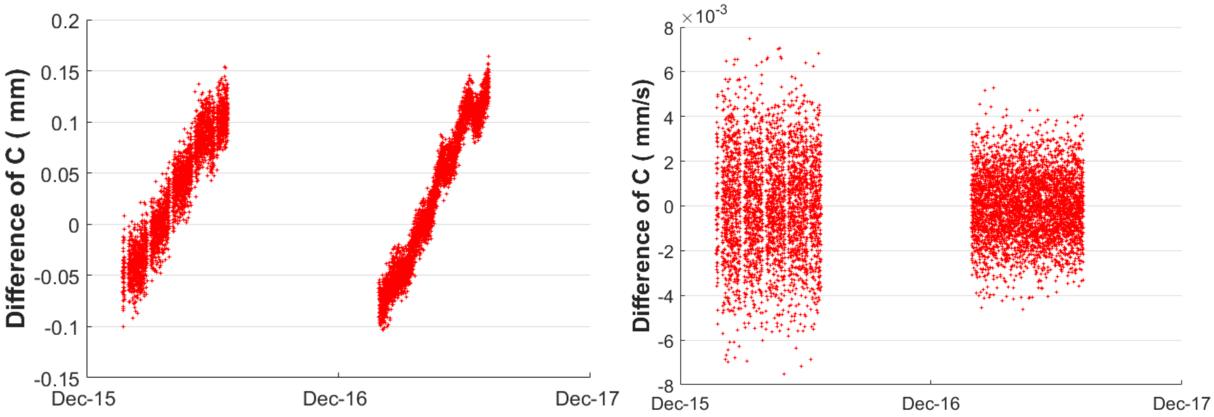

Fig. 2 Difference of Computed values of observables between LUGREAS and GEODYN-II (left one is two-way range, right one is two-way range rate)

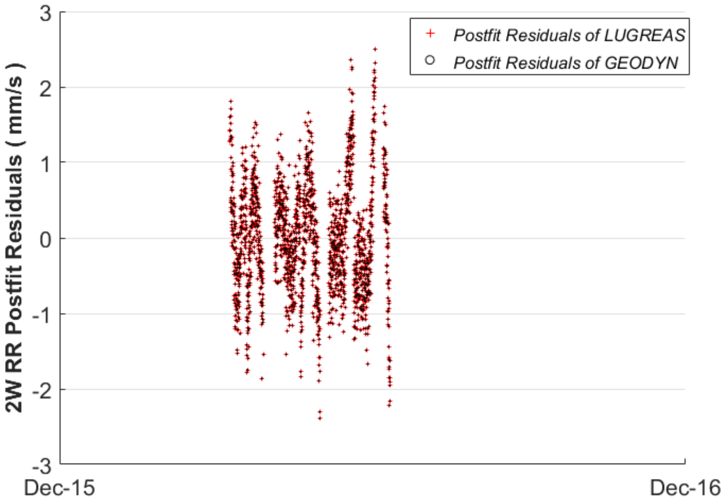

Fig. 3 Post-fit residuals from LUGREAS and GEODYN-II for arc 2007-12-15

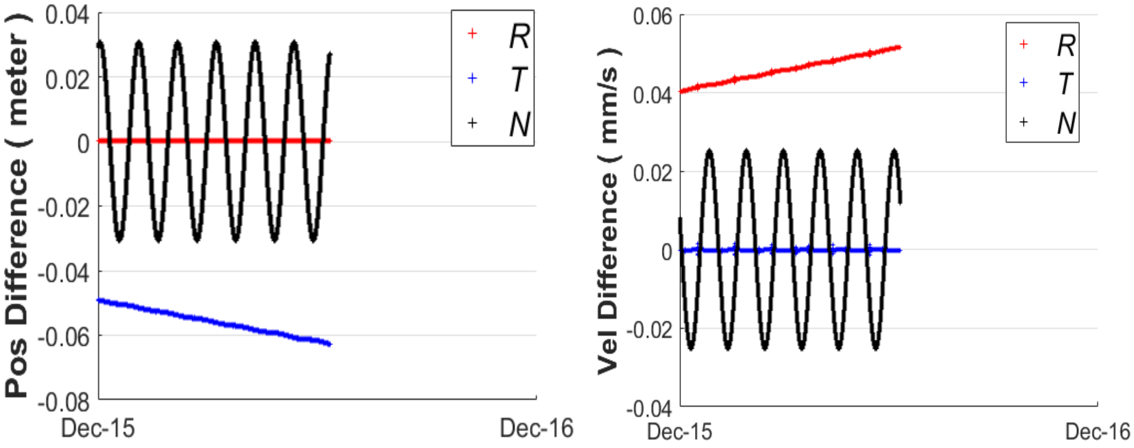

Fig. 4 Post-fit orbit difference between LUGREAS and GEODYN-II for arc 2007-12-15

HIGH-PRESSURE MINERALS IN EUCRITE REVEAL A SMALL SOURCE CRATER ON VESTA.

Run-Lian Pang[1], Ai-Cheng Zhang[1,*], Shu-Zhou Wang[1], Ru-Cheng Wang[1] & Hisayoshi Yurimoto[2], [1]State Key Laboratory for Mineral Deposits Research, School of Earth Sciences and Engineering, Nanjing University (pangrulian@163.com), [2]Department of Natural History Sciences, Hokkaido University (yuri@ep.sci.hokudai.ac.jp).

Introduction: Hyper-velocity collisions between celestial bodies create impact craters on the surfaces of planets and asteroids and may result in the formation of high-pressure minerals. These minerals are essential to constrain the prevailing Pressure-Temperature-time (P-T-t) conditions characterizing these shock events. Recently, the DAWN mission revealed that impact craters are abundant on the surface of the asteroid 4 Vesta, including two giant impact basins known as Rheasilvia and Veneneia [1]. In contrast to the widespread impact craters on the Vestan surface, very few high-pressure minerals have been discovered in HED meteorites. Up to date, high-pressure minerals have only been reported in one shocked eucrite [2]. In this study, we report the high-pressure minerals tissintite, vacancy-rich clinopyroxene, and super-silicic garnet in the shocked eucrite Northwest Africa (NWA) 8003 in addition to coesite and stishovite. These high-pressure minerals provide important constraints on the P-T-t conditions of shock metamorphism in NWA 8003. Given these conditions, we further estimate the possible sizes of the impact craters from which HED meteorites with high-pressure minerals might have originated.

Results: NWA 8003 is a basaltic eucrite that consists mainly of pyroxene and plagioclase with a subophitic texture. Most of the pyroxene grains in the host rock show augite exsolution lamellae. Most of the plagioclase grains adjacent to melt veins are fully transformed into maskelynite, whereas those farther from the melt veins are usually partially transformed into maskelynite. Shock melt veins are common in NWA 8003 and high-pressure minerals are found in or/and around these melt veins.

Petrography of shock melt veins: Most of the melt veins in NWA 8003 are relatively thin (<200 μm wide) and consist predominantly of fine-grained clinopyroxene. A few wide melt veins in NWA 8003 exhibit complex zoning in their mineral assemblage (Fig. 1). They may consist of an edge zone dominated by fine-grained clinopyroxene, a middle zone composed of eclogitic mineral assemblage (garnet + rod-like coesite + clinopyroxene ± glass), and a central zone of garnet + glass.

Characterization of high-pressure minerals: Fine grained silica aggregates (FSAs), which consist of coesite, stishovite and amorphous silica, are observed within most melt veins (Figs. 2a-2b). Coesite grains form a thin rim on a large core dominated by lamellae-like stishovite and silica glass (Fig. 2a).

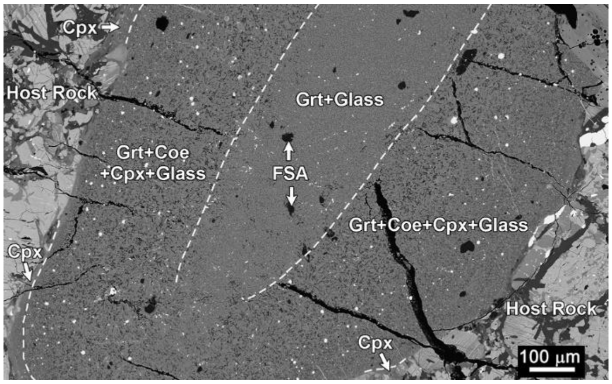

Figure 1. Back-scattered electron image of a typically zoned shock melt vein in NWA 8003. Cpx: clinopyroxene; Grt: garnet; Coe: coesite; FSA: fine-grained silica aggregate.

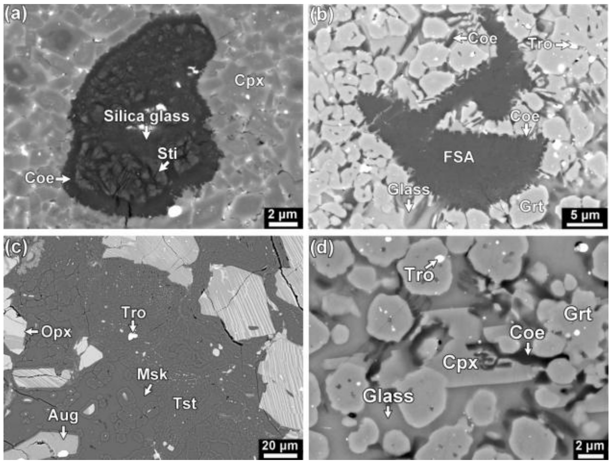

Figure 2. (a) A FSA within a melt vein composed of fine-grained clinopyroxene. Granular coesite forms the rim of the aggregate while stishovite and silica glass occur at the core. (b) Fine-grained silica aggregates dominated by coesite. (c) tissintite occurs in maskelynite adjacent to shock-melt veins. (d) A typical area showing the textural association of garnet, rod-like coesite, and clinopyroxene embedded in glass. Cpx: clinopyroxene; Coe: coesite; Sti: stishovite; FSA: fine-grained silica aggregate. Tro: troilite; Grt: garnet; Msk: maskelynite; Aug: Augite; Tst: tissintite; Opx: orthopyroxene.

Tissintite, a high-pressure polymorph of Ca-rich plagioclase with a clinopyroxene structure, is commonly observed in maskelynite adjacent to melt veins. It appears to have nucleated and grown on relict mineral fragments in maskelynite (Fig. 2c). The tissintite in NWA 8003 has an average chemical formula $(Ca_{0.64}Na_{0.09}\square_{0.27})(Al_{0.99}Fe_{0.01})(Si_{1.62}Al_{0.38})O_6$ with high vacancy concentrations on the M2 site.

Vacancy-rich clinopyroxene (Fig.1. Fig. 2a) in both thin and wide melt veins is characterized by a complex chemical composition, with much higher Al_2O_3 concentration and more abundant Ca-Eskola (Ca-Esk, $Ca_{0.5}\square_{0.5}AlSi_2O_6$) components than the pyroxenes in host rock.

Garnet occurs as fine dendritic or anhedral-euhedral grains (Fig. 2d) in the zoned melt veins of NWA 8003. Garnets in the ecologitic assemblages and central zone are super-silicic, containing 6–13 mol% majorite components.

Disscussion: Among these high-pressure minerals mentioned above, tissintite, vacancy-rich clinopyroxene, and super-silicic garnet are reported in HED meteorites for the first time. In addition, this is the first time that tissintite has been observed in samples other than those from shocked Martian meteorites [3].

Formation mechanisms of high-pressure minerals. The lamellae-like texture of stishovite in NWA 8003 implies a structure-controlled phase transformation, which is consistent with a solid-state phase transformation mechanism. Amorphous silica was originated later from stishovite during adiabatic decompression, since stishovite is sensitive to heating. The texture of granular coesites in the rim of FSA indicates crystallizating from the silica glass. Textural and compositional evidences indicate the super-silicic garnet, the associated clinopyroxene and rod-like coesite in NWA 8003 they crystallized from high-pressure melts.

Constraints on the shock conditions. Several indicators could potentially be used to constrain the prevailing shock conditions affecting NWA 8003. However, there are limitations for some of them. Firstly, it is not appropriate to applying static high-pressure phase diagrams to interpret the coexistence of stishovite and coesite since they have formed through different mechanisms. Secondly, the exact stability field of tissintite remains unknown because it is absent in the phase diagram of plagioclase. Therefore, it is difficult to constrain the formation pressure based on the presence of tissintite alone. Thirdly, vacancy-rich clinopyroxene has a wide stability field (from <2 GPa to >20 GPa) [4] ,it is difficult to constrain their formation conditions in NWA 8003.

Based on the static high-pressure experiments targeted in anhydrous mid-ocean ridge basalt [5], an eclogitic mineral assemblage containing glass indicates a pressure between 5 GPa and 10 GPa. Static high-pressure experiments on natural mid-oceanic ridge basalt reveal that the Si and Al concentrations in super-silicic garnet are a function of pressure their chemical compositions [6]. By adopting the correlation diagram for atomic numbers of Si and Al of garnet in the experiment, the chemical composition of super-silicic garnet in the eclogitic assemblages reveal that solidification of melt veins (1mm in width) in NWA 8003 began at a pressure of >~10 GPa and ceased when the pressure dropped to <~8.5 GPa. If assuming a shock pressure of ~10 GPa, the melting temperature of such a basaltic material similar to that found in NWA 8003 should be >1900 ^{o}C based on the phase diagram for mid-oceanic ridge basalt [4].

Estimating the impact velocity and crater diameter. By applying simulation models developed in previous studies [7], we can calculate the impact velocity and size of the impactor that produced the shock melt veins in NWA 8003, as well as a lower limit to the diameter of the source crater. If we assume impactors spanning a range of densities (basalt, ordinary chondrite, and iron), an impactor of 0.16–0.18 km in size is required to produce an impact pressure of 10 GPa, vertically impacting the basaltic surface of Vesta with an impact velocity of 1.2–1.7 km s–1. The corresponding diameter of the transient impact crater would be 2.8–3.2 km (uncertainty of a factor of 2).

Implication. The impact velocity (~1.5 km s–1) that is required to account for the formation of the high-pressure mineral assemblages in NWA 8003 is consistent on magnitude with the average impact velocity (~5 km s–1) at in the main asteroid belt [8]. The diameter of the transient impact crater required to account for the high-pressure mineral assemblages in NWA 8003 is also comparable to the sizes of most impact craters (>4 km) on the surface of Vesta [2]. This result indicates that HED meteorites with similar high-pressure mineral assemblages might not necessary originate from the two giant impact basins on Vesta, as proposed in the literature. Addtionally, high-pressure minerals that formed under similar shock pressures might be more common in HED meteorites than previously thought.

References:

[1] Miyahara, M. et al. (2014) PNAS. 111, 10939–10942. [2] Marchi, S. et al. (2012) Science 336, 690-694. [3] Ma, C. et al. (2015) Earth Planet. Sci. Lett. 422, 194–205. [4] Zhao, S. et al. (2002) Earth Planet. Sci. Lett. 307, 517–524. [5] Yasuda, A. et al. (1994) J Geophys. Res. 99, 9401–9414. [6] Aoki, I. and Takahashi, E. (2004) Phys. Earth Planet. Inter. 143–144, 129–143. [7] Melosh, H. J. Impact Cratering: A Geological Process. (Oxford Univ. Press, 2009). [8] Bottke, W. F. et al. (1994) Icarus 107, 255–268.

This study was supported by grants from the Natural Science Foundation of China (41373065), State Key Laboratory for Mineral Deposits Research, Nanjing University (ZZKT-201322), and the Fundamental Research Funds for the Central Universities.

Navigation and localization of planetary rover towards orbital and ground imagery. Wenming Zhao[1,2], Xiaohua Tong[1]

[1] College of Surveying and Geo-Informatics, Tongji University, 1239 Siping Road, Shanghai 200092, PR China (e-mail: mengjingzhao@126.com)
[2] School of Geographic Information and Tourism, Chuzhou University, 1528 Fengle Road, Chuzhou 239000, PR China(e-mail: mengjingzhao@126.com)

Introduction: In recent few decades, planetary rover will still play a key role in extraterrestrial exploration. Traditional planetary rover localization methods(such as Visual Odometry etc.) are relative methods, and are accompanyed by drift error due to their incremental mode of operation[1]. Communication delay is also a thorny problem during the rover navigation process[2]. Thus accurate global ocalization is of high importance for planetary rovers to the future outerspace missions, particular to the Lunar or Mars Sample Retrun mission(for example, the upcoming Chang'E 5 mission). Using prior information to refine the localization has been the main approach in mobile robotics during the past decades[3]. In the last recent years, ESA has funded a research through the Network/Partnering Initiative(NPI) to develop methods concerning the global self-localization of rovers[4].

In this paper, based on methods from morphological analysis, object segmentation and extracting, image matching , pattern recognition etc., imagery feature library can be created from both orbital images and ground rover images, then map matching(via vector matching, not using traditional image matching) based global localization method can be used to guide the navigation and localization of the planetary rover. The types of image feature include crater, rock, gully, aerolian feature, wrinkle ridge etc. Except extracting these image features, the 3D geometry topology relations between them will also be considered to improve the robustness of the localization method.

Employing the aforementioned method, high precision global positioning results can be obtained. In addition, on account of using map matching method and offline processing mode for orbital image feature library extracting, less computing resources are required, meeting the demanding for the limited hardware resources available on a planetary rover. Therefore, served with optimized algorithms and suitable hardware configuration, the efficient self-localization of a planetary rover in an absolute frame of reference is feasible. It provides vital safety guarantee for planetary rover in Space exploratory.

References:

[1] Emmanouil Hourdakis and Manolis Lourakis(2015) IEEE/RSJ Int. Conf. Intelligent Robots and Systems, 111-116.

[2]Evangelos Boukas, Antonios Gasteratos et al.(2014) IEEE International Conference on Robotics and Automation (ICRA)

[3]Evangelos Boukas, Antonios Gasteratos et al.(2014) International Symposium on Artificial Intelligence, Robotics, and Automation in Space(i-SAIRAS)

[4]Evangelos Boukas, Antonios Gasteratos et al.(2015) In Symposium on Advanced Space Technologies in Robotics and Automation (ASTRA)

NWA 7188: A MONOMICT EUCRITE WITH A HIGH DEGREE OF PARTIAL MELTING GENESIS INDICATED BY ITS ANOMALOUS FE/MN RATIOS.

Shaofan Che[1], Qi He[1] and Long Xiao[1] [1]Planetary Science Institute, Department of Earth Sciences, China University of Geosciences, Wuhan. 1183029169@qq.com

Introduction: Eucrites are differentiated achondrites and share a common provenance with howardites and diogenites. Homogenous oxygen isotopic compositions of “HED” group[1] suggest an origin from a same parent body, and this homogenization of oxygen isotopes was a consequence of high degrees of partial melting. Researches into this unique asteroid will provide a profound insight into the formation and evolution of terrestrial planets, especially Earth. This work focuses on the petrographic description and geochemical analysis of an eucrite NWA 7188 using a Quanta 200 scanning electronic microscope and a JXA-8230 electronic microprobe, respectively. Based on these data, we propose an outline of the geological settings involved in its formation. NWA 7188 has an abnormal Fe/Mn ratio, a widely used index for distinguish differentiated achondrites supposed to come from distinct parent bodies[1], and we attribute this anomaly to a relatively higher partial melting event of its precursor.

Results: NWA 7188 was previously classified as an unbrecciated eucrite. However, we have identified three petrologically distinct regions in our sample: gabbroic clasts, variolitic clasts and a granulitic matrix, which make it a monomict eucrite. There are exsolution phenomena in almost all pyroxenes, yet the width and density of exolution lamellae vary among different petrological regions. In addition, pyroxenes in variolitic clasts present obvious Fe-Ca zoning and those in matrix also show a heteogenity among different grains in Ca contents, while those in gabbroic clasts have rather homogeneous compositions. These three fractions have similar pyroxene ($En_{26.5\text{-}35.6}Wo_{1.6\text{-}41.1}Fs_{29.6\text{-}64.9}$) and plagiocalse ($An_{76.4\text{-}91.8}Or_{0.1\text{-}3.2}$) major element compositions with other basaltic eucrites[2], although plagioclases in variolitic clasts have higher An% than the other two fractions.

Discussion: We plot NWA 7188 pyroxene compositions onto the Fe/Mn diagram (Fig. 1) and noticed that almost all the data points obviously deviated from the Vesta line[3] as defined by HED meteorites, while approaching the Mars line. However, as indicated by its An% contents, NWA 7188 is certainly not a martian meteorite. This Fe/Mn anomaly made us probe into factors controlling the Fe/Mn variations in differentiated achondrites. Firstly, the Fe reduction event happened in the early solar nebular could have caused the differentiation between Fe and Mn in meteorites[4]. After plotting Fe/Mn with Fe/Mg data (Fig. 2), however, we find that NWA 7188 appears to be magmatically related with other HED meteorite samples as they could be derived from a common primitive achondritic material by different degrees of partial melting. Secondly, olivine and pyroxene fractional crystallization could have reverse effects on the Fe/Mn ratios of the residual melt[5]. Regarding HED meteorites, we also find influences of these two major minerals on the Fe/Mn ratios with the ratios decreasing from dunites to orthopyroxenites and increasing from cumulate eucrites to basaltic eucrites. Nonetheless, we do not identify olivine or cumulate pyroxene grains in NWA 7188, excluding their influences on our sample. Thirdly, Fe^{2+}, Fe^{3+} and Mn^{2+} tend to present different partitioning behaviors between Ca-rich and Ca-poor pyroxenes in igneous and metamorphic rocks[6,7]. Although NWA 7188 and other HED meteorites also show this effect and diogenites and cumulate eucrites do show great Fe/Mn variations associated with Wo% contents (Fig. 3), there is no obvious distinction in Fe/Mn ratios between the Ca-rich and Ca-poor pyroxene pairs in individual basaltic eucrites. We assume that the Fe/Mn ratios of HED meteorites' pyroxenes are mainly controlled by Mg^{2+} which is supposed to enter pyroxene crystal lattice earlier than Fe^{2+} and Mn^{2+}. The prior entrance of Mg^{2+} in pyroxenes occupies too many crystal lattice vacancies, restraining the further entrance of Fe^{2+}. In contrast, Mg may have a much smaller restraining effect on Mn, a minor element in pyroxene. As the Mg# gradually decreases following the magma general evolution trend, increasingly more crystal lattices are released to accept more Fe^{2+}, making pyroxenes' Fe/Mn ratios approach a constant value as shown by basaltic eucrites. Other factors including oxygen fugacity and exsolution of metalic phases may also pose some influences on the Fe/Mn ratios, yet we do not take these factors into consideration for no correlated evidence has been found in NWA 7188.

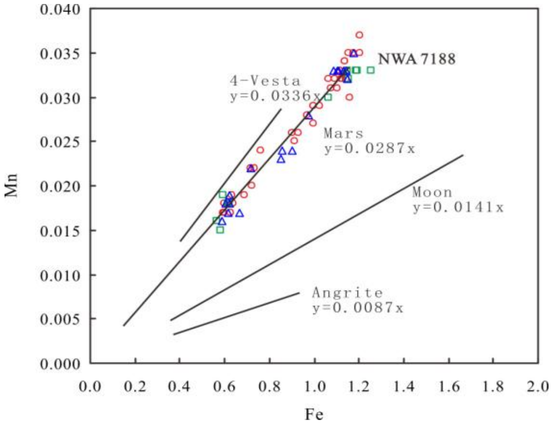

Fig 1: NWA 7188 pyroxenes' Fe (afu) vs. Mn(afu) plot. Red circle: gabbroic clasts; green square: matrix; blue triangle: variolitic clasts. Fe/Mn ratio lines for different parent bodies after Papike (2003).

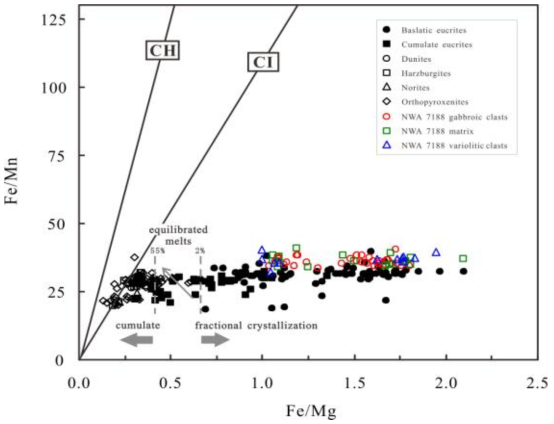

Fig 2: Fe/Mg vs. Fe/Mn diagram (Goodrich, 1999). The region refined by two vertical dashed lines represent the equilibrated melts originated from primitive achondritic material (as defined by CH and CI chondrite solid lines) by various degrees of partial melting (2% - 55%).

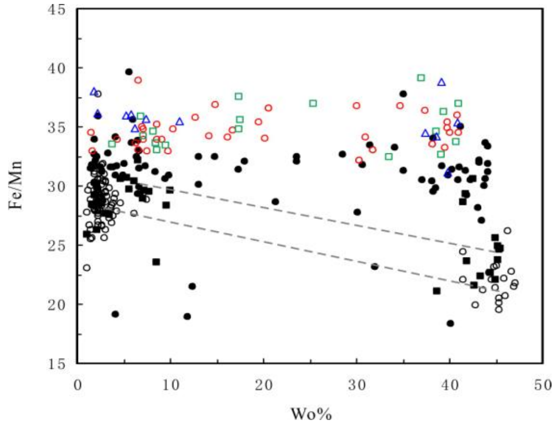

Fig 3: Relationship between Fe/Mn ratios and Wo% contents. Dashed lines connect average Ca-rich and Ca-poor pyroxene pairs in diogenites and cumulate eucrites. For symbols see Fig. 2.

References:

[1] Wiechert, U. H. et al. (2004) *EPSL, 221(1)*, 373-382. [2] Mittlefehldt, D. W. (2015). *Chemie der Erde-Geochemistry*, 75(2), 155-183. [3] Papike, J. J. et al. (2003) *American Mineralogist*, *88(2-3)*, 469-472. [4] Goodrich, C. A. and Delaney, J. S. (2000). *GCA*, 64(1), 149-160. [5] Delaney, J. S. et al. (1979, March). *LPSC* (Vol. 10, pp. 277-279). [6] Fleet, M. E. (1974). *CMP*, 47(3), 207-214. [7] Fleet, M. E. (1974). *CMP*, 44(4), 259-274.

Research on Microwave Thermal Emission Features At Aristarchus Plateau with CELMS Data.

Rui Zhao[1], Zhiguo Meng[1, 2, 3, *], Zhuanchuan Cai[2] and, Jinsong Ping[3]. 1. College of Geoexploration Science and Technology, Jilin University, Changchun, 130026, China (mengzg@jlu.edu.cn). 2. Faculty of Information Technology, Macau University of Science and Technology, Macau, China; 3. Key Laboratory of Lunar and Planetary Exploration, CAS, Beijing 100012, China.

Introduction: The Aristarchus plateau is one of the most geologically diverse regions of the Moon. It has long been a popular target for lunar geological and geochemical investigations due to its unique topographic features and volcanic complexes. High resolution topography data obtained from Lunar Orbiter Laser Altimeter (LOLA) indicated that the part of the high relief areas within the plateau had existed prior to the formation of the Imbrium basin [1]. Reflectance spectral analyses over the plateau indicated nortic compositions as the major materials in the subsurface of this region [2]. Mustard et al. (2011) found unique low-Fe feldspathic materials on the central peak of the Aristarchus, arguing that plagioclase-rich upper crust existed beneath the plateau [1]. Recently, Carlton Allen utilized Diviner data found that during the eclipse the temperature difference between the pyroclastic and mare before the eclipse are attributed to difference in albedo and the eclipse temperature difference and cooling/warming rate are attributed to differences in thermal inertia related to the concentrations of exposed rock [3].

However, the previous studies are mainly bsed on the visible data, surface mineralogic composition with the earth-based spectral reflectance and superficial thermal activities with the thermal infrared data. And the penetration depths of these data are rather poor [4]. In this paper, the spatial and temperal changes of the thermal emission (MTE) at Aristarchus Plateau are thoroughly stuided with the the microwave sounder (CELMS) data from Chang'E-2 satellite.

Method: In this study, we use the microwave sounder (CELMS) data from Chang'E-2 satellite, the ($FeO+TiO_2$) abundance derived from Clementine UV-VIS data, the surface slope and rougness estimated with LOLA data, and the rock abundance data evaluated with Diviner data.

The region is located between Mare Imbrium and Oceanus Procellarum ranging from 21°-31°N, 57°-43°W, which consists of Aristarchus Crater, Prinz Crater, Herodotus Crater and the largest sinuous rille on the Moon, Vallis Schroteri. The microwave emission features in these areas are of special significance to study the evolution of the Aristarchus Plateau.

The penetration depth of the CELMS data can be up to about 10 m in 3GHz [4, 5], and the CELMS data are sensitive to the substrate thermal features of the lunar regolith, which provide a potential chance to study the thermal features on the Moon surface. The data are allocated into 24 hours, with the calcaulated hour angle.The brightness temperature maps for every hour are generated with Gauss algorithm with the 0.25° ×0.25° spatial resolution.

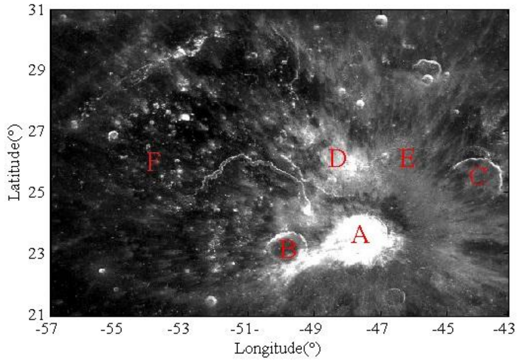

Fig.1 Aristarchus plateau; A=Aristarchus Crater, B=Herodotus Crater , C=Prinz Crater, D,E,F=high TB areas

To further study the interia MTE of the lunar regolith at the Aristarchus plateau, the temperature differences between noon and drawn (Fig.2) and those between 3.0GHz and 37GHz are generated.

Results and Conclusions: The results indicate that, generally, the MTE at the Aristarchus plateau is faily cold at daytime and hot at nighttime, which clearly present the scope of the Aristarchus plateau. Meanwhile, the brightness temperature distribution at daytime and nighttime at Aristarchus plateau are distinctly different from that those at the nearby regions of Oceanus Procellarum and from that at Aristarchus crater, which means that the construction of Aristarchus plateau is different from that of Oceanus Procellarum and that of Aristarchus. This agrees well with the previous conclusion that the Aristarchus plateau are mainly composed by lunar pyroclastic despoits. The result also hints that the absorption coefficients of the lunar pyroclastic deposits will be farily strong. Moreover, the Aristarchus Plateau presents high T_B at 37 GHz at midnight, while the T_B at the east part of the Plateau becomes much lower than that at the west part. This reveals that the constructions of the lunar regolith are almost homogeneous at the penetrated depth of the 37-GHz microwave over whole Aristarchus Plateau, while the materials of the lunar regolith at the penetrated depth of the 3-GHz microwave are distinctly different from that on the surface at the east part of the Plateau. Furthermore, the brightness temperature difference of the Aristarchus crater is huge, while the distribution of the highest values are changing with frequencies, which presents that the structure of Aristarchus crater is changing with depth.

Acknowledgements: *This work is supported by the National Natural Science Foundation of China (No. 41371332, 41590851), and the Science and Technology Development Fund of Macau (No. 110/2014/A3, 091/2013/A3).*

References:[1] Mustard J. F. et al. (2011) *JGR, 116, E00G12.* [2] Chevrel S. D. et al. (2009) *Icarus, 199, 9-24.* [3] Carlton A. et al. (2016) *LPS 47th*, Abstract # 1309. [4] Meng, Z. G., et al. (2014) *Planet. Space Sci., 101, 1-11.* [5] Jin, Y. Q., (2003) *Chin. J. Radio Sci., 18(5), 477-486.*

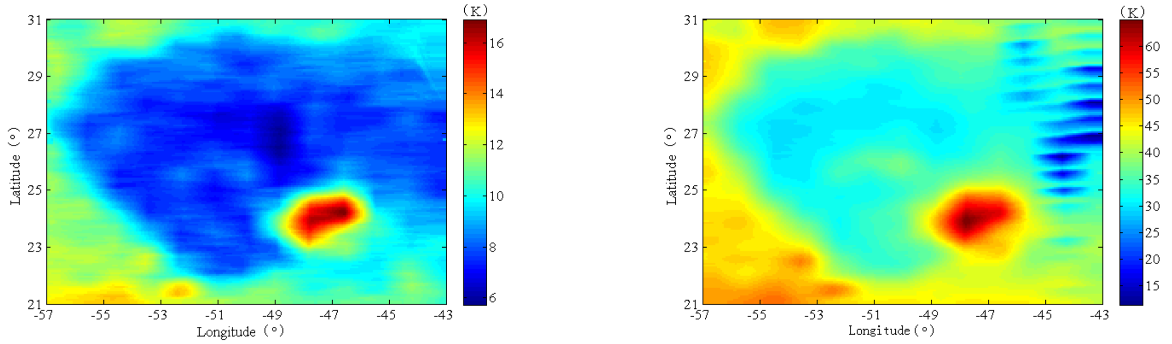

(a) 3.0GHz (c) 19.35GHz

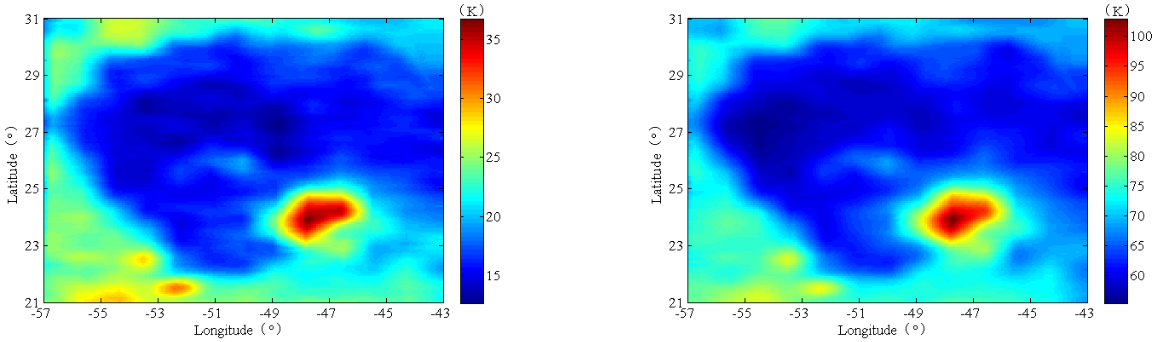

(b) 7.8GHz (d) 37GHz

Fig.2 Distribution of brightness temperature difference between noon and dawn at Aristarchus Plateau

DISTRIBUTIONS OF MINERAL ASSEMBLAGES OF THE ARISTARCHUS CRATER

C. Q. Liu[1], Z. C. Ling*[1] [1]Institute of Space Sciences, Shandong Provincial Key Laboratory of Optical Astronomy and Solar-Terrestrial Environment, Shandong University, Weihai 264209, China, (zcling@sdu.edu.cn)

Introduction: Located on the western nearside of the Moon, Aristarchus crater is a prominent Copernican crater for its anomalous brightness relative to other craters of similar age and size on lunar surface [1].

The rock types of Aristarchus region are abundant, such as basalt, anorthosite, KREEP and so on [2], and it is dominated by noritic compositional signatures [3, 4]. The crater was formed at the contact between Procellarum and an uplifted block of lunar crust [5]. It's a common thought that the crustal rocks are emplaced with the Imbrium impact and then adjusted after the formation of Imbrium basin [1, 6-8].

Visible near-infrared (VNIS) spectroscopy is one of the most popular methodologies in lunar remote sensing studies. In this abstract, we apply high spectral (~ 10 nm constant with 85 bands) and spatial resolution (~ 140 m/pixel) data from the Moon Mineralogy Mapper (M^3) onboard Chandrayaan-1.

Regional Settings and Methods: Fig. 1 (a) shows the 2.9 μm image of the region we studied including Aristarchus crater. It's easy to find that the Aristarchus crater is anomalous brightness relative to the regions around, indicating the freshness of the crater ejecta and a young age of this crater (~150 Ma) [9], consistent with low optical maturity.

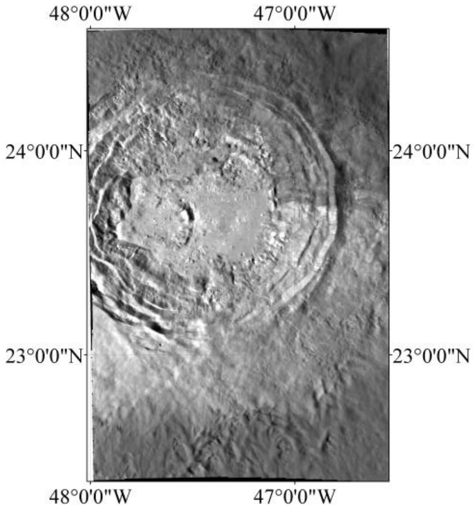

Fig. 1 M^3 data image acquired at 2.9 μm of the study region.

The M^3 team has developed several mineral indicators for guiding to analyses of the fundamental mineralogical properties of lunar surface [14]. For example, three parameters shown in Table 1 are used in this abstract to capture the dominant modes of spectral variance caused by space weathering, mafic silicates, and soil maturity, like the integrated band depth at 1 μm (IBD1) and 2 μm (IBD2) and reflectance at 1.58 μm (R1580).

Table 1 Formulations of three mineral indicator parameters

Parameters	Formulation
IBD1	$\sum_{n=10}^{45}(1-\frac{R(n)}{R_C(n)})$
IBD2	$\sum_{n=50}^{72}(1-\frac{R(n)}{R_C(n)})$
R1580	reflectance at 1.58 μm

These parameters are present in Fig. 2 as color composite with IBD1 in red, IBD2 in green, and R1580 in blue. Red areas with more obvious absorption feature of 1 μm should be associated with olivine; green areas with high values of integrated band depth at 2 μm indicate pyroxene-rich lithology; and the blue ones may be dominated by plagioclase for the high reflectance values at 1.58 μm.

Based on the locations and color composite shown in Fig. 2, eight areas are selected for detailed evaluations of their mineralogy assemblages. No. 1 (magenta), No. 2 (cyan) and No. 8 are areas from ejecta of Aristarchus. No. 7 and No. 4 are selected from the floor of the crater. No. 3 (yellow), No. 5 and No. 6 are from the crater wall.

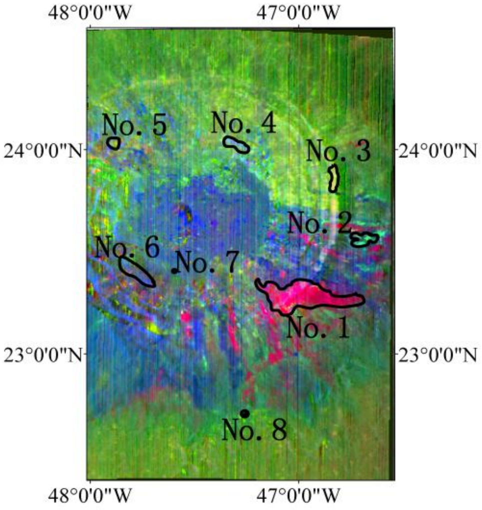

Fig. 2 Color composite of spectral parameters and the regions we selected of Aristarchus crater; Red: IBD1; Green: IBD2; Blue: R1580.

We extract the M^3 spectra of eight regions (shown in Fig. 3) by ROIs of 4 pixels and get mean spectra at every one of them. Continuum removal methods with different locations are adopted as follows: 1) for pyroxene-dominant spectra (No. 2, No. 4 and No. 8), the locations of 0.73 μm, 1.41 μm, and 2.58 μm are used; 2) for olivine-bearing spectra, the locations are selected at 0.73 μm, 1.62 μm, and 2.58 μm.

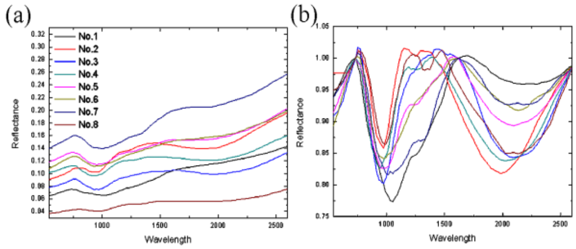

Fig. 3 (a) M^3 reflectance spectra of the 8 regions above; (b) the same spectra with continuum removed.

Modified Gaussian Model (MGM) deconvolution [10, 11] is applied to analyze mineral chemistries from the spectral data collected. The absorption features of orthopyroxene (opx) are at 0.94-0.98 μm and 1.88-2.06 μm, while those of clinopyroxene (cpx) are at around 1 μm and 2.3 μm [12, 13]. What's more, those of olivine are at around 0.87-0.884 μm, 1.05 μm and 1.234-1.261 μm [2]. The MGM results are shown in Table 2 and Table 4.

Table 2 MGM results of No. 2, No. 4 and No. 8.

No.		2		4		8	
Parameters	wavelength	center	STR.	center	STR.	center	STR.
opx	1μm	926	0.14	901	0.17	934	0.11
	2μm	1911	0.20	1905	0.16	1868	0.14
cpx	1μm	1014	0.09	1022	0.12	1031	0.13
	2μm	2266	0.07	2261	0.10	2280	0.16
opx/(opx+cpx)	1μm	0.60		0.58		0.45	
opx/(opx+cpx)	2μm	0.74		0.60		0.46	

Result: MGM results suggest that areas No. 2, No. 3, and No. 4 are dominated by orthopyroxene (opx/(opx+cpx)≈0.62), which corresponds to crustal composition, while the other areas are clinopyroxene dominant (opx/(opx+cpx)≈0.47).

Olivine is found within areas No. 1, No. 3, No. 5, No. 6 and No. 7, indicating its wide presences in the ejecta, floor and wall of Aristarchus crater. The olivine composition may be excavated from a shallow pluton, or an olivine-rich region of the Imbrium ejecta, or derived through melting and excavation of olivine-rich Procellarum basalts [1]. Olivine chemistry is toward the Mg-rich endmember (Fo≈53-59) at area No. 1, No. 3, No. 5 and No. 6 but Fe-rich endmember (Fo≈46) at the area No. 7. A different content of olivine in the mixture with pyroxene appears in different areas (~ 0.15-0.59). Moreover, we find the olivine accompany with different opx/cpx assemblages. We prefer more than one mechanism as stated above might account for the olivine-rich features in this region. For future work, we will conduct more detailed analysis with more additional spectra to better understand the mineral diversities of this unique site on the Moon.

Acknowledgement: This research was funded by the National Natural Science Foundation of China (41373068), Natural Science Foundation of Shandong Province (JQ201511 and ZR2015DQ001), and Young Scholars Program of Shandong University, Weihai (2015WHWLJH14).

References: [1] Mustard J. F. et al. (2011) *JGR, 116*. [2] Ling Z. C. et al. (2013) *Scientia Sinica Physica, 43*, 1403. [3] Lucey P. G. et al. (1986) *JGR, 91*, 344-354. [4] Chevrel S. D. et al. (2009) *Icarus, 199(1)*, 9-24. [5] McEwen A. S. et al. (1994) *Science, 266*, 1858-1862. [6] Moore H. J. (1965) *U.S. Geol. Surv., Geol. Invest. Map*, 1-465. [7] Guest J. E. (1973) *Geol. Soc. Am. Bull. 84*, 2873-2894. [8] Zisk S. H. et al. (1977) *Moon, 17*, 59-99. [9] Zanetti M. et al. (2013) *LPSC, 44*, Abstract #1842. [10] Sunshine J. M. et al (1990) *JGR, 95:* 6955-6966. [11] Sunshine J. M. et al (1998) *JGR, 103:* 13675-13688. [12] Kramer G. Y. et al. (2013) *Icarus, 223*, 131-148. [13] Klima R. L. et al. (201) *Meteoritics and Planetary Science, 42*, 235-253. [14] Isaacson P. J. et al. (2011) *JGR, 116*, E6.

Table 3 MGM results of No. 1, No. 3, No. 5, No. 6 and No. 7.

No.		1		3		5		6		7	
Parameters	wavelength	center	STR.	center	STR.	center	STR.	center	STR.	center	STR.
oliv	0.85μm	857	0.13	847	0.08	867	0.11	870	0.10	879	0.08
	1.050μm	1056	0.25	1046	0.14	1052	0.13	1056	0.12	1061	0.16
	1.250μm	1240	0.15	1225	0.04	1246	0.09	1242	0.08	1254	0.12
opx	1μm	933	0.05	917	0.17	930	0.08	933	0.06	939	0.04
	2μm	1966	0.04	1976	0.15	1926	0.09	1961	0.06	1958	0.06
cpx	1μm	982	0.05	992	0.10	986	0.09	981	0.06	985	0.05
	2μm	2329	0.05	2299	0.12	2265	0.10	2268	0.06	2275	0.07
Fo #		59		72		53		56		46	
oliv/(oliv+opx+cpx)		0.60		0.15		0.32		0.38		0.50	
opx/(opx+cpx)	1μm	0.50		0.64		0.49		0.48		0.48	
opx/(opx+cpx)	2μm	0.43		0.55		0.47		0.49		0.46	

Primary Ejecta Distribution of the Orientale Basin on the Moon.

Minggang Xie and Meng-Hua Zhu, Lunar and Planetary Science Laboratory, Macau University of Science and Technology, Taipa, Macau (xieminggang13@gmail.com).

Introduction: The Orientale basin, formed ~ 3.8 billion years ago [1], is the youngest multi-ring basin on the Moon. Due to the relatively young age, the Orientale basin suffered minor geological modification since its formation [2, 3]. Its well-preserved morphology, therefore, provides a best choice to study the thicknesses of primary ejecta for large-scale impact basins on the Moon. Here, we propose a model that considers the erosion of partially filled pre-Orientale craters (PFPOCs) to re-investigate the thickness distribution of primary ejecta of the Orientale basin. The LOLA DEM model [4] was used for measurements of elevations.

Methods: Craters undergo some degree of degradation since its formation because of topographic diffusion arised from the formation of small impact craters [5], and seismic shaking [6-8]. In this work, we assume the topographic diffusion is the main factor accounting for the degradation of complex craters.

The procedures are briefly illustrated as follows: (1) we used a variety of initial crater profiles to create a variety of degraded profiles that matched with the crater diameter of each measured PFPOC; (2) we emplace a variety of primary ejecta thickness on the degraded profiles to produce model profiles; (3) Two parameters (exposed rim height and average exposed rim-floor depth) are calculated for every model profiles, and are measured for PFPOCs from the DEM; (4) A best-fit model used to match measurements with simulations gives primary ejecta thicknesses.

Results and Disscusions: The model-derived primary ejecta thickness (green triangles) are displayed in Fig. 1. A nonlinear least square fit to primary ejecta thicknesses by using $d = T_{PE\_R}\left(r/R\right)^{-b}$ (where δ is the thickness at distance r, T_{PE_R} is the thickness at the basin rim, R = 465 km, b is the exponent) gives T_{PE_R} = 0.85 ± 0.53 km and b = 2.8 ± 1.9 (95% confidence intervals) (see the green line). Our result is smaller than previous results [e.g., 9] (the gray dashed line).

Assuming that the total mass of primary ejecta is equal to the mass of excavation, we derived apparent radius R_{TC} = 200 km, which is consistent with the estimates from gravity inversions [e.g., 10, 11]. The primary ejecta thickness is often defined either by Eq. (1) [12] or (2) [13].

$$d = 0.14 R_{TR}^{0.74}\left(r/R_{TR}\right)^{-3} \tag{1}$$

$$d = 0.033 R_{TR}\left(r/R_{TR}\right)^{-3} \tag{2}$$

where R_{TR} is rim-to-rim radius of transient crater, and all values are given in meters. The value of R_{TR} is ~1.2 times of R_{TC} [14,13], then R_{TR} is 240 km. For comparison, the thickness distribution of primary ejecta was shown in Fig. 1, in which the blue and black lines were calculated after Eq. (1) and (2), respectively. It turns out that the model-derived primary ejecta thicknesses are consistent with Eq. (2). This result agrees with the measured results of complex craters [15], which implies that Eq. (2) gives a good estimate of primary ejecta thickness for complex craters. The widely cited Eq. (1) gives a very poor estimate. It might be due to the fact that it was established from inadequate lunar data and inconsistent with the general form of either empirical or theoretical studies of craters [13].

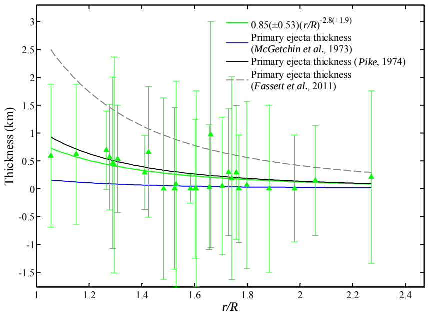

Fig. 1 Distribution of primary ejecta thicknesses (green filled triangles). The green line represents the best fit of the primary ejecta thicknesses.

References: [1] Greeley et al. (1993), *JGR, 98*(E9), 17,183-17,205. [2] Spudis P. D. (1993), *The Geology of Multi -Ring Basins*, Cambridge Univ. Press. [3] Kreslavsky M. A. and J. W. Head (2012), *JGR*, 117, E00H24. [4] Smith D. E. et al. (2010), *GRL*, *37,* 18. [5] Soderblom L. A. (1970), *JGR, 75,* 2655-2661. [6] Schultz P., and Gault D. (1975), *LPSC*, *6*, 2845-2862. [7] Richardson J. E. et al. (2004), *Science, 306* , 1526-1529. [8] Richardson J. E. et al. (2005), *Icarus, 179*, 325-349. [9] Fassett C. I. et al. (2011), *GRL*, *38*, L17201. [10] Wieczorek M. A., and Phillips R. J. (1999), *Icarus, 139*, 246-259. [11] Hikida H., and Wieczorek M. A. (2007), *Icarus, 192*, 150–166. [12] McGetchin T. R. et al. (1973), *EPSL, 20*, 226 – 236. [13] Pike R. J. (1974), *EPSL*, *23*, 265–271. [14] Baldwin R. B. (1963), *The Measure of the Moon*, The University of Chicago Press. [15] Krüger T. et al. (2014), *LPSC, Abstract* #1834.

RESEARCH ON ILLUMINATION CHARACTERISTIC OF ARISTARCHUS PLATEAU BY USING DEM DATA AND LUNAR EPHEMERIS.

Zhang Jidong[1] (Jilin University, Changchun; zhangjd14@mails.jlu.edu.cn) and Ping Jinsong[2] (National Astronomical Observatories of China, Beijing; jsping@bao.ac.cn).

Introduction: Aristarchus plateau is of complex geological condition and it has been widely concerned. We analyze the illumination characteristic of this area with the high resolution DEM data and NASA JPL DE405 lunar ephimeris. We use the NOVAS software to calculate the location of lunar and sun and take the libration into consideration. We calculate the height angle of sun, analyze the topographic effect with a high temporal resolution (3h) and consider the illumination below the horizon. We generate illumination fraction maps with the resolution of 0.01 ° for the year of 2015 (fig.2) and the resolution of 0.1 in 1, 9.3, 18.6 and 30 years for Aristarchus plateau (-52 °E - -47 °E, 22 °N - 27 °N). We also choose five places A (Vaisala crater), B (the highest place of Aristarchus plateau), C (the east edge of Aristarchus crater), D (Herodotus crater) and E (the plain of northwest Aristarchus plateau) as the typical areas to study. The results show that illumination characteristic is of great association with the topographic feature, 99.98% of the illumination fraction is between 0.3 and 0.5132, the minimum value is 18.07%, the region with high elevation will enjoy more illumination compare with the low-lying areas. The bottom of Aristarchus crater and Herodotus crater will be illuminated greater nearly 40% than the edge in one year, which may make a great geological condition differences of this region. The Illumination fractions of the five areas tend to be stable. The illumination characteristics of crater are of special significance to study the evolution of the lunar exploration and worth to further study.

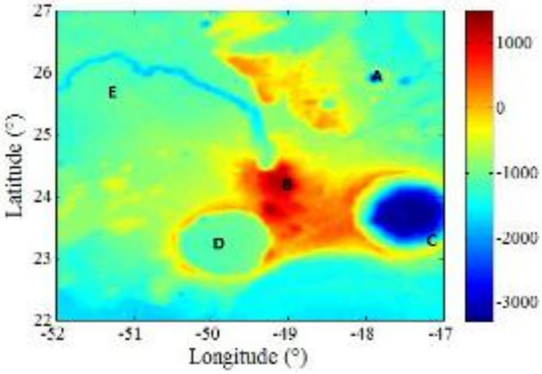

Fig.1 DEM map of Aristarchus plateau

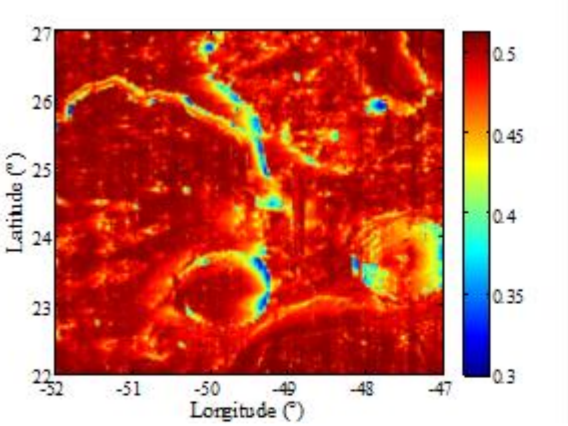

Fig.2 the illumination fraction over 0.3 of the year of 2015

References: [1] Hao W F, LI F, Yan J G, et al. (2012) *Chinese J . Geophys*, 55(1). [2] H. Noda, et al. (2008) *GEOPHYSICAL RESEARCH LETTERS*, *35*, L24203. [3] E. Mazarico, et al. (2010) *Icarus*, 1066-1081. [4] D.B.J. Bussey, et al. (2010) *Icarus*, 558-564. [5] D. Ben J. Bussey, et al. (1999) *GEOPHYSICAL RESERACH LETTERS*, 26, 9, 1187-1190.

DISTRIBUTION OF CH_4 IN TITAN'S THERMOSPHERE AND EXOSPHERE.

Fayu JIANG[1+], Jun CUI[1#], Jiyao XU[2], [1] National Astronomical Observatories, Chinese Academy of Sciences, China, [2] State key Lab. of space-weather, Chinese Academy of Sci., China *([#]Corresponding author: cuij@nao.cas.cn, [+]Presenter)*

Abstract: he escape rate of a light atmospheric constituent from any Solar System body could be either obtained from the fluid approach with known density profile within the thermosphere, or obtained from the kinetic approach with known velocity distribution near the exobase. Previous works along these different lines of reasoning do not provide a consistent picture of CH_4 escape on Titan. Here we reanalyze the CH_4 structure in Titan's upper atmosphere and exosphere with the Cassini Ion Neutral Mass spectrometer (INMS) data acquired over ~50 Cassini flybys with the satellite. These data have been re-calibrated with the updated algorithm of ram enhancement including gas leak through the INMS chamber vent that has not been considered in previous works. We find that, within the traditional framework of the collisionless Chamberlain theory, the mean CH_4 corona temperature is ~260 K, substantially higher than the mean isothermal temperature of 140 K inferred from the N_2 distribution below the exobase. This implies strong heating of CH_4molecules in Titan's upper atmosphere, but the corresponding CH_4 escape flux is still many orders of magnitude lower than the value implied by diffusion model calculations. To solve this enigma, we have attempted two alternative forms of CH_4 velocity distribution at the exobase, including a bi-Maxwellian distribution and a kappa distribution. For each case, we require that the exospheric CH_4 densities are well reproduced by the values obtained from the Liouville theorem, and at the same time, the CH_4 escape flux calculated from the integration of the velocity distribution well reproduces the diffusion model result.

Subsurface Structure Analysis of Chang’E-3 Landing Site.

Jialong Lai , Yi Xu, Xiaoping Zhang and Zesheng Tang , Macau University of Science and Technology, Macau (jiallai2014@gmail.com).

Introduction: The volcanic and tectonic histories of a planet are consequences of internal processes of heat and mass transfer [1]. Although the details of these processes and their causative are beyond our current ability to understand, there are several straightforward relationships between a planet's internal thermal evolution and the volcanic and tectonic history. So obtain the structure of the lunar mare subsurface and establishing its thickness as a function of time is an important goal in setting constraints on the petrogenesis of lunar mare basalts and their relation to the thermal evolution of the Moon [2]. Early work focused on estimating the total thickness of mare basalt fill in the mare basins, and a variety of techniques were used, such as approach based on crater morphometry, crater penetration, stratigraphy [3].

At present, the geological structures in the lunar maria can be directly investigated using the observation data ofthe Lunar Radar Sounder (LRS) onboard Kaguya, which detected echoes from layers at depths of several hundred meters [4]. Unfortunately, they didn't get the subsurface structur in some high titanium region such as the Chang'e-3 landing site. The preliminary results about deep subsurface structure from the 60 MHz channel were presented inXiao et al. [2015] and Zhang et al. [2015], but their results are controversial concerning the number and depth of subsurface layers. Now Chang'e-3 yutu rover with LRS get some data from the Moon, in this paper, we utilized these data to discuss the subsurface structure of these high titanium region, and trying to unraveling the timing, duration and thickness of mare volcanism on this region.

The Chang’E-3 Lunar Penetrating Radar Experiment: On December 14, 2013, China’s Chang’E-3 (CE-3) spacecraft successfully landed in the northern Mare Imbrium at 44.1213°N, 19.5115°W. The landing site is within an ‘Middle’ Eratosthenian-aged geologic unit, consisting of high titanium mare basalts, and the north of the landing site, about 10 kilometer(km), is the boundary with an older low titanium mare basalt [5]. These geologic units indicate that Mare Imbrium underwent prolonged magmatic activity and thus its subsurface stratigraphic structure might be very complicated.

CE-3 LPR is an ultra wide band impulse ground penetrating radar (GPR) operating at two channels - center frequencies of 60 and 500 MHz [6], The bandwidths of the two channels are 40 and 450 MHz, respectively, corresponding to a range resolution of 3.75 and 0.3 m in vacuum . Here, we report the results from the 60 MHz channel, because we need a level of hundred meters depth's subsurface structure results, and the other channel can't detect such depth. Figure 1 was taken by the descent camera of Chang'E-3 when the lander was lowered to around 150 meter height. The black line shows the motion path of Yutu rover. In order to increase the contrast of the 60 MHz data, to reduce the background, noise and the clutters' influence, the raw data were processed with repetitive observation removal, horizontal band removal, band-pass filtering and wave-front divergence compensation in layered medium structure [7]. Figure 2 shows the processed radar data image from G to L.

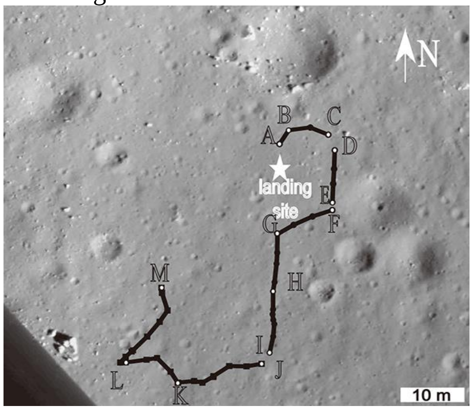

Figure 1. An image from CE-3 landing camera showing the route of the Yutu rover, the star is the CE-3 landing site, and A, … L, M are surface navigation points.

Subsurface Structure at the CE-3 Landing Site: From Figure 2 five layers can be recognized, named a, b, c, d, e, respectively. As the landing site is within an Eratosthenian-aged geologic unit, and the lower paty didn’t find any obviously basalt layer [8], so a is considered as Eratosthenian basalt. Figure 2 reveal that the basalts at the landing site extend to 28.5-35.0 ± 1.5 m with the relative dielectric constant 6.5 [9], which is well consistent with previous results of Scaber et al. (30-35 m, range from 10-63 m [10]), Hiesinger et al. (32-50 m, +11/-5 m [11]) and Chen et al. (15.65-43.72 m [12]).

There are two clear interface at depth ~30 m and ~40 m, and between these two interface, the echos are much lower than the layers a and c, which may indicate the region b is an relatively uniform layer, so the layer b is interpreted to be the paleo-regolith formed layer. And the layer thichness is between 5.5 to 9.2 m with an uncertainty ± 3 m.

The layer c have a thickness range from ~40 to ~60 m, and the echos in this layer are have the same characteristic of layer a, so the layer c is interpreted to be another basalt layer. As b is the weathering layer of c, so the real thickness of this layer ~26.6± 4.7 m.

The layer boundry depth of d and e is ~194.6 and ~ 339.6 m, respectively, which is well consistent with previous results of Pommerol A. et al. (Around 10 km north away from the landing site, the shallower interface 247 ± 127 m and the deeper interface 488 ± 210 m [13]), and layer d and e maybe the extend of these two layers. These two layer is interpreted to be basalt layer and the average thickness of these two layers are 136.6 ± 6.5 m and 145.0 ± 6.7 m, respectively. There are several horiz ~200 m depth, which may indicate several small eruption. Tab.1 shows the average thickness change of these four basalt layers.

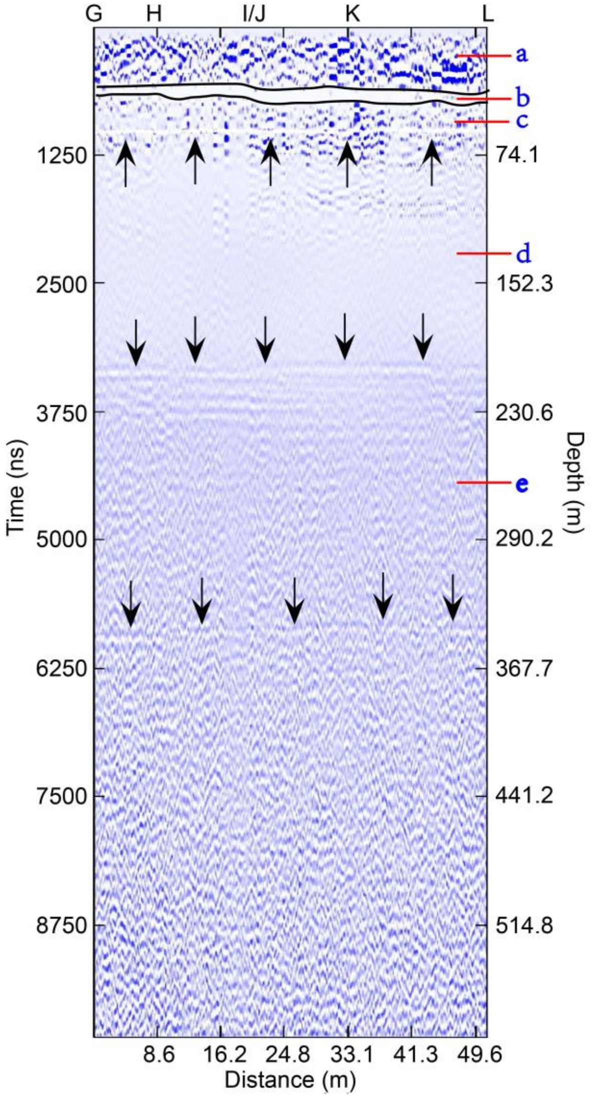

Figure 2. LPR image at 60 MHz from Point G to L along the Yutu survey line. The depth is calculate with dielectric constants 6.5.

Layer name	Thickness (m)	Uncertainty(±m)
a	28.5-35.0	± 1.5
b+c	26.6	± 3
d	136.6	± 6.5
e	145.0	± 6.7

Table.1 The average thickness change of four basalt layers.

Discussion: According to the LPR data, the near surface structure at the CE-3 landing site are very complex, and can be constructed as (from top to bottom): Eratosthenian period basalt layer a (~29.9 m) , paleoregolith layer b (~6.9 m), basalt layer c (~26.6 m), Mare Imbrium period layer d (~136.6m) and e (~145.0 m). Based on the estimated thickness of each basalt layer, Tab.1 shows the average thickness change of the four basalt layers detected by LRS. The most prominent feature of Tab.1 is the dramatic thickness change from layer d to layer c, indicating that the amount of lava flows drops with time and providing some hints of lunar internal energy history. Wilhelms et al. mentioned that many large magmatic activities occurred before the Eratosthenian period, but during the Eratosthenian period large magmatic activity stagnated and only small local magmatic activity happend[14]. In Tab.1, we can observe the thickness of basalt layer changes between d and b+c, which may imply the lunar internal energy change from Mare Imbrium period to Eratosthenian period.

Acknowledgements: CE-3 data were provided by the Lunar and Deep Space Exploration Department, National Astronomical Observatories, Chinese Acadmy of Sciences (NAOC). Supported by the Key Research Program of the Chinese Academy of Sciences (grant KGZD-EW-603), the Science and Technology Development Fund of Macau under grant No.048/2012/A2, 039/2013/A2, 091/2013/A3 and 020/2014/A1.

References: [1] J.W. Head and S.C. Solomon (1980) LPS. XI, ~421; [2] Head and L.Wilson, (1992) GEOCHIM COSMOCHIM AC, 56(6), 2155-2175; [3] Head, J. W. (1982) Moon and Planets, 26, 61–88; [4] Ono et al. (2009) Science, 323(5916), 909-912; [5] Bugiolacchi R. and Guest J.E. (2008) Icarus,197(1), 1-18. [6] Fang G. Y. et al. (2014) RAA, 14, 1607–1622; [7] Daniels D. (2004) London: IEE Press; [8] Lai Jialong et al. (2015) PSS; [9] Heiken G. et al. (1991) CUP Archive; [10] Schaber G.G. (1973) LPSC Vol.4 73; [11] Hiesinger H. (2002) GRL, 29(8),89-1; [12] Chen Y. et al. (2015) LPSC Vol. 46, p. 1806; [13] Pommerol A. et al. (2010) GRL, 37(3), 93-101; [14] Wilhelms, D. E. et al., (1987) No. 1348;[15] Quaide, W. & Oberbeck, V. (1975) The Moon, 13(1-3), 27-55;

NUMERICAL MODELING OF EJECTA DISTRIBUTION AND CRATER FORMATION OF LARGE IMPACT BASINS ON THE MOON.

M. -H. Zhu[1], [1]Space Science Institute, Macau University of Science and Technology, Macau, mhzhu@must.edu.mo.

Introduction: Large impact basins are the most prominent and oldest landforms on the Moon. Although only a relatively small number of roughly ~ 50-60 basin structures are known, these basin-forming impacts produce large volumes of impact melt and ejecta that may cover an area with a radius several times larger than the basin size. Only a few such events may have completely resurfaced the Moon by inverting the crustal stratigraphy, and by emplacing impact melt and originally deep seated crustal or mantel material into the near surface strata. Several attempts have been made to model the formation of impact basins using so-called hydrocodes [e.g. 1-5] using basin morphology and gravity signature as constraint. The ejecta distribution (thickness of the ejecta blanket as a function of distance) has not been considered due to the relatively poor preservation of the ejecta deposits of the old basins that have been modified by impact gardening. However, in a recent study the ejecta distribution at the youngest impact basin, Orientale, has been reconstructed [6] and serves as additional constraint for numerical modeling of basin formation [7]. We present a systamtic study of ejecta distribution at large impact basins as a function of impactor properties (size and velocity) and target properties (crustal thickness and thermal gradient). The goal is to predict the thickness, composition (crustal or mantle material) of the ejecta blanket as a function of distance.

Modeling: We used the multi-material, multi-rheology 2D iSALE [8,9,10] shock physics code to simulate basin formation. We carried out a suite of impact models: impact velocity: v=10, 20 km s^{-1}; impactor diameter L=50-100 km; crustal thickness h=30, 60 km; thermal gradients according to [1, 2, 3]. The rheological and thermodynamic behavior of the crust and the mantle material is modeled assuming as gabbroic and dunitic composition, respectively. The models consist of the ANEOS equation-of-state for gabbro and dunite, combined with a strength and damage model [10] using parameters according to [1, 11].

Ejecta Thickness Estimation: We use tracer particles that are initially placed at the center of each computational cell to record the launch angle and velocity at the time of ejection. Assuming pure ballistic flight of the ejecta, we reconstructed the parabolic trajectory of each tracer to calculate its velocity and deposition distance. We assume that each tracer represents the mass of the cell it was initially located in. The surrounding surface of the crater was subdivided into discrete concentric rings. The ejecta thickness was then calculated from the number of tracers that land in each ring.

Results: Fig. 1 shows the modeled ejecta thickness (L=100 km, v=12 km/s) as a function of distance from basin center for three temperature gradients. In all of the three different impact scenarios the total amount of ejected material is almost the same. The ejecta thickness decreases proportionally to a power-law with an exponent e = -3, which is similar to that derived from the laboratory experiments [12]. It indicates that the power-law function to parameterize the ejecta thickness as a function of distance can be extrapolated to large-scale impact basin. However, the decay exponent of the power-law function differs depending on the thermal gradient. For example, the ejecta deposit is thicker close to the crater rim and decreases more rapidly to a distance of 1400 km (3R) in the case of the warm target (e = -3.6) than for the cold target (e = -3.2). It is because that the launch angle of most ejecta is > 45° for the warm target but approximately 45° for the cold one. For the same velocity ejecta with a launch angle close to 45° are deposited the furthest whilst shallower or stepper ejection angles results in shorter deposition distances.

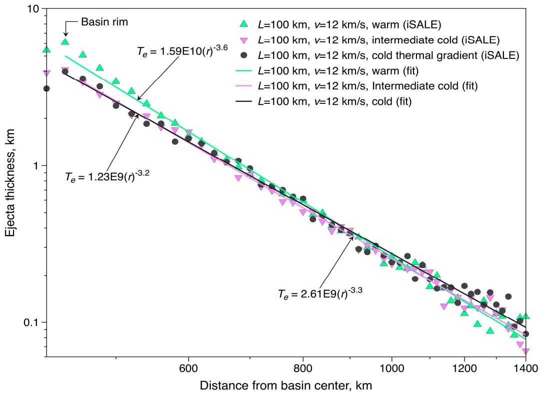

Fig. 1. The ejecta thickness of the vertical impact (L=100 km, v=12 km s^{-1}) on warm, intermediate, and cold target.

References: [1] Ivanov et al. (2010) *GSA Special Paper,* 465. [2] Miljkovic et al. (2015) *EPSL,* 409. [3] Potter et al. (2013) *JGR,* 118. [4] Potter et al. (2012) *JGR,* 39. [5] Melosh et al., 2013 *Science,* 340. [6] Fassett et al. (2011) *GRL,* 38. [7] Zhu et al. (2015) *LPSC,* Abstract #1832. [8] Amsden et al. (1980) LANLP, LA-8095. [9] Wünnemann et al. (2006) *Icarus*, 180. [10] Collins et al. (2004) *MPS,* 39. [11] Pierazzo et al. (2005) *GSA Special Paper*, 443. [12] Stöffler et al. (1975) *JGR*, 80.

TYPE DISTRIBUTION PATTERNS OF CAIS FROM DIFFERENT CHEMICAL GROUPS OF CARBONACEOUS CHONDRITES. D. DAI[1], C. ZHOU[1,2] and H. WANG[1,2]. [1]Institute of Geology, Hunan University of Science and Technology, ddqygf@163.com, [2]Institute of Geochemistry, Chinese Academy of Sciences, 1364049229@qq.com.

Introduction: Ca-, Al-rich inclusions (CAIs) provide an essential record of processes that occurred in the early solar nebula. Their isotopic anomalies, primordial ages (~4.568 Ga), and elemental compositions imply that they formed under nebular conditions prior to rocky planet formation[1].

CAIs may be texturally divided into coarse-grained and fine-grained inclusions. Most coarse-grained CAIs are compact Type A (melilite-spinel rich), Type B (melilite-fassaite rich) and Type C (anorthite-fassaite rich). The most common fine-grained inclusions are melilite-spinel rich (fluffy Type A) and spinel-pyroxene inclusions[2,3]. The most extensive studies of CAIs have been performed on carbonaceous chondrites.

In this paper, we report petrographic types of CAIs in order to investigate the type distribution patterns of CAIs from different chemical groups of carbonaceous chondrites.

Samples and Experiments: Some polished thin section was prepared for the 7 meteorites, i.g. GRV 020025(CM2), 021579(CO3), 022459(CV3), 023155(CV3), 050179(CM2), Allende(CV3), Murchison(CM2)[3,4].

CAIs were mainly located using the back-scattered electron (BSE) image mode of the electron probe microprobe analyzer (EPMA) JXA-8230 in the College of Earth Sciences, Guilin University of Technology.

Type distribution patterns of CAIs: *CAIs in CM2.* A total of 17 CAIs were found in the two sections of Murchison. All of the CAIs are heavily altered, with no melilite. 9 CAIs are referred to as fluffy Type A inclusions, other 7 assemblages are referred to as spinel-pyroxene inclusions, having spinel cores and Ca-pyroxene rims. All 4 CAIs in GRV 050179 are similar to fluffy Type A inclusions, although they are all heavily altered. 11 CAIs were found in GRV 020025. Six out of 11 CAIs are classified as fluffy Type A inclusions, and Spinel-pyroxene inclusions are the second most abundant CAIs in GRV 020025, with 4 inclusions found in the section. Only a spinel spherule was found in GRV 020025.

CAIs in CO3. Thirteen CAIs were found in GRV 021579. Spinel-pyroxene inclusions are the most abundant type of CAIs in GRV 021579, and 8 out of 13 were found. Four CAIs are referred to as fluffy Type A inclusions. Only one spinel-pyroxene inclusion is referred to as spinel-spherule, because of its rounded shape and occurrence of Ti-Al-rich Ca-pyroxene (fassaite) intergrown with spinel in the core. 88 CAIs were found in Yamato-81020. Type A inclusions are the most abundant (39 out of 88), and Spinel-pyroxene inclusions are the second abundant (23 out of 88). A unique feature of Yamato-81020 is abundant anorthite-pyroxene-rich inclusions (22 out of 88). These inclusions are similar to the anorthite-spinel-rich inclusions (ASIs) in the Ningqiang carbonaceous chondrite, and the latter were proposed to be produced by alteration of type As with melilite replaced by anorthite and Ca pyroxene[5]. The other 3 CAIs are grossite-rich (2) and fassaite-rich (1) assemblages.

CAIs in CV3. Sixty-two CAIs were found in 4 sections of Allende. Most of them (60 out of 62) are type A CAIs and spinel-pyroxene, and 5 CAIs are similar with CTA. Spinel-pyroxene inclusions are the second abundant (20 out 62). The 2 else CAIs are a fragment of the spinel-hibonite spherule and a hibonite-rich inclusion. All of the three CAIs in GRV 022459 are fluffy Type A inclusions. 4 out of 5 CAIs in GRV 023155 are classified as fluffy Type A inclusions, and only one spinel-pyroxene inclusion was found in the section.

CAIs in Ningqiang. One hundred twenty-three CAIs have been found in Ningqiang carbonaceous chondrites[6]. 117 out of 123 are Type A and spinel-pyroxene inclusions, and six coarse-grained RIs are probably once melted (3 type Bs, 2 POIs and 1 type C).

Discussion and Conclusions: The most extensively studied CAIs in CV chondrites, especially in Allende, are coarse-grained inclusions, such as Types B, C and compact Type A. This gave an impression of high abundances of the coarse-grained inclusions in these meteorites. The coarse-grained CAIs are usually millimeter- or centimeter -sized, so they can be easily recognized. In contrast, hibonite-rich inclusions are the most intensely studied CAIs in CM chondrites[7], because hibonite is one of the earliest condensates and its typical blue color can be easily recognized. However, it is obvious that the different chemical groups of carbonaceous chondrites contain similar CAIs. The two predominant petrographic types of CAIs are fluffy Type A and spinel-pyroxene inclusions. Most CAIs in the chondrites that are classified into different chemical groups share similar type distribution patterns, and this discovery suggests a similar origin of CAIs in various chondrites.

Acknowledgements: This work was supported by the Natural Science Foundation of China (Grant No. 41103032) and Scientific Research Fund of Hunan Provincial Education Department (Grant No.15B080).

References:[1] Amelin Y. et al. (2002) *Science, 297,* 1678-1683. [2] Lin Y. et al. (2006) *MPAs, 41,* 67-81. [3] Dai D. et al., (2004) *Acta Geologica Sinica, 78,* 1042-1051. [4] Dai D. et al., (2015) *Earth, Moon and Planets, 115,* 101-114. [6] Lin Y. and Kimura M. (1998) *MPAs, 33,* 435-446. [6] Lin Y. and Kimura M. (2003) *GCA, 67,* 2251-2267. [7] Ireland T. (1988) *GCA, 52,* 2827-2839.

H_2O ICE LAYERED DEPOSITS ON THE NORTHERN PLAIN OF MARS.

S.S. Krasilnikov[1,2], R.O. Kuzmin[1,3], [1]Vernadsky Institute of Geochemistry and Analytical Chemistry of RAS, 119991 Moscow, Russia, zergovski@geokhi.ru, [2]Moscow State University of Geodesy and Cartography, Moscow, Russia, [3]Space Research Institute of RAS, 117342 Moscow, Russia.

Introduction. Permanent north polar cap is mostly composed of the polar layered deposits (PLD) and has basically ice H_2O composition [1,7]. This layering suggests the consecutive accumulation of ice over a long period with different impurity fraction of dust (fig.1). PLD compose of 70% of H_2O ice volume and 30% of dust material [1,3]. The isolated remnants of ice deposits with similar layered structure are located outside of polar cap edge (fig.2).

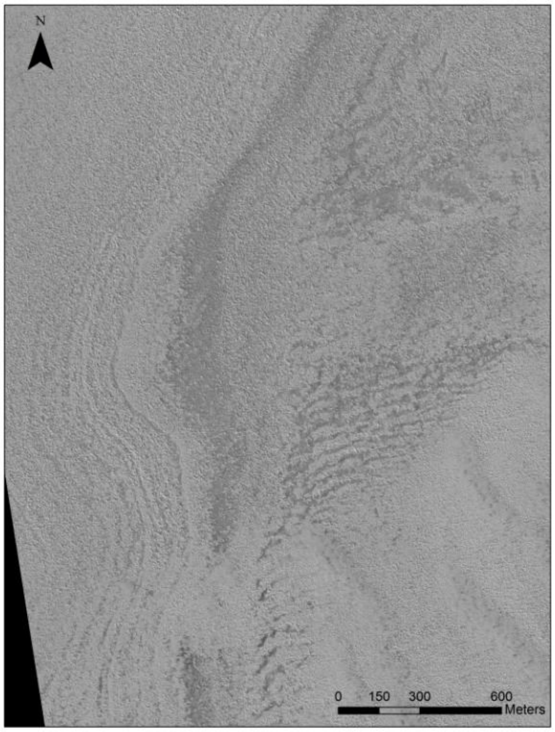

Fig.1. The massif of ice H_2O layered deposits. The image with high resolution of HiRISE camera ESP_027637_2545 with 74,5 °N 97,8 °E coordinates.

Types of layered H_2O ice deposits massifs around the northern polar cap. In conducted research we found two groups of ice and snow deposits spreading on the Martian northern plain. In these groups multi-year ice sheet of ice/snow H_2O was distinguished excluding layered structure and massifs of layered ice H_2O deposits. These multi-year ice/snow massifs are distinguished well on the CRISM's mosaics of the spectral index of H_2O ice (mapped on 1,5 μm wavelength) and don't show visible layered structure. The absence of the layered structure says about intermediate stage of ice deposits formation with positive or negative dynamics of evolution. Positive dynamics of H_2O accumulation make possible formation of multi-year ice/snow. Negative dynamics for H_2O means degradation of ice layered massifs, which resulted to camouflaging of a layered structure. For systematic analysis of an ice deposits spreading, we used both the CRISM's mosaic of the water ice spectral index images for the northern polar area, mapped during the summertime Ls = 128 °–160 ° [1] and the mosaic of THEMIS IR day images [2].

For morphological study of layered H_2O ice deposits massifs, we analysed a high resolution CTX and HiRISE images. Based on this analysis we distinguished several morphological types of layered H_2O ice deposits massifs with different location. Conducted morphological analyses let us to divide the formations in two groups [5]:

1. Layered H_2O ice deposits massifs overlapped the plain surface.
    a. Fully or partly overlapped crater/crater rim;
    b. Located on the crater floor and on the outers craters slopes;
    c. Located on the crater floor like isolated massifs;
    d. Located on the plaine surface.
2. Layered H_2O ice deposits massifs which are covered by younger eolian deposits.

In the first group we included the layered ice deposits massifs, which overlapped other landforms. Second group includes areas with layered ice H_2O deposits which are exposed from younger eolian deposits.

Depending on ice deposits massifs location on the surface they are subjected to different influence of the solar radiation. For example, at notably rough surface and craters gain shadows and a local temperature may to be reduced fall. It allows to saving the ice deposits in the summertime in the studied area within 70 ° - 85 ° belt of northern latitudes.

Our mapping results show that depending of degradation extent of H_2O ice layered deposits some latitudinal zonality in spreading of the landforms is detected.

Full or part overlapping of craters by polar cap ice H_2O layered deposits are observed in the marginal zone

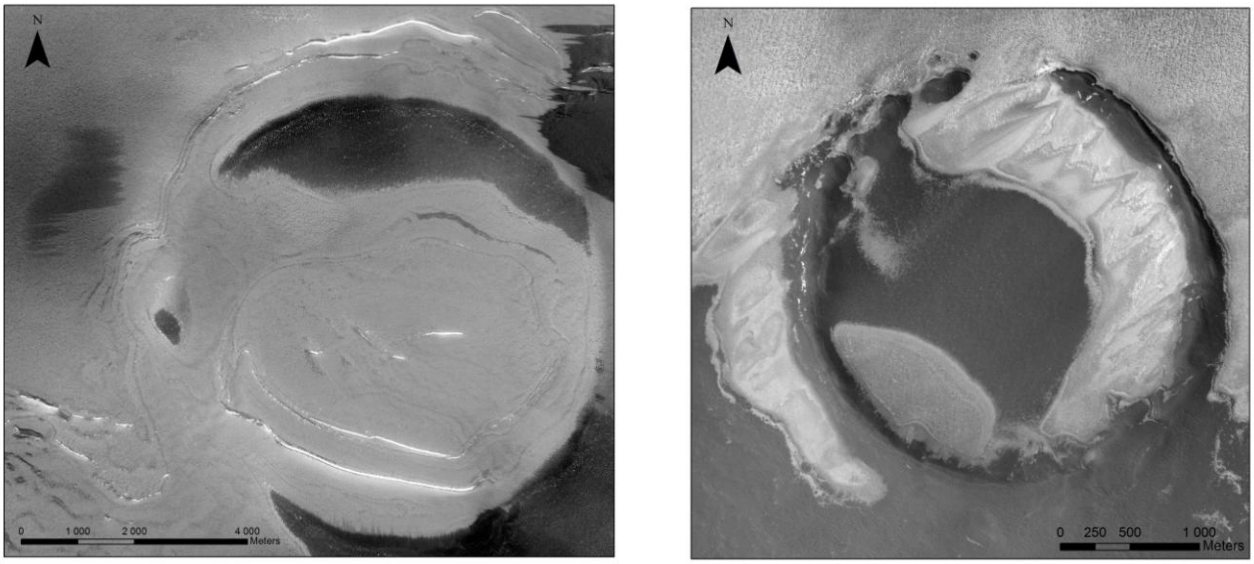

Fig.2. Filling of crater by the ice H_2O layered deposits outside of polar cap edge (left, CTX B21_017825_2587_XI_78N226W) and similar deposits in the crater inside of polar cap (right, CTX P22_009577_2604_XN_80N051W).

of the northern polar cap. Outside of polar cap the H_2O ice layered deposits could be accumulated on the shaded rims of craters and go down to the floor (mean latitude of spreading is 75 ° – 80 ° of northern latitudes) (fig.2). To the south, the H_2O ice layered deposits occupy outer craters slopes and on the crater floor (mean latitude of spreading is 77 °– 79 °of northern latitudes). More to the south, the layered ice deposits occupy the crater floor and often are overlapped by younger eolian deposits (mean latitude of spreading is 71 ° – 77 ° of northern latitudes).

South of 70 ° northern latitudes layered deposits within the impact craters without ice are spreading. It is not excluded that these layered deposits were formed due to sublimated of the ice layered deposits filled the craters interiors. On the 70,4 °N 266,4 °E and 67,2 °N 249,5 °E two unique objects in the form of lobate moraine-like ridges (LMLR) on their inner craters slopes and concentric moraine-like ridges (CMLR) on the outers slopes were observed [4,6]. That can be interpreted as the ice avalanche on the inner crater slope [6] and slowly viscoplastic movement of ice deposits on the outside slopes. The presence of such landscapes testifies that local massifs of water ice deposits might to be accumulated on the crater's rims on this latitudes during a previous climate epochs.

Conclusion. Observing similarity of layering structure between H_2O ice layered deposits massifs and ice layered deposits of the northern polar cap may indicate on similar genesis of both deposits types. Possibly, the studded H_2O ice layered deposits massifs might represent relicts of more extensive northern polar cap existed in the previous climate epochs.

Acknowledgements. Krasilnikov S.S. worked on geomorphological analysis at MIIGAiK and was partly supported by Russian Science Foundation, project #14-22-00197. We acknowledge Shkarbanenko K.V.

References: [1] Brown A. J. et al. (2012) *JGR*, 117, 19 p. [2] Christensen P. R. et al. (2004) *Space Sci. Rev*., 110, 85–130. [3] Cull S. et al. (2010) *JGR*, 115, 14 p. [4] Garvin J. B. et al. (2006) *Meteorit. Planet.*, 41, 1659–1674. [5] Krasillnikov S. S. (2013) *Lomonosov 2013 conf*, 2 p. (In Russian). [6] Krasilnikov S. S. et al. (2016) *LPS 47th*, Abstract 1881. [7] Zuber M. T. et al. (1998) *Science*, 282:2053–60.

SHOCK-PRODUCED BASALTIC BRECCIA IN THE XIUYAN IMPACT CRATER, CHINA.

F. Yin and X. Y. Chen. Department of Geology, Hunan University of Science and Technology, Xiangtan 411201, China. E-mail: fengite@hotmail.com.

Introduction: The Xiuyan impact crater, a bowl-shaped simple crater about 1.8 km in diameter, is located in Liaoning Province of northeast China. The crystalline basement rocks of the crater is made up of the early Proterozoic metamorphic rocks composed of granulite, amphibolite, gneiss, tremolite marble, and marble. A borehole was drilled in the center of the crater revealed that the crater is filled by the upper 107 m thick lacustrine sediments and the lower 188 m thick impact breccias [1]. The impact breccia unit is loosely consolidated and consists mainly of lithic impact breccias and some suevites [2]. The lithic impact breccia is composed of gneiss, granulite, amphibolite, basalt and marble fragments up to 30 cm in size, and mainly occurs in the depth interval of 107-260 m. The suevite mainly occurs in the depth interval from 260 to 295 m. The suevite is composed of fragments of gneiss, granulite, amphibolite, quartz, and feldspar, fine-grained matrix, as well as glass inclusions. A basaltic breccia is clarified from the lithic breccias of the crater. Here we report the preliminary investigation in shock metamorphic features of the basaltic breccia.

Results and discussion: The basaltic breccia consists of a number of basalt fragments and 20-30 percent fine-grained matrix (Fig.1). The basalt fragments are angular and subangular and have grain sizes ranging from 0.2 to 3 cm. No shock metamorphic features are observed in the basalt fragments. The fine-grained matrix essentially consists of subangular mineral clasts, predominantly feldspar, pyroxene and quartz. Other clasts are basalt, calcite, and amphibole. Some of the mineral clasts show undulatory extinction and randomly oriented, nonplanar irregular fractures. These shock effects indicate shock pressure < 10 GPa [3]. Quartz with multiple planar deformation features (PDFs) was identified in the matrix. But only 2 percent of quartz grains in the matrix display PDFs. One to two sets of PDFs are observed in a single quartz crystal (Fig. 2). 29% of the quartz grains with PDFs contain 2 sets of PDFs. The PDFs are rhombohedron forms of $\omega\{103\}$, $e\{104\}$, and $\pi\{102\}$ with frequency of 83.9%, 12.9% and 3.2%, respectively. The predominant occurrence of PDFs {103} + {104} in quartz suggests a shock pressure 10-20 GPa [4]. The occurrence of irregular fractures and undulatory extinction in mineral clasts and of PDFs in quartz from the basaltic breccia provides crucial evidence for shock metamorphism of target rocks and confirms the impact origin of the basaltic breccia.

Fig.1. Basaltic breccia composed of basalt fragments and fine-grained matrix

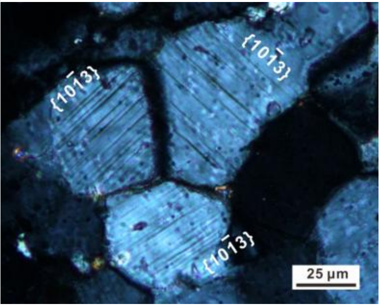

Fig.2. PDFs in quartz grains in cross-polarized light.

References: [1] Chen M. et al. (2010) Chinese Sci. Bull., 55, 1777-1781. [2] Yin F. and Chen M. (2014) Contrib. Mineral. Petr., 167, 999. [3] Stöffler D. et al. (1994) Meteorit. Planet. Sci. 29, 155-181. [4] Grieve R. A. F. et al. (1996) Meteorit. Planet. Sci. 31, 6-35.

Acknowledgements: This work was supported by National Natural Science Foundation of China (41503062 and 41372209).